Bioinspired MWCNT-reinforced alumina composite materials



Koen Evers

Mansfield College

University of Oxford

A dissertation submitted for the degree of

Doctor of Philosophy

Trinity 2019

Dedicated to my parents

Herman Evers & Carla Kaandorp

for their love and support

and for the wizard's wand that got me through Hogwarts.

Abstract

Nacre, a ceramic composite found in seashells, has baffled scientists due to its extraordinary mechanical properties. Consequently, nacre has been a main source of inspiration to create strong and tough ceramic composites that mimic nacre's microstructure. The precise microstructural features responsible for its unique combination of high strength and toughness are however debated, and efforts to mimic and improve upon nature's design have not led to commercial applications of ceramic nacre-like composites.

This dissertation details the replication of nacre's microstructural architecture with technical ceramics and nanomaterials. Instead of nacre's calcium carbonate building blocks, alumina was used, and instead of its organic phase, multi-walled carbon nanotubes (MWCNTs) were incorporated. To design a nacreous microstructure, freeze casting of alumina nanoparticles was used to template a microstructure of aligned lamellae over macroscopic length scales. Although successful, the fabricated lamellar microstructures' macroscopic orientation was hard to consistently reproduce using this technique and the resulting composites, unlike nacre, fail in a completely brittle fashion. Therefore, alumina platelets that closely resemble the platelets in nacre were investigated. A recipe to homogeneously coat these platelets *in situ* with MWCNT was developed, and MWCNT growth and catalyst modification was studied in-depth. The resulting combined building blocks were sintered into a composite that displays a graceful failure mechanism like nacre does, with several toughening mechanisms observed to be active. In addition, nacre-like alumina/MWCNT composite materials have been synthesised using a variety of MWCNT dispersion techniques. All studied nacre-like composites showed characteristic macroscopic interlocking behaviour and remain interlocked after crack initiation which prevented complete failure and gave these composites a residual strength. Pure nacre-like alumina specimens have also been tested in high strain rate and impact tests, where these materials showed a significant improvement over non-textured alumina.

Acknowledgements

During my DPhil I have had the pleasure of meeting and working with many extraordinary people, whom I would like to gratefully acknowledge.

First and foremost, I would like to express my gratitude to Professors Nicole Grobert and Richard I. Todd, who believed in me and gave me both intellectual freedom and support whenever I needed it. They took me into their research groups which became like a family and resulted in friendships that will last for many years to come. Their supervision during my project was invaluable to the development of the project and my personal development as well.

Within the *Nanomaterials by Design* research group, I would specifically like to mention Shayan Meysami whose enthusiasm for science inspired me. I owe him a debt of gratitude for always being there to give advice and training on all things CVD during the start of my Dphil. I would also like to acknowledge Vitaliy Babenco for his scientific rigour and for spending valuable time to try to develop methane-based CVD growth of carbon nanotubes on my scaffolds. Frank Dillon not only taught me safety within the lab, I gained particular skill in understanding the Irish accent. I was lucky to be surrounded with a wonderful NbD team, who created a great atmosphere both socially and scientifically. I would like to extend a huge thank you to Pablo, Albert, Pierre, Jesus, Ruth, Santamon, Karwei and especially Dominique who taught me how to create SPIONs and who took initiative organising amazing trips and get-togethers that will stay with me as valuable memories. I am very grateful to Ruth, Santamon and Jesus who all read parts of this dissertation and provided valuable feedback. A special thanks to Thomas Ibbetson, Adam Mellul and Gil Chambers who did their research projects under my supervision. They always kept positive and pushing forward no matter what difficulties the freeze casting technique threw at them.

Within the *Ceramics* research group, Tom, Jiawei, Alexander, Andrew, Mi and Jesse made sure there was always a place for me in the heart of the materials department, even though I gave away my desk space halfway through the DPhil. They, and close neighbours Sue and Nipho, provided a relaxed working environment where everyone was keen to help each other.

Other groups within the Department of Materials also met me with welcoming arms. I would like to thank Professor Jason Smith for being an approachable and interested advisor and for keeping in touch by organising termly materials' drinks at Mansfield College, Professor Patrick Grant for granting access to his Fast Sintering Press, Professor Andrew Watt for allowing me to use his four point probe, and Professor James Marrow for allowing access to his X-ray Microscope Facility and 3pt bend Jig. Andrew Lui kindly provided trial tomography images on my samples, Flynn Castles did not pause for one moment to 3D print freeze-casting moulds for me, and Phil Earp showed me how to use Aviso software and GOM Aramis adjustable camera system. Professors Andrew Watt, Jan Czernuska, and James Marrow provided valuable feedback and advice in their function of assessor during my transfer and confirmation vivae.

I would also like to acknowledge the invaluable contributions of support staff. Radka Chakalova put in many hours to train and help me with cutting my samples on the dicer, even when blades where being damaged, and was always there for me when I needed ultra-pure water. Jeffrey Fullerton helped cutting high impact samples. Philip Holdway helped run XRD experiments. Greg Cook was always there when equipment was broken and provided much needed vacuum pump maintenance and SEM support. Richard Turner supported me when it came to the handling of compressed gas cylinders and electronics such as the camera setup and PID temperature controller. Robin Vincent was an incredible help, machining parts for my freeze casting setup, ranging from copper to acrylic and insulating foams. Tony Wheeler trained and supported me in the materials workshop, even manufacturing a whole new piece to fit my sample in a flatbed grinder. OMCS staff was always there with impeccable maintenance and support of characterisation equipment.

During my DPhil I collaborated with, visited, and learned from other research groups. In this regard, I would like to express my deep gratitude towards Claudio Ferraro who taught me how to freeze cast at Imperial College London, his time and effort shall not be forgotten. Todd Rushing invited me to the ERDC in Vicksburg, Mississippi, where I got the chance to see their research, present my work and test samples using their facilities. Harshit Porwal showed me Queen Mary University of London where we devised a collaborative project of which parts ended up in my first 'first author' paper. Simone Falco's enthusiasm to shoot at ceramics lead to another paper and enjoyable collaboration.

I am thankful to Mansfield College for its provisions, giving me the unforgettable and unique experience that I could never dream of. I am grateful to my brother Rik Evers for his review of parts of this dissertation and for putting things in a black and white perspective. I am also grateful to Sam and Dean Winchester who provided supernatural support when I needed it most.

Finally, I would like to acknowledge my funding bodies; my University and College fees were covered by full-time EPSRC DTP studentship #EP/M508111/1. A stipend towards my living costs was provided by ERDC grant #W911NF-12-1-0616, combined with funds from Professor Nicole Grobert and the Materials Science department of the University of Oxford. In addition, I like to acknowledge financial support in the form of travel grants from the Society for the Advancement of Material and Process Engineering (SAMPE) and Mansfield college.

Declaration

This dissertation is submitted for the degree of Doctor of Philosophy in Materials Science at the University of Oxford. No part of this dissertation has been accepted or is currently being submitted for any degree, diploma, certificate or other qualification in this University or elsewhere. This dissertation is entirely my own work, except where indicated.

Publications

The following published journal articles relate to the work conducted in this dissertation:

Chapters 3,5

MWCNT-coated alumina micro-platelets for nacre-like biomimetic composites
K. Evers, H. Porwal, R.I. Todd, and N. Grobert. *Carbon (2019)*
https://doi.org/10.1016/j.carbon.2019.01.060

Chapters 4,5

Nacre-like alumina with unique high strain rate capabilities
K. Evers, S. Falco, N. Grobert and R.I. Todd. *Journal of the European Ceramic Society (2019)*
https://doi.org/10.1016/j.jeurceramsoc.2019.09.015

Contents

Abstract i

Acknowledgements ii

Declaration v

Publications vi

Chapter 1 – Introduction 1

1.1 The need for fracture-resistant ceramics 1

1.2 Biological materials and bioinspiration 2

1.3 Nacre 4

1.3.1 The mechanical properties of nacre 4

1.3.2 Sliding of platelets 12

1.3.3 Role of the interface in nacre 14

1.4 Materials inspired by nacre 20

1.4.1 Nacre-like thin films 20

1.4.2 Lamellar freeze cast composites 20

1.4.3 Composites using micron-sized platelets 21

1.4.4 Choice of interface in bio-inspired composite materials 22

1.5 Carbon nanotube reinforcement 25

1.5.1 Types of carbon nanotubes and their properties 25

1.5.2 Influence of microstructure and defects on the mechanical response of CNTs 26

1.5.3 Tensile experiments on single CNTs 27

1.5.4 MWCNTs in composite materials 30

1.6 Aim of dissertation 33

Chapter 2 – Freeze-casting nacre-like porous scaffolds 34

2.1 Introduction 34

2.1.1 Freeze-casting 34
2.1.2 Lamellar freeze-casting 35
2.1.3 Current methods to achieve lamellar alignment 37
2.1.4 The effect of additives in freeze-casting 40
2.2 Materials and methods 43
2.2.1 Ceramic slurry 43
2.2.2 Freeze-casting 44
2.2.3 Sample preparation and characterisation 46
2.3 Results and discussion 47
2.3.1 Controlling the microstructure 47
2.3.2 Upscaling and reproducibility 49
2.3.3 Freeze-casting of alumina platelets 53
2.4 Conclusions 56
Chapter 3 – MWCNT growth and coating of bioinspired alumina. 58
3.1 Introduction 58
3.1.1 Carbon nanotube growth through chemical vapour deposition 58
3.1.2 Key CVD parameters for CNT growth on bioinspired alumina 61
3.2 Materials and methods 62
3.2.1 Acid treatment of scaffolds 63
3.2.2 Catalyst particle creation and dispersion procedure 64
3.2.3 CVD synthesis of MWCNTs on alumina 66
3.2.4 Substrate materials 69
3.2.5 Characterisation 70
3.3 Results and discussion 71
PART A - *In-situ* MWCNT-infiltration of freeze-cast alumina scaffolds 71
3.3.1 Catalyst-free CNT growth in freeze-cast alumina scaffolds 71
3.3.2 CVD with ultra-small iron oxide nanoparticles 79
3.3.3 CVD with commercial iron oxide nanoparticles 81

PART B - *In-situ* coating of MWCNTs on alumina platelet powders....84
3.3.4 Aerosol assisted CVD using ferrocene....85
3.3.5 CVD using commercial iron oxide nanoparticles - Effect of annealing and H_2....87
3.3.6 Improvement using wet catalyst dispersion....89
3.3.7 Effect of annealing atmosphere on MWCNT crystallinity and growth....90
3.3.8 Catalyst immobilization through spinel formation....92
3.3.9 Stability of the catalyst during CVD....95
3.3.10 MWCNT growth from iron oxide coated alumina platelets....98
3.4 Conclusions....100
Chapter 4 – Formation and properties of nacreous alumina 102
4.1 Introduction....102
4.2 Materials and methods....104
4.2.1 Ceramic manufacturing....104
4.2.2 Characterisation....105
4.2.3 Three-point bend testing....105
4.2.4 Split Hopkinson pressure bar testing....106
4.2.5 Impact testing....107
4.3 Results and discussion....109
4.3.1 Sintering and microstructure of nacre-like alumina....109
4.3.2 Mechanical response in bending....113
4.3.3 Influence of nanoparticle inclusions....117
4.3.4 Mechanical response under dynamic loading....119
4.3.5 Mechanical response upon impact....121
4.4 Conclusions....126
Chapter 5 - Nacreous MWCNT/alumina composites 127
5.1 Introduction....127
5.1.1 MWCNT/alumina composite materials....127
5.1.2 Acid treated MWCNTs in alumina matrices....128

5.2 Materials and methods....130
5.2.1 MWCNT dispersion method....131
5.2.2 Glass phase coating method....134
5.2.3 Sintering method....135
5.2.4 Density measurements....137
5.2.5 Characterisation....138
5.3 Results and discussion....139
PART A – Bioinspired alumina scaffolds....140
5.3.1 Freeze-cast MWCNT-infiltrated composites....140
PART B – MWCNT-coated alumina platelets – Low temperature sintering....143
5.3.2 Nacre-like composites using sonicated MWCNTs....143
5.3.3 Nacre-like composites using acid treated MWCNTs. 145
5.3.4 Nacre-like composites using graphite reinforcement. 152
PART C – MWCNT-coated alumina platelets – High temperature sintering....154
5.3.5 Alumina platelets with powder mixed MWCNTs....154
5.3.6 Nacre-like composites using CVD-grown MWCNTs – Densification. 158
5.3.7 Nacre-like composites using CVD-grown MWCNTs – Mechanical properties. ...162
5.3.8 Viability of the CVD approach in lab-scale composite manufacturing....167
5.3.9 Nacre-like composites using shear mixed MWCNTs 172
5.3.10 Nacre-like composites using MWCNT aerogels....177
5.3.11 Nacre-like composites using graphite inclusions 180
5.3.12 Glass phase coating of nacre-like alumina platelets....182
5.4 Conclusion....188
Summary and Outlook **190**
Bibliography **194**

Chapter 1 – Introduction

1.1 The need for fracture-resistant ceramics

One of the main challenges in Materials Science is to create ever stronger and tougher materials for applications where high loads are present. A main materials-design problem in that regard is that strength and toughness, the two key structural properties, tend to be mutually exclusive[1]. When trying to toughen materials, fracture toughness is often achieved at the cost of strength.

For engineering applications such as aircraft parts, jet engines, armour, nuclear containment vessels, gas pipelines, and medical implants, many types of steel alloys have been developed[2]. However, ceramic materials have covalent or ionic bonds between atoms which are much stronger than metallic bonds, generally resulting in much stronger materials[3], even more so if we consider their specific strength. The fact that ceramics are generally much lighter than steel, also means that by using ceramics we can save a significant amount of fuel or energy and at the same time help satisfy the global requirement of reducing CO_2 emissions. In addition, ceramics can withstand very high temperatures, do not corrode and have in addition to their superior strength, high hardness values (and thus wear resistance).

The reason that ceramics are often not suitable for many of the applications where steel is used nowadays, is their low toughness due to their brittle nature; they are unable to relieve stress by yielding. Flaws that are present in a ceramic material are crack initiators; bigger flaws concentrate stress and cause the material to fail catastrophically. In most engineering applications, catastrophic failure is simply not a viable option.

Another disadvantage of ceramics (with the exception of glasses) is that they cannot be shaped and machined as easily as metals. Instead, ceramics have traditionally been formed

into complex shapes by using different types of casting whereby ceramic powders are moulded into a temporary shape, often by mixing with liquids and binder materials. This temporary shape, called a "green body", is then sintered at high temperature with or without applying pressure to densify the material. Another way to shape ceramics is by making a cement; ordinary cement consists mainly of calcium silicate powder, mixed with water. In the case of cement, bonds are formed chemically through hydration reactions, and the formation of ionic-covalent bonds "cure" the cement. However, this is not a densification process; the hydration reaction is accompanied by an increase in volume. Even in reinforced cements, entrapment of air and incomplete packing of particles give cement inferior properties to those of pure ceramics.

To exploit the properties of ceramics in engineering applications, the main objective is to overcome their brittle nature by improving their fracture toughness while retaining high hardness and strength values. The large number of potential applications for such materials is a huge incentive to look for ways around the brittle nature of ceramic materials.

1.2 Biological materials and bioinspiration

In the past decade, scientists have discovered that ceramics that do not fail in a brittle manner already exist in nature in the form of composites; through millions of years of evolution, animals and plants have evolved to be maximally adapted to their environment, and their natural tissue has evolved with them. Through the principle of 'Survival of the Fittest', biological materials resulting from different evolutionary pathways can be expected to have outstanding properties tailored to their function. The realization that increased efficiency, optimization and specialization are common forces in both biology and engineering is the reason that the field of materials science, which emerged in the 1950s, began to look seriously at these materials from the 1990s onward[4]. Biological materials such as wood, bone, coral and nacre are composite materials (which all biological materials are, in one form or another[5]) which have outstanding mechanical properties that outperform their individual counterparts

in a way that modern science has not reproduced as of yet. This is where bioinspiration turns into the goal of biomimicry, with the promise of using the architecture nature provides to create composite materials which are lighter, stronger and tougher than existing materials.

However, as Fratzl[6] points out, when we let biological materials inspire us to design better materials, we have to take into account that evolution is done under biological constraints, and that the end product which we see now is not an optimisation of mechanical properties alone. For example, our bones are also the body's ion reservoir and has a function in calcium homeostasis in addition to providing the body with a strong, tough, and self-healing structure – the problem solved by nature is one done under constraints that are not the same as those we have when developing a new material.

A major advantage we have over natural organisms is the choice of materials; most of the structural materials used by nature are polymers or composites of polymers and ceramic particles[6], while we have a much greater choice and can incorporate for example metallic elements which are very rare in biological tissue, or make use of tailored molecules synthesized in the lab.

While from the above it may seem that we have fewer constraints than nature imposes on biological materials, both in choice of element and function, nature works under the principles of (biologically controlled) self-assembly. The final result in natural materials is obtained by an algorithm embedded in a genetic code instead of by replication of a design. External factors can influence the execution of the algorithm without any change in the genetic code, changing the direction of growth or even the structure itself. Self-assembly through this process provides hierarchical control over the structure at all length scales and this is nature's key to successfully creating a biological composite material[6,7].

1.3 Nacre

One of the most interesting materials from a mechanical point of view is nacre. Nacre, also known as mother of pearl, is the skeletal structure found in Gastropoda, Bivalvia and Cephalopoda mollusc shells, and is much stronger than any other mollusc shell structure independent of the type of loading[8]. Nacre is a ceramic/organic composite consisting of 95% aragonitic $CaCo_3$ platelets and ca. 5% organic material[7,9]. It consists of lamellar platelets approximately 0.5 μm thick[7,9] and 5-10 μm wide[1] arranged in a 'brick-and-mortar' structure in an organic matrix of 20-50 nm thickness[10]. Layers of organic material of 20 μm have also been identified in Abalone nacre[7], of which it is thought that these form during periods of minimal shell growth. These separate the 'brick-and-mortar' layers of around 300 μm thick. Gosline *et al.* [11] suggest only a high concentration glycine and alanine while more recently Levy *et al.*[12] find five major amino acids in the organic material in nacre: glycine (29%), valine (24%), lysine (21%), leucine (8.3%) and arginine (4.3%).

1.3.1 The mechanical properties of nacre

The strength of nacre

The mechanical properties of nacre were for the first time investigated by Currey[8,11,13,14] in 1976. Further studies emerged in the 21st century. From all the reported strength values in literature[9,11,15–17], it can be concluded that nacre is strongest when broken 'across' brick-and-mortar layers (Figure 1.1). From the data available in the literature, it can be concluded that

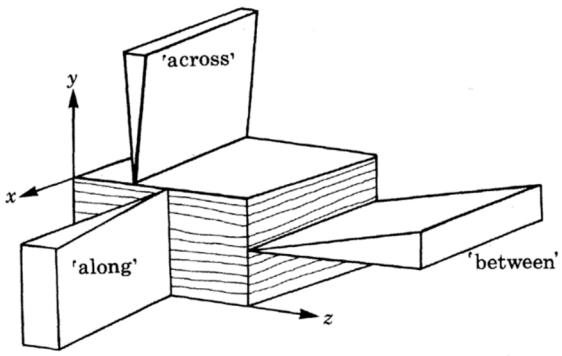


Figure 1.1 – Wedges showing the directions in which the cracks travel, assigning nomenclature for cracks travelling in different directions in nacre. The ''along'' direction is often called ''parallel'' and the ''across'' direction is called ''perpendicular'' direction. (Adapted from Currey *et al.*[8])

the strength of nacre is highly dependent on the species, but is generally measured to be around 200 MPa in flexural tension, with a compressive strength between 400-600 MPa[14]. To know how much of an enhancement the nacre structure gives in terms of strength, it is vital to compare the measurements of the strength of nacre with the strength of monolithic aragonite (calcium carbonate).

In the literature two values for the strength of monolithic aragonite are reported: 30 MPa[4,18,19] and 100 MPa[20–22] Note that all of these authors do not reference their values or give information on how this strength value is obtained, or often even what kind of strength it represents. No conclusive experimental or theoretical data on the actual strength value of monolithic aragonite could be found. It is therefore not clear what the exact improvement on strength is.

This is likely due to the fact that in ceramic materials such as calcium carbonate, the strength is dependent on the critical flaw size. In contrast to ductile materials, ceramics are brittle materials where macroscopic plastic deformation is essentially absent. Their strength depends not only on how much stress or strain the material can endure, but is mostly a function of the presence and distribution of defects, *e.g.*, microcracks[23]. So, in brittle materials, the fracture stress will not be a material constant like the yield strength in metals but will depend on the size of pre-existing defects. Getting an absolute value for comparison may be even more meaningless, as flaws in monolithic aragonite may differ significantly from those in the platelets of nacre due to their different modes of formation, and as a result the influence on strength of the brick-and-mortar structure of nacre is difficult to ascertain. Tensile strength values around 200 MPa are however quite high for a material which is built up for more than 95% of a relatively weak material like calcium carbonate. In addition, we observe a completely different mechanical response in nacre compared to monolithic ceramics, in which not brittle fracture but a more ductile, graceful failure is observed, as seen in Figure 1.2.

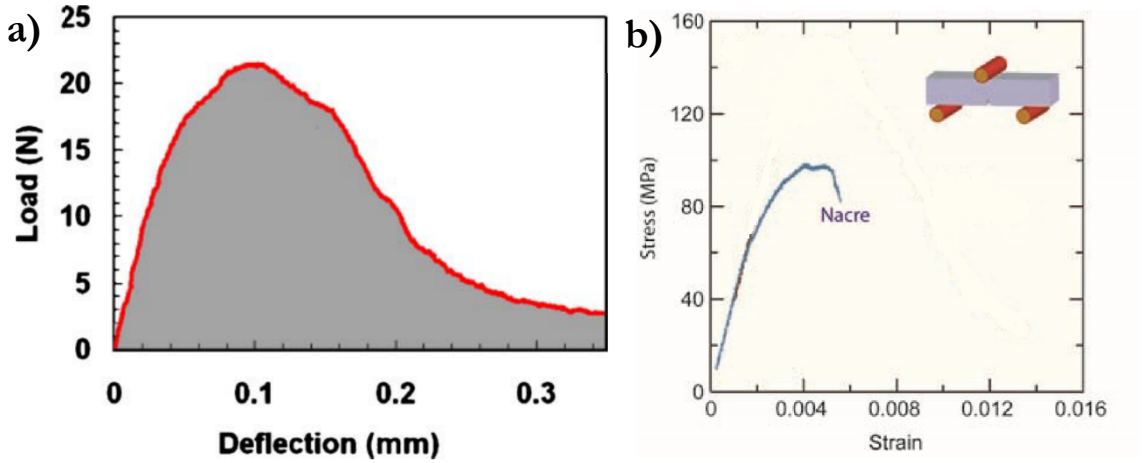


Figure 1.2 – a) Load deflection curve (Adapted from Barthelat *et al.*[51]) and b) stress strain curve (Adapted from Munch *et al.*[80]) for a nacre specimen in a three-point bend experiment.

The size of the platelets in nacre is an important consideration with respect to material strength. In monolithic ceramic materials, large flaws can locally intensify the stress in a material, and initiate crack growth, resulting in a much-reduced apparent strength. This strength variance is calculated by Lin *et al.*[24] for aragonitic platelets. Since critical flaws within an individual platelet greater than the platelet size are not physically possible, we can substitute critical crack size for platelet size and conclude that the strength of individual platelets increases with decreasing platelet size.

On the nanoscale however, there may be another effect that is in drastic contrast to the classical engineering concept of stress concentration at macroscopic flaws. Gao *et al.*[25] calculate that there exists a critical thickness of platelets, below which the material becomes insensitive to flaws due to uniformization of the stress field, and below which the strength equals that of a defect-free crystal. They approximate that this critical thickness is 30 nm. Although nacre platelets have a thickness of several hundreds of nm, Gao *et al.*[25] show that even for bigger platelets, the strength is improved over a bulk material, approaching the theoretical strength of a perfect crystal the thinner the platelets get.

The toughness of nacre

The fracture toughness properties of nacre were for the first time determined by both Currey[8,11,26,27] and Jackson *et al.*[15]. From these initial reports by Currey and Jackson, researchers have consistently copied a disputable claim of a 3000-times increase in work of

fracture, and made the additional mistake of claiming that the fracture toughness K_c (not the work of fracture) is 3000 times that of monolithic aragonite[18,24,28–31]. Other papers reports the fracture toughness K_c increase in terms of "three orders of magnitude" [32] "two to three orders of magnitude"[33,34] or "(many) orders of magnitude"[35,36]. This claim has also made its way into books[37]. Medeiros *et al.*[38] estimate the fracture toughness of nacre to be 1000 times that of aragonite minerals with no reference on how this value was obtained. Barthelat *et al.*[39] also quote nacre to be 1000 times tougher, referring to an overview of natural material's mechanical properties made by Wegst *et al.*[21] who denote toughness as J_c (normally regarded as the nonlinear elastic fracture toughness) but reference Jackson et al.[15] who reported G_c (strain energy release rate) values. In addition, the largest difference between calcite (which has a trigonal structure compared to the orthorhombic structure of aragonite found in nacre) and mollusc shell reported are taken while the property chart of nacre made by Wegst *et al.*[21] spans an order of magnitude. It is therefore good to emphasise here the difference between work of fracture, critical strain energy release rate (G_c), linear-elastic fracture toughness (K_c), and nonlinear elastic fracture toughness (J_c).

Work of Fracture [WoF]

Work of fracture is calculated from the total energy required to fracture a sample. It is measured as the area under the load deformation curve (also reported as the force deflection curve) after complete failure of a notched specimen, divided/normalized by two times the cross-sectional area of the fracture[8,40]. It is thus an energy value with units of $\mathrm{Jm^{-2}}$. There is, however, a wide range of fracture velocities possible, and it is concluded by Davidge[41] that rapidly moving (unstable) cracks absorb more energy than slow moving (stable) cracks. Indeed, the fracture energy measured as the area under load-displacement curve is only meaningful if the crack propagates in a stable manner so that it unloads to zero load smoothly. If the crack does not propagate in a stable manner, the total work of fracture value does not only include energy that was used for crack extension but, especially in brittle

materials, has other components: elastic strain energy is released in the form of sound, kinetic energy and heat.

Toughness at initial crack propagation [K_{Ic}]

The standard means today of quantitatively assessing the fracture resistance of most materials is to use fracture mechanics, in which the material is considered to be nominally elastic[23]. In fracture mechanics, one can characterise the fracture behaviour using an energy-based fracture approach and define the critical energy release rate or toughness G_c, which is the critical rate of change in potential energy per unit increase in crack area where a crack starts to grow. The fracture initiation behaviour can also be characterised using a stress intensity approach. In that case a stress intensity factor K is defined, representing the local crack driving force. K_I is the crack driving force for tensile opening of the crack (mode I). When K_I reaches a critical value, $K_I=K_{Ic}$ it is called the fracture toughness. This is only valid if small-scale yielding conditions apply[23].

Under plane-strain conditions, where the only non-zero strain components act in one plane only, ceramic materials behave essentially elastically until the fracture stress is reached and rapid fracture occurs, and K_{Ic} can be considered a true material property. Various fracture toughness (K_{Ic}) measurements of different types of nacre are provided in Table 1.1. As discussed above, many authors in the literature overstate the improvement in fracture

Type of Nacre	Fracture toughness K_{Ic}	Source
Pinctada	$3.9\pm0.8\ \mathrm{MPa}\sqrt{\mathrm{m}}$	Jackson *et al.*[15]
H. Rufescens	$2.9 \pm 0.6\ \mathrm{MPa}\sqrt{\mathrm{m}}$	Fleischli *et al.*[10]
P. Penguin	$4.4 \pm 0.8\ \mathrm{MPa}\sqrt{\mathrm{m}}$	Fleischli *et al.*[10]
L. Fibrosa	$6.79\pm1.53\ \mathrm{MPa}\sqrt{\mathrm{m}}$	Sun *et al.*[34]
Red Abalone	$8 \pm 3\ \mathrm{MPa}\sqrt{\mathrm{m}}$	Sarikaya *et al.*[42]

Table 1.1 – The fracture toughness K_{Ic} of nacre for different mollusc species.

toughness that the nacre microstructure gives by orders of magnitude. Authors who do not make this overestimation often take the fracture toughness of monolithic non-biogenic aragonite as 1 $\mathrm{MPa}\sqrt{\mathrm{m}}$, such as Lin *et al.* [24], Sun *et al.*[36] and Meyers *et al.*[4], but none of those authors provide any data to support their statements, or reference this number.

From Vickers' indentation tests Olusunle *et al.*[43] measure a toughness of 0.0217 $\mathrm{MPa}\sqrt{\mathrm{m}}$ for natural calcite in air, but two years before this publication, Quinn and Bradt[44] have shown that Vickers indentation is not suitable for the measurement of fracture toughness in ceramics. Some of the problems with the method they identified, are multiple cracks and excessive shattering around the indentation, often used optical crack length measurements which are subjective and prone to large errors, and lack of a universally accepted equation[45]. They show that for the same material, a large variability of K_{Ic} values can be obtained when measured using Vickers indentation with errors of more than 50% of the measured value. For materials that exhibit R-curve behaviour such as nacre, additional problems are identified by Kruzic *et al.*[46] For these materials only one point on the R-curve is sampled by the indentation fracture test, and that point will depend on the load used unless the R-curve plateau has already been reached. In materials without R-curve behaviour such as α-SiC and ceramic glass a dependence on indentation load has also been identified[46]. Kruzic *et al.* also note that sub-critical crack growth can occur after indentation (for example when desiccating hydrated samples to make observations in an SEM) and that the soft phase in biological materials makes them prone to even larger errors than normally expected.

Kamat *et al.*[47] theoretically predict a fracture toughness for non-biogenic aragonite of 0.25 $\mathrm{MPa}\sqrt{\mathrm{m}}$. Lv *et al.*[48] measure the fracture toughness K_{Ic} of natural calcite in 3pt bending, and obtain a value of 0.2±0.07 $\mathrm{MPa}\sqrt{\mathrm{m}}$. Although Aragonite is a polymorph of $CaCO_3$, the value of aragonite should resemble that of calcite quite closely – instead of the guesswork that many authors seem to rely on. From Kamat *et al.*[47] and Lv *et al.*[48] we can conclude that aragonite has fracture toughness between 0.2-0.25 $\mathrm{MPa}\sqrt{\mathrm{m}}$. Now that we have established

this reference point, we can make a fair comparison between nacre and the fracture toughness values for monolithic aragonite presented in Table 1.1 and conclude that the fracture toughness (K_{Ic}) increase due to the microstructure is between 11.5-44 times depending on the species examined; Much smaller than the often reported 3000 times increase.

Increased toughness during crack-growth and R-curve behaviour

While the toughness at initial crack propagation K_{Ic} (often termed crack initiation toughness although it measures the initial crack propagation and not the creation of a crack) has traditionally been used to quantify toughness in ceramics, nacre differs from common ceramics in that it develops its primary toughening during crack growth. Several toughening mechanisms are discussed in the sections below which lead to toughening after crack initiation and the occurrence of stable crack growth after fracture initiation. Especially extrinsic toughening mechanisms affect toughness after crack growth and have little effect on K_{Ic} before significant crack growth has occured[2]. Therefore, a single-valued K_{Ic} does not entirely capture the toughening in nacre.

Generally, two types of toughening mechanisms are considered; intrinsic and extrinsic toughening mechanisms. Intrinsic toughening is mainly seen in ductile (metallic) materials. Intrinsic toughening mechanisms act primarily ahead of the crack tip and involves suppressing damage in the form of microcracking or micro void formation (plasticity)[2]. While this approach is largely ineffective with traditional ceramic materials, in natural ceramic composites such as nacre a form of plastic deformation ahead of the crack tip does occur, such as the formation of dilatation bands by sliding platelets (See also Figure 1.5) and wide distribution of damage in the form of contained microcracking within the ceramic layers[2].

Extrinsic toughening involves microstructural mechanisms that act primarily behind the crack tip to effectively reduce the crack-driving force actually experienced at the crack tip[2], such as crack bridging, and they are thus dependent on crack size.

For materials like nacre where the toughness of the materials changes (increases) depending on the size of the crack, it is therefore good to define a crack-growth toughness which indicates the increased resistance to further crack propagation in the material as a function of crack size; this measurement in terms of the toughness versus crack extension is known as the R-curve, and does not depend on initial notch size[23].

Nonlinear elastic fracture toughness [J_{Ic}]

When more plastic/inelastic deformation is present such as in the case of nacre, nonlinear-elastic fracture toughness J_c may provide an improved assessment of toughness. J_c is the critical nonlinear strain energy release rate, equivalent to G_c under linear elastic conditions[2]. It is calculated directly from the strain field of a crack through a J-integral, which is a path-independent contour path integral, with zero value if no crack is present in the contour[49]. While initial methods require precise measurement of crack lengths, more sophisticated methods using Digital Image Correlation (DIC) have emerged to determine the J-Integral[50]

The nonlinear-elastic fracture toughness J_c at different crack extensions have been measured in nacre of several different mollusc species[51,52] resulting in the R-curves shown in Figure 1.3. Interestingly, the increasing slope and higher toughness in data by Rabiei *et al.*[52] in Figure 1.3a correlates with the aspect ratio of aragonite tablets. Pen shell has the highest aspect ratio and lowest toughness (J_c), and pearl oyster has the lowest aspect ratio and significantly higher toughness (J_c).

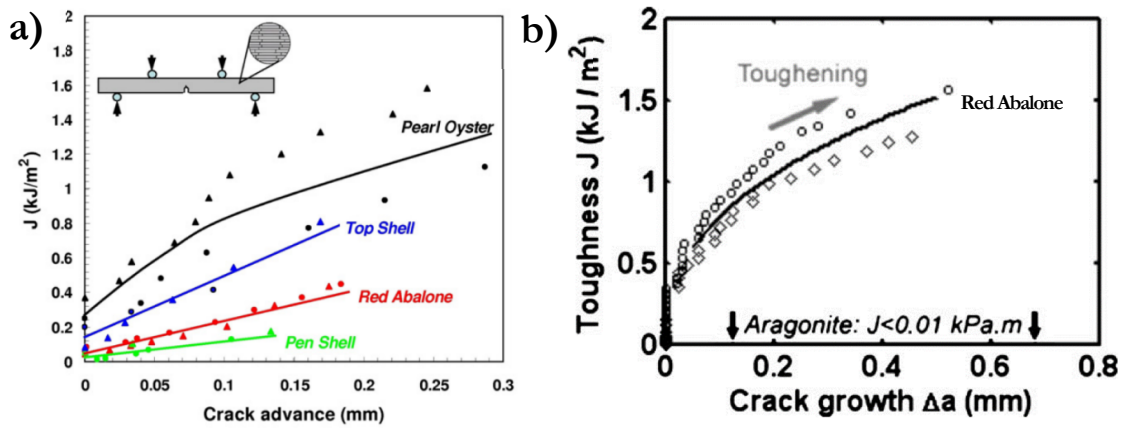


Figure 1.3 – R-curve data on nacre; a) four different types of nacre investigated by Rabiei *et al.*[52] b) two R-curves for Red Abalone shell with a logarithmic function fit, investigated by Barthelat and Espinoza[51].

1.3.2 Sliding of platelets

A prominent role in the toughening of nacre, is thought to be energy dissipation through a platelet-platelet sliding process[52,53]. In many studies an optically white looking 'process' zone is observed ahead of the crack tip[52,54,55] (Figure 1.4). When looking at this zone on the microscale, we can see dilatation bands where sliding has occurred (Figure 1.5). The stress-whitening indicates sliding tablets around and ahead of the crack tip exposing organic ligaments. Rabiei *et al.*[52] show that the size of this 'process zone' increases for tougher types of nacre; For Penn Shell the zone is just 0.05 mm while for Pearl Oyster the zone is up to 1 mm. As Pearl oyster is much tougher than Penn shell (Figure 1.3), this indicates that platelet sliding ahead of the crack tip plays a large role in the toughening of nacre.

The reason that sliding enhances the toughness of nacre is because energy is dissipated during the sliding process[53] which can be considered as an enlargement of the plastic zone. Ritchie *et al.*[1] point out that enlarging the plastic zone is an intrinsic toughening mechanism, effective against initiation and propagation of cracks.

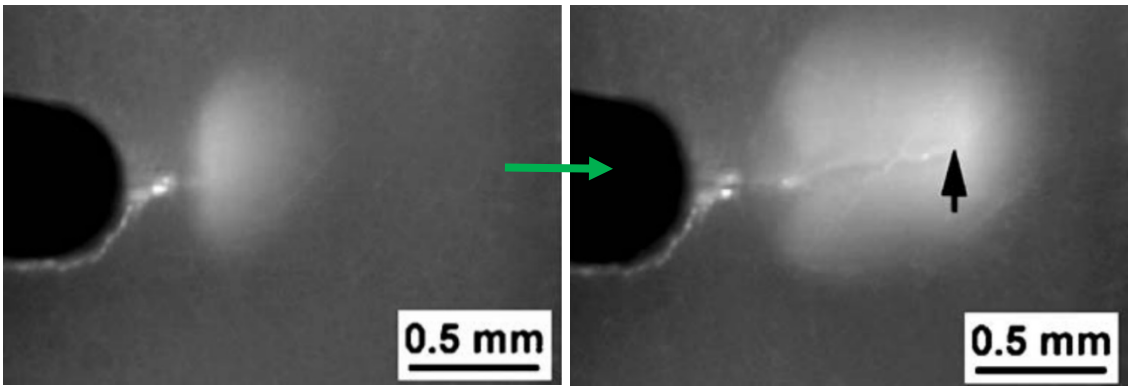


Figure 1.4 – Polished notched sample under increasing load. Left: Stationary crack, increasing inelastic zone. Right: crack advance, leaving a wake of inelastic deformations. The approximate crack tip position is marked with a black arrow. (Adapted from Barthelat *et al.*[51])

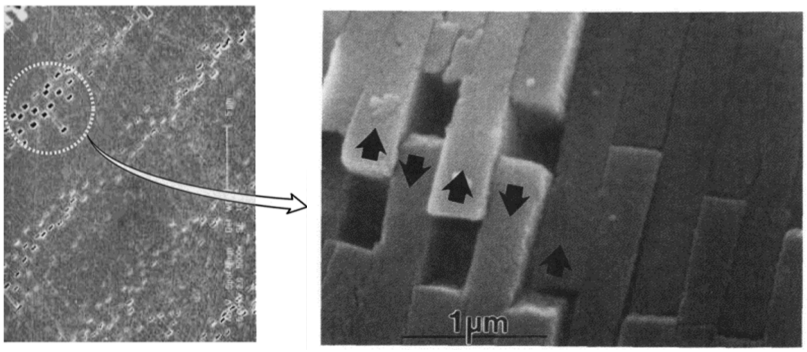


Figure 1.5 – SEM images of the dilatation bands found in nacre upon tensile straining along the plate axis. (Adapted from Evans *et al.*[63] and Sarikaya *et al.*[42])

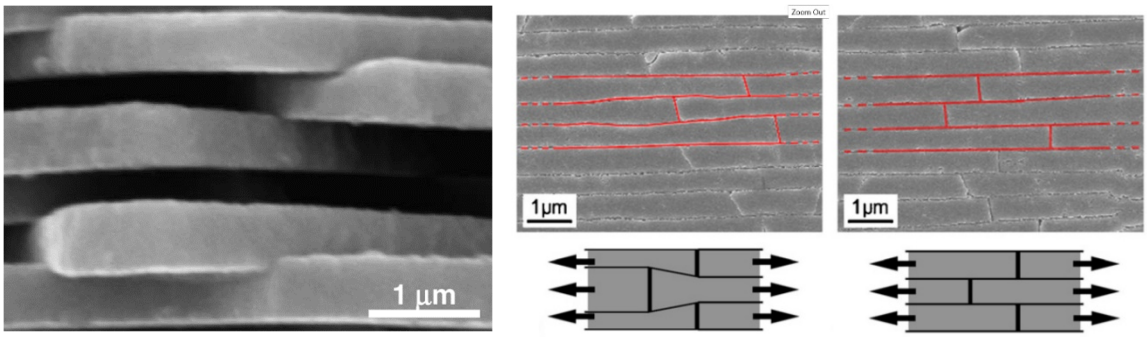


Figure 1.6 – platelet interlocking observed by Katti et al.[19] and two types of platelet geometry, ''dovetail'' and ''flat'' observed by Barthelat et al.[56].

It is likely that surface-waviness is a large contributor of surface friction[51,56]. In two dimensions, the shape of a platelet can be very similar to a dovetail, which is a locking device widely used in mechanical assembly[56]. These dovetails promote interlocking of platelets. In contrast to traditional dovetails however, the angle is not so high; the geometry is such that progressive pull-out is allowed. Barthelat *et al.*[56] argue that not all platelets in nacre seem to have this waviness though, as they observe both flat, regular and inverted dovetail structures in nacre (Figure 1.6). Nevertheless, the physical constraint against free movement of platelets that waviness can provide seems to be key to the strength and toughening of the nacre microstructure, suggesting that interlocking and accumulative pull-out of the platelets is the dominant toughening mechanism[53].

Recently, Askarinejad *et al.*[57] have shown through both numerical and experimental analysis of platelets in a brick-and-mortar arrangement that increasing platelet waviness increases the material stiffness, toughness and strength. Katti *et al.*[19] found that in a model with and without platelet interlocking, modelled nacre with interlocking platelets had a significantly increased strength.

A factor that comes into play in the interlocking and pull-out/sliding behaviour of nacre platelets, is platelet overlap. Both numeric[58] and experimental[52,57] efforts show that overlap of platelets is key to having simultaneous high strength and high toughness. Wei *et al.*[58] show in their model that when the overlap length increases, the stiffness and strength of nacre improves while some ductility is sacrificed. These views correspond with the notion of sliding of wavy platelets.

1.3.3 Role of the interface in nacre

The interface between the platelets in nacre plays a prominent role when platelet-platelet sliding occurs. 3 main interfacial features have been identified in natural nacre; Organic molecules, surface asperities and inter-platelet bridges. The experimental evidence for these features, together with a schematic model of their behaviour during sliding (shear) and expected (micro) mechanical response is depicted in Figure 1.7. (Note that after the inter-platelet bridges break, they may start to act as surface asperities.)

Inter-platelet protein layer

The most important (mechanical) aspect of the protein layer between the platelets, is that the shear in the protein layers provides sufficient inelastic deformation to permit redistribution of stress around stress-concentration sites[2]. The load transfer through brick/mortar interfaces provides increased strength by relieving stress. Okumura *et al.*[59] show that indeed the stress at the crack tip is lower than in usual isotropic elastic materials. Yao *et al.*[60] show that if the mortar phase is compliant and ductile such as in nacre, the large discrepancies between mortar and brick in stiffness tend to mitigate stress concentration in the bricks.

Arrest and deflection of cracks through the organic layer (Figure 1.8) increase toughness by increasing the crack length and thus the surface area of the crack. In addition, if the crack is not going straight (in the Mode I direction, normal to the maximum tensile stress), the driving force for it is reduced. Cracks are often not only deflected but branch out into multiple cracks[9,16], causing the crack and crack stresses to be delocalized. In addition, it has been observed that the soft organic phase displays considerable deformation before failure[19]. The protein-fibres accommodate platelet pull-out and the fibres can be seen to bridge platelets in the crack wake (Figure 1.7a)[15].

Smith *et al.*[61] proposed that the fibrous protein molecules also provide strength to the material because they are tied up with intermediate-strength sacrificial bonds (or 'modules'), a process previously observed for titin proteins by Rief *et al.*[62].

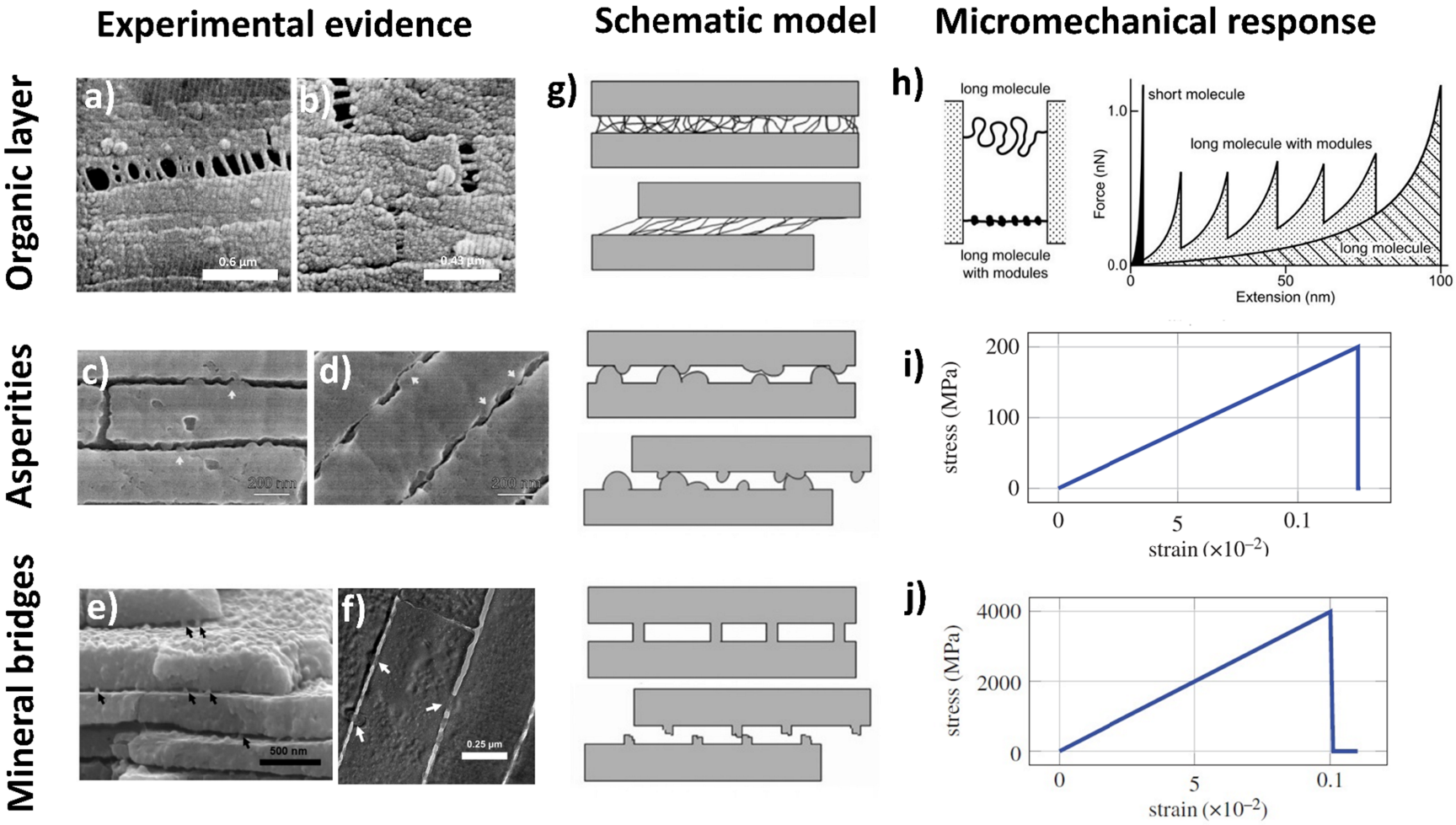


Figure 1.7 – The three main interfacial features of nacre and their micromechanical response. a) SEM image of organic fibres bridging platelets across a delamination crack and b) between ends of platelets that are being ‘’pulled out’’(Adapted from Jackson *et al.*[15]). c-d) SEM images of Cross section of abalone nacre at the lamellae boundary. Arrows highlight locations where nano-asperities interpose (Adapted from Wang *et al.*[17]). e) SEM image of mineral bridges (marked by arrows) between aragonite tiles after 9 h of hydrazine deproteination (Adapted from Lin *et al.*[328]) f) TEM image of a nacre cross-section showing mineral bridges (marked by arrows) between tile interfaces (Adapted from Lin *et al.*[328]) g) Schematics of the micromechanical behaviour of two nacreous platelets in shear with different interfaces (Adapted from Sun *et al.*[36]) h) Force-extension curves for three different kinds of organic molecules. (Adapted from Smith *et al.*[61]) i) Stress–strain behaviour of asperities on the microscale (calculated) (Adapted from Askarinejad *et al.*[67]) j) Stress–strain behaviour of mineral bridges on the microscale (calculated) (Adapted from Askarinejad *et al.*[67])

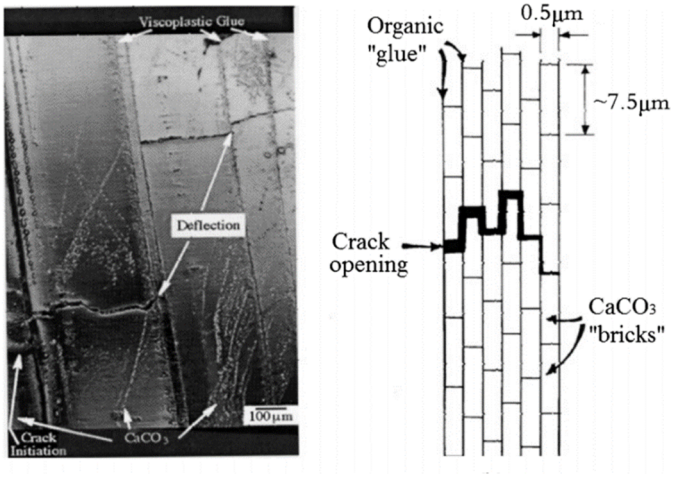


Figure 1.8 – Cross-section of abalone shell showing how a crack, starting at the left, is deflected by the layer between lamellae. (Adapted from Sun et al.[36])

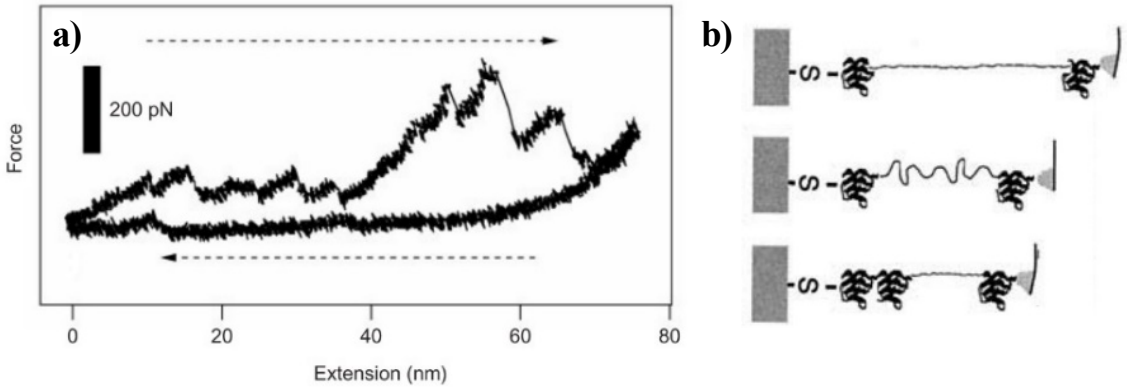


Figure 1.9 – a) Consecutive force-extension curves, obtained using an atomic force microscope, from pulling on a platelets of a freshly cleaved abalone nacre surface (Adapted from Smith *et al.*[61]). b) Unfolding of sacrificial inter-chain bonds ('modules') which are thought to be responsible for the sawtooth pattern (Adapted from Rief *et al.*[62]).

The total force must then be applied over much larger extensions which means that the area under the force/extension curve would be larger and more energy is needed to break the fibre. This hypothesis comes from observed sawtooth patterns in the force extension curves of platelets being pulled apart (Figure 1.9). Neves *et al.*[29] show that in seashells the strength is greatly degraded when the organic layer is removed.

Surface asperities

Wang *et al.*[17] and Evans *et al.*[63] theorize that surface roughness/asperities give a frictional resistance during sliding, increasing the toughness of nacre. Meyers *et al.*[7], Song *et al.*[64] and Schäffer *et al.*[65] report a density of 60, 105 and 115 asperities per square μm respectively, of which a fraction is believed to be (broken) mineral bridges. The height of these asperities is examined by Barthelat *et al.*[66] for red abalone nacre (Haliotis Rufescens) and varies from 10-30 nm, with a spacing in the order of 100-200 nm, varying across a sample.

Theoretical studies by Evans *et al.*[67] show that increasing the amount of asperities does yield higher strengths, and simulations by Zhang *et al.*[68] looking at the strengthening effect of interfacial interlocking, confirm that interlocking asperities increase the strength of the interface. However, there also exist some theoretical studies that have discounted the idea that asperities (significantly) increase friction; Katti *et al.*[19,69] used simulations with and without surface asperities and found a negligible effect on modulus and strength, and suggest another function for the nanoasperities, i.e. increasing the total surface area to bind more organic material to the aragonite platelets.

Despite these contradicting theoretical studies, it seems likely that surface asperities and surface roughness plays a role in the mechanical response of nacre. To prove this experimentally, Niebel *et al.*[70] took alumina microplatelets and modified the surface roughness through adsorption of silica nanoparticles of varying size to deliberately tune the surface of alumina microplatelets with nanoasperities. They showed that the flexural modulus, strength and toughness of composites made with these roughened platelets are greatly improved compared to flat platelets regardless of the size of the asperities.

Mineral bridges

Lin and Meyers[7] hypothesise that the presence of the mineral bridges can explain the high tensile strength values for nacre. These bridges, as observed in nacre, have a diameter of approximately 50 nm, and a tensile strength no longer determined by the critical crack size, but by the theoretical strength. In fact the size of the mineral bridges are so small that they are within the length scale put forward by Gao *et al.*[25] where materials become insensitive to flaws, and have therefore high strength values. Song *et al.*[64] go even further that we should classify nacre as a brick–bridge–mortar" (BBM) microstructure and show that in the field near the crack tip, the mineral bridges play a main role in withstanding the external load.

In nacre, the number of bridges seems to be optimized for tensile strength[24]; a higher number would lead to tensile fracture of the tiles with loss of stress transfer behaviours. Fan *et al.*[71]

confirm Lin and Meyers' views through calculation, and show that the length of the crack extension in an organic matrix layer without the mineral bridges should be four times that of a real crack measured from the experiments of nacre. They conclude that the mineral bridges effectively hinder crack extension. Shao *et al.*[72] model the fracture behaviour of nacre platelets with bridges (in periodic arrays), and calculate an optimal bridge width between 10-40 nm. Their results also show that the strength of the interface is not affected by the organic phase.

Due to advances in 3D-printing techniques, the effect of mineral bridges between platelets on the strength and toughness of the material can now be studied experimentally. Recently, Gu *et al.*[73] showed that in 3D-printed synthetic nacre, in both materials with and without mineral bridges, small micro-cracks start to form in the soft phase, allowing progressive energy dissipation and blunting the load concentration at the crack tip which increases material toughness. The mineral bridges however had a large effect on the mechanical response and (flexural) strength and toughness of the material (Figure 10). From their stress strain data it can be concluded that the structure is very sensitive to the ratio of 'soft' to hard

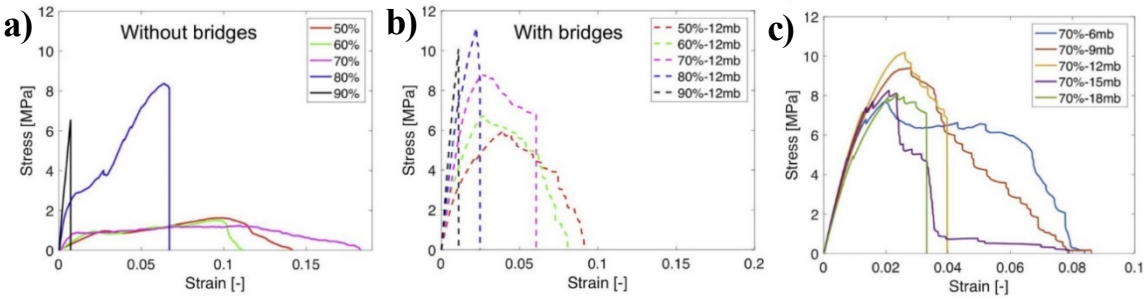


Figure 1.10 – Stress strain curves of tensile tests on 3D printed nacre mimetic materials, showing the effects of a) soft phase content b) soft phase content when including 12 mineral bridges (mb) per platelet and c) varying amounts of mineral bridges (Adapted from Gu *et al.*[73]).

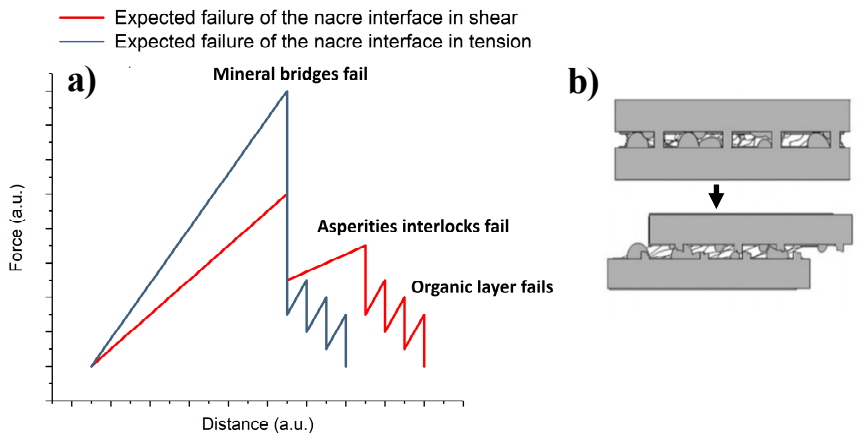


Figure 1.11 – a) Expected micromechanical force-distance curves for the interface in nacre in shear and tension, and b) schematic of the nacre interface with mineral bridges, asperities and organic molecules. (Adapted from Sun *et al.*[36])

phase (Figure 10a) and that in all cases strength is improved by mineral bridges (Figure 10b). For composites consisting of 70% stiff material ('bricks'), it was shown that increasing the mineral bridge density beyond 9 per platelet degraded fracture toughness to values without mineral bridges while mineral bridges are shown to improve strength values almost independent of bridge density (Figure 10c).

Combined interface

Taking into account the different contributions to the mechanical behaviour of the interface constituents in nacre, we can conclude that when platelets slide, the interface fails in 3 distinct steps; first the mineral bridges carry the load. Then, when these mineral bridges break as the stress reaches their strength, the proteins and interlocking asperities (or broken mineral bridges) are the only elements that carry the load[67]. These much weaker parts then consecutively fail depending on the protein length and sacrificial bonds in the organic structure (Figure 1.7h). Progressive failures of the organic matrices, mineral bridges and asperities make nacre exhibit significant toughness on the macroscale. On the macroscale, Begley *et al.*[74] show that to have the highest strength and toughness in the structure, the vertical and horizontal interfaces have to yield first, after which the interfaces should rupture consecutively; the expected stress strain curve for the brick-and-mortar microstructure is depicted in Figure 1.12. To replicate nacre, the interface has to be deformable/ductile, to allow for the redistribution and dissipation of strain energy. At the same time, the interface has to be weaker than the platelets themselves to prevent platelet breakage, and strong enough to resist crack propagation.

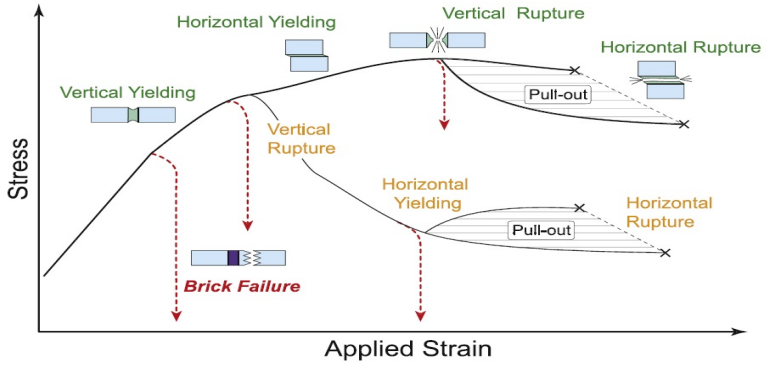


Figure 1.12 – a) Schematic illustration of the possible failure sequences in brick and mortar composites: the desired path is highlighted in green, which corresponds to strong, stiff, ductile materials. (Adapted from Begley *et al.*[74])

1.4 Materials inspired by nacre

1.4.1 Nacre-like thin films

Layer-by-layer (LBL) assembly and vacuum filtration has been used by various researchers to create nacre-like thin films. LBL assembly of montmorillonite (MTM) clays reach considerable stiffness and strength[75,76]. However, the toughness as seen in nacre is never observed and these materials have a very low Young's modulus[77]. Bonderer *et al.*[78] use LBL assembly of alumina platelets and chitosan (a linear polysaccharide) and find that the platelet aspect ratio determines if platelet pull out or if platelet fracture dominates. Composites with 15 vol % alumina platelets show tensile strengths up to 315 MPa and an inelastic deformation (ductility) of 17% which should lead to high toughness. Das *et al.*[76], who use PVA-coated MTM platelets in combination with self-assembly through vacuum filtration, confirm that platelet based composites go from ultra-stiff to ultra-tough depending on their aspect ratio. Yao *et al.*[79] use the same technique with chitosan-coated MTM platelets, and show that the aligned structure is a clear improvement over a non-aligned structure, but high strength, toughness or elastic modulus values are not reached.

1.4.2 Lamellar freeze cast composites

To create larger aligned samples with a well-defined layered microstructure, freeze casting has recently been further developed. In Robert O. Ritchie's group at the University of California, Berkeley, freeze-casting has been successfully used to yield nacre-like alumina composites. Lamellar microstructures have been combined with PMMA[80–82] , an Al-Si metal phase[83] and most recently with a bulk metallic glass phase[84]. Of these studies, the highest toughness ceramic composite was made by infiltrating freeze-cast scaffolds with PMMA[81]. These materials display a fracture toughness above 30 $MPa\sqrt{m}$ at a tensile strength of 200 MPa. Prior to MMA infiltration (which was later polymerized), a piranha solution was used to promote the formation of hydroxyl groups, which then link a grafting agent (γ-MPS) dissolved in acetone. The objective was to create a covalent bond between γ-MPS molecules

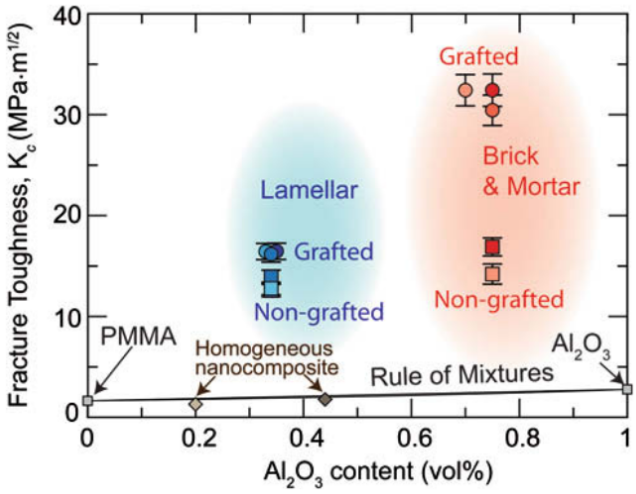


Figure 1.13 – Fracture toughness measurements for lamellar and brick-and-mortar Al_2O_3–PMMA composites, showing their exceptional fracture toughness as compared to that of their constituent phases (Adapted from Launey et al.[81]).

and the hydroxyl groups on the ceramic surface. The γ-MPS molecules then act as a coupling agent between the PMMA and the alumina surface. From their data (Figure 1.13) they show that this grafting step had a huge impact on the toughness of the material.

When using a stronger (and heavier) bulk metallic glass to infiltrate freeze cast scaffolds[84], nacre-like behaviour was highly dependent on the temperature of the glass infiltration. At high temperature infiltration, nacre-like toughening mechanisms such as crack deflection and brick pull-out were observed, and as a result these composites displayed rising R-curve behaviour, with crack-growth toughness rising to the order of 14 $MPa\sqrt{m}$. The strength of these materials however was drastically reduced to between 100-200 MPa (especially considering that the metallic glass alone had a strength of ~1700 MPa). A similar reduction in strength was found in high toughness laminated composites with an Al-Si metal phase[83].

1.4.3 Composites using micron-sized platelets

More recently, platelets similar in size to the $CaCO_3$ platelets found in nacre, have been of much interest in nacre-like composite manufacturing. Calcium phosphate platelets[85] arranged by evaporation-induced self-assembly have shown nacre-like failure with strengths up to 250 MPa and a fracture toughness of 2 $MPa\sqrt{m}$, with crack-growth toughness rising to 8 $MPa\sqrt{m}$. Alumina platelets have especially been of much interest. They have been

compacted with epoxy[86,87], polymer[88–90], borosilicate[91], titania[92] and silica-calcia[35] phases. The most impressive results to date with these platelets are composites made through a combination of glass, alumina nanoparticle and alumina platelets by Bouville *et al.*[35], which have shown both high strengths above 350 MPa as well as high toughness and R-curve behaviour with crack-growth toughness rising above 20 $\mathrm{MPa}\sqrt{\mathrm{m}}$. From their account however, these results are hard to reproduce.

1.4.4 Choice of interface in bio-inspired composite materials

The material properties of the three types of interfaces principally used in previous work of bioinspired materials, namely ceramic, metallic and polymeric interfaces are compared in Table 1.2 and Figure 1.14. Not included in Table 1.2, is their different chemical and temperature resistances which is a major factor for the application of these materials. For example, successful lamellar composites with polymers such as PMMA[93], PVA[94] and chitosan[78] are all comprised of at least 20 wt% polymeric phase which severely reduces their workable temperature range and chemical stability. Using high temperature and chemically resistant compounds such as ceramics can provide efficient energy dissipation by frictional sliding and breaking of ceramic bridges, and a tailored, completely ceramic mortar can

Material	Modulus (GPa)	Strength (MPa)	Failure strain (-)	Density (g/cm^3)
Ceramics				
SiC	400	500	0.0013	3.2
Al_2O_3	370	600	0.0016	3.9
BC	450	530	0.0012	2.5
Metals				
Ni	200	100	0.5	8.9
Al	70	100	0.2	2.7
Mg Alloy	45	400	0.14	1.9
Ti6Al6V	110	830	0.11	4.4
Polymers				
PS	2	30	0.55	1.0
PMMA	2	50	0.6	1.2
MWCNTs	270-950 (axial)	>2000	0.12	1.7

Table 1.2 – The material properties of the three main 'mortar' phase materials used to create nacre bioinspired composites, compared to those of MWCNTs. (Adapted from Begley *et al.*[74], MWCNT data from Yu *et al.* [96] and Peng *et al.*[116])

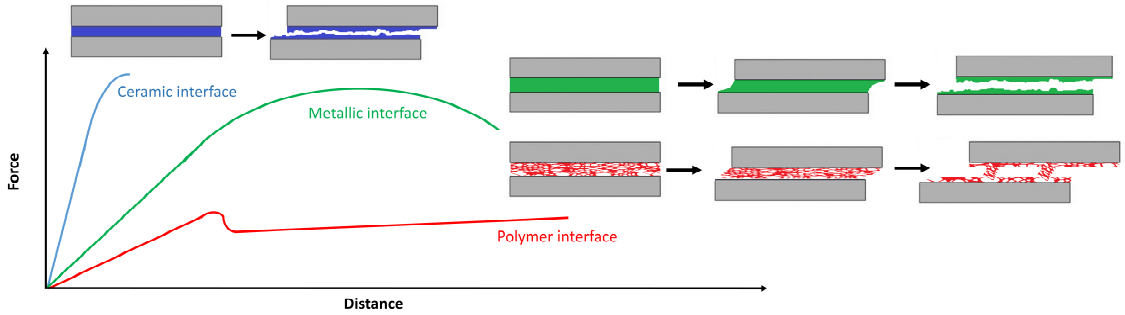


Figure 1.14 – Expected Cohesive behaviour of interfaces between platelets in bioinspired materials.

provide toughening as it has previously been established that stiffness ratios between ceramic brick and mortar can be tuned to reduce stress concentrations at the crack tip[95]. However, effective sliding of the hard alumina layers over one another when load is applied, thereby dissipating strain energy, is unlikely to happen to the same extent in purely ceramic composites due to their extremely low failure strain. This would result in a much lower toughness than polymer based composites. Infiltrating the ceramic layers with metals would provide a 'lubricant' that can also bear a lot more load than polymers (by an order of magnitude). The trade-off with using metals instead of polymers is mainly their higher density and much lower failure strain, which reduces the effective sliding distance. However, increasing the yield strength of the interface allows for more efficient transfer of loads to the bricks, driving up the modulus, strength and work to failure of the final composite.

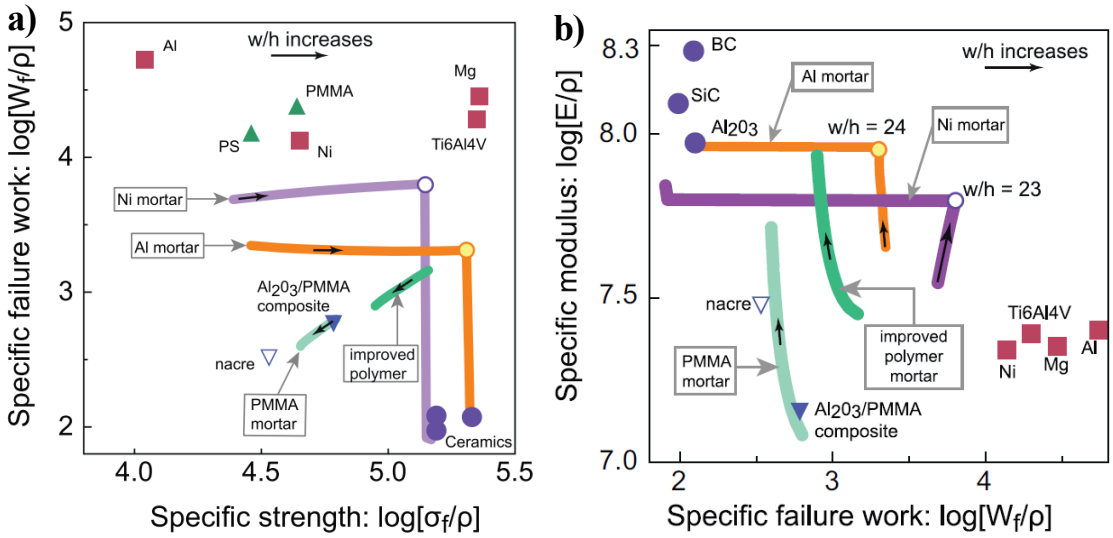


Figure 1.15 – Logarithmic Ashby property maps comparing projected performance of various nacre-like composites with ceramics, metals, and polymers. The micromechanical predictions of nacre-like composites are shown as thick lines, with the arrows indicating the direction of increasing aspect ratio w/h of the bricks. (Note that the volume fraction of mortar varies along the prediction curves since the mortar thickness is held fixed as the brick size varies. Improved polymer means a high strength (~150 MPa) (Adapted from Begley *et al.*[74])

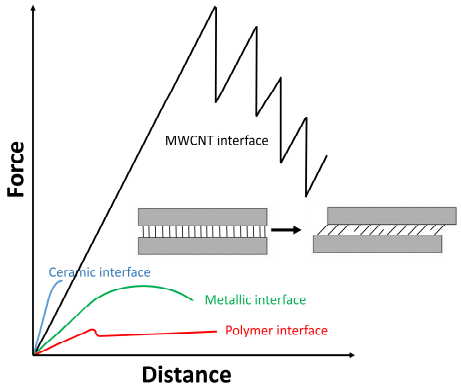


Figure 1.16 – Expected cohesive behaviour of interfaces between platelets in bioinspired materials compared to a MWCNT interface.

Begley *et al.*[74] have taken the data in Table 1.2 and computed the (density-normalised) elastic modulus, work of fracture and specific strength of individual materials, nacre, and nacre-like composites with a polymer and metallic mortar phase (Figure 1.15). The importance of constrained plasticity and ductile straining of interfaces become clear when comparing the work to failure values. We observe from the thick lines in Figure 1.15 that both polymer and metal mortar materials provide an improvement over natural nacre, with their strength dependent on the aspect ratio of the used platelets. Increasing the strength of the interface while maintaining the ductility/sliding potential of the interface greatly enhances both fracture toughness and strength, as seen when the strength of the polymer was improved ('improved polymer') or metals were incorporated.

To make the next step in biomimetic nacre-like composite materials, Multi Walled Carbon Nanotubes (MWCNTs) are considered here. MWCNTs can stretch up to 12% before breaking, are lightweight and can have incredibly high strength (Table 1.2). MWCNTs are therefore particularly interesting to function as lubricant and viscoelastic glue. When connecting platelets with MWCNTs, it is expected that platelets will be able to easily slide until MWCNTs stretch between platelets. Then, variance in defectiveness and total length of MWCNTs will cause fractions of MWCNTs to break in a similar manner as fibres in Nacre. This can delay complete rupture and give the same progressive failure mechanism as seen in nacre (Figure 1.16). For this reason, the properties and previous use of such materials are examined more closely in Section 1.5.

1.5 Carbon nanotube reinforcement

Carbon nanotubes (CNTs) have the highest specific strength measured to date[96], are stiffer than diamond in the axial direction[97] and are extremely flexible in the transverse direction[98]. In contrast to carbon fibres, CNTs are hollow tubes made up of 'rolled up' graphitic sheets, which also makes them very lightweight materials, and excellent candidates for consideration as reinforcing materials in nacre-inspired composites.

To understand the reinforcement potential of CNTs, it is important to have a good understanding of the mechanical properties of individual CNTs, especially as CNTs can have vastly different properties depending on their microstructure. In 1.5.1 therefore, the different forms of carbon nanotubes and their resulting properties are discussed. In 1.5.2 and 1.5.3 the theoretical as well as experimental performance in tensile tests for individual CNTs is reported, and in 1.5.4 existing challenges for CNT-based composites are examined.

1.5.1 Types of carbon nanotubes and their properties

CNTs are generally differentiated by both the number of graphitic layers and the way those layers are 'rolled up'. When considering the number of layers, the simplest forms of CNTs are single walled carbon nanotubes (SWCNTs), made up of 'rolled up' graphene just one atom thick. Because of their relative simplicity, SWCNTs have been of great interest from a theoretical viewpoint and have been used as a model material to understand how their mechanical properties depend on their structural parameters. The more complex multi walled carbon nanotubes (MWCNTs) are much more difficult to model. This is because in addition to a varying number of layers with associated strains, each layer can be 'rolled up' differently. In addition, there can be crosslinking between the layers, and forces between the layers play a role as well. Due to these complexities, the mechanical properties of MWCNTs are not successfully modelled as of yet, and one has to rely solely on experimental data in addition to the mechanical models of SWCNTs which by extension can give an indication of the mechanical properties of individual layers of MWCNTs.

Both types of CNTs have been used in composite research, but of the two, MWCNTs are easier and cheaper to produce in bulk, and have the additional benefit that a multi-layered structure brings; defects in one layer do not necessarily disrupt the tubular structure as much, and functionalisation only has a minor impact on the strengths of the tubes[99]. It is also good to note that SWCNTs in alumina composites densified in Spark Plasma Sintering (SPS), break down between 1250-1350 °C[100]. MWCNTs are therefore of greater interest for composite reinforcement and have been used in about 90% of ceramic composites with CNT reinforcement[101].

In addition to their promising mechanical properties, CNTs have exceptional thermal properties. MWCNTs have shown a thermal conductivity of more than 3000 $Wm^{-1}K^{-1}$ at room temperature[102], while SWCNTs have shown a thermal conductivity of 10000, 5000 and 2500 $Wm^{-1}K^{-1}$ at room temperature for a 1,2 and 3 nm thick tube respectively[103]. Additional data taken above room temperature show that thermal conductivity goes down exponentially with increasing temperature[104]. While the longitudinal thermal conductivity is very high, bulk samples with tangled SWCNTs have shown much lower thermal conductivities[105], with thermal conductivities measured no greater than 35 $Wm^{-1}K^{-1}$. This underlines the importance of CNT alignment for high thermal conductivity in composites.

1.5.2 Influence of microstructure and defects on the mechanical response of CNTs

SWCNTS are a perfect model material to understand how the properties of CNTs change with their crystallographic orientation (or in other words, the way they are 'rolled up'). The several ways to roll up a SWCNT are often represented by a pair of indices (n,m). The integers n and m stand for the unit vectors in the honeycomb crystal lattice of graphene. When m = 0, a SWCNT is labelled "zigzag" and has metallic properties, when n = m, a SWCNT is labelled "armchair" and is a moderate semiconductor, and for other cases a SWCNT is labelled "chiral" where if (n – m) is a multiple of 3, the nanotube is semiconducting with a very small band gap[106].

In addition to the band structure and resulting electrical properties, theoretical models show that mechanical properties of SWCNTs are also dependent on how the SWCNT is rolled up. Theoretical models predict that SWCNTs in the 'armchair' configuration are both 10-30% stronger and can be stretched about 50% more than SWCNTs in the 'zigzag' configuration[107–109], with 'armchair' SWCNTs displaying tensile strengths of 126.2 GPa[107,108] and failure strains up to 23.1%[107,108]. The strength values of SWCNTs in the 'armchair' configuration are very close to the intrinsic breaking strength of free-standing monolayer graphene membranes by nano indentation in an atomic force microscope 130 GPa[110].

While this gives a good idea of the ultimate potential of defect-free SWCNTs, such pristine SWCNTs have not been produced experimentally, especially in bulk form for the incorporation in composite materials. It is therefore important to take defects into account. Mielke *et al.*[111] investigated the influence of vacancy defects on SWCNT strength and critical strain, using a quantum mechanical (QM) calculations approach. Their results show that a single defect can halve the maximum strain that an (armchair) SWCNT can handle before breaking (from 0.3 to 0.15) and lower the strength by about 25% (from 135 GPa to 99 GPa). Molecular mechanical (MM) calculations done by the same group yield results that are about 40% lower in both stress and strain values[111,112]. For this reason a more precise combined quantum mechanical/molecular mechanical (QM/MM) method was used, which yielded similar results to the QM calculations[112]. The effect of defects is also studied by Lei *et al.*[113] in their Molecular Dynamic Finite Element Method (MDFEM), who calculate that the ultimate stress decreases by almost 38% and the ultimate strain decreases by 33.2% due to the appearance of a defect. They note however, that when they increase the number of defects further to a total of 4, the ultimate stress and strain only changes minimally.

1.5.3 Tensile experiments on single CNTs

Important for the application of CNTs in composite materials, is the validation of these models to experiments where SWCNTs are physically measured. It is however extremely

difficult to isolate and attach a single SWCNT to do a tensile test. To circumvent this difficulty, small bundles/ropes of multiple SWCNTs attached to an AFM tip have been measured by Yu *et al.*[114] who measured an average breaking strength of 30 GPa. Chang *et al.*[97] attempted to solve the clamping issue by creating long SWCNTs which were over their full length in contact with a Si/SiO substrate. If this is done with a long enough SWCNT, in theory no clamping is needed as for every 1 μm of contact length between the SWCNT and the substrate, up to 10 nN can be exerted due to the Van der Waals forces as calculated by Son *et al.*[115]. This theoretically enables high strain measurements without slippage. However, some slippage was still observed beyond an observed strain of 3%, with the SWCNTs remaining suspended. In their experiment, the large variation in maximum strain (6-24%) and failure stress (38-99 MPa) is attributed to the different contact quality.

For MWCNTS, experimental methods are currently the only way to unravel their mechanical properties. MWCNTs are easier to test in a nanoscopic tensile setup because of their increased size. However, measuring isolated MWCNTs in tension is still extremely difficult, and many factors come into play such as the introduction of defects during the creation or dispersion of the MWCNTs. The attachment to a tensile device is a very precise exercise and the observation method is likely to use electron irradiation to image the MWCNT (such as SEM and TEM) which can modify the MWCNTs *in situ*. This is especially clear from a study published in Nature by Peng *et al.*[116], who report a direct measurement of tensile strength of MWCNTs by using a miniature tensile testing setup. They show that in all non-irradiated cases, only one layer of the MWCNT breaks. However, after irradiation with electrons in TEM, the stiffness and maximum load of the MWCNT increases, and the strength, strain and modulus decreases. This is likely due to induced crosslinking of nanotube walls as the number of broken walls or 'shells' goes up significantly after irradiation. Using their system in-situ in a TEM, they are capable of precise determination of CNT diameter and number of walls and can measure stress and strain at the same time. They measure a maximum stress of 110 GPa and maximum strain of ~12%. The most extensive dataset to date, in terms of

number of MWCNTs measured, is by Yu *et al.*[96] who used an atomic force microscopy (AFM) cantilever probe to measure the tensile strength of individual MWCNTs, attached to the AFM tip through solid carbonaceous deposits. The tensile strength of MWCNTs in their work ranges from 11 to 63 GPa with a mean strength value over 19 measurements of 27.84 GPa.

The highest experimentally determined MWCNT strength has been reported by Demczyk *et al.*[117] They measure a tensile strength of 150 GPa at a 5% maximum strain, although it is good to mention that they report a 5-10% error margin on TEM magnification, and a 20% error margin in the force constant of the AFM cantilever used for calibration. Similar to Peng *et al.*[116] and Yu *et al.*[96] they observe a "sword in sheath" breakage, showing that tubes are elongated after breakage, due to a pull out of the inner part of the tube from the outer walls. Unfortunately, they do not report other tensile measurements using their setup although they speak of a multitude of tubes tested. They are therefore likely representing a maximum strength value.

The highest experimentally determined MWCNT maximum strain has been reported by Falvo *et al.*[118]. They measure local strains though bending as large as 16% by considering the radius of curvature of the bend and note the lack of any signs of catastrophic damage even at such high strains. They note that MWCNTs are extremely flexible and can resist failure on repeated bending so much, that the separation of a tube by repeated bending was never observed.

From all these reports, it is clear that there is a large range of failure stress and strain values reported, often even within the same experiment. It is likely that these are due to the variety of MWCNTs tested, with different sizes and types of defects, inherent to the production method or dispersion and/or purification afterwards. Although mass-produced MWCNTs for composite fabrication do likely have defects, the strengths of defective SWCNTs calculated and experimentally measured are still more than an order of magnitude larger than

that of carbon fibres used in conventional composite manufacturing (Currently, the strongest carbon fibres commercially available are from TORAYCA® T1100G with a reported tensile strength of 7 GPa) and much larger compared to the 1 – 2 GPa for most high-strength steels[117] In addition, CNTs offer a much sought after weight benefit due to their tubular carbon-based structure.

1.5.4 MWCNTs in composite materials

Although the mechanical properties of isolated MWCNTs have been studied extensively, as of yet there is a large mismatch between experimental data of isolated MWCNTs, and experimental data of MWCNT reinforced composites. Translating the high strength and strain values of MWCNTs to composite materials has been held back by three main challenges; the fabrication of pure and defect free MWCNTs, the dispersion of these into a composite matrix (without damaging them), and the poor connectivity between MWCNTs and the ceramic matrix[119,120].

Several researchers have tried to overcome these challenges and aimed to incorporate CNTs in composite materials to enhance their mechanical properties. Considering the often seen inhomogeneous dispersion of CNTs in the matrix[119], one of the difficulties is that high surface area nanomaterials like MWCNTs easily agglomerate, held by their van der Waals forces (~500 eV/μm of tube length[121]). It has been found that the most effective way to break these bonds is by producing a strong shear force in the liquid medium, for which ultrasonic waves are commonly used[122]. However, it has also been shown that mean tube length decays as $t^{-1/2}$ during ultrasonic treatment[121]. The time needed to disperse CNTs varies on degree of entanglement, aspect ratio and type of tube and may be required to be up to 24 hours[121]. This does therefore severely limit CNT length. Another limitation when dispersing CNTS through sonication is the introduction of defects in the CNTs, which research has shown occurs even when using short sonication times[122]. To disperse the naturally hydrophobic CNTs in an aqueous solution using sonication, a dispersant such as Sodium dodecyl sulphate (SDS) is required to prevent re-agglomeration. Typically, 1g/L dispersant

and 1g/L CNT powder is used in dispersing solutions. While the dispersant prevents the CNTs from (re)agglomerating, the dispersant will be incorporated into the matrix and is not always chemically compatible with the matrix. For example in CNT-cement composites dispersants can have a particularly harmful impact as they can inhibit cement and concrete hardening, by interfering with the hydration reaction of cement[123].

In addition to dispersants, pre-treatment and purification steps are often required to generate a good quality CNT reinforcement. Especially in the case of arc-discharge CNT powders, which naturally contain large graphitic particles, soot and metal catalysts. Pre-treatments such as acid reflux procedures are also used to detangle the CNTs by chemical modification of the CNT surface. These acid reflux treatments introduce defects in the CNTs as well[119] which in turn diminish their mechanical, thermal and electrical properties. It is therefore good to realize that any composites made with processed MWCNTs will not have the properties of long defect free CNTs.

In addition to these challenges, it is also good to realize that in strength calculations of single MWCNTs such as done by Yu *et al.*[96], the tensile strength of the individual MWCNTs is calculated from the cross-sectional area S of the outermost layer of the MWCNT, with $S=2\pi rd$, where d is the inter-layer separation of graphite, 0.34 nm. In other words, the study assumes that only one layer (a single outer layer) is broken, which they justify by their observation of a 'sword-in-sheath' type fracture where the inner layer of one end is pulled off from the outer layer of the second end, resulting in the initial length of their MWCNTs (in 16 of 19 test cases) being much smaller than the length of the two broken fragments (in fact, often the sum of the broken fragments was near twice the initial length). Therefore, this does not represent an 'engineering strength' as for reinforcement purposes we should not use the cross-sectional area of the outermost layer, but the complete cross-sectional area of the MWCNT. Therefore, these strength values are an unrealistic depiction of the achievable strength of MWCNT in composites. If we calculate the true engineering area for a used ~22 nm thick MWCNT (reported tensile strength 35-39 GPA), the full cross sectional area is

121π nm^2 while the study for this MWCNT used an area of 7.48 π nm^2. The study is therefore overestimating the (engineering) strength of these MWCNTs by more than 16 times and the likely correct strength for the reported MWCNTs is between 2.16-2.41 GPa.

1.6 Aim of dissertation

The aim of this dissertation is to detail the synthesis, development and characterisation of novel ceramic composites that combine the microstructural architecture of nacre with carbon nanotubes. In addition, this work aims to gain a better understanding of the effect microstructural features, with a focus on CNT inclusions, on the mechanical properties of created nacre-like alumina/CNT composites. To satisfy the aim of this dissertation, the following objectives are identified:

1. Develop a freeze-casting apparatus capable of growing templated lamellar scaffolds and develop methods to create large-scale alignment for completely nacre-mimetic aligned composites (Chapter 2).

2. Investigate the homogeneous infiltration of these aligned freeze-cast scaffolds with multi-walled carbon nanotubes (MWCNTs) and create a recipe for homogeneous, high-quality and reproducible MWCNT-coating on the scaffold and alumina platelet building blocks that closely resemble the platelets of nacre (Chapter 3).

3. Explore the sintering of alumina platelets in spark plasma sintering (SPS) and optimize the sintering conditions to generate a nacre-like microstructure and relate grain growth and other microstructural features to the mechanical response of the resulting ceramics (Chapter 4).

4. Investigate different methods of creating nacre-like composites by varying the MWCNT dispersion method and sintering conditions and relate the resulting features to the mechanical response of nacre-like composites (Chapter 5).

Chapter 2 – Freeze-casting nacre-like porous scaffolds

In this chapter, the creation and manipulation of aligned porous ceramic microstructures is discussed, which can be used as a scaffold for bioinspired composites. If these ceramic scaffolds are aligned in an anisotropic 'lamellar' fashion, the scaffold (also referred to as 'green body') can be infiltrated with a second phase material such as multi-walled carbon nanotubes (MWCNTs), explored in Chapter 3. This provides a promising new way to create artificial nacre. The porous microstructures discussed in this chapter are generated through freeze-casting, also commonly referred to as ice-templating[124–126] or freeze-gelation[127–129].

2.1 Introduction

2.1.1 Freeze-casting

Freeze-casting is a technique based on the solidification of a liquid, generally water, in a well-dispersed slurry of insoluble particles, subjected to a directional temperature gradient. The temperature gradient prevents ice crystals from nucleating at random in the volume. Instead, ice nucleation happens on one side of the slurry and progresses along the temperature gradient, which is controllably changed, effectively moving the ice front. The growing ice front will reject the suspended particles, segregating the particles from the ice and effectively templating the material. After the whole slurry is completely frozen, the ice is sublimed out and a porous scaffold remains. The freeze-casting procedure is depicted in Figure 2.1. The resulting porous scaffold can be used as is, or in the case of a ceramic, it can be sintered, resulting in a high surface area solid scaffold. The sintered scaffold can be further infiltrated with a filler material and then sintered again to manufacture composites with a high level of microstructural control.

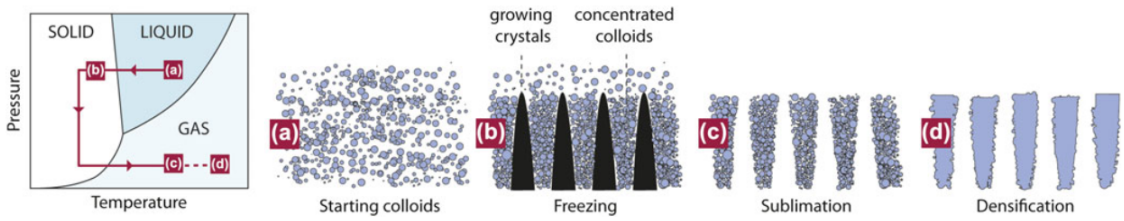


Figure 2.1 – Diagram depicting the freeze casting process, adapted from Deville *et al.*[329]

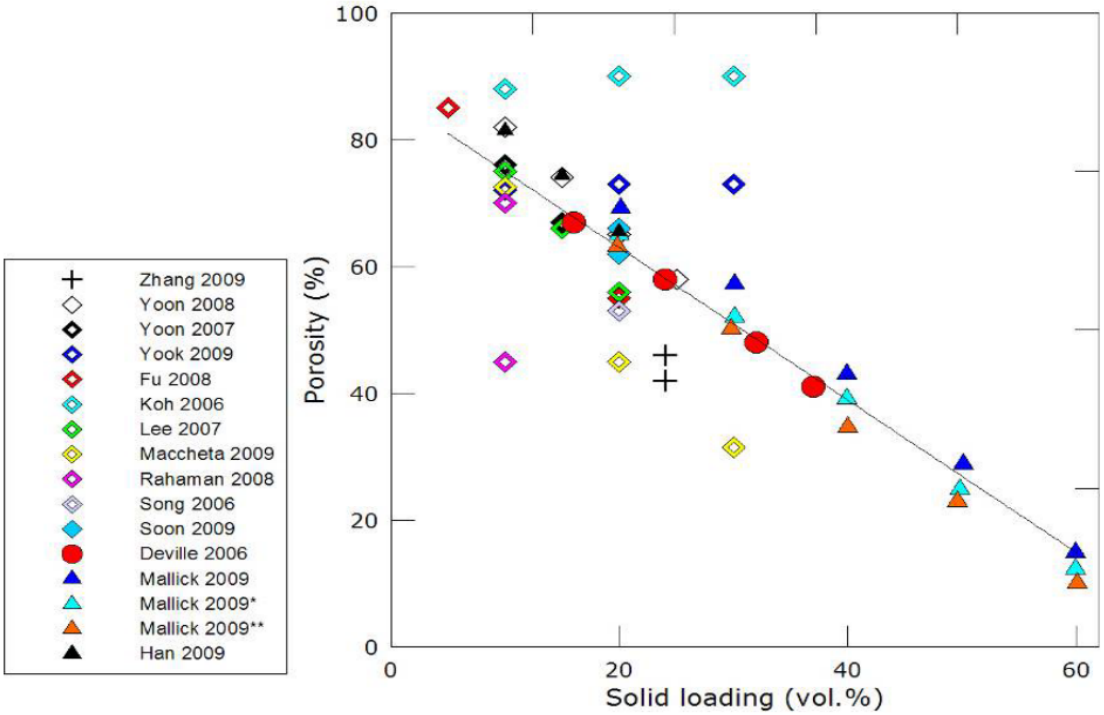


Figure 2.2 – Porosity versus solid loading in freeze cast ceramics. (Adapted from Deville *et al.*[330])

Freeze-casting can be used with a broad range of suspended particles as long as the dispersion is stable. This is because the formation mechanism (the rejection of particles from the growing solvent crystal) is mostly based on physical interactions. It is particularly interesting to template ceramic materials which are otherwise hard to template because of their brittleness and temperature resistance. By varying the amount of suspended ceramic particles in an aqueous slurry, referred to as the solid loading, it is possible to modify the porosity of the sample. Sylvain Deville[130] did a comparative literature review on the effect of solid loading on final porosity, showing a linear relationship between the two parameters. (Figure 2.2)

2.1.2 Lamellar freeze-casting

To mimic the nacre microstructure, it is of vital importance that freeze-casting results in a lamellar microstructure, and that these lamellae are aligned in one direction over a long range.

Miller *et al.*[131] point out the similarities between freeze-casting and the dendritic and lamellar solidification of pure metals and binary alloys; the ceramic particles can be seen as the solute in the dispersion medium, while the dispersion medium acts as the solvent. To create a lamellar structure Deville *et al.*[132] state that two requirements must be satisfied[124]. Firstly, the ceramic particles in suspension in the slurry must be rejected from the advancing solidification front and entrapped between the growing ice crystals. Secondly, the ice front itself must have a columnar or lamellar morphology.

Deville *et al.*[133] in a later work show that they can successfully utilise the directed freeze-casting technique to create lamellar alumina scaffolds from powder with an average grain size of 0.3 μm. They showed (Figure 2.3) that the wall thickness can be tailored by changing the ice front velocity and were able to achieve a wall thickness around 1 μm. The finer microstructure and thin walls are due to a decreasing tip radius of the growing ice crystals when the magnitude of cooling ahead of the solidifying interface is increased.

Therefore, by increasing the ice front velocity it is theoretically possible to reach dimensions in the order of the platelets of nacre. Lamellar freeze-casting has been studied in situ by Deville *et al.*[134] using tomography. They show that two types of crystals nucleate; randomly

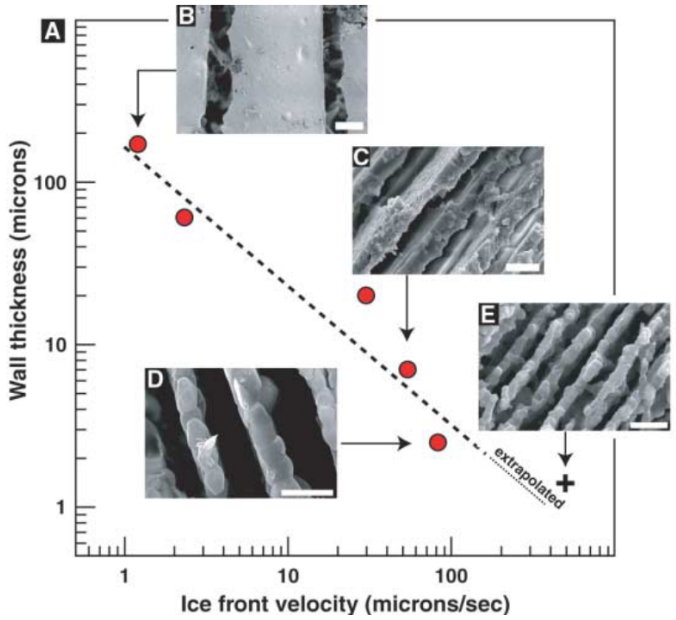


Figure 2.3 – (A) Effect of the speed of the solidification front on the thickness of the lamellae for alumina samples fabricated from powders with an average grain size of 0.3 mm (B to E). The scanning electron micrographs shown in the graph correspond to cross sections parallel to the direction of movement of the ice front. Sample (E) was obtained with ultrafast freezing to gauge the thickness limit achievable by this technique. Scale bars indicate (B) 50 mm, (C) 10 mm, (D) 5 mm, (E) 5 mm, and (F) 500 mm. (Adapted from Deville *et al.*[133])

oriented crystals in the xy plane, and crystals growing in the z-plane (the direction of the freezing front/temperature gradient). While both nucleate homogeneously on the freezing surface, after a short distance the z-crystals become dominant, leaving a lamellar structure behind.

2.1.3 Current methods to achieve lamellar alignment

To create nacreous bioinspired structures, not only lamellar ice fronts and z-direction alignment is necessary, but alignment of the lamellae in the x or y direction needs to be achieved as well. In freeze-casting, traditionally only one freezing gradient is used which can therefore only control growth in one direction. Different techniques have been proposed to modify the technique to further manipulate the microstructure in a bid to achieve nacre-like lamellar alignment.

Alignment by using a magnetic field

One of those technique is to use an external magnetic field; Porter *et al.*[135] include magnetic iron oxide particles in a freeze-cast TiO_2 slurry, and apply a magnetic field of 0.12 T while freeze-casting. This results in alignment of lamellae parallel to the magnetic field. Porter *et al.*[135] show that aligned samples have double the compressive strength and modulus values of non-aligned samples in the Y direction. However, increasing the concentration of iron oxide particles above 1wt% decreased the strength, Young's modulus and density of the samples. Interestingly however, water itself is known to be influenced by magnetic fields as well, resulting from the dipole nature of the H_2O molecule. Toledo *et al.*[136] find experimentally that an external magnetic field influences the number of hydrogen bonds, the structure of liquid water, and the self-diffusion coefficient of the water molecules, which is also confirmed through molecular dynamics (MD) simulations by Chang *et al.*[137]. It is thus important to note that although alignment seems to improve under influence of a magnetic field, it is currently not certain that this is because of the addition of magnetic particles, or because of the modification of the water's hydrogen-bonding.

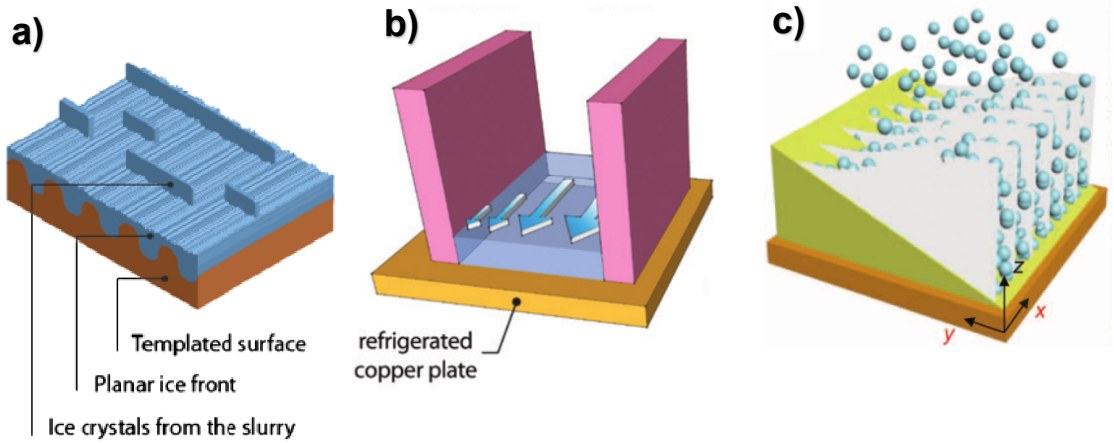


Figure 2.4 – Three methods shown to align lamellae in freeze cast materials a) Patterning, Adapted from Munch *et al.*[138] b) Freezing under flow, Adapted from Bouville *et al.*[139] c) 1-dimensional ice nucleation, Adapted from Bai *et al.*[140]

Alignment by pre-patterning

Another method of aligning the lamellae has been successfully used by Munch *et al.*[138], who align the microstructure by pre-patterning the copper cold finger. This is done by making unidirectional scratches on the polished surface of the surface where the ice initiates growth. An additional vibration was applied to homogenize the cooling suspension. The lamellae orient perpendicularly to the linear patterns, as shown in Figure 2.4a. The orientation of the lamellae in this way is attributed to the preferred nucleation at sharp angles of the pattern. Pattern sizes varied between 40 and 100 μm for 10–50 μm lamellae, respectively.

Alignment by freezing under flow

Bouville *et al.*[139] use a system whereby they freeze-cast under flow to align the microstructure (Figure 2.4b). The suspension at the open end of the mould is recirculated. The slurry that has been in contact with the copper plate during flow is colder, and ice starts to nucleate when the temperature equals the freezing temperature of the slurry. This method significantly improves lamellar alignment, but in terms of long scale dimensions, only a limited extent of alignment (~2 mm) was obtained in the plane parallel to the cold finger by using freeze-casting under flow. The same restriction in alignment area is seen in works where patterning is used to align the microstructure (~4 mm)[140].

Alignment by using a dual temperature gradient

An interesting method is discovered by Bai *et al.*[140], who use a 20 vol% hydroxyapatite (HA) slurry on a tilted PDMS wedge between the slurry and the copper cold finger (Figure 2.4c). The slurry then starts freezing from the bottom to the top of the wedge with ice crystals nucleating first at the bottom end of the wedge. In the case of a perfect slope this means that the ice nucleates on a 1-dimensional line instead of on a 2-dimensional surface. Bai *et al.*[140] claim that this method yields long scale alignment over the 25 mm mould. However, upon close inspection what is called 'alignment' here is actually the number of continuous domains; lamellae that are given the same colour are clearly oriented in different directions In Figure 2.5. Figure 2.5 shows that while a long-range continuous domain is created by using a freezing rate of 5 °C/min and higher, and for slope angles of 10° and higher, within one domain lamellae can have more than a 90° rotation relative to one another. While continuous

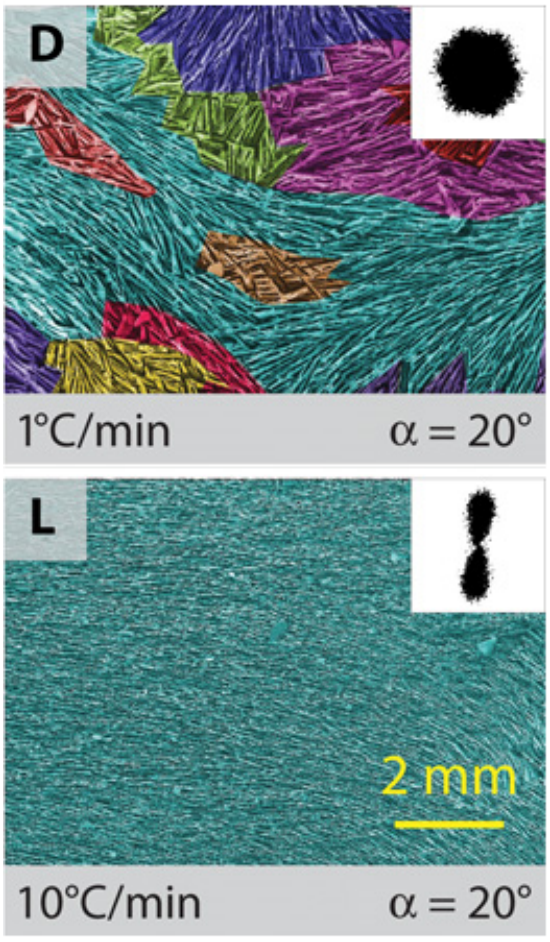


Figure 2.5 – Domain orientations of HA scaffolds fabricated under different cooling rates and using PDMS wedges with various slope angles (Adapted from Bai *et al.*[140]).

domains are likely to yield more alignment than separate domains, reproducible large-scale alignment (cm scale) in freeze-cast scaffolds has yet to be shown.

2.1.4 The effect of additives in freeze-casting

The freeze-cast microstructure can be further modified by including additives into the ceramic slurry. Additives can make three main modifications to the microstructure:

1) Bridge density and shape (between lamellae)
2) Surface roughness (of ceramic walls)
3) Pore width and pore structure

Bridge density and shape

Bridge forming between lamellae is due to the splitting and healing ice crystal tips. When ceramic particles are encapsulated in this process, bridges between lamellae are formed. A particular bridge structure can be observed for different additives, due to the different inter-particle forces within the slurry leading to different chances of splitting and healing of ice crystal tips.

Surface Roughness

Surface roughness can be understood by considering the eutectic phase diagram for the water-additive mixture. Considering the phase map for NaCl in water (Figure 2.6); it can be observed that when cooling the mixture, the fraction of saltwater in the solution becomes lower and more concentrated with salt until NaCl crystallizes out of the solution at -21.1C because of saturation of the remaining saltwater. The (ice/$NaCl{\cdot}2H_2O$ crystal) phase is a mixture of separate $NaCl{\cdot}2H_2O$ crystals and ice crystals (not a homogeneous mixture) and will leave behind a sharp faceted microstructure after the phase disappears with sintering. A different mechanism is observed with sucrose and trehalose in water[138]. Munch *et al.*[138] show that the addition of sucrose and trehalose exhibits rounded smooth features on the surface, which is probably due to an absence of crystallisation as observed with a water-NaCl mixture.

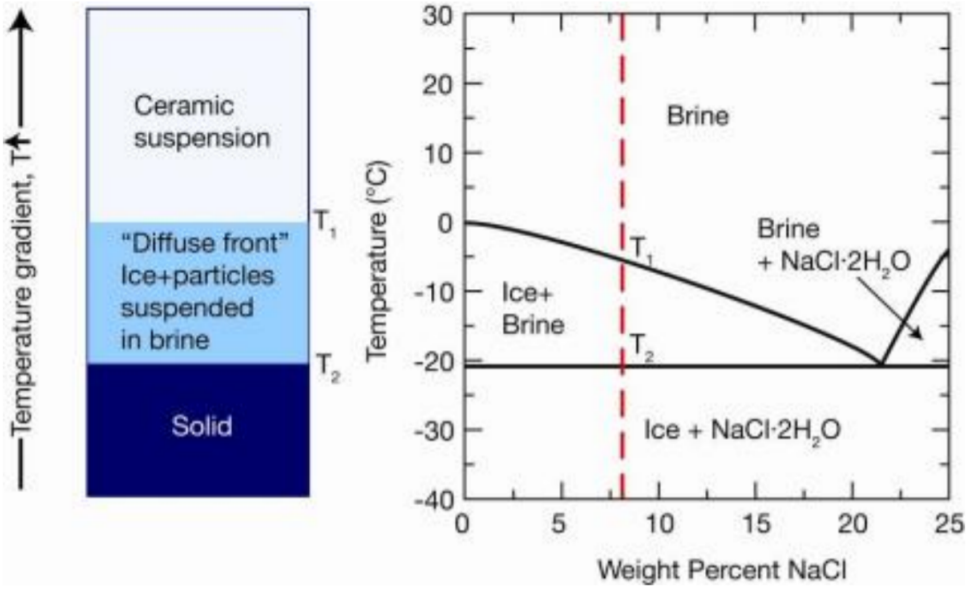


Figure 2.6 – Water-NaCl phase diagram (Adapted from Munch *et al.*[138]).

Pore width and pore structure

Munch *et al.*[138] successfully created lamellar alumina scaffolds from 0.4 μm alumina powder and show that relation between wall thickness and freezing time seen by Deville *et al.*[133] (Figure 2.3) is reproduced, independent of the type of additive used (Figure 2.7). The thickness of the walls however is modified, with ethanol showing much thicker walls and therefore a larger lamellar 'wavelength' and pore width. The observed difference in pore

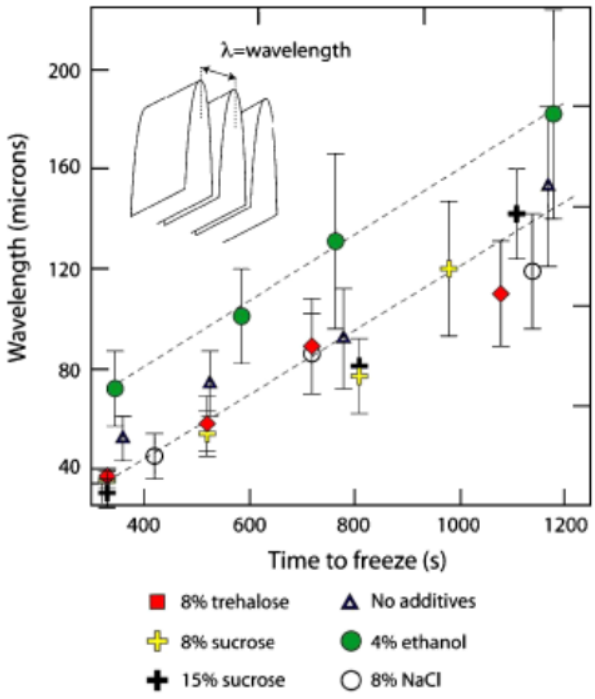


Figure 2.7 – Wavelength versus time-to-freeze for 2-cm-tall samples. Error bars represent the standard deviation (4100 measurements for each data point). (Adapted from Munch *et al.*[138])

sizes depending on additive can be explained looking at the viscosity of the suspensions: the freezing front experiences higher resistance in the freeze-casting process at higher viscosities and obtains relatively thicker lamellae. Viscosity is also inherently related to freezing temperature. Mixtures with high viscosity are harder to freeze and therefore should have lower freezing temperatures. This is quantified by Zeng *et al.*[141] in their paper where they report that for mixtures ranging from 10% ethanol-water to 30% ethanol-water the freezing point drops from -4 °C to -14 °C, and that for a 1-propanol-water mixture in the same concentrations the freezing point drops from -1.3 to -8.3.

The increased viscosity of water-ethanol mixtures can be explained by considering hydrogen bonding in the mixture. It is known that the hydrogen bond strength of water-hydrogen becomes stronger with increasing ethanol concentration, resulting in the strong hydrogen-bonding between ethanol and water[142]. Additionally, these strong bonds may disrupt the crystallization of ice and result in the different surface roughness. However, when ethanol and 1-propanol are considered, their densities (789 kg/m^3 and 803 kg/m^3 respectively) are very similar and thus 10% ethanol and 10% 1-propanol have about the same amount of OH groups to potentially use for hydrogen bonding. The answer to their different effect in freezing temperature modification lies in the longer chain; 1-propanol is more of a non-polar hydrocarbon than ethanol, and thus less soluble due to the repulsive carbon chain.

2.2 Materials and methods

2.2.1 Ceramic slurry

0.3 μm alumina powder (Baikalox SMA6) was dispersed in deionized water with 1.4wt% DolapixCA as a dispersant (Zschimmer&Schwartz) and 1.4wt% Polyvinyl alcohol (PVA, Sigma Aldrich) as a rheology modifier and binding agent. The PVA was solubilized by mixing 10wt% PVA in deionized water and stirring for 24 hour stirring at 80 °C, and added in aqueous solution. Slurries were prepared with either 3wt%, 5wt% and 10wt% saccharose (Analar Normapur D(+) Saccharose) or 3wt% ethanol. All additive weight percentages are a percentage of the liquid weight not of the total weight. All slurries were ball milled overnight and then degassed for at least 30 min after which a magnetic stirring bar was inserted, and the slurry was slowly stirred in a covered Pyrex beaker to ensure homogeneity before pouring. In a second setup used at the University of Oxford, Dispex A40 was used as a dispersant with 0.4 μm alumina particles (AES11C), with the rest of the parameters kept the same.

For platelets, on recommendation of Sylvain Deville[35], the slurry constituents were slightly altered. A 37wt% alumina platelet (Ronaflair white sapphire) slurry with 3wt% 0.2 μm alumina nanoparticles (TMDAR) (when used) was prepared with 0.5 Alwt% Darvan 7NS (Vanderbilt) as a dispersant and 0.3 Alwt% Carbopol ETD 2691 as a binding agent. (In their original recipe, 7.5wt% nexil20k colloidal silica and 2.5% calcium carbonate were used, which may change interparticle forces). As the slurry was quite viscous, this recipe was later altered to provide lamellar alignment: A 0.1M NaOH solution in deionised water (instead of pure deionised water) with 0.3wt% DispexA40 (instead of Darvan 7NS) was effective in aligning the lamellae. The mixture was sonicated in a sonic bath for 20 minutes to ensure dispersion and degassed in a vacuum oven before freeze casting.

2.2.2 Freeze-casting

The freeze-casting setup consisted of a liquid nitrogen bath, in which a copper rod ('cold finger') was placed. A band heater was mounted on the copper rod connected to a PID temperature controller. Different copper 'set up' pieces were used with varying slopes, which could be fitted on the copper cold finger. Around this surface, a plastic mould was placed which acted as the container for the ceramic slurry. The mould was washed and lightly scrubbed with water and soap before each use after which vacuum grease (Dow Corning) was used on the outside to ensure a watertight seal. The copper set-up pieces were washed as well and polished or patterned as required, and then left to sonicate in acetone for 10+ minutes.Two different freeze casting setups were used, one made at Imperial College London in the group of Eduardo Saiz (Figure 2.8a-b), and one created by the Author with the help of technicians Robin Vincent & Richard Turner at the University of Oxford (Figure 2.8c-d).

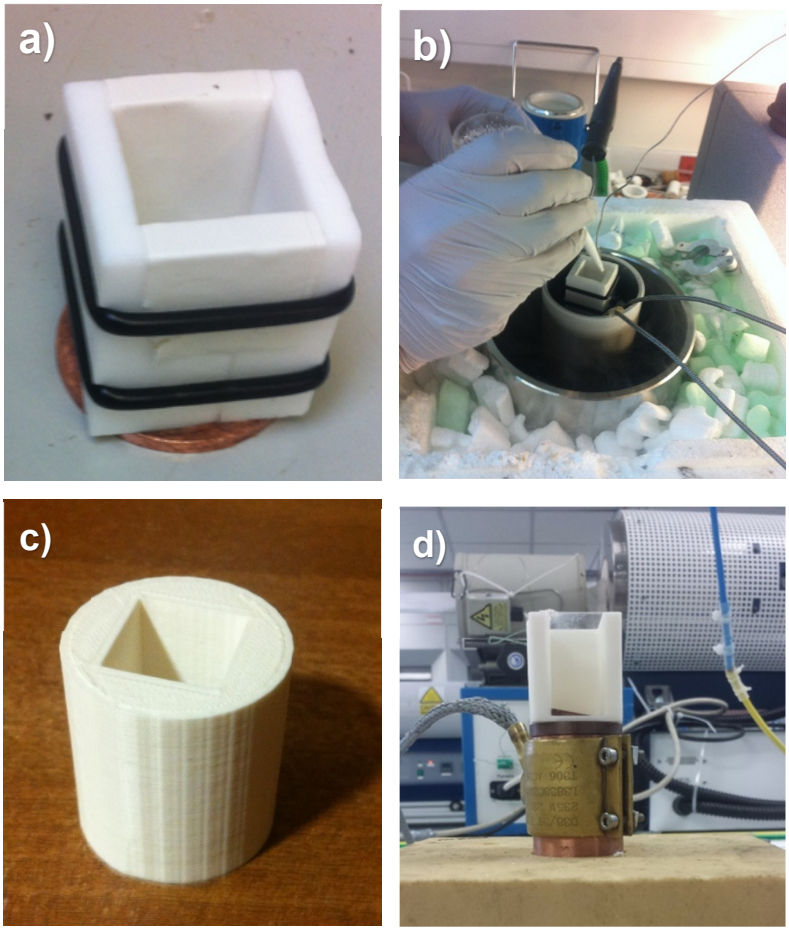


Figure 2.8 – a-b) mould and freeze casting setup used at Imperial College London and c-d) mould and freeze casting setup used at the University of Oxford.

While the principle and setup are quite similar, a few modifications were made. At Imperial College London, the copper cold finger was not directly in contact with liquid nitrogen but was placed in ethanol. The copper was seen to react with the ethanol and the indirect cooling was deemed unnecessary. Therefore, at the University of Oxford, the copper rod was directly placed in a bath of liquid nitrogen. The material of the bath was made out of insulating foam instead of steel in an effort to minimize the evaporation of liquid nitrogen, and instead of a 1-piece mica insulated band heater (Omega), a brass encapsulated sealed nozzle heater (Acim Jouanin) was fitted to the copper cold finger. The moulds at Imperial College London were 2-piece PDMS, which required rubber bands to hold the mould together, which were quite hard to remove after freezing. Therefore, 3D printed moulds were manufactured with the help of Flynn Castles for the setup in Oxford. An added benefit of this manufacturing process is that instead of a solid mould, a hollow honeycomb structure could be printed inside the mould, increasing its insulating properties. An attempt was made at manufacturing a mould with an acrylic window as depicted in Figure 2.8d, but the slurry was prone to leakage between the window and the copper set-up piece, altering the experiment in a way non-representative of the experiments performed when the acrylic window was not used. As the freezing front during freeze casting has already been studied extensively[140], these were not further developed.

The set-up pieces' surface was modified in several ways; They were either polished, directionally scratched with P80 silicon carbide paper, or covered with PVC adhesive tape (Scapa), pre-scratched with a scalpel. In some experiments, an acrylic surface and/or wedge was also attached to the copper using a thin layer of vacuum grease.

The temperature controller was set at room temperature and when a stable temperature reading was obtained, the slurry was poured to the side of the mould wall to prevent bubble formation during the pour. Because of the volumetric expansion of ice, the mould was only filled about 80% full. The temperature was then ramped down using a PID controller using a set ramping rate of 1-20 °C /min from room temperature down to a setpoint of -150 °C.

During freeze-casting, small amounts of liquid nitrogen were added at intervals of 5-10 minutes to keep the level of liquid nitrogen and thus the cold source constant, ensuring a stable cold source. Adding too much nitrogen casting results in drastic overshoot, followed by a correction from the heat source that evaporates liquid nitrogen quickly, giving rise to fluctuations in the cooling speed. On the other hand, not topping up frequently meant that the cold source was not powerful enough to ensure a stable decrease in temperature. After freezing the mould was removed and transported quickly to a 1L Freeze-drying chamber (Labconco, US) for ice sublimation. Sublimation was done for 48 hours.

2.2.3 Sample preparation and characterisation

When imaging the resulting scaffolds, especially in samples were platelets are used, the surface was seen to be altered by the cutting method; particles and platelets are seen to align with the cutting blade, obscuring the microstructure. Therefore, samples were sintered in a furnace at 1500 °C for 2 hours. (Except for extremely porous platelet scaffolds where the platelets lacked connectivity.) The scaffolds became brittle after sintering, and especially well aligned samples were prone to break by shear forces in the direction of alignment. However, slow speed diamond saw cutting and subsequent light polishing and washing off the debris yielded highly visible microstructures. For aligned microstructures, an Zeiss Xradia Versa 510 X-ray microscope for tomography was used to confirm large scale 3-dimensional alignment using a 4x objective, 50kV voltage, 80μA current, 30s exposure time, and a resulting voxel size of 4.852x4.852x4.852 μm. Scanning electron microscopy (SEM) images were taken using 5 kV acceleration voltage and 200 pA beam current on a JSM-840F (JEOL instruments) and Merlin (Zeiss) SEM. Optical images were taken using a Leica Microsystems M165 optical microscope with 16.5:1 zoom optics of samples for which SEM resolution was not necessary to observe alignment. The orientation of lamellae was colourized using ImageJ, with open source plugin OrientationJ.

2.3 Results and discussion

**Part of this work was done together with Claudio Ferraro [CF], Adam Mellul [AM] and Thomas Ibbetson [TI]. Their initials are included in the subscript of Figures they contributed to.*

2.3.1 Controlling the microstructure

To control the shape of the lamellae, different additives were used to modify the microstructure. Munch *et al.*[138] observe smooth features when adding sugar, which is also seen to promote the evenly distributed growth of homogeneous and regular dendrites over

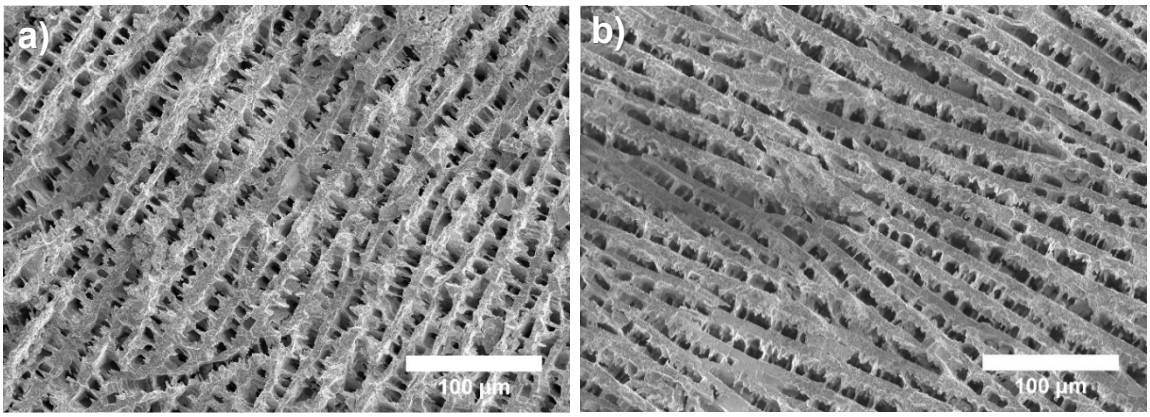


Figure 2.9 – SEM-images of an 20wt% alumina suspension in water frozen at 15 °C/min with a) 5wt% dissolved saccharose and b) 10wt% dissolved saccharose *CF

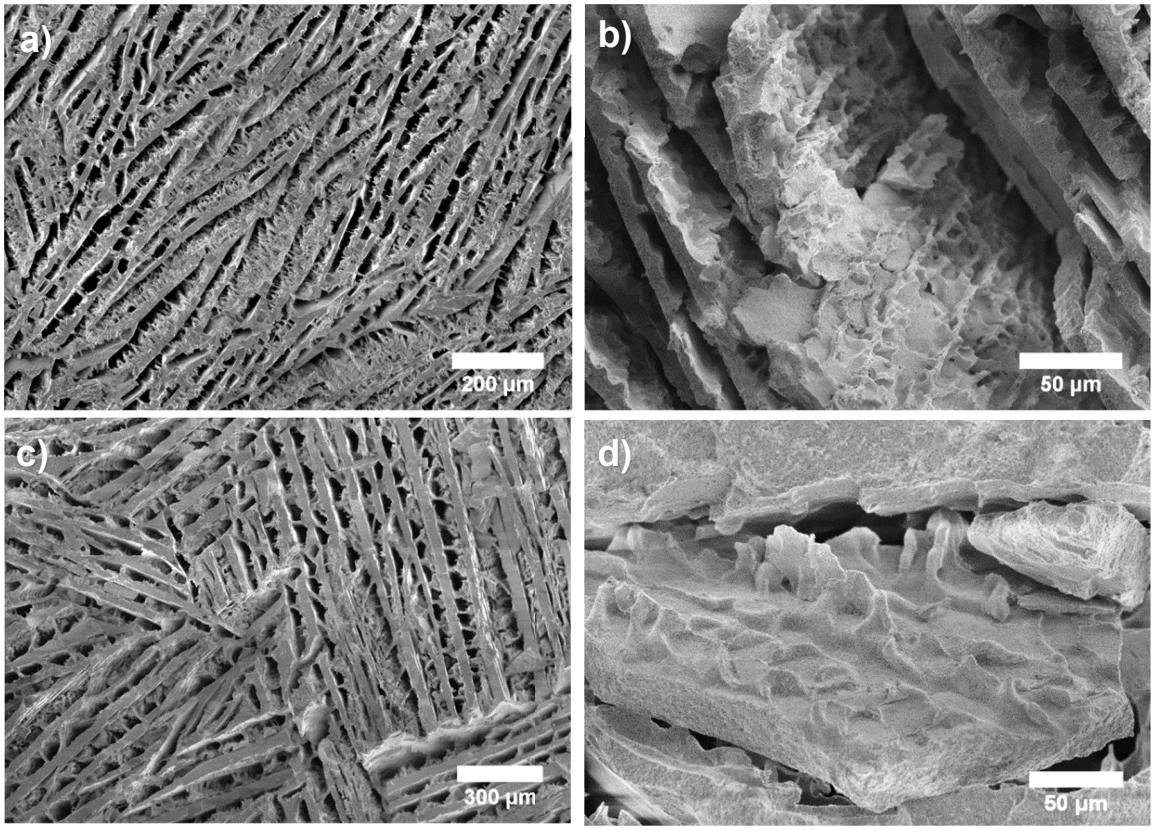


Figure 2.10 – SEM-images of a 50wt% alumina suspension in water frozen at 5 °C/min with a-b) 5wt% dissolved saccharose and c-d) 5wt% dissolved ethanol. *CF

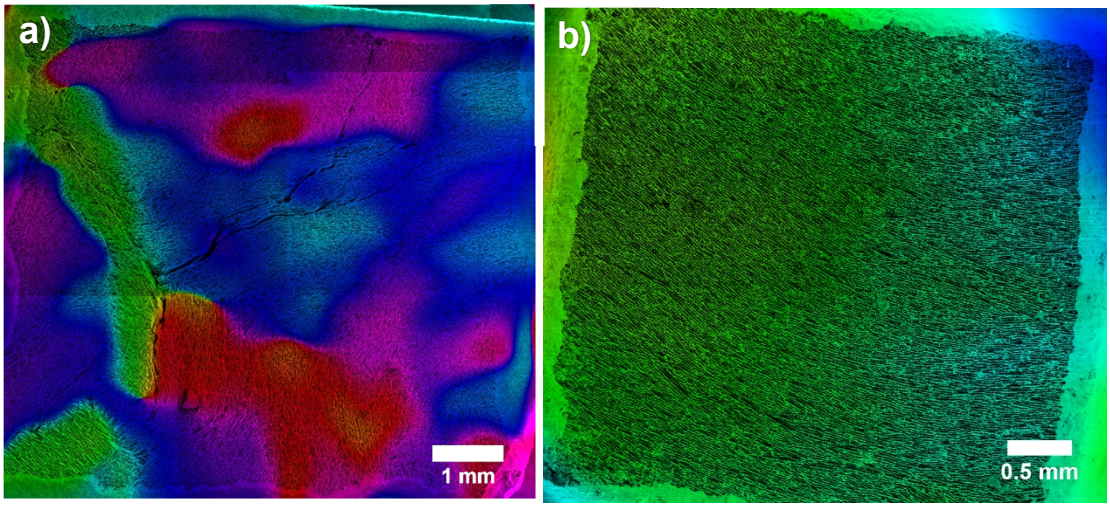


Figure 2.11 – Artificially coloured SEM images of the top of a freeze-cast scaffold to visualize the degree of alignment.in a freeze-cast scaffold of 20wt% alumina suspension in water frozen at 15 °C/min with a) 5wt% saccharose on a flat copper surface and b) 10wt% saccharose on a 10° sloped copper surface.

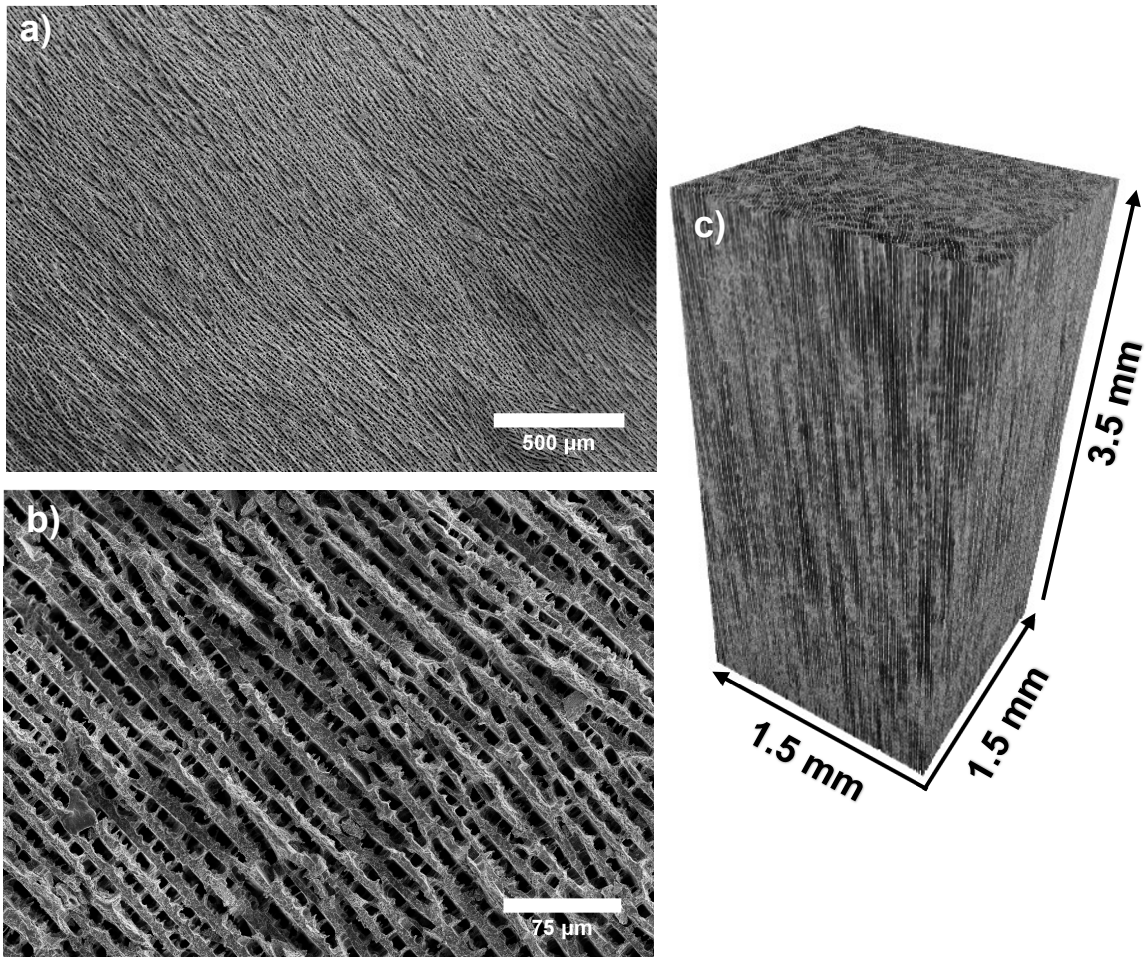


Figure 2.12 – a, b) SEM images of a freeze-cast scaffold of 20wt% alumina suspension in water frozen at 15 °C/min with 10wt% saccharose on a 10° sloped surface, showing full alignment. c) 3D reconstructed tomography image showing that alignment is not just local but persists in 3 dimensions.

the surface of the lamellae. This is here reproduced in Figure 2.9. When increasing the sugar content, the number of bridges decreases and become more regular and evenly spaced. The phenomenon of having both a smooth side and a rough side of the lamellae (Figure 2.9b and Figure 2.10a,c) has been described before by Deville *et al.*[124] who determined that this

phenomenon is due to the anisotropy of interface kinetics; the temperature gradient and preferred dendritic growth direction in the sense of interfacial energies do often not align. As additives such as sugar in this case vary the viscosity and interfacial tension[143], it is likely that this phenomenon is also affected by the amount of sugar used as an additive. Regular dendritic growth and bridge forming is also observed when comparing sugar with ethanol as an additive (Figure 2.10). It stands out that scaffolds generated with ethanol have slightly thicker lamellae with smoother surfaces and less bridge forming.

Initially, the works of Munch *et al.*[138] are followed whereby the surface of the mould is patterned in order to achieve alignment. However, as can be seen from Figure 2.11a, only clusters of alignment are present and large-scale alignment is not obtained. The crack formation in the middle of the sample is due to the cutting procedure where the original scaffold had to be reduced in size for SEM imaging. To improve the alignment, the works of Bai *et al.*[140] are followed who use a tilted slope to initiate ice growth 1-dimensionally. Since a fast cooling rate in combination with a sloped surface has shown to be advantageous in getting a good alignment in experiments by Bai *et al.*[140], instead of using a PDMS wedge, a more conducting wedge of pure copper with a 10° slope is used here. As shown in Figure 2.11 and 2.12, almost complete alignment is obtained using this method.

2.3.2 Upscaling and reproducibility

Following the successful alignment of the microstructure in 2.3.1, the setup was replicated and adjusted to be able to freeze-cast a large amount of cm-scale aligned scaffolds for up-scaled production. First, the patterning method outlined in works of Munch *et al.*[138] was investigated more in-depth as this technique promises higher control and a simpler setup. Munch *et al.*[138] hypothesize that a preferred nucleation at sharp angles of the pattern is the reason for alignment perpendicular to the created linear patterns and note that further investigations will be necessary to clarify these aspects (Unfortunately, the method of patterning is not described in their works).

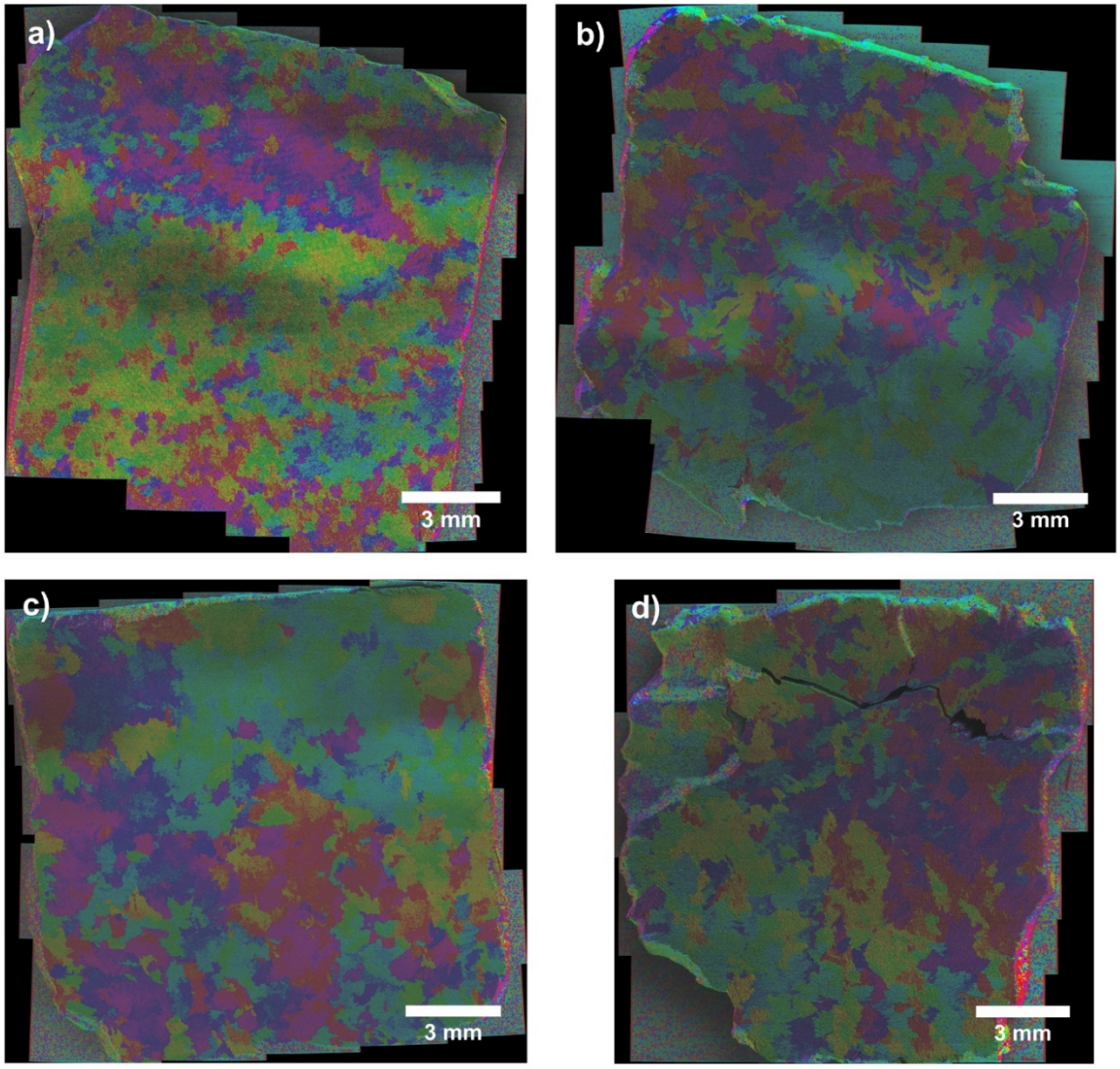


Figure 2.13 – Artificially coloured SEM images of the top of freeze-cast scaffolds, to visualize the degree of alignment after freeze casting with a 50wt% alumina suspension in water with 10wt% PVA on a) a polished copper surface b) a patterned copper surface using P80 sandpaper c) a patterned PTFE tape surface scratched with a scalpel every mm d) a scratched plastic surface. *AM

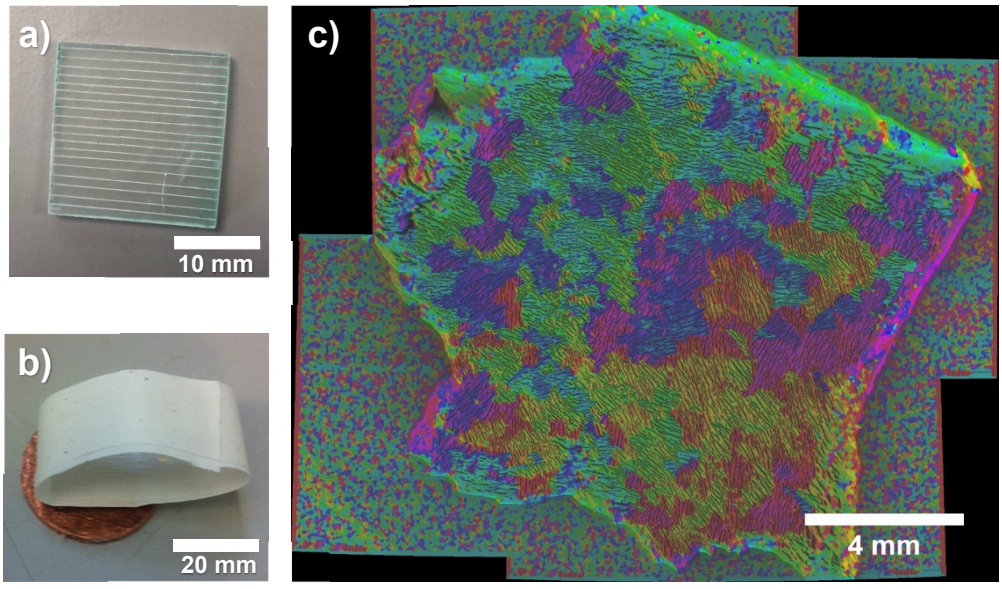


Figure 2.14 – a) patterned plastic and b) patterned tape used for ice initiation, and c) An artificially coloured SEM image of the top of a freeze-cast scaffold to visualize the alignment, showing that the algorithm precisely and realistically applies artificial colouring depending on lamellar orientation. *AM

Figure 2.15 shows that by using PTFE tape patterned with straight lines using a scalpel (Figure 2.14b), it is possible (after careful removal of the tape after freeze-drying) to image the surface where the ice initiated. Indeed, it is seen that the sharp edges of the pattern have initiated lamellae and show dendritic growth, supporting the hypothesis put forward by Munch *et al.*[138]. In addition to this patterning method, patterns are generated using silicon carbide paper which have previously been used by Launey *et al.*[81] and which seem to generate aligned lamellae at least on a mm scale. The resulting microstructures are imaged in SEM and the alignment of these lamellae is colour coded using ImageJ/OrientationJ (Figure 2.13). As the algorithm needs to recognize the lamellae, high magnification images are needed. To therefore visualize the large-scale alignment, multiple high-resolution images are stitched together in Figure 2.13. The downside to this is that in the stitched images, the lamellae are

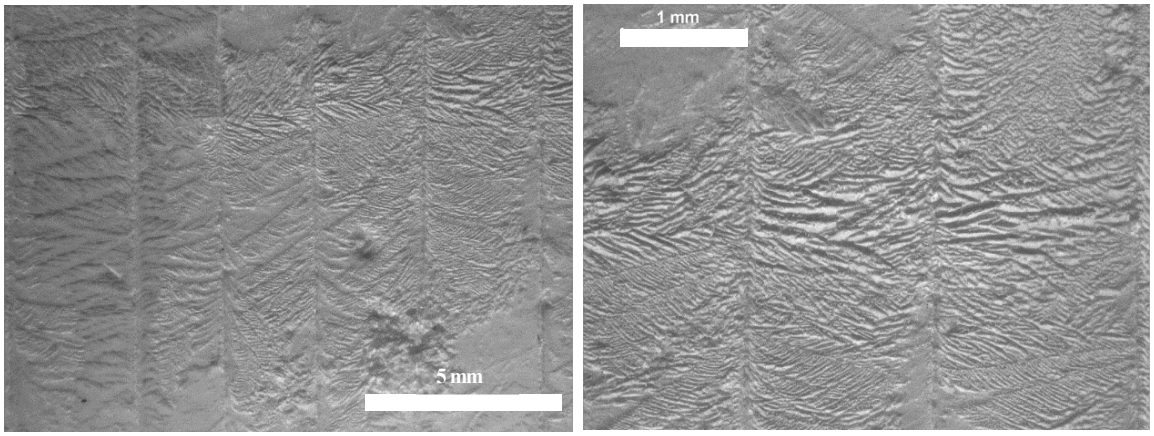


Figure 2.15 – Optical images of the bottom surface of a freeze cast scaffold, patterned using straight lines cut into PTFE tape, showing dendritic growth nucleated at the edges of the lines, growing perpendicular to the patterning direction *AM

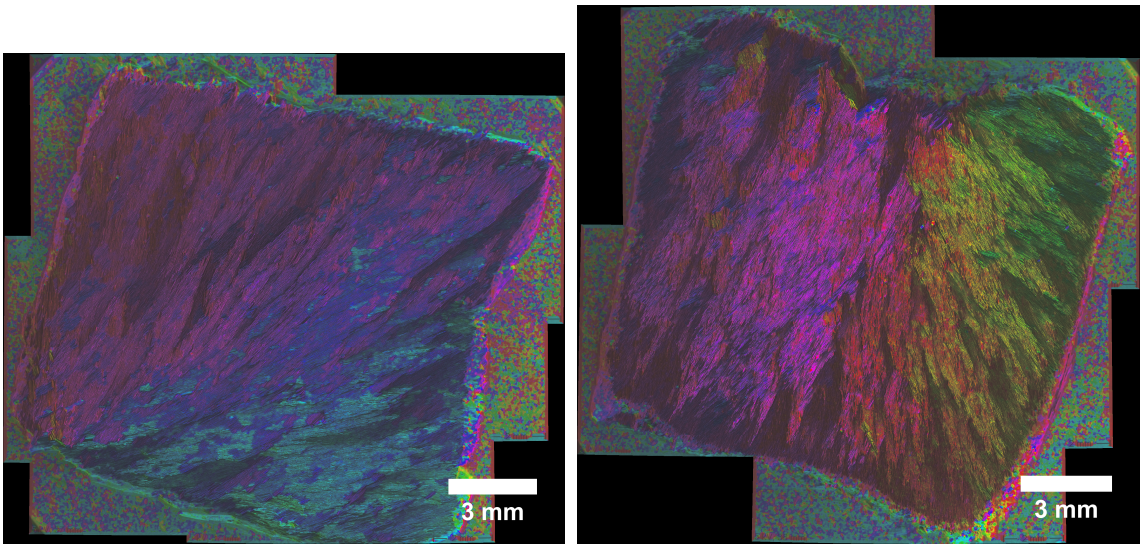


Figure 2.16 – Artificially coloured SEM images of the top of two freeze-cast scaffolds, visualizing the degree of alignment when using a slurry of 50wt% alumina suspension in water with 10wt% PVA on a polished copper surface with a 10-degree slope *AM

not visible anymore. Therefore, Figure 2.14c is included to show a close-up of one of the samples, verifying that the algorithm has applied its colouring correctly. As observed in Figure 2.13c-d, the patterning technique, although seemingly initiating ice growth (Figure 2.15), does not yield large scale alignment of lamellae. Therefore, a dual temperature gradient as proposed by Bai *et al.*[140] was used, using both a polished copper wedge (Figure 2.16) and a pre-patterned copper wedge (Figure 2.17). Unfortunately, the results reported in Figure 2.11b and 2.12 were not reproduced. When a tilted polished copper wedge was used, the structure shows one big domain that initiates from the bottom of the wedge, but not from a

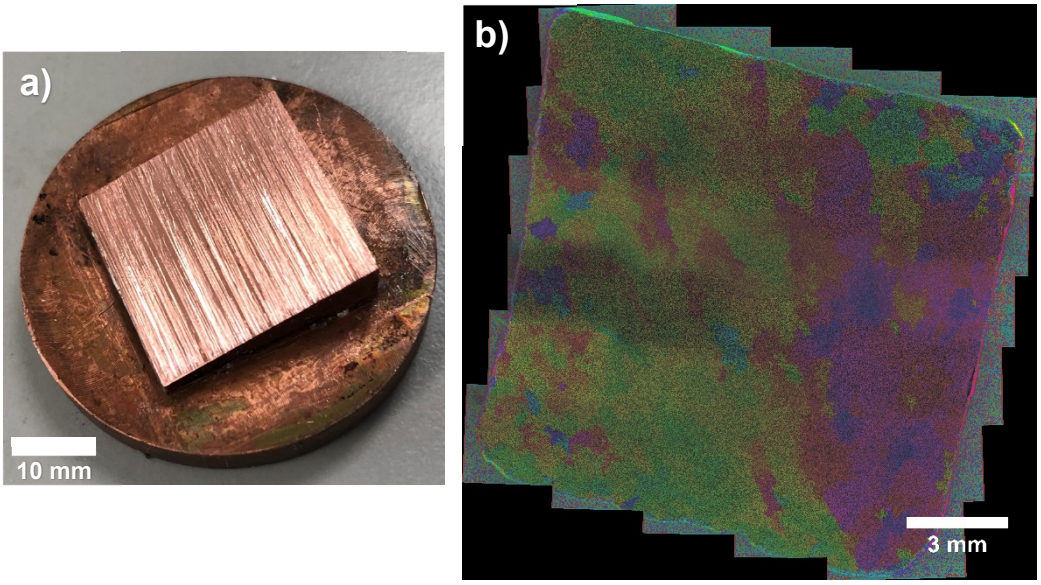


Figure 2.17 – a) Copper wedge with a 10-degree tilt, patterned using silicon carbide paper. b) Artificially coloured SEM image of the top of the scaffold to visualize the degree of alignment in the resulting microstructure using the patterned and 10-degree tilted copper wedge, and a 50wt% alumina suspension in water with 10wt% PVA. *AM

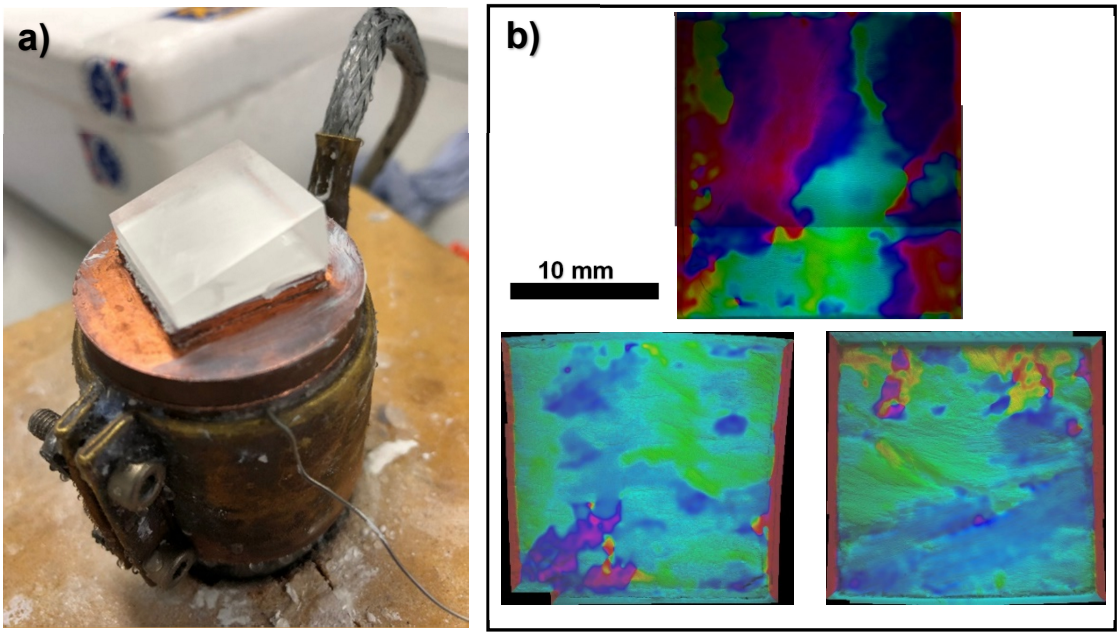


Figure 2.18 – a) acrylic wedge with a 10-degree tilt, mounted on the copper cold finger. b) Artificially coloured optical images of the top of the scaffolds to visualize the degree of alignment in the resulting microstructure using the acrylic wedge and a 50wt% alumina suspension in water with 10wt% PVA.

1-dimensional line – the ice initiation is from a single point resulting in lamellar growth branching out from that point (Figure 2.16). To ensure alignment, the patterning technique used by Launey *et al.*[81] is combined with a dual gradient in an effort to help align the domain. Although the structure shows large areas of alignment (Figure 2.17), multiple misaligned domains exist in the microstructure. An argument can be made that a wedge of copper does not provide a large enough temperature gradient as the conductivity of copper is extremely high compared to the polymer wedge used by Bai *et al.*[140] Therefore, a similar acrylic wedge was manufactured to ensure a larger temperature gradient along the slope (Figure 2.18a). For this system, no improvement in alignment of the lamellae was observed, and every freeze cast seemed to have a unique microstructure with multiple aligned lamellar domains throughout (Figure 2.18b).

2.3.3 Freeze-casting of alumina platelets

Alumina platelets are much harder to freeze-cast because their volume and weight are orders of magnitude larger than alumina nanoparticles. Alumina platelets are prone to sediment in suspension and therefore the viscosity needs to be increased to prevent an uneven solid concentration and resulting density gradient in the freeze-cast scaffold. A high viscosity slurry however also affects the freeze-casting dynamics. In addition to a depression in freezing point which is inherent to all additives in water, the movement of platelets into aligned lamellae is likely inhibited by a high viscosity slurry. Therefore, the viscosity has to be carefully controlled to be high enough to yield a homogeneous mixture during freeze casting procedure while at the same time keeping the viscosity low enough for lamellar growth. (In addition, de-gassing a slurry that is too viscous can be a serious challenge)

For this reason, Hunger *et al.*[144] used a chitosan–gelatin biopolymer to freeze-cast alumina platelets. However, they only obtain a cellular structure with pockets of alignment. The group of Sylvain Deville, who have previously manufactured ceramic composites with these platelets[35], kindly communicated their experimental recipe used for freeze-casting platelets.

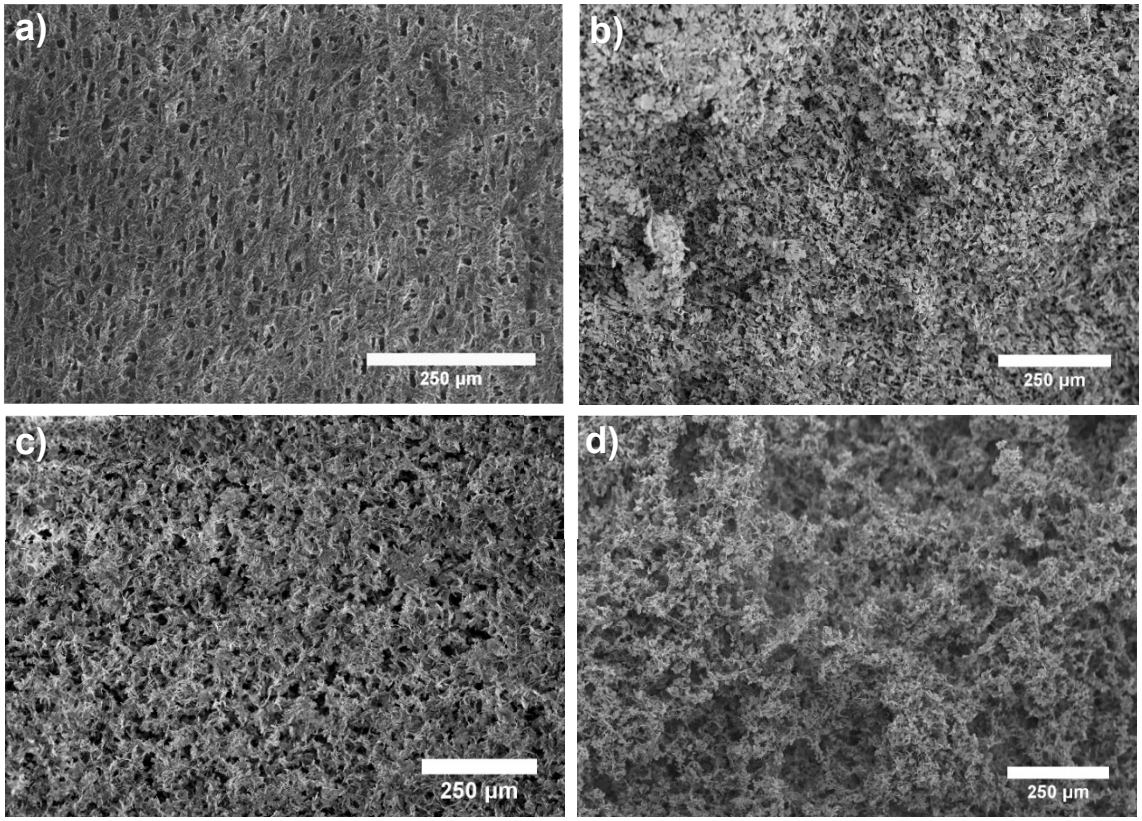


Figure 2.19 – SEM images of freeze-cast scaffolds, from slurries containing a) 50 wt% b) 36 wt% c) 20 wt% and d) 9 wt% alumina platelets. *CF

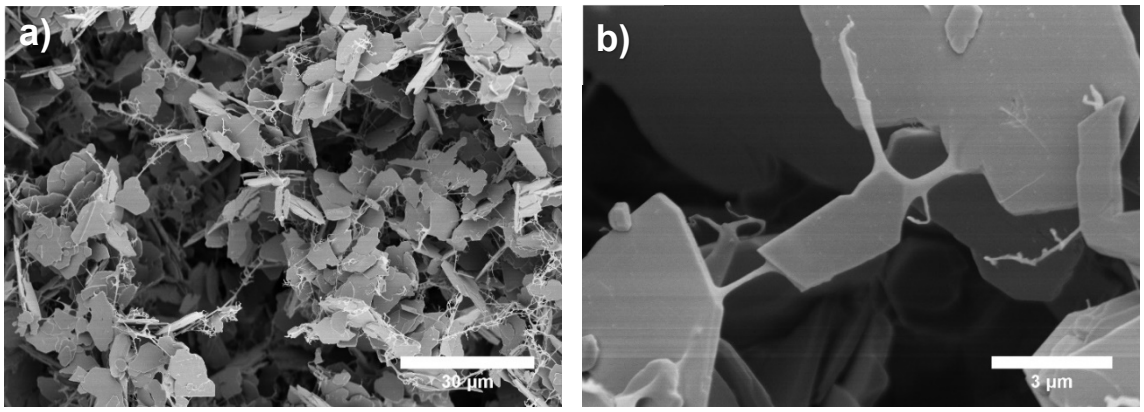


Figure 2.20 – SEM images of a freeze-cast scaffolds, from a slurry containing 9 wt% alumina platelets, showing that a large number of platelets are just held together by the Carbopol binder when the solid loading of the slurry is very low.

Although they do not show the freeze-cast platelet microstructures in their publication, their work on platelet microstructures is at the forefront of the field and a valuable starting point to generate lamellar, aligned porous scaffolds of alumina platelets. Their recipe was used with a -10 °C/min freezing rate. However, the resulting slurry was extremely thick and viscous, hindering the formation of ice crystals and inhibiting the formation of lamellae. Therefore, the alumina platelet content was reduced in a series of freeze-casts to see the effect of solid loading on the microstructure. It can be seen from Figure 2.19 that all freeze-casts have a cellular microstructure. For lower solid loadings the scaffold became very hard to cut, as it

was incredibly porous. A 20 wt% slurry resulted in a 94-96 % porous sample, and as can be seen in Figure 2.20, at 9wt% the platelets were often held together exclusively by the polymer binder and are very easily collapsible.

In an effort to generate a lamellar structure, a slower freezing speed of -1 °C/min was used to prevent trapping of the micron sized platelets and allow them to pack more easily in lamellae. As the platelets are already nacre-like, the resulting larger sized lamellae are not a concern. The slower freezing rate did still provide a cellular structure, so the pH of the solution was adjusted from around 7 to 12 to aid dispersion, as Singh *et al.*[145] show that a well-dispersed suspension of alumina is more easily obtained with high surface charge density to generate strong repulsive forces[145]. It was seen that a stable solution could be obtained with half the amount of Carbopol, indicating that dispersion was significantly improved.

The resulting microstructure shows that this approach was successful in generating a lamellar structure of platelets (Figure 2.21a). However, sodium crystals were observed on the platelets

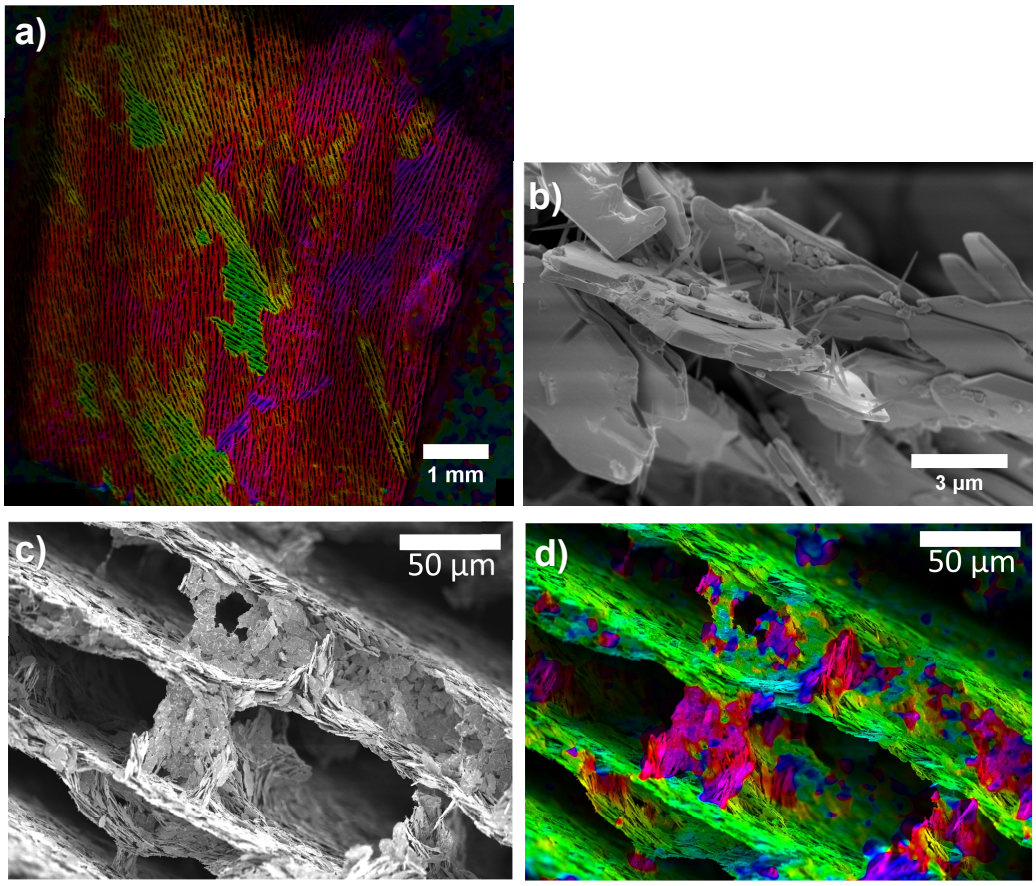


Figure 2.21 – SEM images of a freeze-cast scaffold, from a slurry modified with NaOH to pH=12. The slurry contained 30 wt% alumina, 0.3wt% dispex, and 0.2wt% Carbopol binder. The images show that a) there is lamellar growth throughout the scaffold with millimetre aligned domains. b) the sodium crystallizes and stays in the structure after freeze drying and c-d) the platelets are all aligned within the lamellae themselves with bridge forming occurring every ~0.1mm. *TI

(Figure 2.21b), and thus other chemicals than NaOH to modify the pH or a washing step are recommended to avoid the remaining sodium contamination. When looking more closely at the lamellae, the platelets are observed to be packed in an ordered and aligned fashion (Figure 2.21c-d), except for the bridges between the lamellae, owing to owing to the trapping of ceramic particles by the growing ice[83]. While some bridges are necessary for the stability of the scaffold, the amount of bridges be modified by including additives in the suspension[83] to maximize the number of aligned platelets within the scaffold.

2.4 Conclusions

Freeze-casting is a versatile technique to design porous microstructures. Here, freeze-casting has been used to generate lamellar microstructures using both nanoparticle-alumina and alumina platelets. Two modifications to the freeze-casting technique have been used to improve alignment of lamellae - ice-templating by generating a pattern on the ice-initiation surface and bi-directional freezing, as well as combinations and variations of these two. Freeze-casting using these modifications has, in previous research, shown to be able to induce lamellar alignment on the millimetre-scale and a transition from multiple to single lamellar domains. In this work an effort was made to further this technology and align a lamellar microstructure over macroscopic length scales, with the purpose of creating a nacre-like bioinspired green body for composite fabrication. While neither technique initially yielded reproducible (macroscopic) alignment, a single domain of connected lamellar growth was observed when the bi-directional freeze casting technique was done using a polished, tilted copper surface. In one case, this yielded a completely aligned large-scale single-domain microstructure. However, when attempting to reproduce this alignment, every sample was seen to be unique. Ice growth initiated from a single point instead of the entire bottom side of the setup, resulting in a single domain of lamellae with multiple orientations. Although the whole sample consists of a single macroscopic domain on the centimetre length scale, due to the variability in microstructures using the same parameters, the method is not considered

reproducible enough for large scale composite manufacturing. The unpredictable nature of the freeze-casting method is seen throughout all experiments. When freeze-casting alumina platelets to generate a more nacre-like scaffold, initially cellular structures were produced, but lamellar structures were obtained by freeze-casting in a basic (pH=12) chemical environment. The resulting scaffolds have a hierarchical microstructure where platelets are aligned within lamellae, which are aligned themselves in millimetre-sized domains.

Chapter 3 – MWCNT growth and coating of bioinspired alumina

This chapter introduces the coating of MWCNT's on alumina surfaces, focused on the underlying mechanisms and challenges involved in applying CVD technology/methodology to generate homogeneously MWCNT-coated composite materials. The first part of this chapter describes the *in-situ* growth of MWCNTs in freeze-cast alumina scaffolds. The second part of this chapter describes the *in-situ* growth of MWCNTs on alumina platelet powders.

3.1 Introduction

3.1.1 Carbon nanotube growth through chemical vapour deposition

The existence of needles comprised of coaxial graphitic carbon, now mostly referred to as multi-walled carbon nanotubes (MWCNTs), was discovered by Sumio Iijima in 1991[146]. Since this discovery, MWCNTs have been a source of much excitement and research, and multiple methods for MWCNT production have been established. Reported methods include pyrolysis[147], ball milling and annealing[148], diffusion flame synthesis[149], laser ablation[150], arc discharge[151], and chemical vapor deposition (CVD)[152]. The latter three methods have received much attention and are now widely used for the production of MWCNTs[153]. The arc-discharge method, used by Iijiama[146] in his discovery, involves an electric arc that vaporizes a graphite anode packed with metallic catalyst particles and graphite powder in inert atmosphere. While the arc-discharge method can produce large quantities of MWCNTs, the volatility of the arc means that the process cannot be well controlled and large amounts of impure materials are generated. Later on, laser ablation was discovered to be able to generate MWCNTs by exposing the graphite anode directly to a high power laser[154]. This method is

able to generate very pure MWCNTs, but does so in very small quantities, even in optimised processes[155,156]. In addition to this trade-off between quantity and quality, these first two methods suffer from a large energy expense to generate the MWCNTs, and the need for specially fabricated graphite targets[157]. The third method, CVD, is an extremely promising technique as it has the potential to achieve both high yield and purity at the same time. Under the name of carbon filaments, threads and fibres, there are reports dating back to France in the 1890s, describing filamentous carbon materials after thermal decomposition of carbon materials[158]. In the 1950s several Russian researchers put out reports describing the formation of filamentous 'layered' carbon through a decomposition process[158–160]. Thus, CVD may be the oldest method in existence to have ever been used to manufacture MWCNTs, even if those researchers may have been unaware of the exact molecular arrangement of the produced fibres.

In CVD, a gaseous carbon source is thermally decomposed at a catalyst site. Although the precise mechanism is still debated, common consensus on the mechanism of growth[158,161,162] is that when the (hydro) carbon precursor comes into contact with a metallic catalyst particle at high temperature, it decomposes and carbon atoms dissolve into the metallic catalyst particle. After reaching the solubility limit, the carbon then starts to precipitate out as a graphitic cylindrical tube which is now known as a MWCNT. Especially important for application is the upscaling potential of the CVD process – in principle, the surface where decomposition takes place can be made as large as needed. In addition, CVD is able to create highly aligned arrays or 'carpets' of MWCNTs[163]. Most importantly, in bioinspired composite manufacturing, the growth of MWCNTs through a CVD process can overcome the issue of an agglomerated and defective MWCNT-phase in composite materials by growing them directly in or on ceramic porous materials or scaffolds[164]. Therefore, CVD is used and further explored in this work. A wide range of factors influences the growth of MWCNTs in the CVD process. These include gas flow parameters such as gas velocity, pressure and concentration, type and amount of hydrocarbon precursor (with associated diffusion and

dissociation rates) and type of carrier gas. In addition, the catalyst properties such as elemental composition[165], oxidation state[166], size[167,168] and amount of catalyst[169] are important factors in MWCNT growth. Moreover, the properties of the material that supports the catalyst, such as surface roughness[170] and elemental makeup[171,172], play a role in MWCNT growth. The temperature[173] and duration of the experiment[174] also play a key role in MWCNT-formation, and a multi-stage process can be used where different gases (such as hydrogen) can be injected into the CVD-system at different times to aid or modify the chemical process of MWCNT-formation. In addition, the CVD process can be more radically modified; different variations of CVD have been established such as plasma-enhanced CVD (PECVD), where the decomposition is initiated by electrical energy input rather than heat, and aerosol-assisted CVD (AACVD), where an aerosol is generated ultrasonically, transporting the precursors to the substrate. As Jones *et al.*[175] point out, there is a "sometimes bewildering array of acronyms" used in conjunction with the acronym "CVD". However, the physical mechanism remains the same and those acronyms mainly indicate the type of precursor, injection method, energy supply or pressure conditions.

It is clear from the above that CVD can give us a very precise control of the MWCNT-growth process as each of those parameters can be tailored with relative ease. In fact, when it comes to precise structural control of MWCNTs, CVD is the only answer[158] and offers the potential of customized structural properties such as length, diameter, and number of graphitic walls. At the same time, the extremely large parameter space presents an enormous experimental challenge, and because CVD parameters are often interdependent, there exist many specific process windows[176]. This often limits the impact of research papers on the subject as changing any of the parameters mentioned above can yield significantly different results. There are however several reports on key parameters which allow us to design a route towards optimized growth conditions in bioinspired alumina scaffolds.

3.1.2 Key CVD parameters for CNT growth on bioinspired alumina

It has been well established that there exist catalyst materials that act as CNT growth-initiators, and transition metal catalysts such as iron, nickel and cobalt have been widely used in this regard in CVD[165]. Their catalytic activity is attributed to their non-filled d-shells, which enables them to interact with hydrocarbons[177]. The high degree of crystallinity that can be obtained in a short timespan demonstrates that carbon atoms are extremely mobile and can diffuse easily over and through the metal catalysts[178]. The size required for these particles to catalyse MWCNT growth is in the range of 0-0.1 um, and results in carbon filaments with similar diameter to that of the catalyst particle[178]. Therefore, in experiments where metal films are deposited, these are often heated/annealed to generate nano-sized particles or "islands" [168,179,180]. Due to the high density of nanoparticles generated from metallic films, these methods often produce vertically aligned MWCNTs (VA-CNTs). It has been shown that when the nanoparticle density is low enough, the Van der Waals force between MWCNTs becomes too weak to align them, which results in a more tangled coverage[181].

A wide range of CVD carbon precursors have been used to grow MWCNTs. While MWCNTs have been grown from more exotic carbon materials such as palm oil[182], in general they fall into two categories: cyclic/aromatic hydrocarbons such as benzene, cyclohexane, xylene, and fullerenes and linear/aliphatic hydrocarbons such as methane, ethylene and acetylene. Some studies comparing these two types of precursors comment that by using either aromatic or aliphatic carbons, specific MWCNT properties can be selected for, such as curly or straight morphology[158] or the number of graphitic walls the MWCNTs consist of[183]. However, due to the interdependence of CVD parameters, these results do not translate well to other CVD systems. Zhong *et al.*[184] identify the growth species from thermally decomposed ethylene, ethanol and methanol CVD. They show that acetylene is formed as a result of hydrocarbon decomposition and is the actual precursor for MWCNT growth. Indeed, of all the carbon precursors, acetylene is especially popular for MWCNT synthesis

due to its low decomposition temperature (450°C)[185,186]. At higher temperatures, very high growth rates and MWCNTs exhibiting a high degree of crystallinity are observed whereby decomposition of acetylene at 800°C appears to yield optimal MWCNT growth[187,188,189].

In addition to catalyst and carbon precursor, one of the main factors that influences CNT growth is the substrate. That the substrate plays an essential role in the growth of CNT's is most clearly seen in experiments by Hasegawa *et al.*[171]. They observe a large difference in CNT-coverage between a SiO_2 and an Al_2O_3 substrate in acetylene CVD; while for the Fe catalyst on SiO_2 some CNTs were observed (submicron thickness layer or less), on Al_2O_3 under the same conditions, a 1 mm thick CNT deposit was observed. The fact that CNTs were observed on both surfaces means that the alumina substrate has an enhancing effect. Kong *et al.*[190] used the same two supports in methane CVD and confirm that only iron oxide on alumina gives abundant CNT growth.

Due to the growth enhancing effect shown on alumina with iron-based catalysts, and the promising reports on CNTs grown with acetylene in terms of energy usage and crystallinity of the resulting CNTs, the growth and distribution/dispersion of MWCNTs utilising iron-based catalysts on alumina is optimised in this work using acetylene-assisted CVD.

3.2 Materials and methods

Freeze-cast alumina scaffolds with lamellar structures were infiltrated with different iron-based nanoparticle catalysts. Nacre-like alumina platelets were both used with the nanoparticle catalysts dispersed on their surfaces and in precoated form. Using a CVD procedure, MWCNTs were grown *in-situ* in the scaffolds and on the alumina platelets. The annealing time and gas composition during annealing were varied, and different gas compositions and growth times were used during the growth stage of the MWCNT to optimize the MWCNT growth. Raman spectroscopy, scanning electron microscopy (SEM)

and Thermogravimetric analysis (TGA) were used to characterize the MWCNT phase while X-Ray diffraction (XRD) was used to monitor catalyst evolution during CVD.

3.2.1 Acid treatment of scaffolds

Where indicated, an acid cleaning procedure was used. The procedure used here was developed for the cleaning of silicon wafers used in CVD by Werner Kern[191] in 1965 while working at the radio corporation of America (RCA). The procedure has from there onwards come to be known as the RCA cleaning method. Originally, the method has three steps: 1) removal of organic materials and particle residues, 2) removal of the oxide layer on the surface (normally with HF), 3) removal of remaining traces of metallic (ionic) contaminants. For the purpose of growing CNTs on alumina, it is not necessary to remove the oxide layer with an HF treatment, therefore this step was omitted. Zhang *et al.*[192] have done extensive research on the method, and using their findings the procedure is modified for alumina scaffolds. The full procedure is listed below:

Step 1: To help make sure any fingerprints, large chunks of fats and other bulky contaminants and particulates were removed the alumina scaffold was soaked in ethanol and left overnight (12 h).

Step 2: Any leftover grease and dirt were then removed in a 30 minutes sonication procedure in a solution containing detergent, ethanol and water in a 1:20:79 vol%. after which the sample was dried using a nitrogen gas gun.

Step 3: To remove the detergent molecules and definitively remove any organics, a piranha solution was prepared of H_2SO_4 and H_2O_2 in a 3:1 vol%. The sample was soaked in this solution for 20 minutes at 80 °C on a hotplate, rinsed in de-ionised (DI) water, after which the sample was dried using a nitrogen gas gun.

Step 4: To remove ionic contaminants and metallic nanoparticles, the industrial cleaning standards SC1 and SC2 (Standard Cleaning 1 and 2 respectively) were used. The sample was

dipped into a solution of NH_3 +H_2O_2 + H_2O in a 1:1:2 vol% (SC1) for 20 minutes at 80 °C, after which it was dipped in a solution of HCl+H_2O_2 + H_2O in a 1:1:2 vol% (SC2) for 20 minutes at 80 °C. Then the acid was washed off with DI water, and dried in nitrogen gas.

3.2.2 Catalyst particle creation and dispersion procedure

Both ultra-small (<10nm) iron oxide nanoparticles and flame-spray-pyrolysis generated iron oxide nanoparticles (~20 nm) were used. Ultra-small nanoparticles are generated in solution, which means that they come in a well dispersed form. These ultra-small nanoparticles have the potential of catalysing small diameter single-walled carbon nanotubes (SWCNTs). Commercial flame spray pyrolysis generated iron oxide nanoparticles can generate MWCNTs, which are more chemically resistant and have larger diameters. While using commercial nanoparticles can yield a more reliable product, these are generated in powder form and thus have to be dispersed before they can be used in the CVD synthesis of MWCNTs.

The ultra-small iron oxide nanoparticles were fabricated using a modified recipe published by Piché *et al.*[193]. 510 mg iron(III)acetylacetonate ($Fe(acac)_3$) precursor was combined with 30 ml of oleylamine in a 3-neck flask. A magnetic stirrer was then cleaned and inserted, and the flask was positioned into a band heater with a rotating magnetic field to stir at 400rpm to homogenize the solution. The flask was then connected to an argon line, thermocouple and reflux cooler, and argon flow was started to evacuate the air. The mixture was then heated in 15 minutes to 225°C, and held at this temperature for 10 minutes, after being cooled naturally. The nanoparticles were then sedimented by centrifugation at 4600rpm, re-dispersed in ethanol and sonicated in a sonic bath for 5 minutes. This was repeated 5 times to wash off residual oleylamine. Finally, the particles were dispersed in cyclohexane and stored in a refrigerator. Infiltration of freeze-cast scaffolds was then done by dripping a 1 mmol suspension of these nanoparticles in cyclohexane onto the top surface of the scaffold. The suspension is propagated through the scaffold by capillary and gravitational forces,

resulting in a dispersion of iron nanoparticles over the outer and inner surfaces of the scaffold.

20 nm flame spray pyrolysis-generated iron oxide particles (Johnson Matthey Technology Centre, Reading, UK.)[194] were dispersed in ethanol through sonication using a sonic horn/tip and vortex mixer with and without sodium dodecylbenzene sulfonate (SDBS) as a surfactant. This dispersion was then drop-casted onto the freeze-cast scaffolds. For platelet-alumina experiments, the nanoparticles were mixed together with the platelets to get a 2 wt% solid catalyst content. The catalyst particles were either dry mixed with the alumina platelets using a vortex mixer for 30 minutes [method A] or sonicated in a sonic bath (700 W) in ethanol for 30 minutes, after which the sample was dried in a vacuum oven overnight [method B].

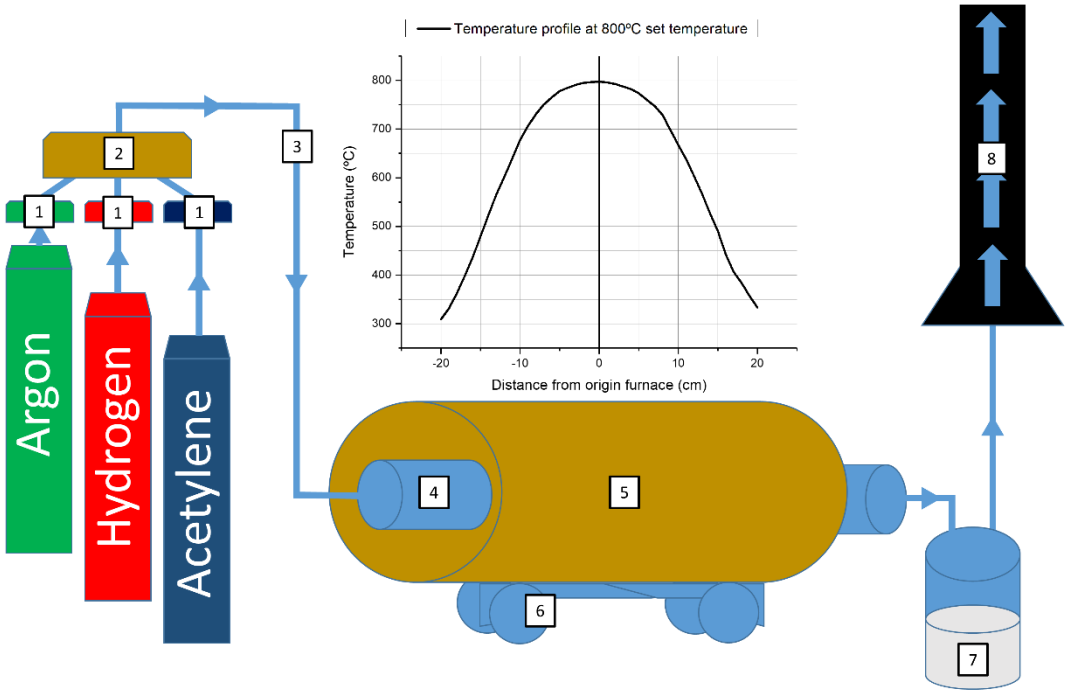


Figure 3.1 – Diagram of the CVD setup: 1) Gas flow controllers of the Inlet gases 2) Multi-gas controller 3) Stainless steel tubing 4) Quartz tube 5) Tube furnace with heating elements and alumina inner tube, with a thermocouple connected to a PID controller 6) Wheels that connect to a rails for furnace movability 7) Bubbler filled with acetone 8) Gas outlet. The temperature profile of the furnace is plotted above the diagram.

3.2.3 CVD synthesis of MWCNTs on alumina

The CVD setup used is depicted is Figure 3.1. The setup consisted of a tube furnace (Elite TSH16/50/180 3216CP) mounted over a quartz tube with inner diameter (ID) measuring 21 or 28 mm. The quartz tube was connected to the gas inlet through individual gas controllers, operated by a multi gas controller (Mass-Flo®, MKS instruments UK ltd). The gas lines were connected to the following gases:

Argon UN1006 EC-no. 231-1470 (compressed) - 99.998% pure
Hydrogen UN1049 EC-no. 215-605-7 (compressed) – 99.99% pure
Acetylene UN1001 EC-no. 200-816-9 (dissolved) – 99.6% pure

On the other side of the quartz tube, an acetone bubbler was connected to have a visual indication of gas flow, to prevent any backflow and to filter outgoing gases. The furnace was mounted on rails to be able to reach target temperature of the alumina substrates in an exponential fashion rather than linearly, eliminating the long exposure of the catalyst particles during heat up of the furnace which is often seen in most other CVD MWCNT syntheses. Using this method, the quality and coverage of the MWCNTs can be directly correlated to the catalyst annealing times and annealing atmosphere at target temperatures. The furnace temperature was calibrated using a K-type thermocouple at the sample position to account for the difference between the furnace sensor and the temperature of the sample (Figure 3.1). As the temperature 5 cm from the midpoint of the furnace was 778 °C, the setpoint was raised to 822 °C to make sure a 10 cm region was created with temperatures between 800-822 °C.

The air was purged out of the system using 1 standard litre per minute (slm) argon. Then, once the furnace reached the set point under argon flow, the furnace was shifted towards the sample, and the CVD procedure with parameters as detailed in Table 3.1 was started.

CVD parameters #	Annealing time in >0.5 slm argon at 800 °C	Annealing time in 30% hydrogen at 800 °C	Precursor gas mixture flow rates	CVD time	Associated figures	Catalyst	Tube ID (mm)
CVDP1	10 min.	-	0.120 slm Ar 0.040 slm C_2H_2	10 min	Fig. 3.2	none	21
CVDP2	10 min.	15 min	0.120 slm Ar 0.040 slm C_2H_2	10 min	Fig. 3.3,3.4	none	21
CVDP3	10 min.	10 min	0.6 slm Ar 0.025 slm C_2H_2	10 min	Fig. 3.5	none	21
CVDP4	10 min	10 min	0.1 slm Ar 0.025 slm C_2H_2 0.075 H_2	20 min	Fig. 3.6,3.8,3.9	none	21
CVDP5	10 min	-	0.1 slm Ar 0.025 slm C_2H_2 0.075 H_2	20 min	Fig. 3.6	none	21
CVDP6	10 min.	-	0.1 slm Ar 0.025 slm C_2H_2 0.075 slm H_2	20 min	Fig. 3.12,3.13	Ultra-small iron oxide NPs	21
CVDP7	10 min.	10min	0.1 slm Ar 0.025 slm C_2H_2 0.075 slm H_2	20 min	Fig. 3.14,3.15	Flame Spray Pyrolysis generated iron oxide NPs	21
CVDP8	10 min.	-	0.6 slm Ar 0.025 slm C_2H_2	30 min	Fig. 3.16,3.17	Flame Spray Pyrolysis generated iron oxide NPs (After acid treatment)	21
(AA)CVDP9	5 min	-	0.7 slm Ar	10 min	Fig. 3.18	Ethylbenzene 95%+5% ferrocene	21
(AA)CVDP10	-	5 min	1 slm Ar 0.3 slm H_2	10 min	Fig.3.18,3.19, 3.20	Ethylbenzene 95%+5% ferrocene	21
CVDP11	0,10 and 60 min	-	0.96 slm Ar 0.04 slm C_2H_2	10 min	Fig. 3.21,3.22	Flame Spray Pyrolysis generated iron oxide NPs (Method A)	28

CVDP12	0,10 and 60 min	-	0.7 slm Ar 0.3 slm H_2 0.04 slm C_2H_2	10 min	Fig. 3.21,3.22	Flame Spray Pyrolysis generated iron oxide NPs (Method A)	28
CVDP13	0,10,20,30,60 min	-	0.96 slm Ar 0.04 slm C_2H_2	10 min	Fig. 3.23,3.24	Flame Spray Pyrolysis generated iron oxide NPs (Method B)	28
CVDP14	0,10,20,30,60 min	-	0.7 slm Ar 0.3 slm H_2 0.04 slm C_2H_2	10 min	Fig. 3.23,3.24,3.26	Flame Spray Pyrolysis generated iron oxide NPs (Method B)	28
CVDP15	60 min under inert, mildly oxidising, oxidising and reducing conditions listed below.	-	0.7 slm Ar 0.3 slm H_2 0.04 slm C_2H_2	10 min	Fig. 3.25	Flame Spray Pyrolysis generated iron oxide NPs (Method B)	28
CVDP16	60 min	-	0.7 slm Ar 0.3 slm H_2 0.04 slm C_2H_2	10 min	Fig. 3.29, 3.30	Xirallic Radiant red/Iriodin.	28

Table 3.1 – lookup-table listing all CVD parameters used for the growth of MWCNTs in this work. Every combination of annealing gases and time, gas flow parameters and catalyst used is linked to a chemical vapour deposition parameter number (CVDP#) which can be found in the text next to relevant data and associated figures.

In the case of alumina platelets, those coated with catalyst particles using method B yielded the highest quality MWCNTs (determined using Raman spectroscopy). So, for these platelets the annealing atmosphere was varied to explore its effect on the formation of MWCNTs. Annealing was done for 60 minutes under the following conditions: Inert (0.2 slm and 0.5 slm argon), mildly oxidising (0.05 slm argon), oxidising (under airflow of 1.62 slm) and reducing (0.1 slm argon/0.1 slm hydrogen) [CVDP15].

After synthesis the furnace was shifted away from the sample and cooled down under argon flow (>1 slm). To prevent any oxidation occurring after synthesis, the sample was taken out after 10 minutes, after which the tube at the sample position reached such a temperature that it could be physically touched. For aerosol-assisted CVD (AACVD) experiments, ferrocene ($Fe(C_5H_5)_2$, Sigma–Aldrich, was purified by sublimation. Ferrocene was then dissolved into ethylbenzene ($C_6H_5CH_2CH_3$) in a 1:20 ratio and loaded into piezo-based aerosol generator,

connected in-line with the gas flow from the gas controller. The substrate area was first heated in air to get rid of any contaminants, after which the quartz tube together with the aerosol unit was flushed with argon at 1 slm for 5 minutes, to purge any air from the system. The aerosol consisting of 95 wt% ethylbenzene and 5 wt% ferrocene was then let into the quartz tube, and the aerosol was allowed to flow through the reactor for 10 minutes, after which the generator was closed off from the CVD system. The distance between the aerosol generator and tube furnace was 7 cm, and it was noted that when this distance was too large (21 cm), growth was severely reduced due to aerosol depositing in between generator and substrate.

3.2.4 Substrate materials

Two types of scaffold were used; firstly freeze-cast alumina scaffolds, as fabricated through the freeze-casting procedure detailed in Chapter 2, and secondly alumina μm-sized platelets.

α-alumina platelets (corundum) were obtained from Antaria Limited, Bentley, Australia, under the brandname Alusion™, who quote a mean diameter of 7.1 μm and a thickness between 300-500 nm. During the experimental work, the patent of these was bought by Merck and the same platelets were rebranded to RonaFlair® White Sapphire. Merck quotes that 80% of the produced platelets are <16.0 μm, with a D50 of 7-11 μm. these platelets were used as the platelet-template for MWCNT growth in CVD and AACVD. Two types of pre-coated alumina platelets were also obtained from Merck: 58031 Xirallic® F60-51 SW Radiant Red, consisting of 47-62 wt% alumina with a 38-48 wt% Fe_2O_3 coating and 158028 Xirallic® T60-10 SW Crystal Silver, consisting of 63-80 wt% alumina with a 0-2 wt% SnO_2 and 20 – 30 wt% TiO_2 coating. Both pre-coated platelets are quoted by the manufacturer to have <5 wt% auxiliary elements, and a D_{10} 7 – 13 μm, D_{50} 15 – 21 μm, and D_{90} 26 – 36 μm. Mica coated iron oxide was also obtained from Merck, brand name Iriodin® 504, lot#1042321000, with a particle size of 5-40 μm.

3.2.5 Characterisation

Raman spectroscopy is one of the most common characterisation techniques for graphitic materials such as MWCNTs[195]. Raman scattering occurs when a photon interacts with molecular vibrations or phonons, and its wavelength is shifted either up or down. Since Raman spectroscopy is a non-destructive method of characterization and does not require physical contact, it is relatively quick and easy to use. The most prominent features in the Raman spectra of graphitic materials are peaks that appear around 1350 cm^{-1} and 1582 cm^{-1}, known as the D (Disordered) and G (Graphitic) band respectively[195]. The D band is a defect-induced feature, while the G band is indicative of sp^2 hybridized carbon[196,197]. The ratio of the D band to the G band intensity, or I_D/I_G peak intensity ratio, was used to reveal the defectiveness of the as grown MWCNTs. Raman spectra were obtained using a 25 mW, λ=532 nm laser (labRAM ARAMIS, Horiba instruments equipped with an Andor CCD detector), using a grating of 1800 grooves/mm and x50 Objective. The laser spot size is 1.18 μm, which means the spatial (diffraction limited) resolution is 0.59 μm. However, due to scattering events the spatial resolution is likely in the order of 1 μm. Each Raman spectrum is an accumulation of five spectra taken at one position. When reporting averaged Raman spectra, Raman spectra were collected at 5 different regions on the sample and averaged, with averaged I_D/I_G values reported ± the standard deviation.

Scanning electron microscopy (SEM) images were taken using 5 kV acceleration voltage on a JSM-840F (JEOL instruments) and Merlin (Zeiss) SEM with Energy dispersive X-ray (EDX) analysis capability. X-ray diffractometry (XRD) using a copper source was used to identify the structure of the catalyst particles before and after annealing treatment. Thermogravimetric (TGA) data were taken using a *Netzsch STA 449 F3 Jupiter* at 10 K/min in dry pure synthetic air, of MWCNTs grown on platelets coated using CVDP14 with 60 minutes annealing in argon. Resistivity measurements were conducted on a Jandel Four-point probe system with a probe spacing of 0.1 cm and currents of $0.1x10^{-3}$ and $0.001x10^{-3}$ A.

3.3 Results and discussion

PART A - *In-situ* MWCNT-infiltration of freeze-cast alumina scaffolds

In this section, the growth of a homogeneous MWCNT phase in freeze-cast scaffolds is investigated. Three ways of growing MWCNTs are explored. Firstly, catalyst-free growth which promises to provide a cheap, metal-free and homogeneous MWCNT phase. Secondly, catalyst-assisted growth using tailored ultra-small dispersed nanoparticles which can potentially generate ultra-small diameter SWCNTs as well as MWCNTs. And lastly, catalyst-assisted growth with larger catalyst particles which are less likely to coalesce during CVD and thus yield a potentially more homogeneous MWCNT phase. The catalyst infiltration method and precursor gas flow and composition are tailored to provide a reliable methodology for *in-situ* MWCNT growth of porous alumina scaffolds.

3.3.1 Catalyst-free CNT growth in freeze-cast alumina scaffolds

Although general consensus in the scientific community is that metallic catalyst particles are deemed a necessity for MWCNT growth[198–200], catalyst-free growth has been reported from alumina particles on a silica substrates[201–203], from anodic alumina pores[204,205] and on a flat alumina substrate[206]. The idea behind 'catalyst free' growth is that alumina itself provides nanoscale nucleation sites for the MWCNTs to grow, without the need for a metallic catalyst particle. It is striking however, that in all of these reports, elemental analysis is not done after MWCNT growth, and thus catalyst-free growth on alumina has not been unequivocally proven. If successful however, this method produces pure-carbon MWCNTs in the sense that no residual metallic catalyst particles are incorporated in the MWCNT structure. Residual metallic catalyst particles can alter MWCNT mechanical and conductive properties, for which reason additional purification methods such as acid treatments have been utilized

to remove these metallic impurities[207]. These post-synthesis treatments are both time consuming and costly and cannot remove all of the metallic particles due to graphitic encapsulation[208]. At the same time, such treatments often leave the MWCNTs defective due to the harsh chemical environment used in their purification.

Catalyst-free growth can yield both a high purity MWCNT phase and is both more economical and environmentally friendly. Therefore, an attempt at reproduction of catalyst-

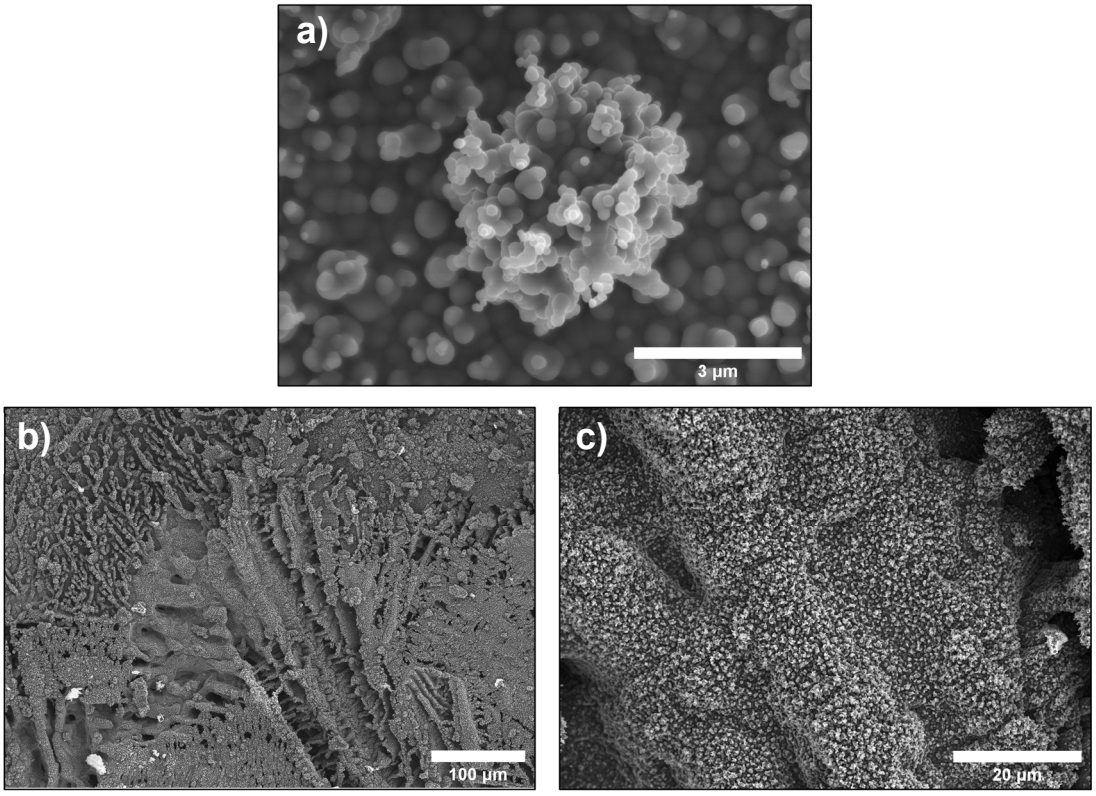


Figure 3.2 – SEM-images of the top of alumina freeze-cast scaffold, replicating the CVD-recipe by Tripati *et al.*[206], showing no CNT growth and severe clogging of the porous channels of the alumina freeze-cast scaffold by amorphous carbon. [CVDP1]

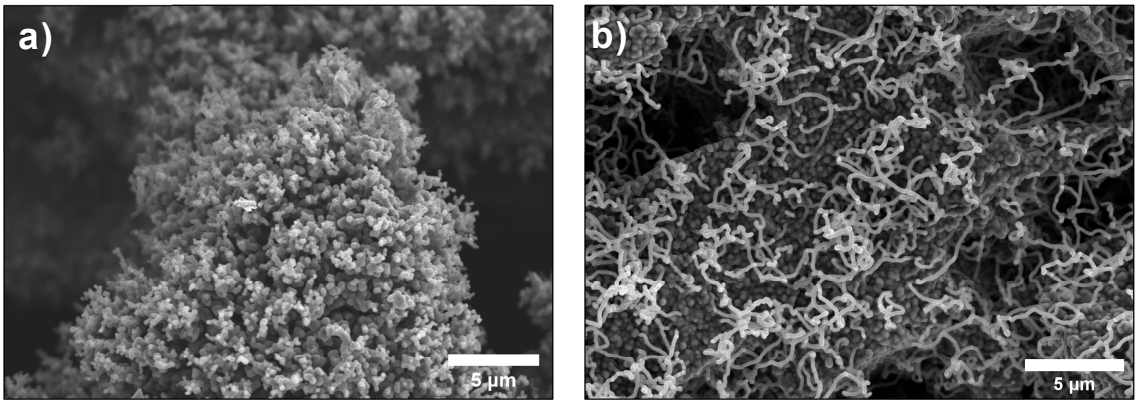


Figure 3.3 – SEM-images of different regions on the outside of an alumina freeze-cast scaffold, replicating the CVD-recipe by Tripati *et al.*[206] with a reducing step before carbon precursor flow is started, showing some regions a) without fibrous carbon and b) with fibrous carbon. [CVDP2]

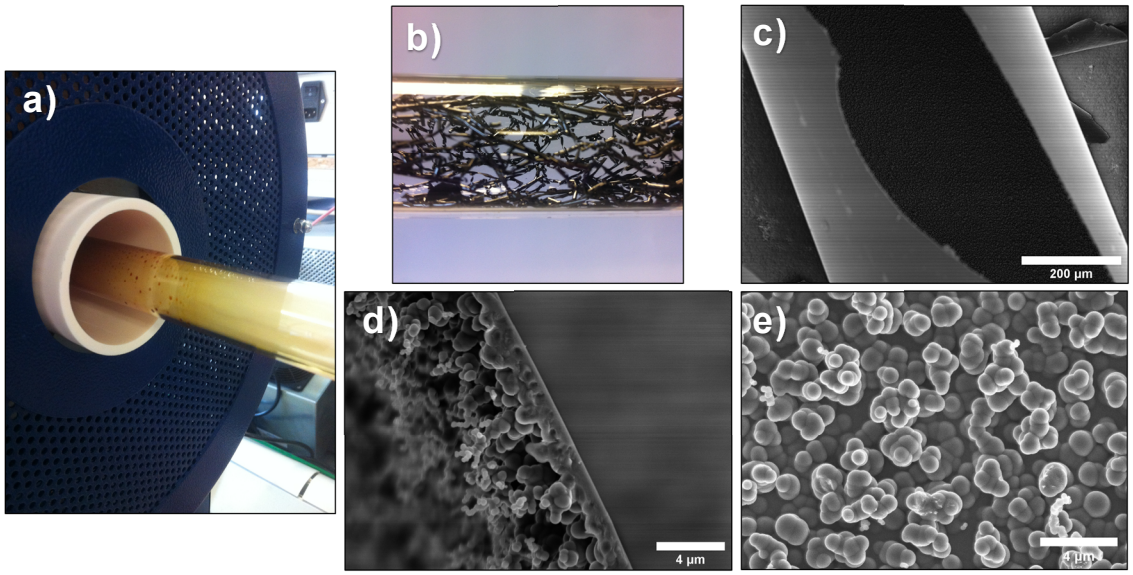


Figure 3.4 – a) Picture of the quartz tube during CVD, showing the formation of a brownish liquid and haze b) The tube at the position of the sample after moving the furnace and flushing with argon. c-e) SEM-images show a close up of a flake collected from the surface of the tube, d) its surface and e) a cross-section of the flake. [CVDP2]

free MWCNT growth as described by Tripati *et al.*[206] was made. The main difficulty in replicating CVD experiments done by others, is that often the volumetric gas flow rate is eported in scientific papers, while the volume or diameter of the quartz-tube is rarely mentioned. As the gas velocity and pressure depend on the size of the quartz-tube, there is therefore some guesswork involved. To have a comparable gas mixture however, the gas ratios were adjusted to be the same as the reported working catalyst-free MWCNT growth by Tripati *et al.*[206]

Figure 3.2 shows that using the recipe provided by Tripati *et al.*[206] (CVDP1) did not yield MWCNT growth, and instead formed a layer of amorphous carbon on the substrate that blocked the pores of the alumina scaffold. It is common use in CVD CNT growth procedures to have a reducing step in the CVD procedure using hydrogen gas before flowing the carbon precursor gas over the substrate. While this is mostly done to reduce the catalyst particles to their metallic state (which for most metallic catalysts provides a higher catalytic yield), this procedure will certainly also affect the substrate itself, and to rule out the substrate effect, a reducing step was added to this procedure, where the alumina substrate was annealed for 15 minutes in a gas mixture containing 30% hydrogen (CVDP2). In addition to similar

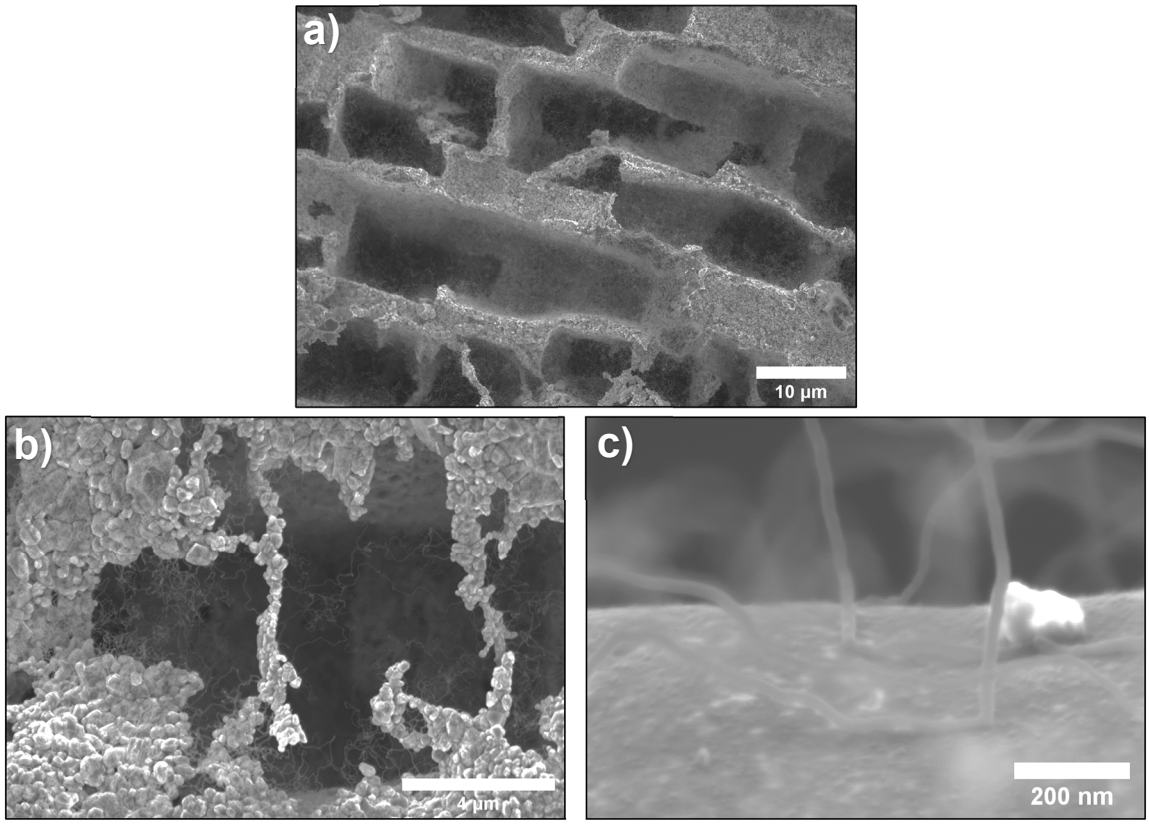


Figure 3.5 – SEM-images of thin CNT growth on an alumina freeze-cast scaffold at different length scales. [CVDP3]

amorphous carbon deposits, some regions of the scaffold had fibrous carbon deposits

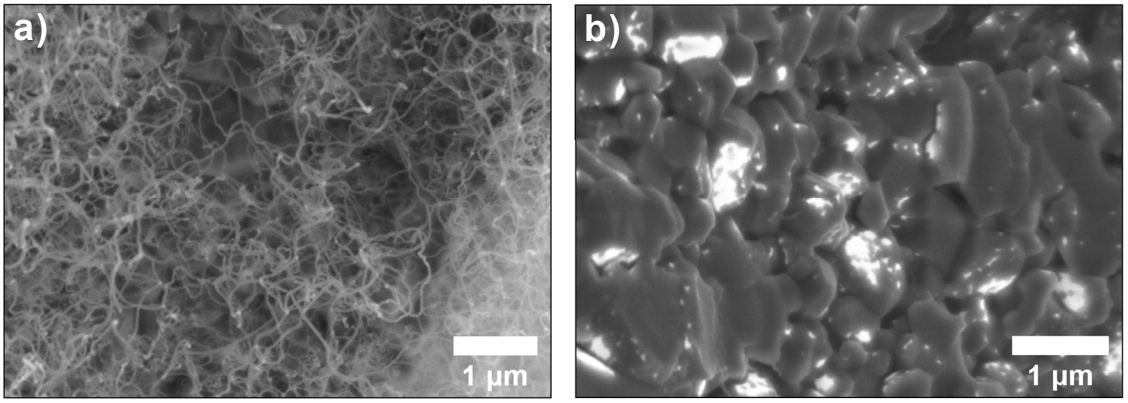


Figure 3.6 – SEM-images of an alumina freeze-cast scaffold, showing a) CNT growth after undergoing a reducing step [CVDP4] and b) showing no CNT growth without a reducing step [CVDP5].

(Figure 3.3) after modifying the CVD procedure by including a reduction step.

In these procedures the quartz tube blackened significantly, indicating a very uneconomic reaction, as most carbon was not converted to MWCNTs. In addition, a brownish liquid and haze is observed during the CVD reaction (Figure 3.4a). This phenomenon was only observed when the precursor is flowing through the tube which means that these are most likely caused by liquid hydrocarbons. When the tube was cooled quickly by moving the

furnace and immediately flowing 0.7 slm Argon through the tube, the black carbon coating on the tube surface reacted by curling up into small silver-coloured tubular flakes, leaving a clean quartz tube surface behind.

Figure 3.4 shows these flakes under argon flow immediately after moving the furnace and provides a close-up of the curled-up carbon material. As the large amount of amorphous carbon generated indicates an excess of carbon precursor, the flow rate was increased to prevent any carbon build-up. Figure 3.5a-b shows the surface of the alumina scaffold after modifying the CVD procedure by increasing the flow rate, while slightly reducing the carbon precursor (CVDP3). This modified procedure showed a good coverage of thin tubes measuring around 20 nm in size (close-up in Figure 3.5c)

Instead of increasing gas flow rates, hydrogen gas inclusion during the growth step can suppress the deposition of amorphous carbon which often accompanies MWCNT formation[209]. This potentially solves the issue of excess carbon at lower flow rates and thus a much more economical CVD procedure can be designed. In addition, it is good to notice that the argon gas used here has a purity of 99.998%, which means that there will be still oxygen molecules present (<1/50000), which can oxidize carbon species. In addition, minor leaks could be present in the CVD system. Hydrogen is expected to scavenge these oxygen species. Indeed, Figure 3.6 shows that when including hydrogen both in a reducing step and during CVD growth, it is possible to grow MWCNTs at 0.2 slm total flow, using 3 times less compressed gas (CVDP4).

Although it was shown that MWCNTs can be consistently grown without catalyst particle infiltration (Figure 3.6a), this growth was dependent on a reduction step in CVD. Without a reduction step (Figure 3.6b) the scaffold blackened, and no MWCNTs were observed. This dependency on a reduction step is not reported in existing literature on catalyst-free MWCNT growth.

Upon close inspection, copper crystals of ~400 nm in diameter were found in some locations after the CVD procedure (Figure 3.7). Copper, here coming from the copper cold finger in freeze-casting, is normally not regarded as a good catalyst for MWCNT growth. Acetylene decomposition over copper has resulted in amorphous carbon instead of graphitic filaments[210]. A theoretical model by Deng *et al.* [211] suggests that MWCNT-growth from copper catalysts is not energetically favourable and therefore poisons MWCNT growth. In addition, the solubility limit of carbon in copper is extremely low and thus MWCNT precipitation extremely poor[212].

Nevertheless, copper catalysts have been reported in CVD resulting in Y-shaped[213] and coil-shaped[214,215] MWCNTs. Copper catalysts on silicon substrate have also resulted in SWCNT carpet growth[216]. Hence, the existence of copper crystals in these scaffolds hints that nanoscale copper could have infiltrated the scaffold during freeze casting and could be responsible for the observed MWCNT growth. Therefore, high-resolution EDX was done to either refute or prove the existence of nano-copper catalyst particles inside MWCNTs.

Figure 3.8 shows that nanoscale copper is present in the MWCNTs. The fact that MWCNTs are only present after a reducing step, indicates that the contamination from the copper cold finger has an oxidation layer, and it is metallic copper which is responsible for the observed MWCNT growth. Indeed, after a modified RCA-cleaning procedure to remove any metallic contaminants, the MWCNT growth could not be replicated on an alumina freeze cast scaffold (Figure 3.9). Considering the lack of elemental analysis in papers claiming catalyst-free growth[201,204–206], copper nanoparticles inside MWCNTs on freeze-cast alumina scaffolds and the complete lack of MWCNT formation of acid-cleaned substrates using the same CVD procedure, it can be concluded that copper remnants from the cold finger are responsible for the observed MWCNT-growth in the freeze cast scaffolds. It seems likely that metallic contaminants are responsible for reported catalyst-free MWCNT growth, and that catalyst-free growth is not achieved to date.

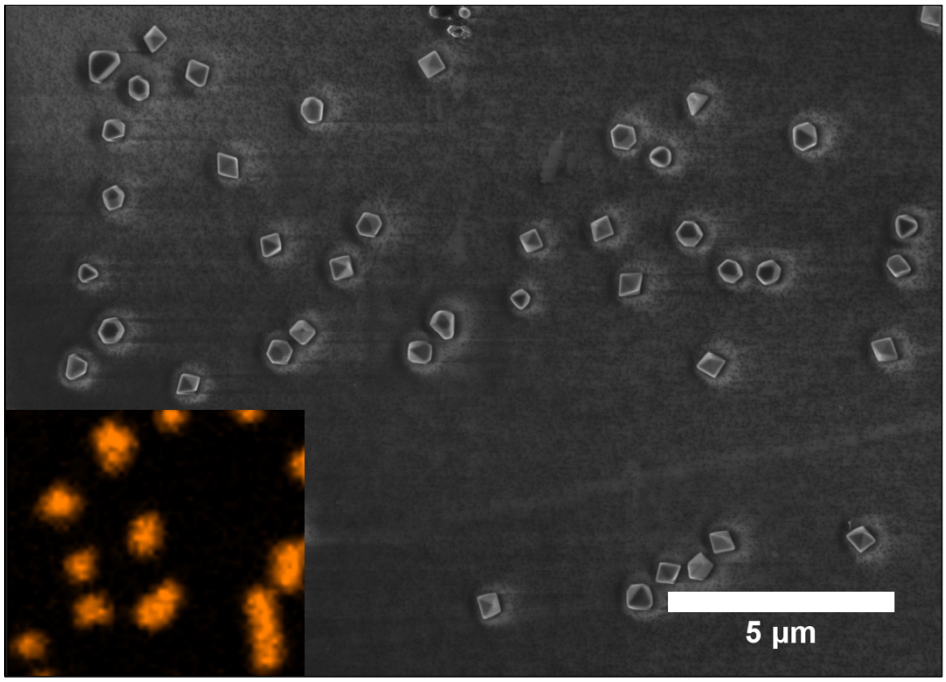


Figure 3.7 – SEM-image showing copper crystals on the surface of the scaffold, indicating contamination from the copper cold finger used in freeze casting. The copper crystals likely formed from this contamination during the annealing step in CVD. The inset shows an EDX map of the copper Lα signal.

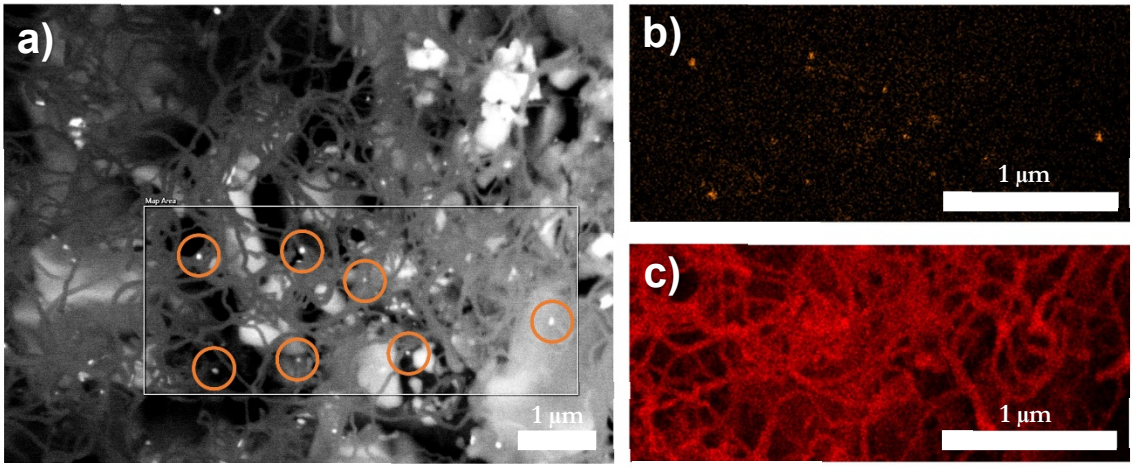


Figure 3.8 – a) High resolution SEM-image of MWCNTs, with nanoparticles displaying a high contrast. b) EDX map of the copper Lα signal identifying the high contrast particles as copper and c) EDX map of the carbon Lα signal. [CVDP4]

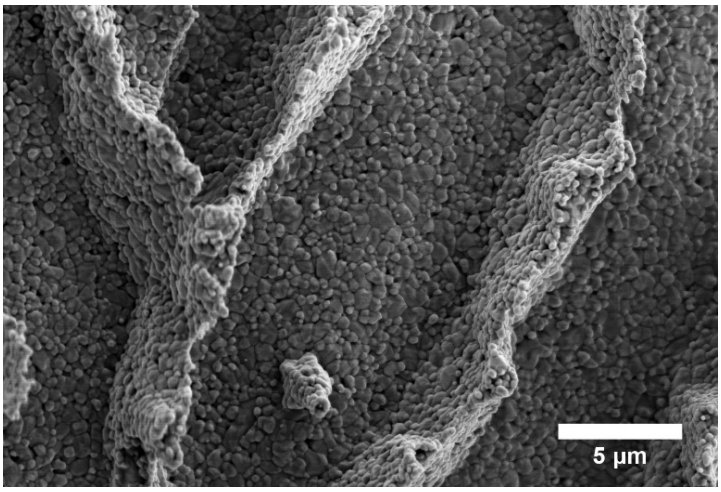


Figure 3.9 – SEM-image showing no CNT growth after cleaning the scaffold with a RCA cleaning procedure. [CVDP4]

Although a good coverage of MWCNT growth has here been achieved from copper particles, control over the dispersion inside the scaffold is not possible. The copper particles are introduced as a contaminant from the copper freeze casting surface, and concentrations may vary between samples. Therefore, using these copper catalysts resulting from the freeze casting procedure will not yield a well-controlled, homogeneous coverage.

In addition, Raman spectra taken from MWCNT-infiltrated freeze-cast alumina scaffolds (Figure 3.10) are like spectra of para-crystalline materials such as carbon black[197], and do not indicate a high amount of graphitisation. A purity assessment using a study on MWCNTs grown by CVD[217] indicates that the measured I_D/I_G ratio of 0.81-0.94 in Figure 3.10 corresponds to a MWCNT content lower than 20% of the total carbon deposit.

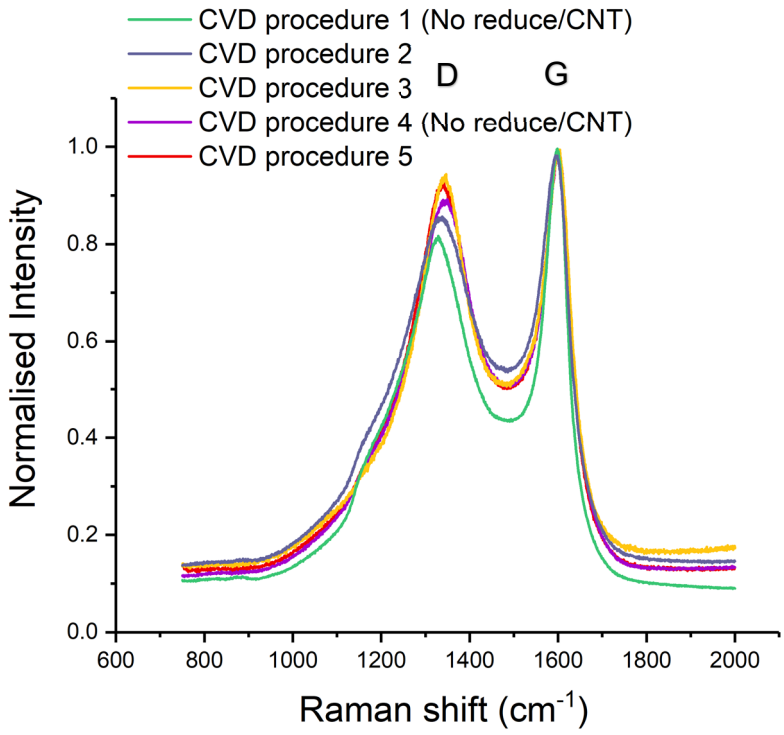


Figure 3.10 – Raman spectra of CVD-grown carbon deposits from copper nanoparticles using different CVD procedures. [CVDP1,2,3,4,5]

3.3.2 CVD with ultra-small iron oxide nanoparticles

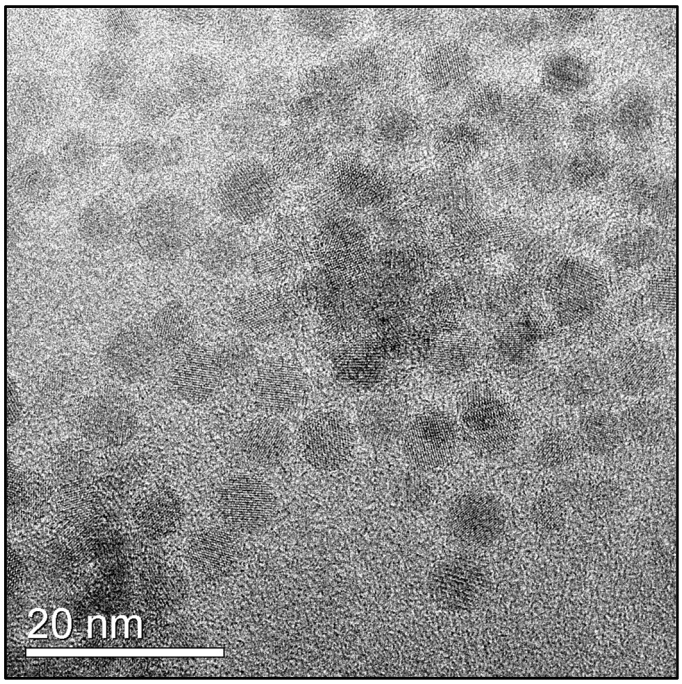


Figure 3.11 – TEM image of iron oxide nanoparticles made by thermally decomposing Fe(acac), with sizes between 4-6 nm.

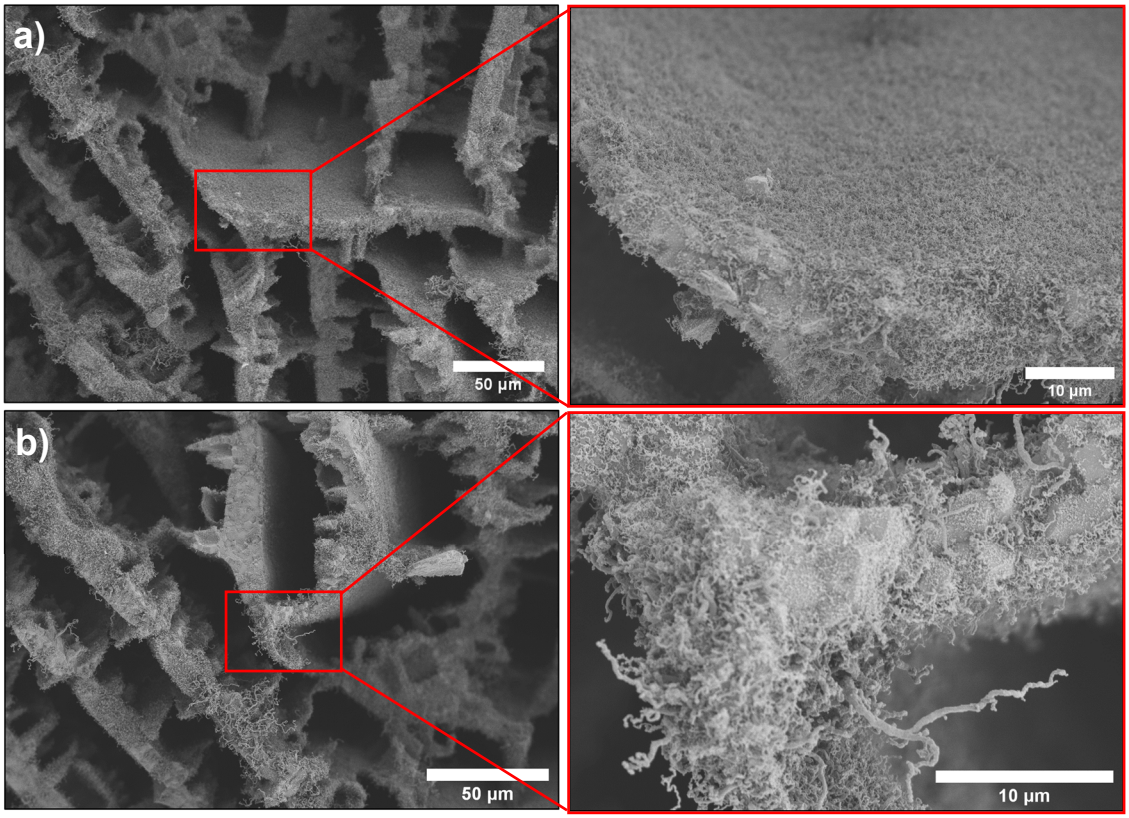


Figure 3.12 – a-b) SEM images of two surface-sites of a MWCNT-coated freeze-cast alumina scaffold, showing a diverse range of fibrous carbon. [CVDP6]

To grow a well-dispersed MWCNT-phase within porous scaffolds in a controlled manner, MWCNT growth initiated from prefabricated metallic-oxide nanoparticles offer control over

the amount and dispersion of grown MWCNTs. These nanoparticles must consequently be well dispersed inside the scaffold themselves, to obtain a homogeneous MWCNT-coating on the alumina surfaces within the scaffold. Iron oxides are the most economical and frequently used choice of catalyst particle for MWCNT growth on alumina as they have been shown to be highly effective on alumina substrates[171,190].

Therefore, ultra-small Fe_3O_4 particles were manufactured from a $Fe(acac)_3$ precursor. TEM analysis was done to confirm their size, which was determined to be between 4-6 nm. (Figure 3.11). Figure 3.12 shows that after infiltration of the alumina freeze-cast scaffolds and following CVD procedure 6 (CVDP6), the surfaces of the scaffold were completely covered with fibrous carbon. In addition to curly thinner fibres with diameters ~50 nm that coat the surface, a fair amount of longer carbon fibres with diameters ~325nm are generated (Figure 3.12b).

To verify that the coating has been done throughout the whole volume of the scaffold, it was broken in half and re-imaged in SEM. Inside the scaffold, it was observed that not all

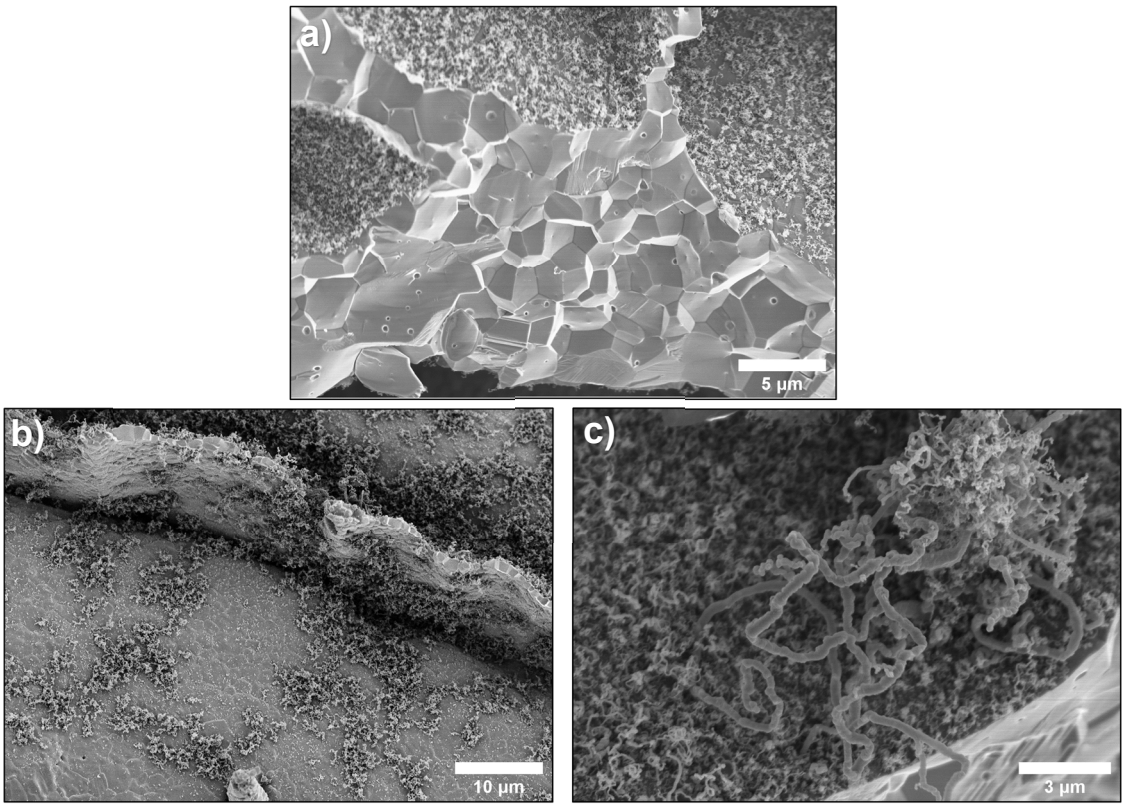


Figure 3.13 – SEM-images of the inside of a MWCNT-coated freeze-cast alumina scaffold, showing a) The fracture surface with MWCNT coating b) Area's with large clusters of MWCNTs and carbon fibres, and c) a zoom-in of a large fibre on the surface. [CVDP6]

areas were coated homogeneously. An example of an area with poor coating is given in Figure 3.13b. In Figure 3.13c, larger clumps of long carbon fibres are observed that stand out from the thin curly tubes on the surface. The broken surface shown in Figure 3.13a gives a good view of the scale of the alumina grains relative to the MWCNT-coating.

The relatively poor growth and fibre formation shown in Figure 3.13c can be caused by interference during the MWCNT-formation process in CVD. The large amounts of carbon containing species that are introduced during the nanoparticle dispersion can play a role; these include the oleic acid capping agent, remnants of oleylamine used during synthesis, and the cyclohexane that the nanoparticles are dispersed in. These are very hard to eliminate for these ultra-small nanoparticles, as removal in the liquid phase makes them prone to agglomeration and any heat treatment on the scaffolds may either cause carbonisation or diffusion of the nanoparticles. The small initial size of the particles used is another likely factor to cause the large carbon fibre formation in CVD; the melting point of small nanoparticles decreases with particle diameter – and the driving force for coalescence (the reduction in surface energy) increases with decreasing nanoparticle size[169]. The nanoparticles are therefore likely to clump together and catalyse large fibre growth instead of small diameter nanotubes, as catalyst size has been linked to fibre diameter[218]. Figure 3.13c shows that indeed fibres are synthesized that are an order of magnitude larger than the fibres on the surfaces, and much larger than the initial nanoparticle catalyst size.

3.3.3 CVD with commercial iron oxide nanoparticles

To improve upon this method, 20 nm commercial flame spray pyrolysis-generated iron oxide nanoparticles[194] were utilised. The benefits that these particles have over the particles that were synthesized using the $Fe(acac)_3$ precursor are threefold. Firstly, their larger diameter (and thus quadratically larger surface area) significantly reduces the driving force for coalescence, as the diffusion coefficient increases with particle size. Secondly, they are not dispersed in oleylamine environment or coated with a capping agent, which can interfere

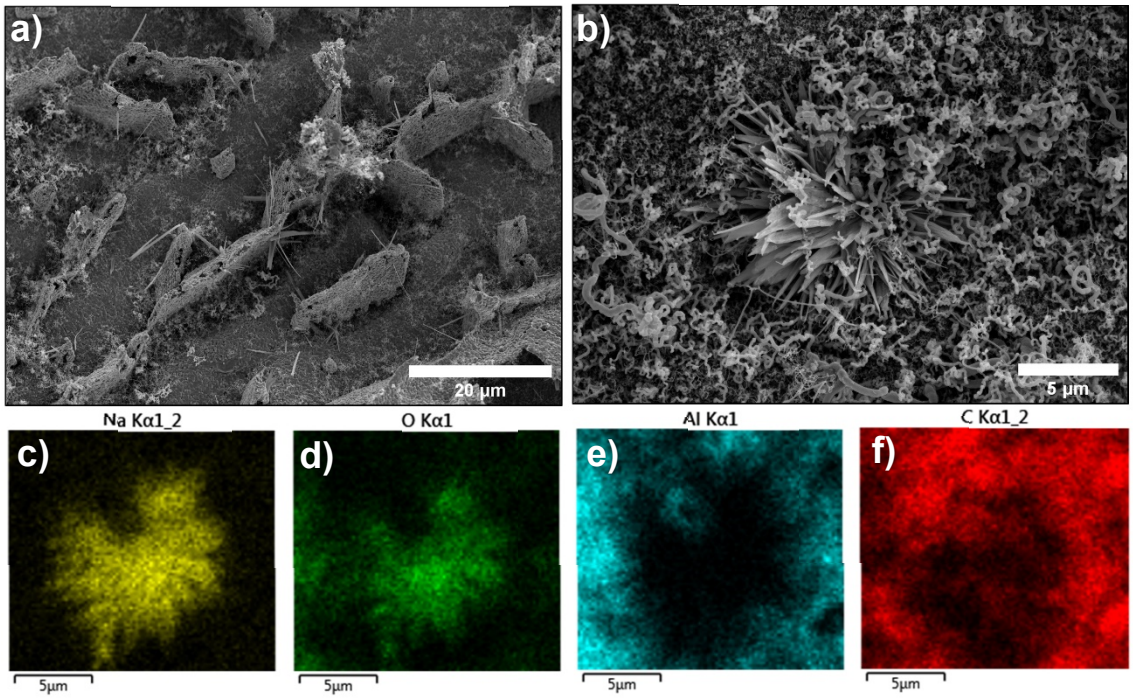


Figure 3.14 – a-b) SEM-images of the inside of a scaffold infiltrated with MWCNTs grown from SDBS-stabilized nanoparticles, showing evidence of the formation of large sodium-containing crystals. c-f) EDX maps of SEM image (b) for c) Sodium, d) Oxygen, e) Aluminium, and f) Carbon, indicating that the crystal is due to sodium contamination from SDBS. [CVDP7]

with the formation of the MWCNTs from the gaseous carbon precursor in CVD. Thirdly, using commercially available nanoparticles eliminates any small scale-synthesis variations in nanoparticle synthesis, and thus makes the research more reproducible and valuable.

The flame-spray pyrolysis generated particles come in powder form, and thus must be dispersed. To disperse these nanoparticles sodium dodecylbenzene sulfonate (SDBS) is used, an anionic surfactant known to disperse iron oxide nanoparticles[219]. Figure 3.14 shows that the sodium containing dispersant SDBS however, does interfere in the CVD procedure to grow MWCNTs. Large sodium-containing crystals were observed in the scaffold after

For this reason, the flow rates were increased (CVDP8). In addition, the scaffold was acid-cleaned, and vacuum infiltrated with a dispersion of iron oxide nanoparticles after which the sample was sonicated in an ultrasonic bath for 20 minutes to disperse the nanoparticles better. After drying, the iron oxide nanoparticle content was calculated to be 1.8 wt% by comparing the weight of the scaffold before and after infiltration. As can be seen from Figure 3.16, a homogeneous MWCNT coverage is obtained both inside and outside the scaffold.

However, Raman spectra indicate that the MWCNTs grown in this way are still quite defective as their I_D/I_G ratio is greater than 1 (Figure 3.17).

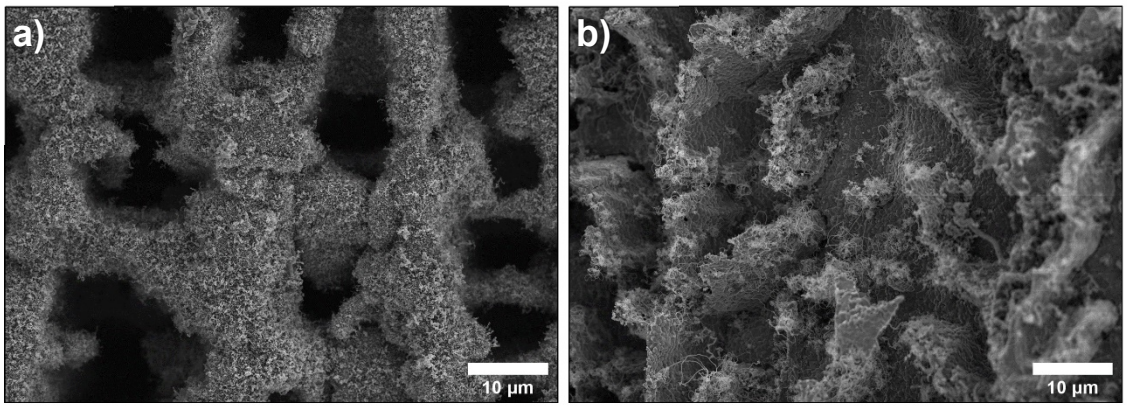


Figure 3.15 – SEM-images of the a) Top-view and b) Inside view of a scaffold infiltrated with MWCNTs grown from FSP iron nanoparticles without SDBS, showing a thinner coverage of tubes on the inside of the scaffold. [CVDP7]

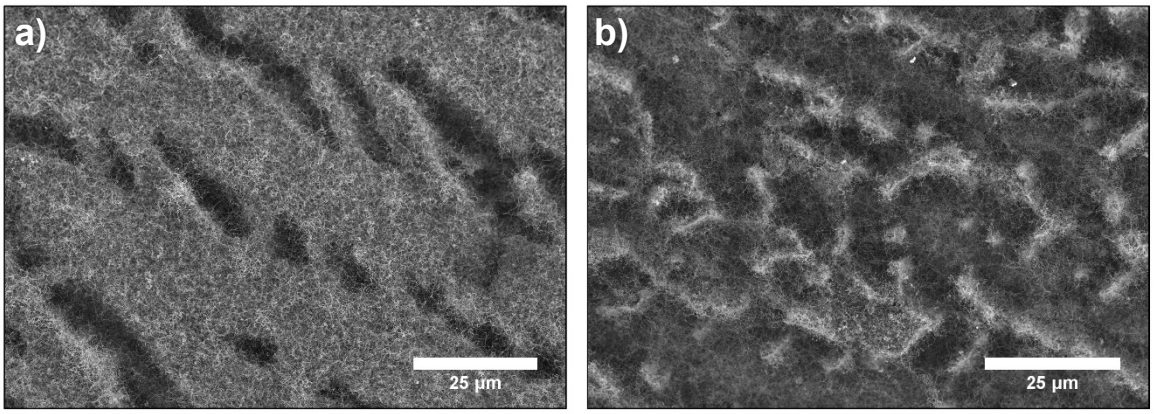


Figure 3.16 – SEM-images of the a) Top-view and b) Inside view of a scaffold infiltrated with MWCNTs grown from vacuum-infiltrated FSP iron nanoparticles without SDBS. [CVDP8]

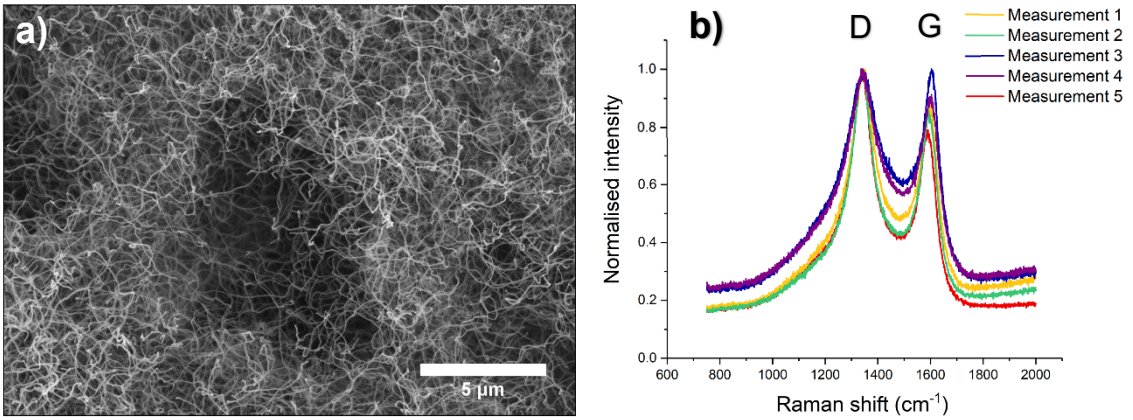


Figure 3.17 – a) SEM-image of a close-up of the MWCNTs grown using [CVDP8] b) Raman spectra showing that there is a high concentration of defective carbon present.

PART B - *In-situ* coating of MWCNTs on alumina platelet powders

From the experiments in Part A on freeze-cast alumina scaffolds, a working recipe for abundant MWCNT growth on alumina is established. In this section, MWCNT growth on another form of alumina is examined which can bring us even closer to the nacre-like structure; monocrystalline, micron-sized alumina platelets. If successful, this procedure could produce MWCNT coated alumina platelets that can act as composite building blocks to generate a bioinspired and multifunctional materials.

The parameters used for MWCNT growth on freeze cast scaffolds will not result in the exact same MWCNT growth on alumina platelets; Ward *et al.*[220] show that surface roughness affects catalyst diffusion, and crystallinity of the substrate affect CNT growth, and these platelets are a very different surface in that regard. It is expected that it is not only possible to translate the growth to these platelet-like scaffolds, but to improve on the quality of the MWCNT phase in terms of reducing defect density, and to gain a deeper understanding of the growth on these platelets so that it can be tailored.

Two different experimental setups were used to grow MWCNTs on the platelets - classical CVD and AACVD. The effect of annealing time, annealing environment, catalyst dispersion and effect of hydrogen on the MWCNT growth in CVD were studied to optimise the MWCNT growth and X-ray diffraction experiments were performed to understand the catalyst behaviour during CVD. Alumina platelets pre-coated with catalyst particles were then used to confirm the translative properties of this research to similar systems, and an optimized recipe as well as increased understanding of the growth dynamics is presented for the manufacturing of high-quality MWCNT-coated alumina platelet materials.

3.3.4 Aerosol assisted CVD using ferrocene

In aerosol assisted CVD (AACVD), the carbon precursor is not supplied in the gas phase, but instead as an aerosol that is generated and fed into the CVD reactor. Ferrocene is of particular interest as it can act both as catalyst and carbon precursor. Large quantities of graphitic MWCNTs can be grown using AACVD, using ferrocene as a catalyst, in the temperature range between 800°C-850°C[221]. A series of works by Meysami *et al.*[222,223] describes an optimised procedure for MWCNT growth in a quartz tube, which setup was followed to investigate the feasibility of creating MWCNT aligned carpets on nacre-like alumina platelets.

The AACVD procedure was conducted with and without 30 vol% hydrogen gas. For both experiments, scanning transmission electron microscope (STEM) images (Figure 3.18) reveal a large degree of incorporation of metal catalyst particles into the structure. While a large

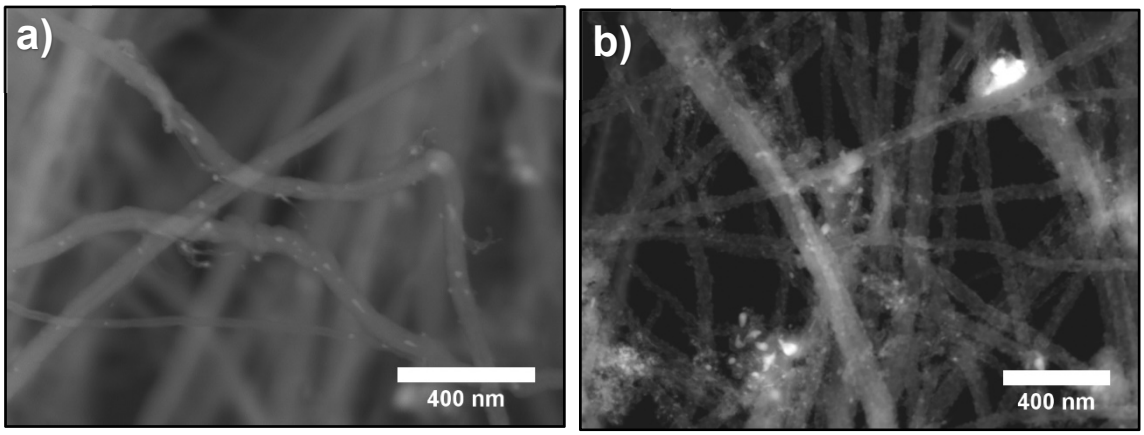


Figure 3.18 – STEM-images show the difference between AACVD-grown MWCNTs on alumina platelets with a) pure argon as a carrier gas and b) Both argon and hydrogen as carrier gas. [CVDP9,10]

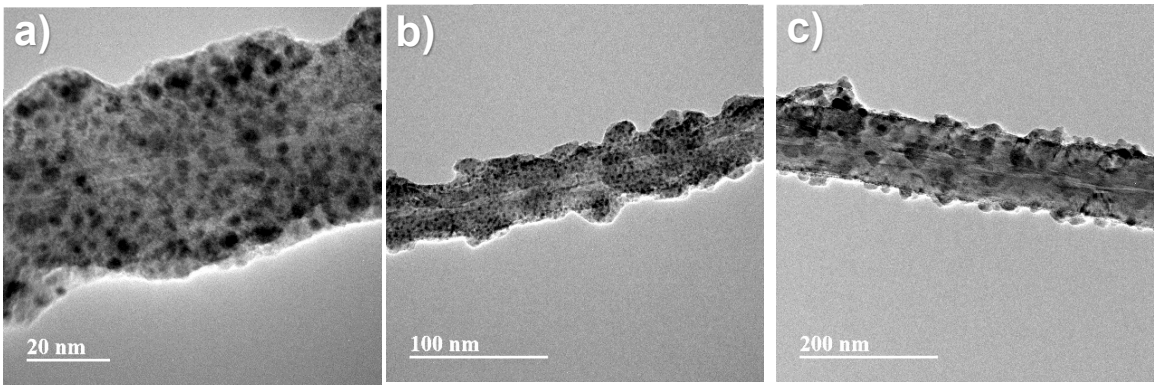


Figure 3.19 – TEM-images of MWCNTs grown with hydrogen assisted AACVD. [CVDP10]

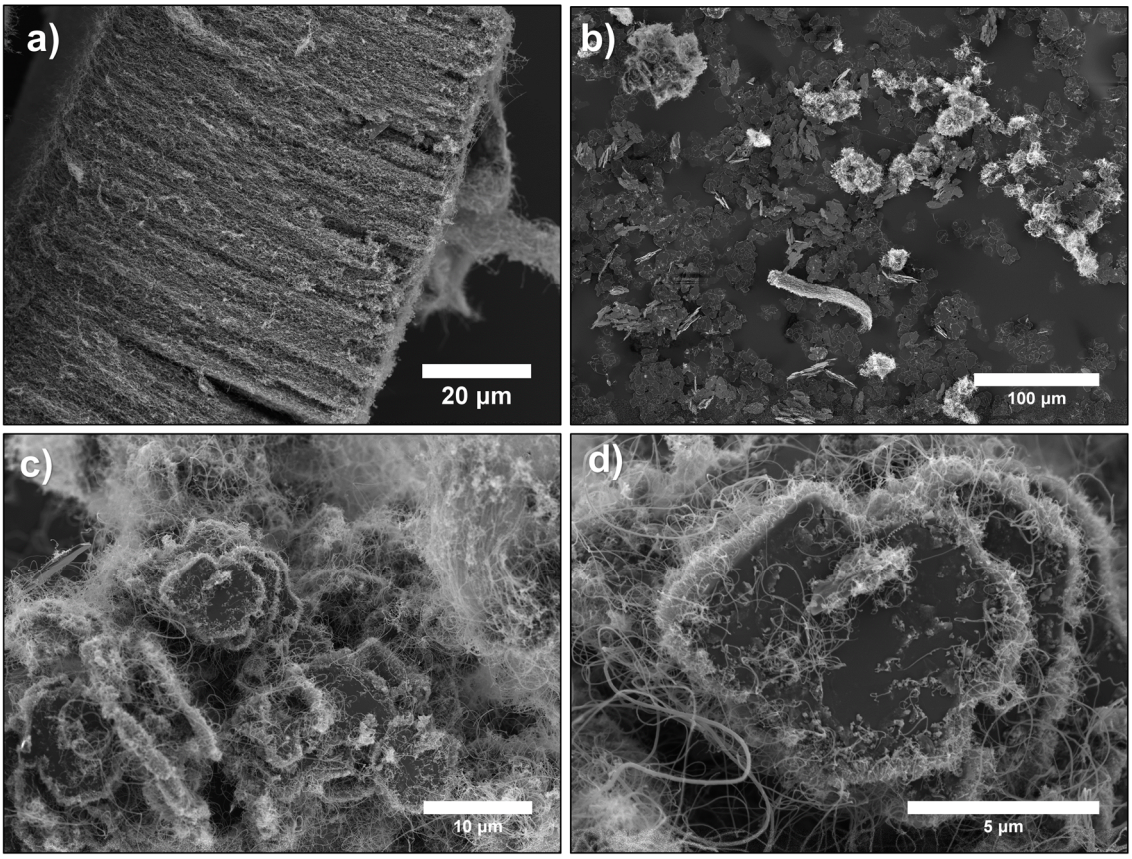


Figure 3.20 – SEM images of AACVD MWCNT growth on a) the quartz tube wall showing aligned carpet growth and b-d) on alumina platelets. The platelets show b) a poorly dispersed MWCNT phase c) irregular growth in area's that do show MWCNT coverage and d) MWCNT growth mostly from the side facets of the platelets [CVDP9].

amount of remaining metal catalyst particles is typical for ferrocene assisted AACVD MWCNT growth, when hydrogen was used in the CVD procedure, the MWCNTs were decorated with an unprecedented number of nanoparticles (Figure 3.19). For all AACVD experiments, a large amount of MWCNTs was found growing in carpet form on the outside of the quartz tube (Figure 3.20a), while only a small percentage of platelets was coated with MWCNTs (Figure 3.20b). In addition, when coated, the MWCNT coating was not homogeneous and irregular (non-carpet like) growth of CNT bundles (Figure 3.20c) was prevalent. The small number of coated platelets were coated mainly on the edges (Figure 3.20d). Han et al[224] show that CNT growth is influenced by the crystallographic orientation of the alumina substrate, where CNTs align on a-plane sapphire, but not on c-plane sapphire. They hypotise that this is due to the high density of atoms lying normal to the [0001] direction of a-plane sapphire which may strongly interact with CNTs and lead to a minimized Lennard-Jones potential. The different behaviour of CNTs depending on the crystallographic orientation of the alumina could be a reason for the preferred growth on the platelet edges.

Because the observed growth is very irregular and the MWCNTs are poorly dispersed, the AACVD method used is considered to be unsuitable for the coating of bioinspired alumina platelets.

3.3.5 CVD using commercial iron oxide nanoparticles - Effect of annealing and H_2

SEM analysis revealed minimal MWCNT growth on platelets prepared using dry catalyst dispersion with commercial flame-spray pyrolysis generated (FSP) iron oxide nanoparticles (method A) that did not undergo annealing prior to MWCNT synthesis, indicating poor catalyst performance. However, complete activation of all catalyst particles was achieved by annealing in an inert atmosphere at 800 °C for 60 minutes, with most catalyst particles growing separated clumps of MWCNTs on the surface. (Figure 3.21). It is well established that hydrogen can significantly increase MWCNT yield in CVD when included in the carbon precursor mixture[225,226]. There are multiple arguments for this observation; hydrogen may prevent MWCNT growth termination by reducing the carbon influx, *e.g.* if the carbon at the surface of the catalyst is not removed fast enough compared to the carbon influx, the surface becomes blocked and MWCNT growth will stop abruptly[158,225,227]. Hydrogen can also interact with the carbon precursor, modifying the decomposition rate[48]. Hydrogen inclusion at different concentrations during CVD growth has also been shown to change the size, shape and phase of iron catalyst particles[228]. Finally, hydrogen may play a role as an oxygen scavenger, creating water vapour, which has been shown to significantly extend catalyst lifetime[229]. When hydrogen was used during synthesis, complete coverage of the platelets was achieved (Figure 3.21). The SEM images show that including hydrogen during synthesis enhances MWCNT growth by growing longer MWCNTs; this means that the catalyst is kept active for a longer time through either one or a combination of the mechanisms mentioned above. For these platelets prepared using method A, the presence of defects in the MWCNTs depended on both the annealing time of the catalyst and the addition of hydrogen during MWCNT synthesis as revealed by the Raman I_D/I_G ratios (Figure 3.22). The I_D/I_G ratio

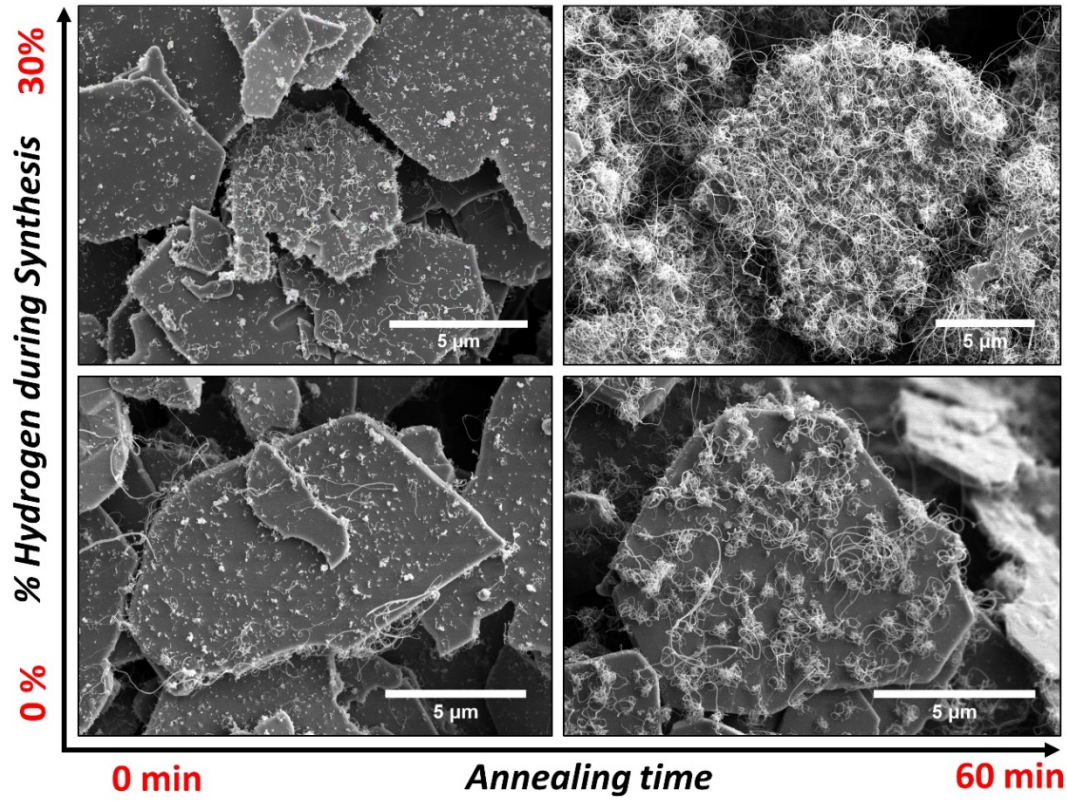


Figure 3.21 – SEM micrographs of MWCNT-coated alumina platelets, showing the effect of annealing at 800 °C in argon before MWCNT synthesis, and the effect of including hydrogen during MWCNT synthesis. Platelets have been coated with nanoparticles using catalyst dispersion method A. [CVDP11,12]

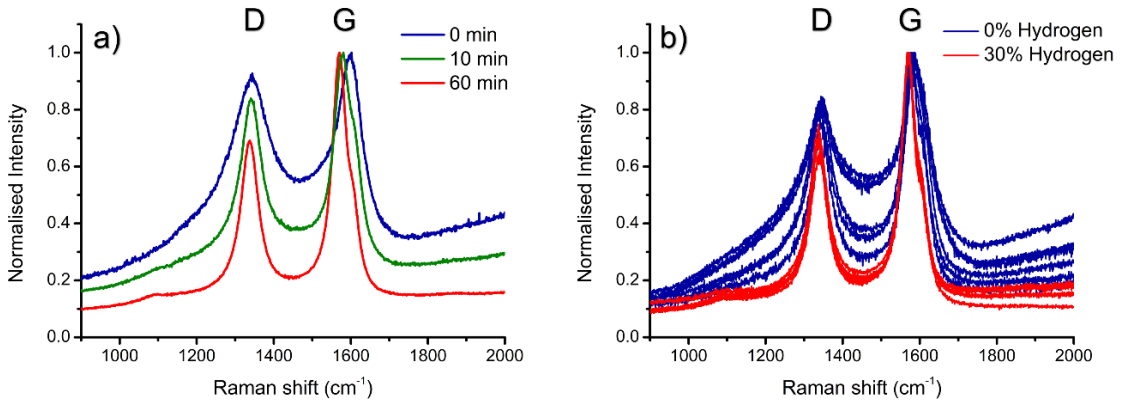


Figure 3.22 – a) Averaged Raman spectra of MWCNTs grown with 30% hydrogen during synthesis, showing less defective MWCNTs after longer annealing times. b) Comparison of Raman spectra of MWCNTs grown after 60 minutes annealing, with and without hydrogen during synthesis. For both graphs the platelets are coated with catalysts following method A. [CVDP11,12]

decreased with increased annealing time (Figure 3.22a). When the catalyst was annealed for 60 minutes and MWCNTs were grown without hydrogen inclusion, an I_D/I_G ratio of 0.82±0.04 was measured (Figure 3.22b). The addition of 30% hydrogen during MWCNT synthesis improved the I_D/I_G ratio to 0.69±0.04.

In addition, the presence of hydrogen resulted in sharp peaks in the Raman spectra; almost no signal in between the D and the G peak at around 1500 cm^{-1} ('D3') was found, in contrast to samples produced without hydrogen. The absence of this peak is common in samples that

are free of amorphous carbon[197]. Annealing platelets prepared using method A for 60 minutes in argon atmosphere and growing the MWCNTs using an acetylene/hydrogen atmosphere thus yielded a highly pure, well-dispersed MWCNT phase with a low concentration of defects.

3.3.6 Improvement using wet catalyst dispersion

Analogous to dry catalyst dispersion (method A), MWCNT growth on platelets with wet catalyst dispersion (method B) was inhibited without a catalyst annealing step, while complete surface coverage was obtained after sufficient annealing of the catalyst. From SEM images, it is observed that increasing the catalyst annealing time increases the amount of CNTs grown (Figure 3.24). After an annealing step of 20 minutes or more, the I_D/I_G peak ratio for MWCNTs grown on platelets prepared using method B was consistently 0.54±0.04 (Figure 3.23a), a significant improvement in MWCNT-quality over those grown on platelets prepared using method A. Raw non-averaged Raman spectra of both catalyst dispersion methods are included here (Figure 3.23b) to show that the I_D/I_G ratio improvement of platelets prepared using method B over platelets prepared using method A from 0.69±0.04 to 0.54±0.04 is consistent for each data point. This improvement in I_D/I_G ratio has most likely to do with the removal of contamination in the powder during the sonication procedure in ethanol as the nanoparticle dispersion did not seem to be significantly improved with this step – some nanoparticle agglomerates could still be observed in the SEM.

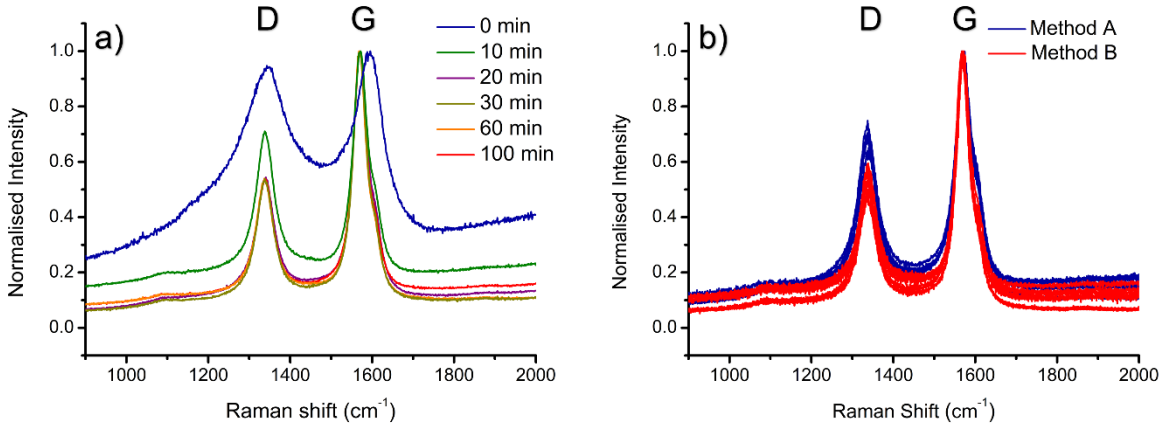


Figure 3.23 – a) Averaged Raman spectra of MWCNTs grown with 30% hydrogen during synthesis after different annealing times b) Comparison of Raman spectra of MWCNTs grown using catalyst dispersion method A and method B after 60 minutes annealing and hydrogen inclusion during synthesis [CVDP13,14].

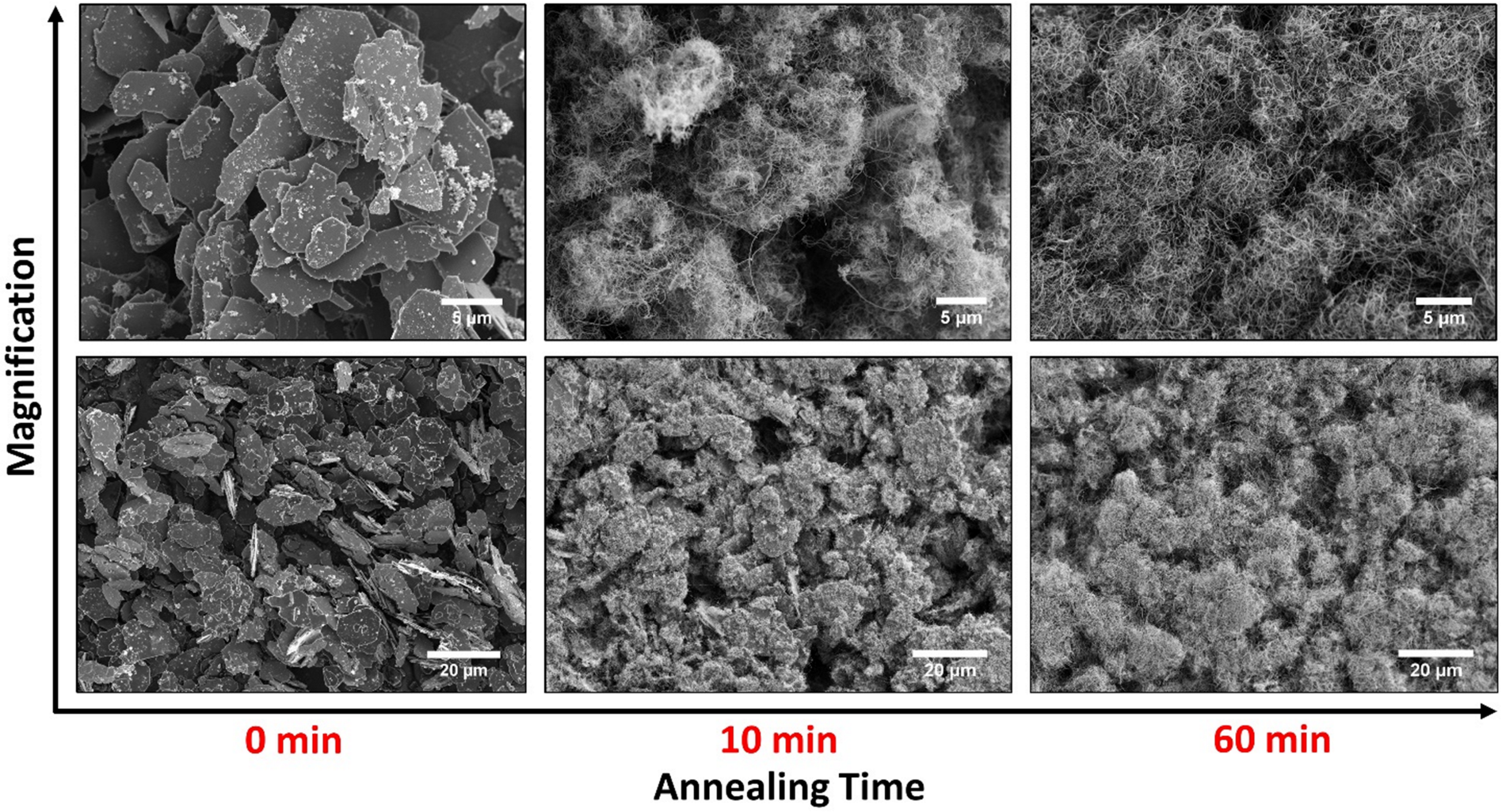


Figure 3.24 – SEM micrographs of MWCNT-coated alumina platelets, showing more MWCNT growth after longer annealing times. Platelets have been infiltrated with nanoparticles using catalyst dispersion method B. [CVDP13.14]

3.3.7 Effect of annealing atmosphere on MWCNT crystallinity and growth

Having established that heat treatment/annealing has a significant effect on the catalyst particles and consequently the MWCNT-growth from these particles, what effect this heat treatment has, *e.g.* what chemical state the catalyst particles are in when they grow MWCNTs is further investigated. To answer this question, the catalyst is forced into either an oxidised or reduced state by manipulating the annealing atmosphere. While some sources report that oxidised iron species are favoured to catalyse MWCNT growth[230,166], reducing iron oxide species during synthesis is most favourable according to more recent reports[231–234]. In the case of iron films, annealing and reducing results in both γ-Fe particles (FCC lattice, austenite) and α-Fe particles (BCC lattice, ferrite), which are shown to have a different MWCNT growth mechanism[232] - α-Fe grows MWCNTs through carbide formation while γ-Fe grows MWCNTs from the pure iron phase.

For platelets prepared using method B, the effect of the annealing treatment on the catalyst particles in an oxidising, reducing and inert atmosphere is shown in Figure 3.25. Annealing in a reducing atmosphere yielded inactive catalyst particles. While this seems to contradict the reports mentioned above, this can be explained by acknowledging the importance of the aluminium oxide support layer in MWCNT growth[172]; the reducing atmosphere may partially

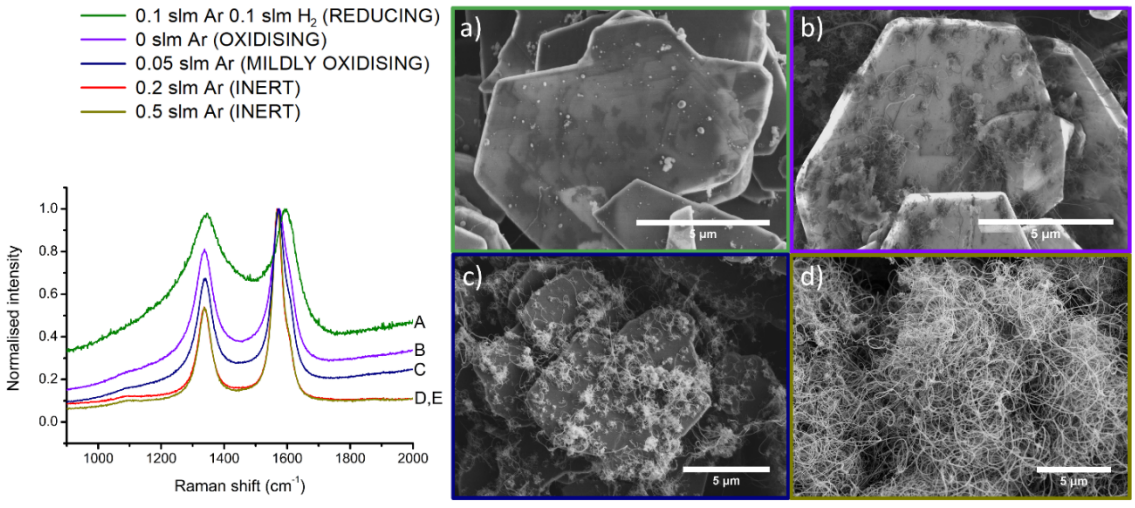


Figure 3.25 – Raman spectra showing the effect of the chemical atmosphere during annealing. SEM micrographs correspond to CNT growth under a) reducing, b) oxidising, c) mildly oxidising and d) inert atmosphere [CVDP15].

or completely reduce the alumina surface, affecting the interaction between the substrate and catalyst particle. The reduction of the alumina support layer is presumably much less of an issue in the case where deposited iron films cover the support layer. When annealed in an oxidising atmosphere (such as in air or low argon flows), the resulting MWCNTs are low in quantity and less in quality (Figure 3.25). Optimal quality and quantity was achieved with an argon flow of 0.2 slm and greater. This most likely indicates that in the used setup this is the minimum flow rate to ensure an inert atmosphere. The need for an inert atmosphere during annealing is shown by the combination of SEM and Raman spectra in Figure 3.25, where it is seen that a non-uniform MWCNT-coverage and defective MWCNTs are obtained when a non-inert atmosphere is used during annealing. It is clear from these experiments that for high-quality MWCNT growth catalysed by iron oxide nanoparticles on alumina, annealing in an inert atmosphere is a prerequisite, as with any other annealing environment poor or no MWCNT growth is observed. From this analysis however, no conclusions can be made on what oxidation state the catalyst particles are in when they grow MWCNTs. It is possible that the catalyst sites are in a reduced oxidation state due to the carbon precursor when MWCNT synthesis is commenced, as it has been shown previously that oxidised Fe can be reduced by acetylene exposure during CVD by hydrogen atoms liberated from hydrocarbon decomposition[158,200]. To better understand what happens to the catalyst particles during the annealing step in inert atmosphere, a closer look is taken at their structure.

3.3.8 Catalyst immobilization through spinel formation

Usually, tailoring the chemical state of individual catalyst nanoparticles through annealing is discouraged because of coalescence and Ostwald ripening, which has been stated to be one of the limiting factors in continued MWCNT-carpet growth[235,236]. In contrast, it can be observed that annealing the iron oxide catalyst particles on the alumina platelet surfaces enhances MWCNT quality and yield, with no significant coalescence occurring and with the catalyst particles immobilised on the alumina surface (Figure 3.26). The immobilisation of iron oxide nanoparticles has been shown before by Homma *et al.*[237] on a Si (001) substrate,

where pure iron nanoparticle catalysts were shown to agglomerate while iron oxide nanoparticle particles did not, even at temperatures of 950 °C.

The ability of iron oxide nanoparticles to facilitate MWCNT growth without coalescing is reproduced here on an alumina surface. Kaneko *et al.*[238] reported impaired diffusivity of iron on alumina substrates where iron-based catalyst particles are seen to diffuse in the alumina substrate during annealing. This insight is key to understand the immobilisation and catalytic activity of iron oxide nanoparticles on alumina supports. While some researchers believe that chemical bonding between a metal catalyst and substrate would prevent the catalytic behaviour of the metal[158], It is proposed here that the iron oxide phase plays a strong role in the formation of an immobilising chemical bond with the alumina surface as

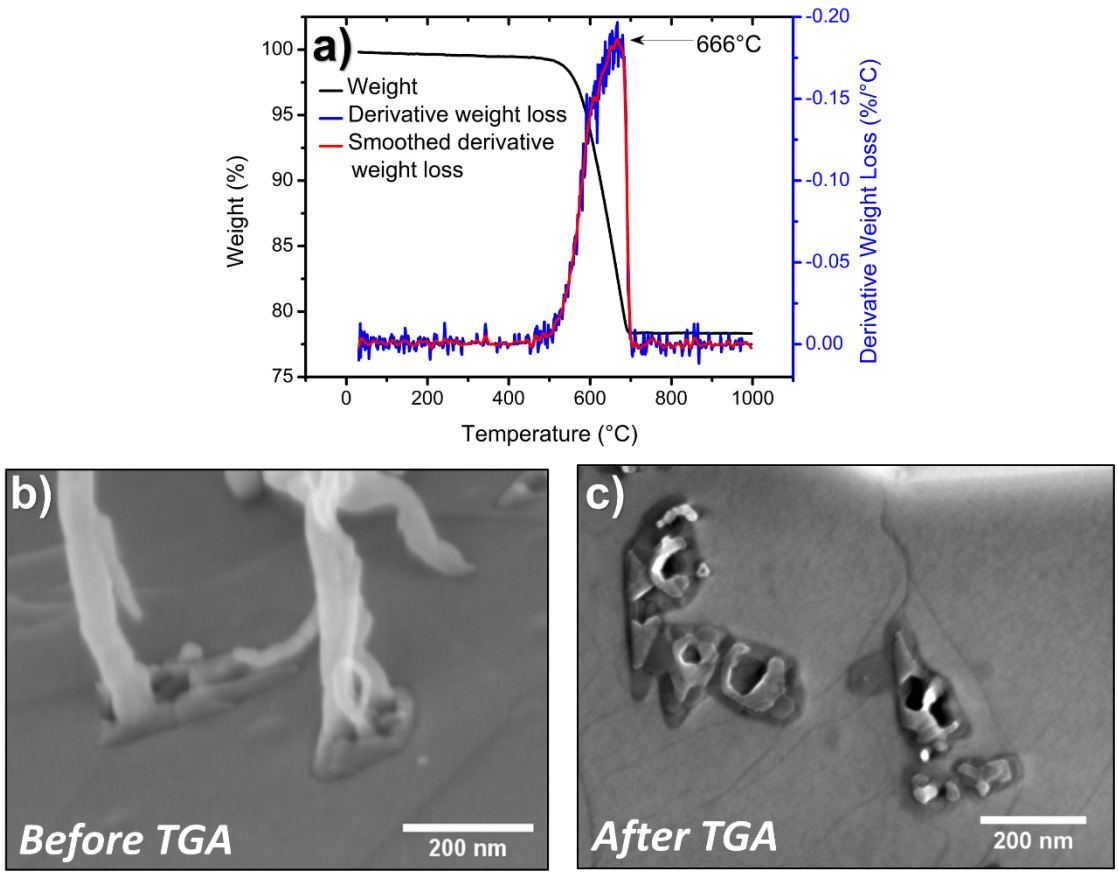


Figure 3.26 – a) TGA curve showing weight loss between 500-700 °C. b) SEM micrograph of a catalyst site before TGA (directly after CVD) and c) SEM micrograph of a catalyst site after TGA (after the MWCNTs are burned away), showing the physical size and attachment of the CNTs to the alumina platelets [CVD?14].

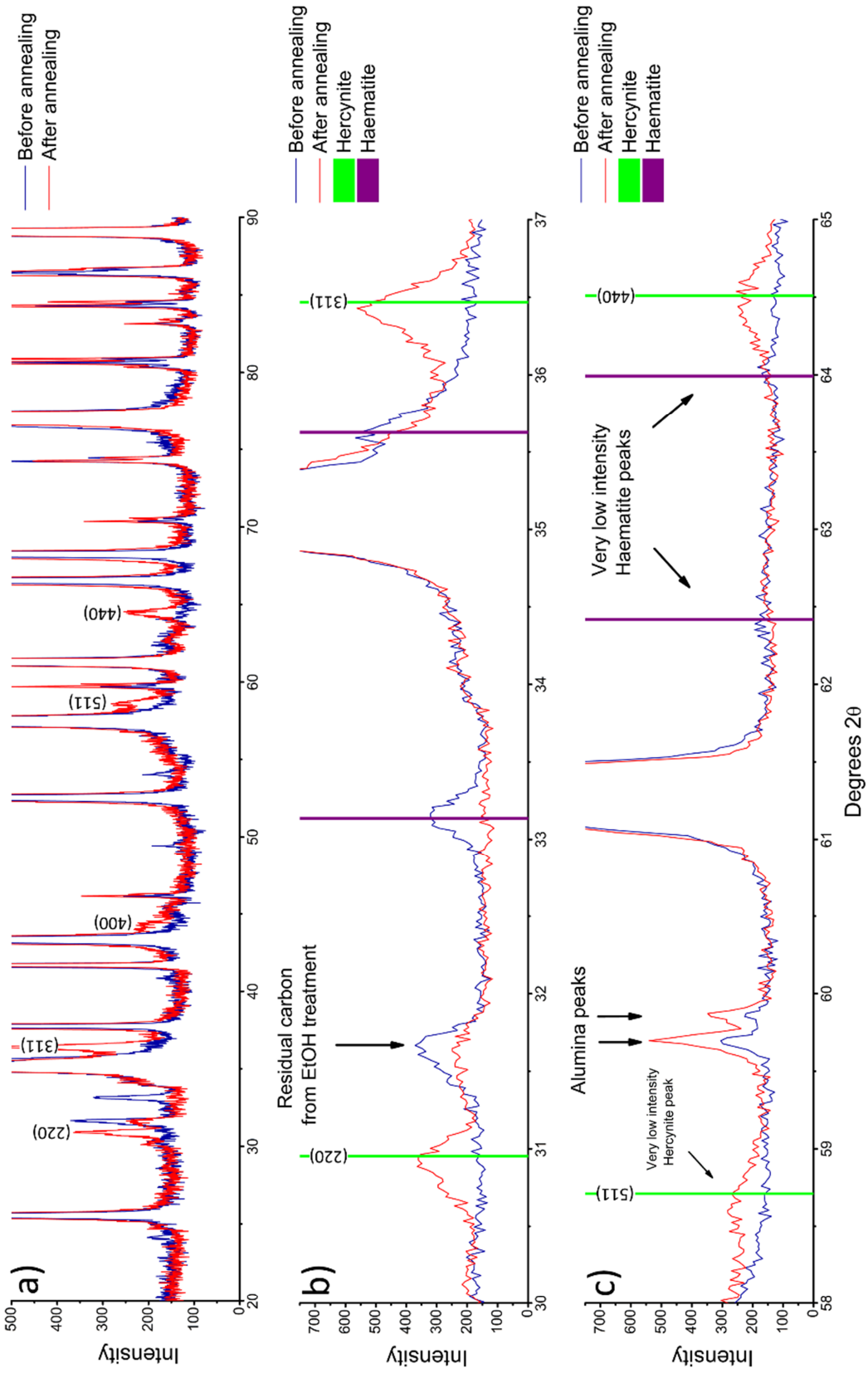


Figure 3.27 – a) XRD Spectra of alumina platelets infiltrated with catalysts following method B, before and after annealing for 60 minutes in inert atmosphere, showing hercynite peaks appearing after annealing (labeled) b-c) A zoom-in of the XRD spectra showing that hercynite peaks show exclusively in the annealed powder while haematite peaks show exclusively in the powder which did not undergo annealing, thus indicating a conversion from haematite to hercynite during the annealing procedure (the large peaks in between are from the large alumina background and are cut off in the y-direction to better show the peaks originating from the 2wt% nanoparticle volume).

NOTE: The indicated peak positions are the <u>theoretical</u> peak positions of hercynite (green) and haematite (purple).

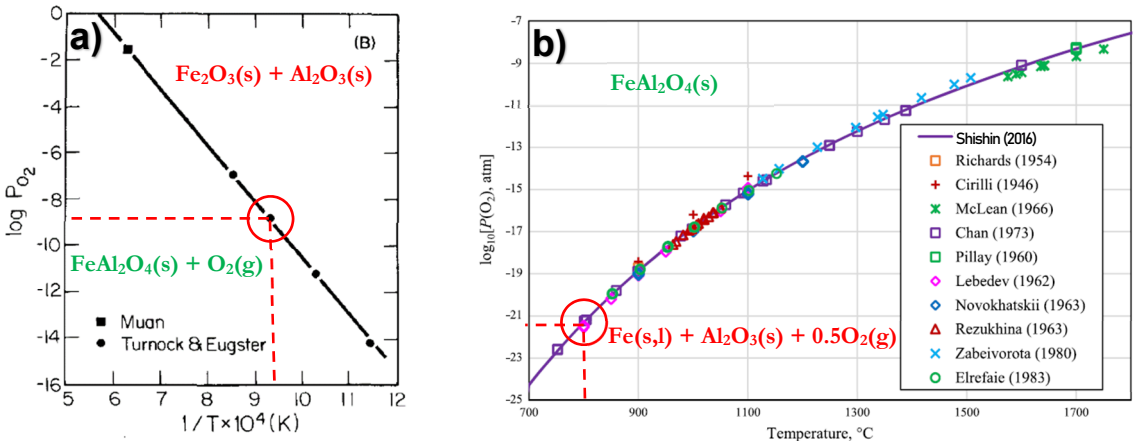
indicated by the lack of coalescence of nanoparticles on alumina platelets. XRD spectra in Figure 3.27 show that the haematite (Fe_2O_3) nanoparticles were converted to hercynite ($FeAl_2O_4$ spinel) in an inert atmosphere. At the same time the XRD spectrum shows that the original nanoparticle phase, haematite, disappears in the annealed sample, indicating a full conversion. Contrarily Co-Al_2O_3 spinel structures have been found before on γ-alumina substrates after annealing[239] which have been suggested to stop catalytic activity[240].

From Figure 3.26 and 3.27 it is clear that the opposite is the case for hercynite spinel and that the formation of the spinel structure is vital to create a strong bond between catalyst and substrate and grow a high quality, well dispersed MWCNT phase. SEM images of annealed catalysts before and after TGA in air clearly show that the catalyst particles have diffused into and/or reacted with the substrate (Figure 3.26). After burning off the MWCNTs, the catalyst sites show holes in the structure which resemble the diameter of the grown MWCNTs and are presumably sites where the MWCNT was attached. From the TGA curve in Figure 3.26a, the amount of MWCNTs grown on platelets prepared using method B was determined to be 21 wt%. The decomposition temperature of the as-grown MWCNTs was 666 °C. This is significant, as Born *et al.*[241] show that this is a typical temperature for CVD-grown MWCNTs after being graphitized by annealing at 1600°C. The high temperature oxidation resistance shown by the TGA data therefore indicate that the synthesized MWCNTs are highly graphitic in nature.

3.3.9 Stability of the catalyst during CVD

To assess the stability of the catalyst during the production of MWCNTs, a closer look is taken in this section at the theoretical and actual oxygen partial pressures for a stable catalyst during the CVD procedure.

Meyers *et al.*[242] at MIT have established the equilibrium oxygen partial pressure as a function of temperature for the oxidation of the hercynite ($FeAl_2O_4$) catalyst as in Figure 3.28a, Equation (1). For the synthesis temperature used in this work, 800 °C, a red line is drawn in



(1) $FeAl_2O_4(s) + O_2(g) = Fe_2O_3(s) + Al_2O_3(s)$
(Oxidation of Hercynite)

(2) $Fe(s,l) + Al_2O_3 + 0.5O_2(g) = FeAl_2O_4(s)$
(Reduction of Hercynite)

Figure 3.28 – Equilibrium partial oxygen pressure (in atm) for the stability of the hercynite catalyst particles vs temperature, adapted from a) Meyers *et al.*[242] for the oxidation of hercynite and b) Shishin *et al.*[243] for the reduction of hercynite.

Figure 3.28, showing that the partial oxygen pressure for which the driving force for this reaction is zero, is $1x10^{-9}$ atm. If the partial pressure of oxygen is greater than this value, the free energy change for the reaction is negative and there is a driving force for hercynite to oxidise.

At very low partial oxygen pressures however, hercynite can reduce to pure Fe and Al_2O_3. Data collated by Shishin *et al.*[243] in Figure 3.28 show the equilibrium oxygen partial pressure as a function of temperature for the reduction of hercynite ($FeAl_2O_4$) as in Figure 3.28, Equation (2). Again, a red line is drawn in the figure for the synthesis temperature of 800 °C, showing that the partial oxygen pressure should be above $1x10^{-21}$ atm for hercynite to be stable (towards reduction) at this temperature.

These studies establish an oxygen partial pressure range between $1x10^{-9}$ atm and $1x10^{-21}$ atm for which the catalyst is stable as hercynite at the reactor temperature of 800 °C.

For the CVD parameters that yield high quality and quantity MWCNTs (CVDP14), the partial oxygen pressure at the catalyst site during CVD is here calculated to see if the catalyst is indeed in the given oxygen partial pressure range. Using the ideal gas law, we can calculate the molar concentration of the total gas mixture at 1 atm and 800°C as in Equation 3.

$$\textbf{(3)}\ [\text{Total gas mixture}] = \frac{P}{RT} = \frac{1\,[atm]}{82.053\,[\text{cm}^3\ \text{atm}\ \text{K}^{-1}\ \text{mol}^{-1}] \times 1073.15\,[\text{K}]} = 1.136 \times 10^{-5}[\text{mol cm}^{-3}]$$

During the production of MWCNTs following CVDP14, a gas mixture is used consisting of 67.3% argon with a 0.002% air impurity, 28.85% hydrogen with a 0.01% air impurity and 3.85% acetylene with a 0.4% air impurity. From these, the molar concentration for each gas within the gas mixture (before any reaction take place) can be individually calculated, with the oxygen gas concentration [O_2] equal to 20.95% of the air impurity (Equations 5-8).

(4) $[\mathrm{Ar}] = 1.1356 \times 10^{-5}[\mathrm{mol\ cm^{-3}}] \times 0.673 = 7.643 \times 10^{-6}[\mathrm{mol\ cm^{-3}}]$

(5) $[H_2] = 1.1356 \times 10^{-5}[\mathrm{mol\ cm^{-3}}] \times 0.2885 = 2.595 \times 10^{-6}[\mathrm{mol\ cm^{-3}}]$

(6) $[C_2H_2] = 1.1356 \times 10^{-5}[\mathrm{mol\ cm^{-3}}] \times 0.0385 = 0.4372 \times 10^{-6}[\mathrm{mol\ cm^{-3}}]$

(7) $[Air] = ([Ar] \times 0.00002) + ([H_2] \times 0.0001) + ([C_2H_2] \times 0.004) = 2.161 \times 10^{-9}[\mathrm{mol\ cm^{-3}}]$

(8) $[O_2] = 2.161 \times 10^{-9}[\mathrm{mol\ cm^{-3}}] \times 0.2095 = 4.528 \times 10^{-10}[\mathrm{mol\ cm^{-3}}]$

Using the ideal gas law PV=nRT, the partial pressure of O_2 before any reaction takes place (and the partial pressure of the other gases in the mixture for completeness) at 800 °C (1073.15 K) can be calculated (Equations 9-12).

(9) PP_{Ar} = RTn/V = 1073.15 [K] × 82.053 [cm^3 atm K^{-1} mol^{-1}] × [Ar] [mol cm^{-3}] = 0.673 atm

(10) PP_{H_2} = RTn/V = 1073.15 [K] × 82.053 [cm^3 atm K^{-1} mol^{-1}] × [H_2] [mol cm^{-3}] = 0.2885 atm

(11) $PP_{C_2H_2}$ = RTn/V = 1073.15 [K] × 82.053 [cm^3 atm K^{-1} mol^{-1}] × [C_2H_2] [mol cm^{-3}] = 0.0385 atm

(12) PP_{O_2} = RTn/V = 1073.15 [K] × 82.053 [cm^3 atm K^{-1} mol^{-1}] × [O_2] [mol cm^{-3}] = $3.985*10^{-5}$ atm

However, during MWCNT synthesis, the oxygen partial pressure will be drastically lower due to the introduction of H_2 gas; in the reactor there is a driving force for H_2 gas to react with O_2 gas to form H_2O. While the equilibrium and rate constants of the oxygen scavenging of H_2 gas in a CVD reactor are not well documented, the dissociation of water into hydrogen and oxygen gas is well understood due to H_2 gas production efforts[244]. The molar equilibrium constant K_C for this reaction at 800 °C (1073.15 K) is given below (Equation 13).

(13) $H_2O(g) \Leftrightarrow H_2(g) + 0.5O_2(g) \quad K_C = 10^{-9.268} = 5.395 \times 10^{-10}$ (@1073.15K)[244]

As this is at equilibrium for this temperature, the equilibrium constant for the reverse reaction is simply the reciprocal (Equation 14), here expressed in non-fractional molecular units.

(14) $2H_2(g) + O_2(g) \Leftrightarrow 2H_2O(g) \quad K_C = (\frac{1}{5.395\times10^{-10}})^2 = 3.434 \times 10^{18}$ (@1073.15K)

(15) $K_C = \frac{[H_2O]^2}{[H_2]^2 \times [O_2]} = 3.434 \times 10^{18}$

The definition of the equilibrium constant in terms of the molar concentration of the constituents is given in Equation 15.

With the previously calculated molar concentration of H_2 and O_2 gas in the reactor, the molar concentration of H_2O can now be calculated using Equation 16.

(16) $\frac{[2x]^2}{([H_2]-2x)^2 \times ([O_2]-x])} = 3.434 \times 10^{18}$

As we are interested in the molar concentration of O_2 gas left in the reactor ([O_2Final]), we

can express this equation in terms of [O_2Final], and simplify the equation by realising that [H_2]>>[O_2] and thus [H_2]-2x ≈ [H_2].

(17) $$\frac{2([O_2]-[O_2Final])^2}{[H_2]^2\times([O_2Final])} = \frac{((2\times4.528\times10^{-10})-[O_2Final])^2}{(2.595\times10^{-6})^2\times[O_2Final]} = 3.434\times10^{18}$$

Solving Equation 17 for [O_2Final] (Here done using the mathematical engine Wolfram Alpha) yields [O_2Final] = 3.54648×10^{-26} [mol cm^{-3}].

(18) PP_{O_2} = RTn/V = 1073.15 [K] × 82.053 [cm^3 atm K^{-1} mol^{-1}] × [O_2Final] [mol cm^{-3}] = $3.123*10^{-21}$ atm

Equation 18 gives the partial oxygen pressure in the reactor using the calculated [O_2] during MWCNT growth in CVDP14, taking into account H_2 partial pressure. As the partial oxygen pressure falls within the oxygen partial pressure range between $1x10^{-9}$ atm and $1x10^{-21}$ established by Meyers *et al.*[242] and Shishin *et al.*[243], it can be concluded that the catalyst is indeed stable as hercynite during MWCNT growth.

Note that the calculated oxygen partial pressure represents the absolute lower bound as calculated from the gas mixture; experimentally the CVD procedure is not done in a perfect vacuum system and therefore minimal amounts of atmospheric air are expected to enter the CVD system through joints, or permeate through tubing. This however minimally increases the oxygen partial pressure due to the nature of the procedure (1 slm flow rate with [H_2]>>[O_2]) which is certainly expected to keep the oxygen partial pressure in the stability range as argued above (see Equation 14).

3.3.10 MWCNT growth from iron oxide coated alumina platelets

The development of a large range of metallic oxide coated alumina platelets which are sold as pigments by Merck are promising materials to create MWCNT-coated alumina building blocks. Especially as iron oxide coatings on flat substrates have yielded aligned CNT carpets of high quality[245] and could be used to generate a highly homogeneous and well-dispersed CNT phase in alumina-CNT composites. Of particular interest is Xirallic Radiant Red, which is a pigment consisting of a homogeneous coating of iron oxide on alumina platelets. First, the stability of the coating was investigated under annealing conditions, to see if any morphological changes occur to these platelets.

Figure 3.29 reveals that the platelets are stable with minimal changes in the microstructure after annealing at 800 °C for 1 h in Argon environment. Therefore, CVD procedure 16 (CVDP16) is applied to these platelets. A significantly different behaviour in CVD compared to platelets with dispersed nanoparticle catalysts could be observed; three different regions are found in the same sample including regions without CNT growth, with short CNT coverage and with long carpet growth (Figure 3.30).

Although these platelets are patented, the manufacturer revealed that these pigments are coated with a polymer to enhance weather resistance. While this is advantageous for their pigment application, the polymer coating will leave a carbon residue behind on the platelets after the annealing step in argon at 800°C, which can interfere with the CNT growth by preventing the carbon precursor to reach the catalyst. Therefore, a 15-minute burning step at 800°C in air was introduced in the CVD procedure, to get rid of this carbonaceous material.

As can be seen in Figure 3.31a, combining both a step to burn away the organic coating followed by an annealing step in argon, is key to covering these in a homogeneous CNT coating. This confirms that the presented recipe used for FSP iron oxide nanoparticles, also works for commercially deposited continuous thin films of catalyst. In addition, the MWCNT coating method shown can be translated to different alumina surfaces but can also be used to coat different substrate materials. In Figure 3.31b, the coating procedure is repeated for iron oxide-coated mica platelets. Mica is commonly used as a reinforcing agent in plastic materials[246], and is therefore an interesting candidate to coat with MWCNTs, as it may enhance the reinforcing ability of these platelets. However, in contrast with the iron oxide coated alumina platelets, the iron oxide coating delaminates from the mica platelets after the CVD procedure. The delamination of the iron oxide coating after CVD in the case of mica platelets, further supports the hypothesis that during the CVD procedure of alumina and iron oxide, a strong bond between catalyst and substrate is formed (e.g. the hercynite-spinel bond formation shown in section 3.3.8)

3.4 Conclusions

MWCNT growth on both bioinspired freeze-cast scaffolds and micron-sized alumina platelets has been investigated. MWCNT growth on freeze-cast scaffolds can be well controlled after removal of metallic contaminants from the freeze casting procedure through an RCA cleaning treatment. A balanced gas mixture as outlined in this work, combined with iron oxide nanoparticle dispersion through sonication yields a homogeneous coverage of CNTs. While Raman spectroscopy reveals that the MWCNTs have a large number of defects, SEM micrographs show a well-dispersed homogeneous MWCNT phase, and further procedures such as sintering and/or annealing can further increase the crystallinity of the MWCNTs.

For iron oxide catalyst particles on the alumina platelet surface, long annealing times improved the yield and quality of the subsequently grown MWCNTs. XRD data show that during annealing in argon atmosphere, the iron oxide particles reacted with the alumina platelet surface to form hercynite. The lack of coalescence during these long annealing times indicates that the hercynite formation gives a degree of immobility to the catalyst sites, resulting in a well-dispersed and homogeneous MWCNT-coverage. The catalyst sites grow high quality and quantity MWCNTs when annealed in argon for more than 20 minutes at 800°C, and by including hydrogen during synthesis MWCNTs can consistently be grown with an I_D/I_G ratio of 0.54 ± 0.04. Exposing the iron oxide catalyst particles to high temperature in an oxidising or reducing environment yielded very poor MWCNT growth. Annealing in inert argon atmosphere for sufficient time (>20 minutes) before MWCNT synthesis is shown to be essential for the activation of these catalyst particles on alumina surfaces and key to growing a high coverage of well distributed MWCNTs on the platelets. The demonstrated scalable approach to grow a homogeneous MWCNT coating with few defects is an attractive alternative to other CNT reinforcing techniques whereby the MWCNTs are often damaged during the dispersion procedure. A MWCNT coating method

has been developed, where iron oxide on alumina is first annealed in an argon atmosphere, after which a 70:30:4 argon:hydrogen:acetylene mixture is exposed to the catalyst at 1 slm for 10 minutes. This method is applicable to create MWCNT/alumina platelet building blocks with different aspect ratios and different shapes to generate a range of tailored MWCNT-reinforced composite structures; MWCNT-coated platelets are promising base materials to be used as a building block for ceramic composites.

Chapter 4 – Formation and properties of nacreous alumina

Because of the unique mechanical properties of the 'brick-and-mortar' microstructure, alumina platelets similar in size to the $CaCO_3$ platelets found in nacre, have been of much interest in composite manufacturing. The flexural strength of individual alumina platelets has been measured to be 5.3±1.3 GPa[247]. They have been compacted with epoxy[86,87], polymer[88–90], metallic[248], borosilicate[91], aluminium borate[249] and silica-calcia[35] phases. In this chapter, these alumina platelets are used to form the grain structure of a pure alumina ceramic and the mechanical behaviour of alumina with a purely nacre-like microstructure without 'soft phase' is investigated.

4.1 Introduction

To effectively mimic the platelets seen in the nacre microstructure, precise control over the grain growth (which has to be minimized to maintain the platelet-like grain structure) while sintering alumina platelets into a dense ceramic is paramount. Conventional sintering does not provide this level of control. Alumina platelets were therefore densified using Spark Plasma Sintering (SPS), also known as Field-Assisted Sintering Technique (FAST). In this technique, discovered by K. Inoue around 1965 but commercialized much later in the 1990s[250], samples are pressed uniaxially inside a graphite die which is subjected to an electric current (Figure 4.1). In the case of sintering pure alumina, it is assumed that it sinters by the heat transferred from the graphite mould and punches[251] while in the case of conductive materials, the sample is heated from within by the current passing through the sample. Using the SPS/FAST technique, alumina can be sintered in greatly reduced times compared to conventional hot-pressing and pressure-less sintering methods[252,253]. In addition to increased

control over the grain size, the lower energy cost and relatively short timescale necessary to produce a sample makes SPS/FAST a very economic manufacturing route.

While SPS/FAST has not been systematically applied to powders of pure alumina platelets, the densification of alumina nanoparticles using SPS has been studied. Shen *et al.*[252] show that for alumina with a grain size of 0.4 μm, fully dense samples can be obtained at 1150 °C in only 5 minutes. A later study by Santanach *et al.*[253] shows that for 0.14 μm particles, full densification is obtained at temperatures of 1100 °C and higher. They see that in their experiments, grain growth only starts at 1200 °C, with significant grain growth at temperatures of 1300 °C and higher. Since alumina platelet powders have a grain size that is much larger, and since the poorer packing of platelet-powders must be considered, these temperatures are taken as a lower bound. The nacre-like alumina has therefore been densified at 1200 °C, 1300 °C and 1400 °C to see the effect on the microstructure and related mechanical properties.

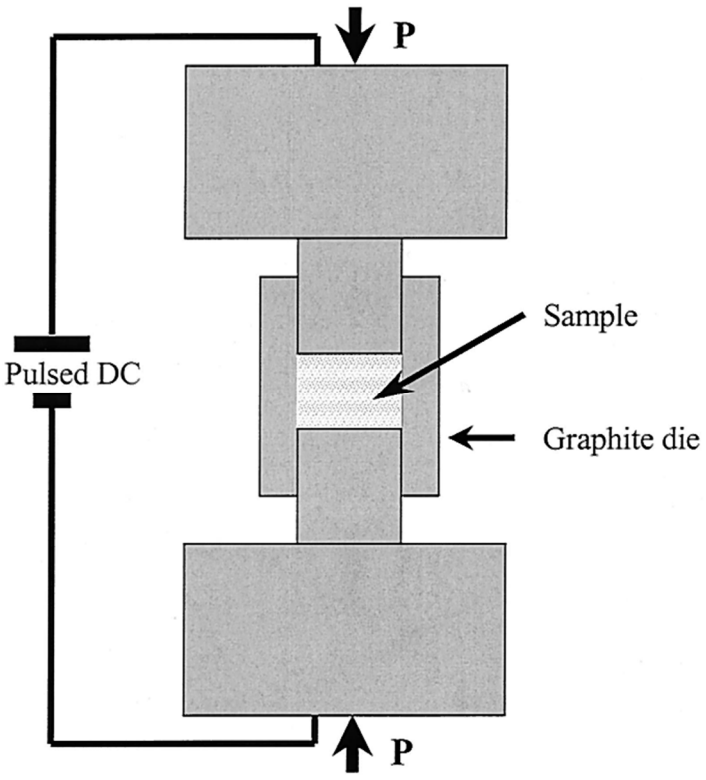


Figure 4.1 – Schematic drawing, illustrating the SPS/FAST setup [Adapted from Shen *et al.*[252]]

4.2 Materials and methods

4.2.1 Ceramic manufacturing

15 g (±1%) of α-alumina platelets in powder form (RonaFlair® White Sapphire, MERCK, median diameter 8.4 μm, thickness 0.2-0.5 μm), was loaded in a graphite die with an inner diameter of 40 mm and outer diameter of 80 mm. The powder was loaded without any de-agglomeration procedure to prevent contamination from dispersants and breakage of platelets in ball milling or other dispersion procedures. To protect the die and punches, the inside of the die and punches was lined with graphite paper (GEEGRAF flexible graphite foil, Gee Graphite). The sample was first pre-pressed using a hydraulic press to 15.5 MPa and then densified using a field assisted sintering technique (FAST) (Dr Fritsch Fast Sintering Press, FSP507) at temperatures between 1200 °C-1400 °C in vacuum (0.3 mbar) with a carbon felt insulation around the die. The temperature was measured at the wall of the die using a pyrometer. The dwell time was 15 min and the heating rate 125 °C/min. The pressure was increased linearly to either 50 or 70 MPa (maximum pressure for an intact graphite die) during heating and maintained at those levels during the entire dwell time. After the sintering process, the sample was cooled naturally without applied pressure to the die, which was measured to be 120 °C/min. The surface of the discs was then ground to smooth the edges and remove residual graphite paper. A monolithic alumina specimen to compare impact and high rate loading behaviour was sintered using 15 g alumina powder with a diameter of 0.4 μm (AES11C, Sumitomo Chemical Co., Ltd.). The same sintering conditions were used as that of the best performing alumina-platelet sample; a dwell time of 15 min at 1300 °C and a 70 MPa sintering pressure, resulting in >99% dense discs.

For alumina nanoparticle addition, 200nm particles (TMDAR, Tai-Mei) were sonicated for 20 m in Type II H_2O with Dispex A40 as a dispersant, after which the alumina platelets were added, and the solution was shaken and sonicated for another 20 m. The suspension was then left to dry overnight.

4.2.2 Characterisation

Density measurements were made using Archimedes' principle, by measuring dry and water-submerged weights. The densities were then presented as a percentage of the theoretical density of α-Al_2O_3, 3.987 g/cm^3 [254]. Error bars represent variability in measured weights. For 3-point bend testing, the discs were polished and cut into 3.6 x 2.7 mm rectangular beams using a diamond saw. For the impact tests and split Hopkinson pressure bar tests, the discs were polished and cut into 12 mm x 12 mm x 2.7 mm square plates and 3 mm x 3 mm x 2.7 mm squares respectively. After failure, the broken or impacted specimens were coated with 15 nm platinum and carefully transferred to a Zeiss Merlin high-resolution scanning electron microscope (SEM), equipped with an in-lens detector. Imaging was done with an acceleration voltage of 5.0 kV and beam current of 200 pA. To image the fracture surface from the three-point bend test, the specimen was coated again with 15 nm platinum after mounting upright and embedded in silver conductive paint to provide a conductive pathway for electrons and thus prevent charging effects. To show the grain boundaries in polished samples, the samples were thermally etched at 100 °C below the sintering temperature for 1.5 h. These thermally etched samples were then used to determine the grain width and length by measuring the distance from edge to edge of the grains (100 and 50 measurements per condition for grain width and length respectively).

4.2.3 Three-point bend testing

The 3.6 x 2.7 mm rectangular beam specimens were subjected to a bend test in a Shimadzu loading frame with a 5 kN load cell. The loading frame was set-up with a three-point bend jig with a 20 mm span between outer rollers, and the cut specimens were loaded in the direction perpendicular to the orientation of the platelets with a stroke speed of 0.5 mm/min. The resulting force-deflection curves were then converted to stress-strain curves using standard formulae outlined in ASTM C1161-13.

4.2.4 Split Hopkinson pressure bar testing

The 3x3 mm square specimens cut from the polished discs were tested under high-rate loading conditions using a split-Hopkinson compression bar. The compressive load was applied in the direction perpendicular to the orientation of the platelets (i.e. along the original disc thickness).

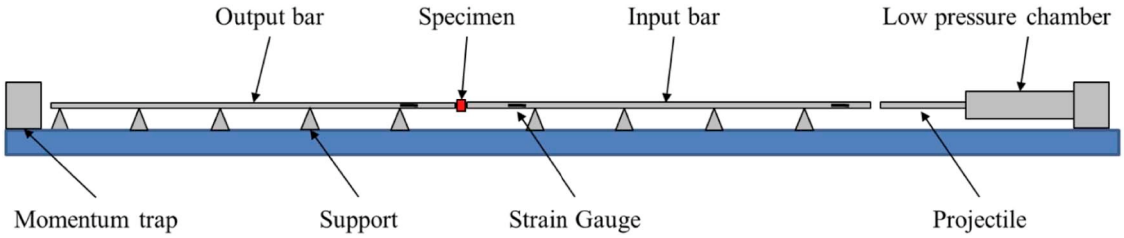


Figure 4.2 – Schematic drawing, illustrating the used Split-Hobkinson bar setup [Adapted from De Cola *et al*.[255]]

The split Hopkinson bar apparatus used (Figure 4.2) consists of three aligned bars (i.e. projectile, input, and output bars) supported by low-friction polymeric circular bearings to avoid movement in the direction perpendicular to the bar axis. The projectile, accelerated using low-pressure compressed nitrogen, impacts the input bar generating a uniaxial stress pulse that travels along the bar and loads the specimen positioned between the input and the output bar.

The input and output bar, both with length of 2.8 m and diameter of 20 mm, are instrumented with strain gauges to measure the stress transmitted (output) and reflected (input) by the specimen. The material stress-strain behaviour is obtained by means of stress wave analysis using the signals measured by strain gauges. For this analysis, an in-house developed Matlab algorithm was used to evaluate the stress-strain condition in the specimen, based on the theoretical framework outlined by De Cola *et al.*[255]. In addition to this analysis, the values of strain are validated with tracking measurements of the end of the bars using Digital Image Correlation (DIC). The tracking of the end of the bars is an extra measure for very stiff materials such as evaluated here, as the very small magnitude of the strain has the potential to introduce a large error value in the wave propagation analysis. DIC of the edge

of the bars can therefore be used to reduce the noise in strain values evaluated by the algorithm.

The tests were recorded using an ultra-high-speed camera (Kirana – Specialised Imaging Ltd.) with a frame rate of $1 \cdot 10^6$ fps. The specimens were also speckled with black paint for possible DIC analysis during the test. However, since the stress-strain measurements from the strain gauges showed dynamic equilibrium of the specimens (i.e. the input force and output force lines were parallel and overlapping, proving that the stress wave was reflected several times within the specimen before the onset of damage), due to the consequent homogeneity of the load, the speckling pattern was not analysed in these experiments.

In the tests presented in this work, disc anvils made of high-grade tungsten carbide (WC) were inserted between the ceramic specimen and the titanium (Ti6Al4V alloy) bars to prevent indentation of the metal. The correct sizing of the anvils (i.e. 10 mm diameter) ensures the impedance matching with the titanium bars, thus avoiding spurious signal reflection at the Ti6Al4V-WC interface. Further details of the apparatus used, and on the one-dimensional wave propagation analysis adopted can be found in works by De Cola[255] and Pellegrino[256].

4.2.5 Impact testing

The 12x12x2.7 mm square specimens cut from the polished discs were attached using a small layer of petroleum jelly to a flat aluminium surface, providing full backing support to the specimen, thus minimizing the occurrence of bending upon impact. The targets were impacted normally to the platelet orientation with spherical steel projectiles of 3 mm diameter. The steel projectiles were accelerated using a single stage gas gun, consisting of a pressurised vessel connected with a valve to a 2 m long barrel. At the opening of the valve, the compressed nitrogen released from the vessel accelerated the projectiles along the barrel. Three light gauges positioned at the end of the barrel measured the speed of the projectile before it impacted the surface of the target. Further details on the equipment used are provided in the work of Falco[257].

The impacts were recorded at an angle with a high-speed camera (FASTCAM SA5 – Photron), with a frame rate of $7.5 \cdot 10^4$ fps, to provide visual information on the crack initiation and propagation within the two materials upon impact. Depth measurements and the rendering of the impact crater were obtained using an Alicona infinite focus 3D profilometer microscope with a 5x objective.

3D profilometry has been performed by Dr. Simone Falco, and all impact and high strain rate split Hopkinson bar tests have been done under his guidance.

4.3 Results and discussion

To investigate nacre-like microstructures using SPS, alumina platelets were sintered at different combinations of sintering temperature and pressure, thus generating a range of materials with distinct microstructural features, mainly in terms of size of the platelet-like grains. Three-point bending tests were then carried out to characterise the mechanical behaviour of the manufactured materials. The different sintering conditions result in a range of nacre-like microstructures that as a result have varying flexural strengths. The material showing the most promising mechanical behaviour was selected for high-rate testing, first under compression using a split-Hopkinson bar apparatus, then upon impact of spherical steel projectiles. Direct comparison of the results of these tests for nacre-like and monolithic alumina specimens show strikingly different failure mechanisms, highlighting a large energy-absorbing capability of the manufactured nacre-like specimens.

4.3.1 Sintering and microstructure of nacre-like alumina

Alumina platelets were sintered at 1200 °C, 1300 °C and 1400 °C at a pressure of either 50 MPa or 70 MPa. The sintering curves in Figure 4.3a give an indication of how well the samples were densified; no piston movement over long times is a good indication that the

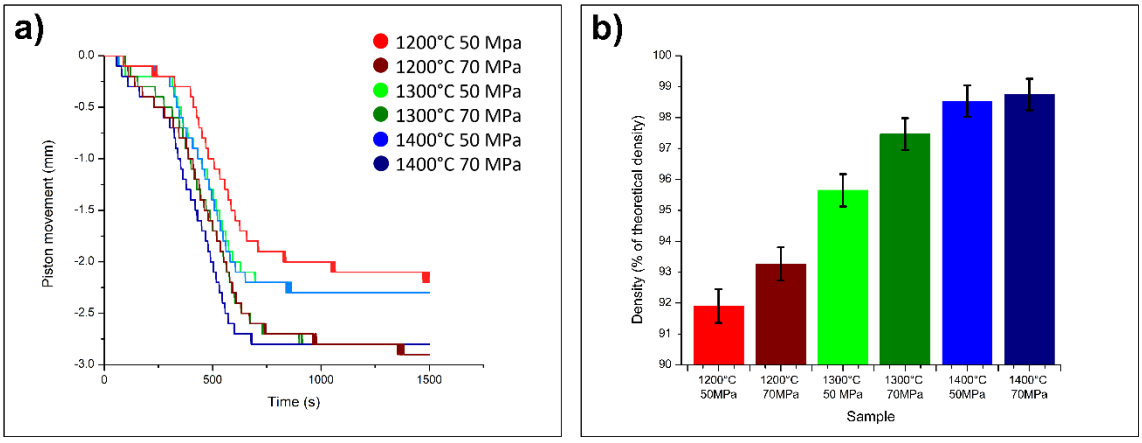


Figure 4.3 – a) Sintering curves for each sintering condition showing piston movement in FAST and b) their densities after sintering.

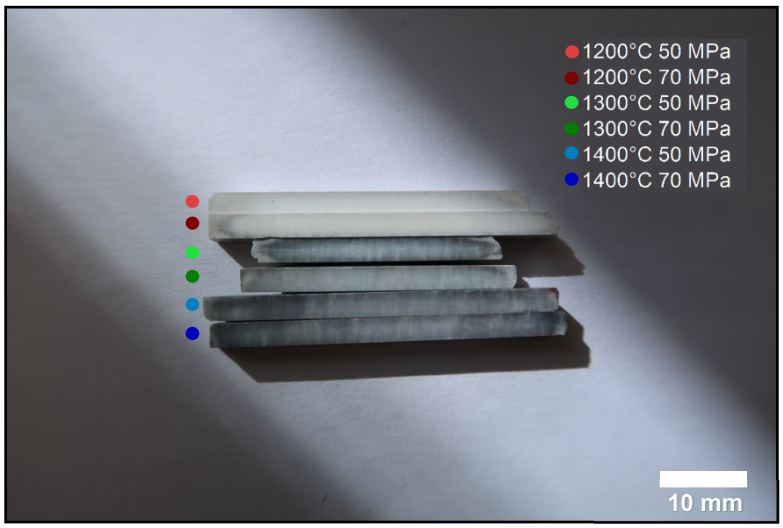


Figure 4.4 – Optical image of the colour change in pure alumina platelet ceramics as a result of the reducing environment during the SPS procedure.

sample is not being densified further under the applied conditions. Both curves at 1200 °C stand out from curves at higher temperatures as they still show piston movement after half of the sintering time has elapsed, indicating a relatively poor density, which is confirmed by the density measurements in Figure 4.3b. The samples sintered at 1300 °C and 1400 °C show no more piston movement within 5 min of reaching the set sintering temperature, indicating maximum achievable density under their respective sintering conditions. At temperatures of 1300 °C and higher, a colour change from white to grey is observed (Figure 4.4). This can be due to the reducing nature of the SPS technique – partial reduction of Al_2O_3 can lead to the formation of oxygen vacancies. Oxidizing in air turned the material back to alumina's characteristic white colour. Alternatively, carbon contamination can have occurred at the higher sintering temperatures. Increased grain growth with increasing sintering temperature is observed (Figure 4.5 and 4.6). While at 1200 °C the grain size is of the order of that of the initial platelet powder, at 1300 °C there is a wider grain size distribution, with both small and large grains co-existing (see also Figure 4.7a). At 1400 °C the grains are an order of magnitude larger than that of the initial platelet powder. The effect of pressure when sintering alumina is to reduce the porosity in the sample, and as pores pin grain boundaries, larger pressures in SPS normally aid grain growth[258]. However, Figure 4.6 shows that for all temperatures, both the grain width and length of the platelet-like grains is smaller at higher pressure. This is especially evident with the samples sintered at 1300 °C. The increased pressure may play a

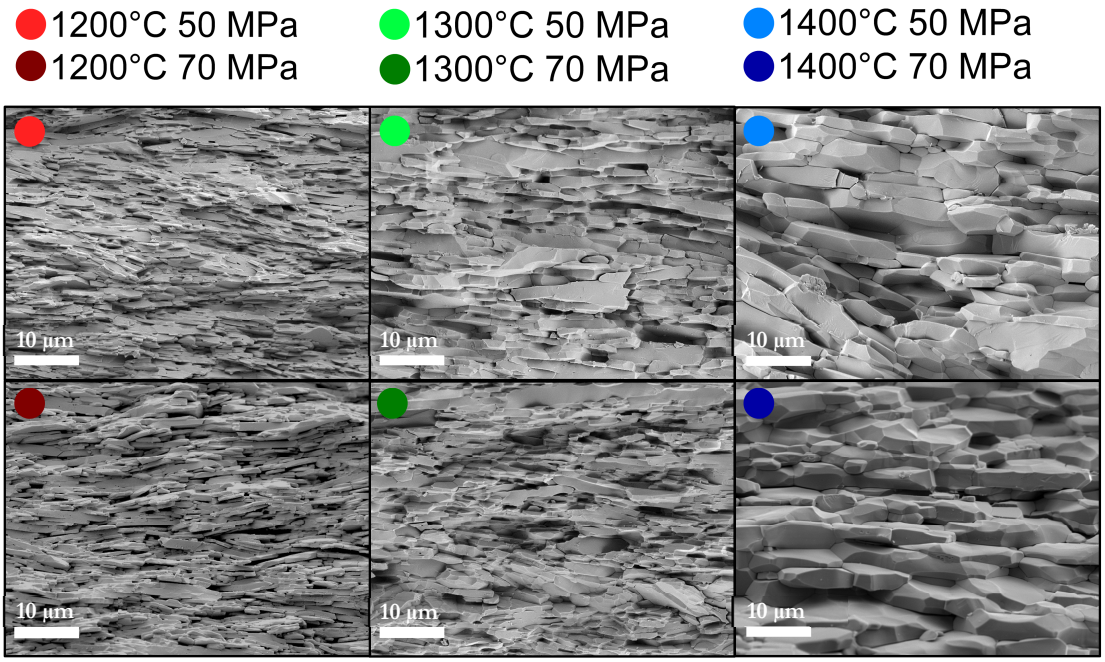


Figure 4.5 – SEM micrographs taken of the fracture surface of the beams after bend testing, showing coarser platelet-like grains with increasing sintering temperature.

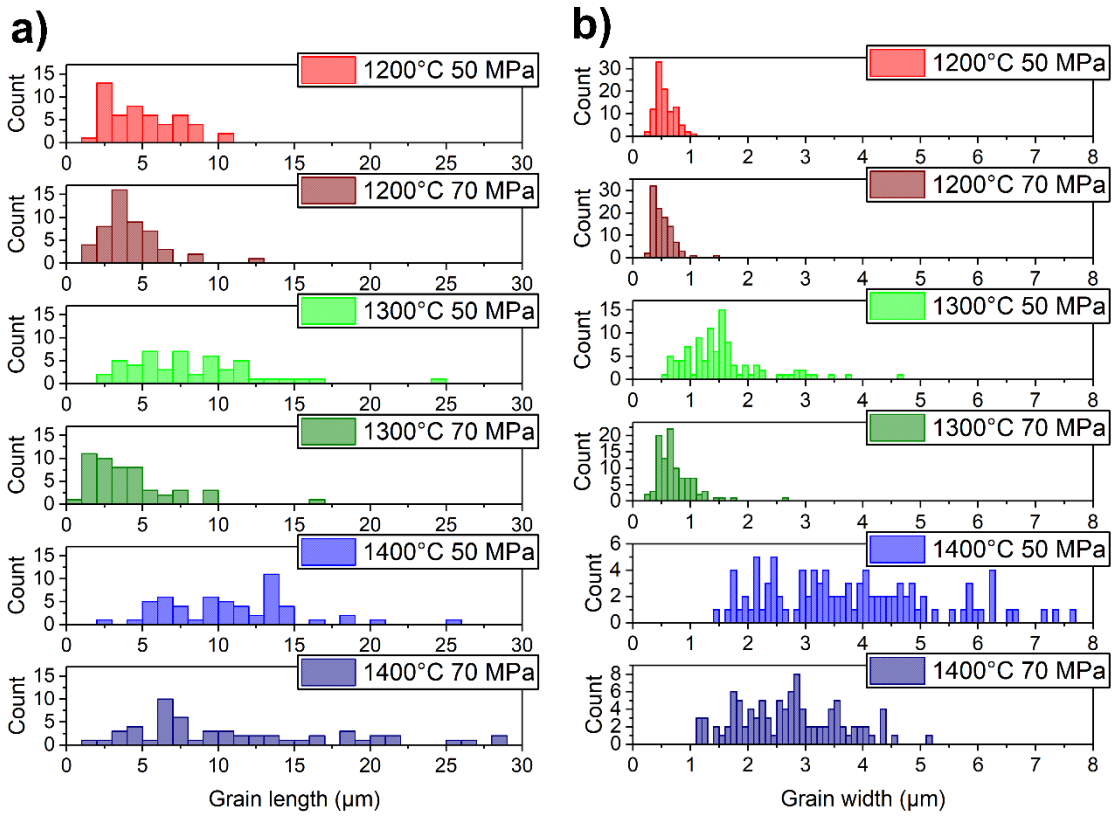


Figure 4.6 – a) Measurements of grain length (bin size: 1 µm) and b) grain width (bin size: 0.1 µm) of platelet-like grains for all sintering conditions used. For all grain size measurements taken at the same sintering temperature, a higher number of smaller grains are observed at higher pressures.

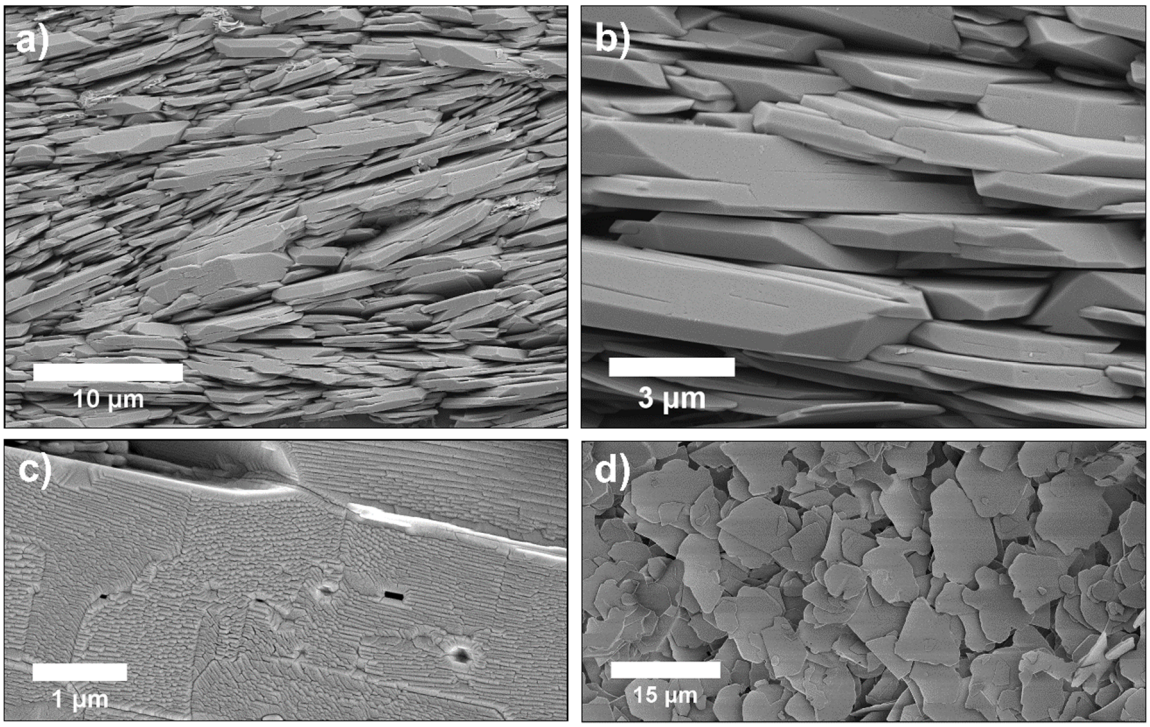


Figure 4.7 – SEM micrographs taken of a-c) the side of the beams sintered at 1300 °C, and d) the platelet-alumina powder that was loaded into the graphite die to create the nacre-like alumina. It is shown that a) starting at 1300 °C, a number of platelets nucleate grain growth and form larger platelets, resulting in a wider grain size distribution. b) Larger grains are shown to be formed by bonding platelets with similar dimension and orientation. c) The thermally etched, polished surface shows the grain or sub-grain boundaries within the platelet-like grains and associated nano-sized voids in the platelet structure.

role in breaking up the platelets during sintering, leading to a smaller grain/platelet size before sintering, resulting in smaller grains in the sintered alumina. The tendency of platelets to align naturally has been shown before in a sedimentation procedure[259]. The pre-pressing procedure combined with the (platelet) particle rearrangement/sliding[260] during the sintering procedure under the applied pressure is likely responsible for the observed large scale-alignment of platelets (and consequently platelet-like grains).

Interestingly, the platelet-like morphology of the grains is maintained at all temperatures regardless of grain growth, although the aspect ratio of the platelet-like grains reduces with increased temperature. After platelets combine to larger platelet-like grains, Figure 4.7c shows that these are often not monocrystalline domains, and Nano-sized voids are present within the platelet structure. While it is possible that slightly misaligned domains and pores may already have existed in the alumina platelet powder, the platelets in the starting powder (Figure 4.7d) can not only grow by classical grain boundary migration, but also by the coalescence of neighbouring platelets. This is presumed to be a consequence of the fact that the crystallographic c-axis [001] is normal to plane of the platelets[261]. The physical alignment

of the platelets (Figure 4.7a-b) in these composites therefore also corresponds to a crystallographic alignment, opening the possibility of grain coalescence. It is also possible that local plastic deformation occurs around mis-stacked platelets during SPS, creating dislocations, which then form subgrains via recovery. Figure 4.7b further shows that the grain growth leads to the formation of platelets with irregular 'wavy' shapes. The 'steps' that are formed can be seen to interlock in a similar manner as described for nacre by Katti *et al.*[28]

4.3.2 Mechanical response in bending

In three-point bending, the nacre-like alumina does not fail in a purely brittle fashion, with a macroscopically flat fracture surface as is normally observed for monolithic alumina. Instead, all samples, regardless of grain size, show evidence of crack deflection and branching as seen in nacre (Figure 4.8 and 4.9). The tortuous and thus prolonged crack paths along the platelets result in macroscopic interlocking after failure which gives the material post-failure load bearing capabilities seen in Figure 4.10. Due to being interlocked both macroscopically and microscopically, the beams stay suspended on the rollers of the bending rig after failing (Figure 4.11). The beams stay so connected that they can easily be transferred without falling apart, which is very rare for a pure ceramic specimen after failure.

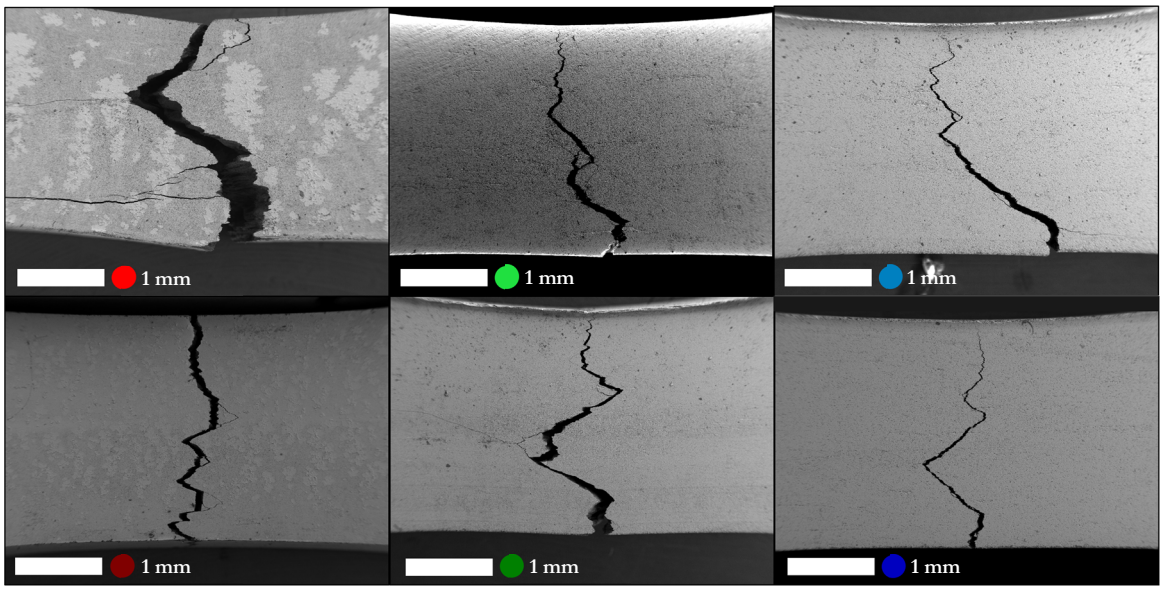


Figure 4.8 – SEM micrographs of the side-view of the beams sintered at 1200°C (red),1300°C (green) and 1400°C (blue) at 50MPa (light) and 70 MPa (dark) after it has failed in three-point bend testing. (The white areas on the red samples are dried NaCl deposits from the diamond saw coolant).

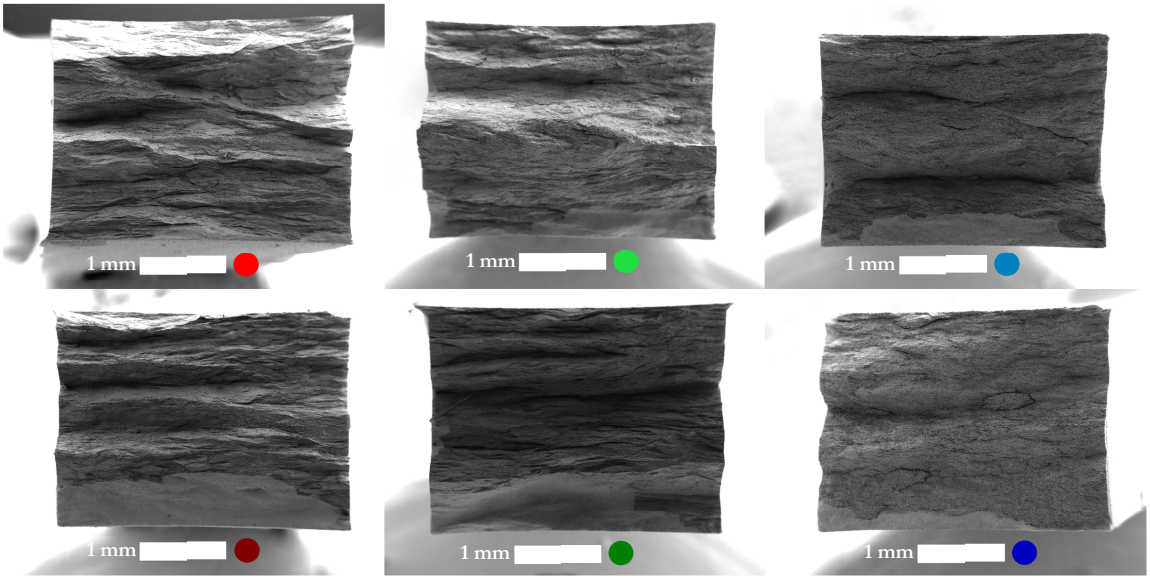


Figure 4.9 – SEM micrograph of the three-point bend testing fracture surfaces of the beams in Figure 4.8. Composites were sintered at 1200°C (red),1300°C (green) and 1400°C (blue) at 50MPa (light) and 70 MPa (dark) (with on the bottom of the samples the conductive silver DAG pathway).

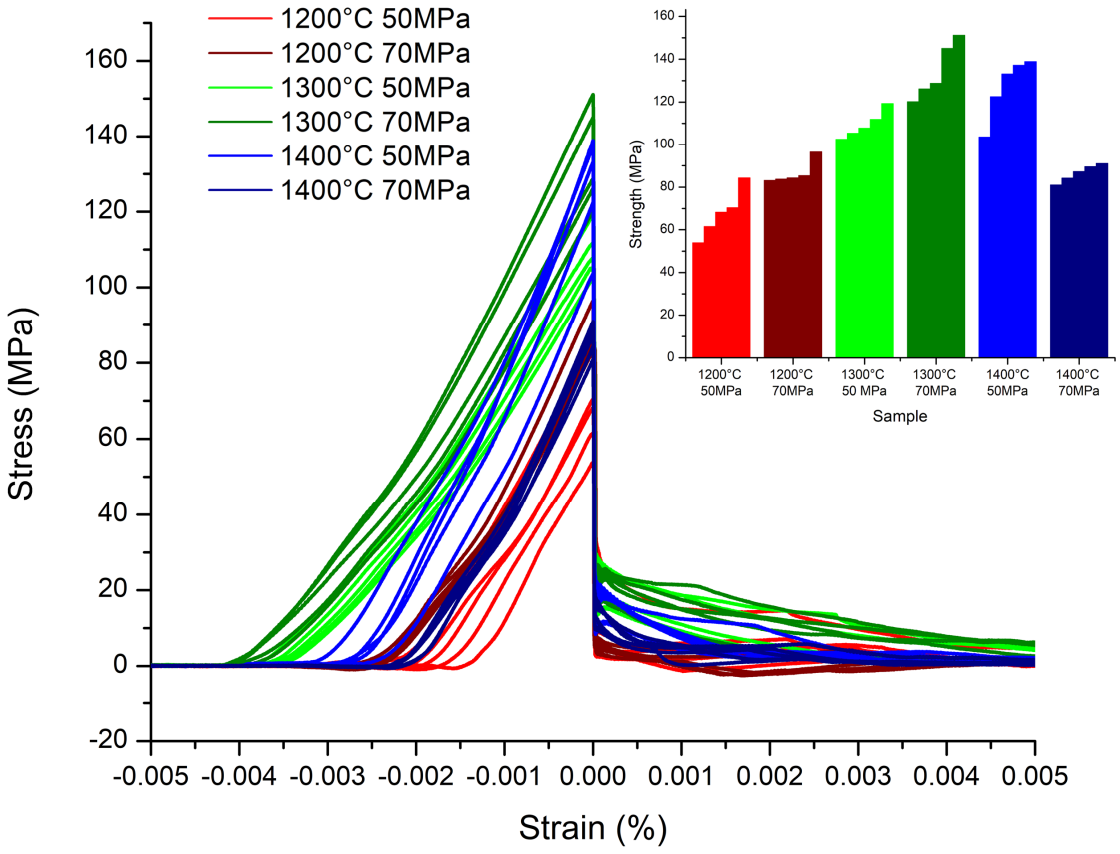


Figure 4.10 – Three-point bending stress-strain curves from samples sintered under different temperatures and pressures, with the strengths reported separately in the inset. The curves are plotted with the point of failure set at zero strain to visualize and quantify the accommodated strain.

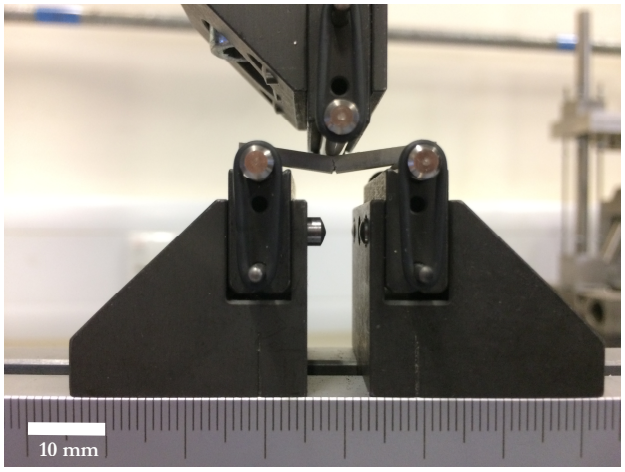


Figure 4.11 – Optical image of a three-point bend test of a nacre-like alumina beam, showing that the specimen stays suspended on the rollers of the bending rig after failing, which is highly uncharacteristic for monolithic ceramics.

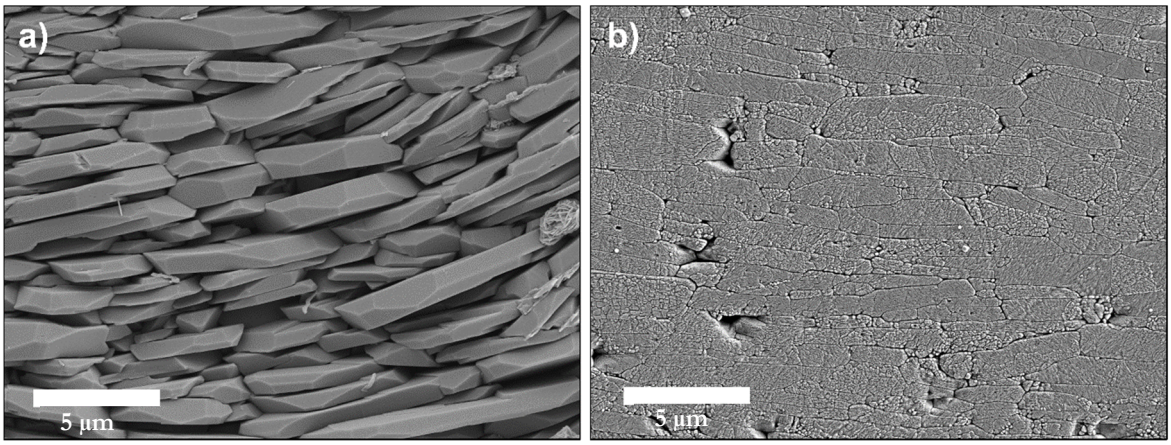


Figure 4.12 – SEM micrographs taken of the side of the beam sintered at 1300°C and 70MPa, showing enlarged platelet-like grains a) after cutting before polishing and thermal etching and b) after polishing and thermal etching. The platelet-like grains have differing sizes and their irregular shape displays 'waviness', promoting interlocking during crack propagation.

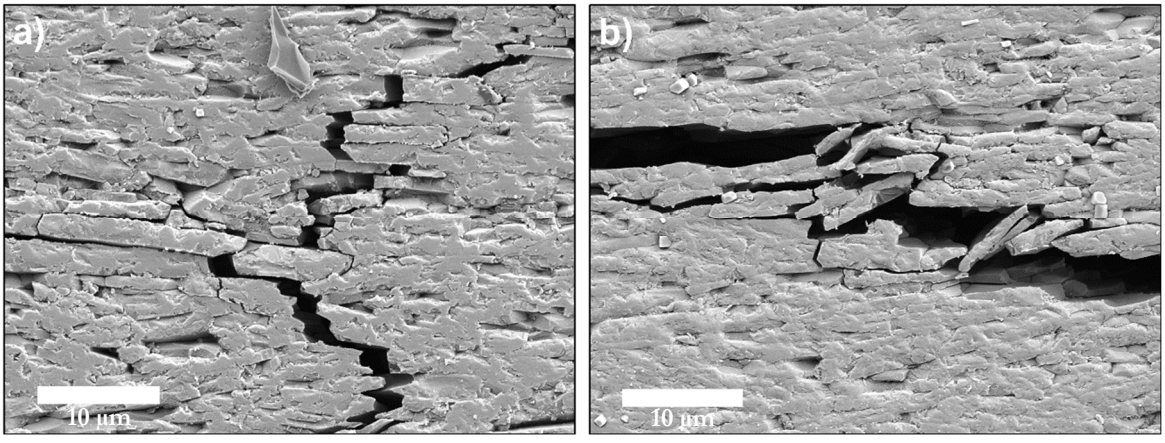


Figure 4.13 – SEM micrographs of a side-view of the beam after three-point bend testing, showing typical crack propagation a) across the sintered nacre-like alumina and b) along the sintered nacre-like alumina.

Samples sintered at 1200°C have comparatively low density and resulting low flexural strength values between 54-96MPa - the platelets compacted with minimal grain growth occurring, but also with minimal bonding. Sintering at 1300°C yielded a higher density material (Figure 4.3) with a wider grain-size distribution (Figure 4.6). The samples which were sintered at 1300°C have much higher flexural strength values, with the sample sintered at 70MPa exhibiting flexural strengths of 120-150MPa. These samples also possessed the greatest residual strength of up to 30MPa after the initial fracture event. The observed improved strength and residual strength are likely due to an increased bonding between platelets, which leads to increased friction during platelet-platelet sliding by having mineral connections between platelets[7,71,262], while at the same time maintaining relatively small platelet dimensions in a large fraction of the bulk.

Figure 4.12 shows that the formation of larger, more irregularly shaped platelets through grain growth also increases average platelet waviness[19] and platelet diameter resulting in a greater bridging and pull-out length. Figure 4.13 shows that these platelet-like grains promote crack deflection and bridging, causing interlocks during crack propagation which restrain the crack faces and toughen the material. The interlocks often cause the crack to branch resulting in a diffuse fracture. The platelet-platelet interlocking is further promoted by the fact that while the platelets are aligned, it is not uncommon for platelets to be slightly tilted with respect to one another. The existence of platelet-like grains with cracks all around them further demonstrates the interlocking behaviour.

Sintering at 1400 °C decreases the strength, which is attributed to the prevalent grain growth shown in Figure 4.5 and 4.6 – The platelet-character of the grains is diminished, which is detrimental for material strength[2]. It is good to note that for alumina platelets sintered at higher temperatures, it is possible to improve the flexural strength by modifying processing parameters such as the heating and cooling rates, dwell time and time of pressure application. These parameters can affect the plastic deformation of the platelets, grain growth, critical defect size and therefore the strength. For example in Chapter 3, platelet-like alumina

sintered using SPS at 1600 °C and 45 MPa exhibits a flexural strength of around ~180 MPa[263]. In addition, alumina platelets sintered with alumina nanoparticle additions and glass[35,249] sintered at temperatures above 1400 °C have shown to be able to yield alumina with a flexural strength around ~300 MPa[35,249]. It is very likely therefore that the processing can be further refined to yield higher strengths. However, for pure alumina specimens made from platelets, the nacre-like character of the alumina grains in materials sintered at temperatures above 1400 °C is drastically reduced due to grain growth, as shown in Figure 4.6. For pure nacre-like alumina examined here, the material sintered at 1300 °C and 70 MPa, which shows both small platelet-like grains and the highest flexural strength of all manufactured samples, was selected for dynamic testing.

4.3.3 Influence of nanoparticle inclusions

While the notion of surface asperities being a large contributor to surface friction in nacre has been largely discounted[19,56,69], recent works[35,249] show that it is possible to improve the

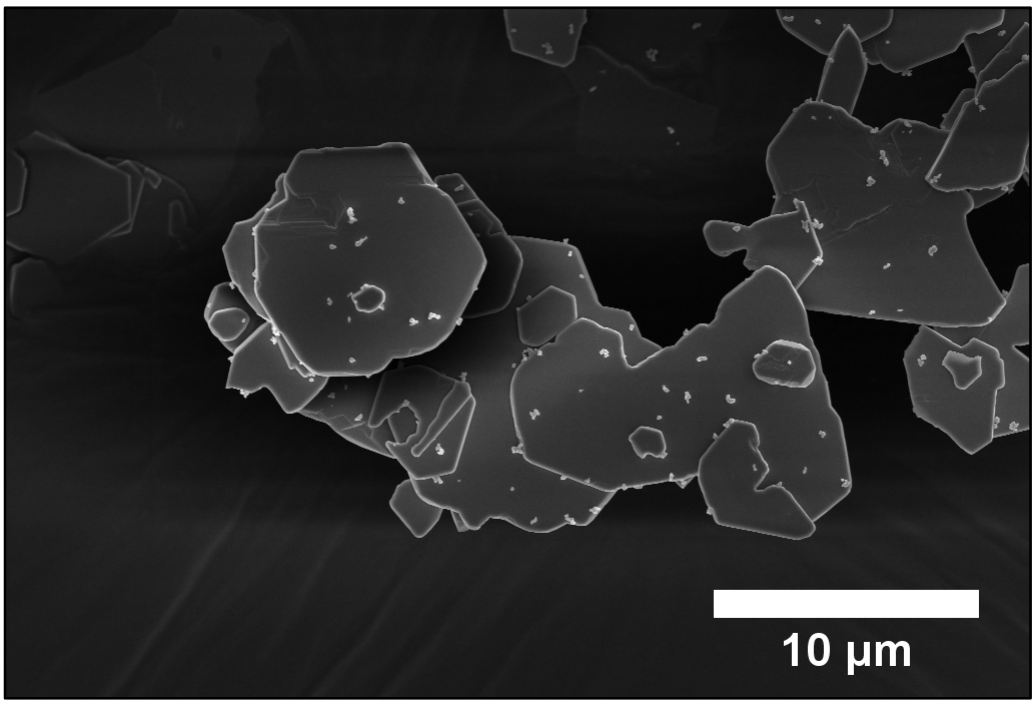


Figure 4.14 – SEM micrograph of an alumina powder mixed with 1 wt% 200 nm alumina nanoparticles, visualizing the coverage and dispersion of such nanoparticles.

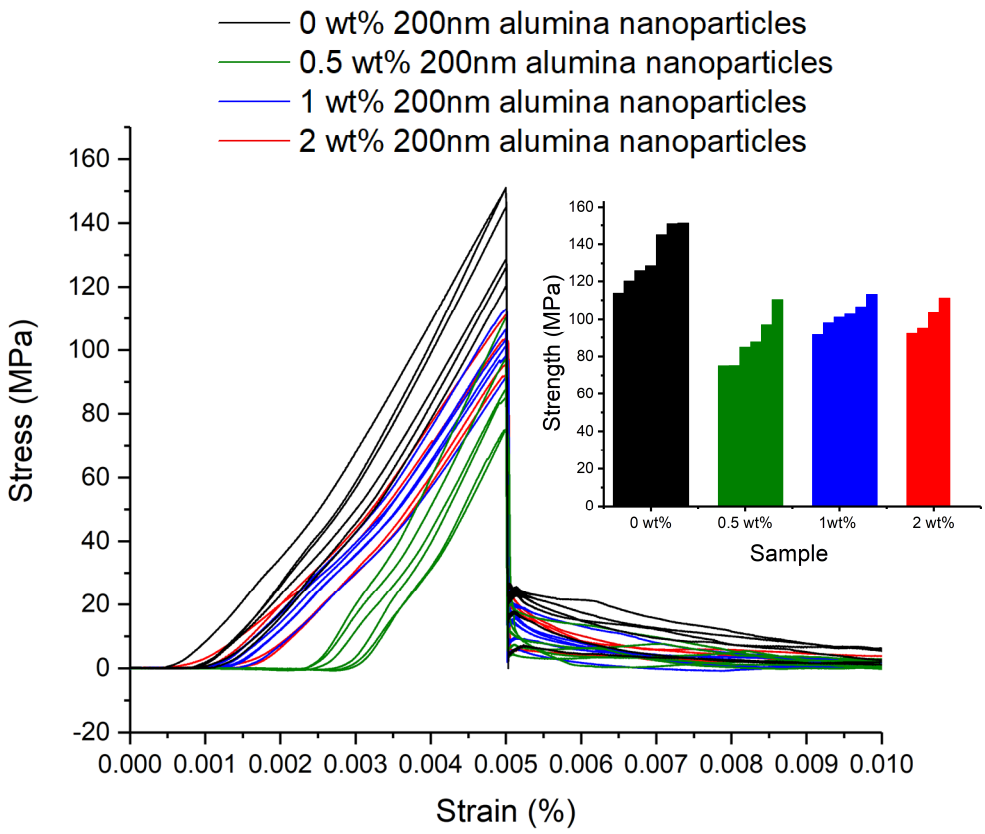


Figure 4.15 – Three-point bend test stress-strain curves of nacre-like alumina samples sintered with different amounts of incorporated nanoparticles, with the strengths reported separately in the inset. The data show that the nanoparticle incorporation diminishes strength without an increase in toughness.

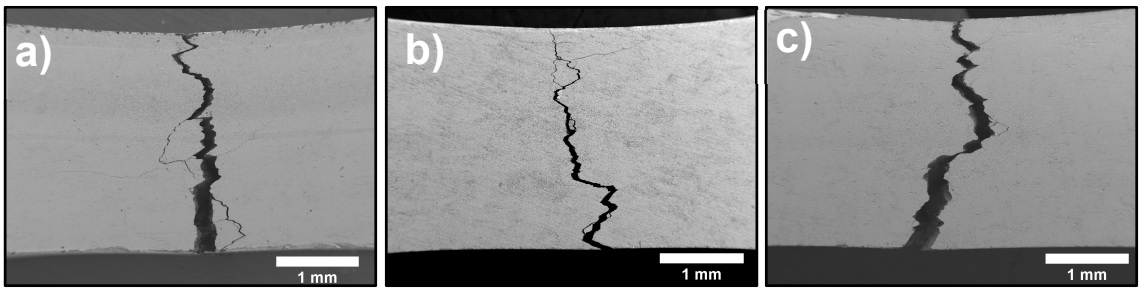


Figure 4.16 – SEM micrographs of nacre-like alumina composites made from alumina platelets and a) 0.5 wt% b) 1 wt% and c) 2 wt% 200 nm alumina nanoparticles.

flexural strength and still obtain significant R-curve behaviour by incorporating alumina and glass nanoparticles in an alumina platelet microstructure. Therefore, different weight percentages of 200nm alumina nanoparticles are here incorporated in the platelet-like structure (Figure 4.14). To incorporate alumina nanoparticles, Bouville *et al.*[35] use ball milling which is known to contaminate the powder[264] and most likely will break the platelets as well. Therefore, the nanoparticles are incorporated through sonication as used by Pelissari *et al.*[27]. The resulting powders were then sintered at 1300°C and 70MPa for 15 m, which are the conditions that give the best results for nacre-like alumina without any nanoparticles. While

the densities of these materials are slightly higher, increasing with nanoparticle content (for a 0.5wt%, 1wt% and 2wt% nanoparticle content respective densities of 98.8% 99.0% and 99.2% are measured), the bend tests in Figure 4.15 show that the material strength is not in the 300 MPa range as found by Bouville *et al.*[35] and Pelissari *et al.*[27]. In fact, the inclusion of nanoparticles reduces the strength of the material by about 30%. The mineral bridges created by the alumina nanoparticles may be restraining the sliding mechanism of the platelets, which reduces the strength of the material. In addition, the toughness of the material is affected as the stronger platelet-platelet interfaces lead to much less macroscopic crack deflection taking place, as shown by the crack patterns in Figure 4.16. As a result, the specimens fall apart more easily due to the lack of interlocking and thus also have less residual strength. The irreproducibility of the results in the literature can be due to the different processing methods which may affect the bridge size and formation during sintering, or the number and distribution of bridges for which the material response in bending may be very sensitive. Due to the strength deterioration observed here, alumina is used without nanoparticle inclusions for tests under dynamic loading and impact.

4.3.4 Mechanical response under dynamic loading

The material exhibiting the highest values of strength and strain to failure (i.e. sintered at 1300°C and 70MPa) was tested under dynamic loading conditions, alongside monolithic alumina, to explore the effect of the platelet-like grains on the high strain rate behaviour of the material.

Split-Hopkinson compression bar tests were carried out on three specimens for each of the two materials considered, nacre-like alumina and monolithic alumina, imposing the same loading conditions, which resulted in a strain-rate of the order of $500 \pm 100\ s^{-1}$. The results are summarised in the stress-strain curves reported in Figure 4.17.

The stress-strain curves of the monolithic alumina (black lines) show a typical brittle behaviour, with elastic deformation followed by sudden failure of the whole specimen.

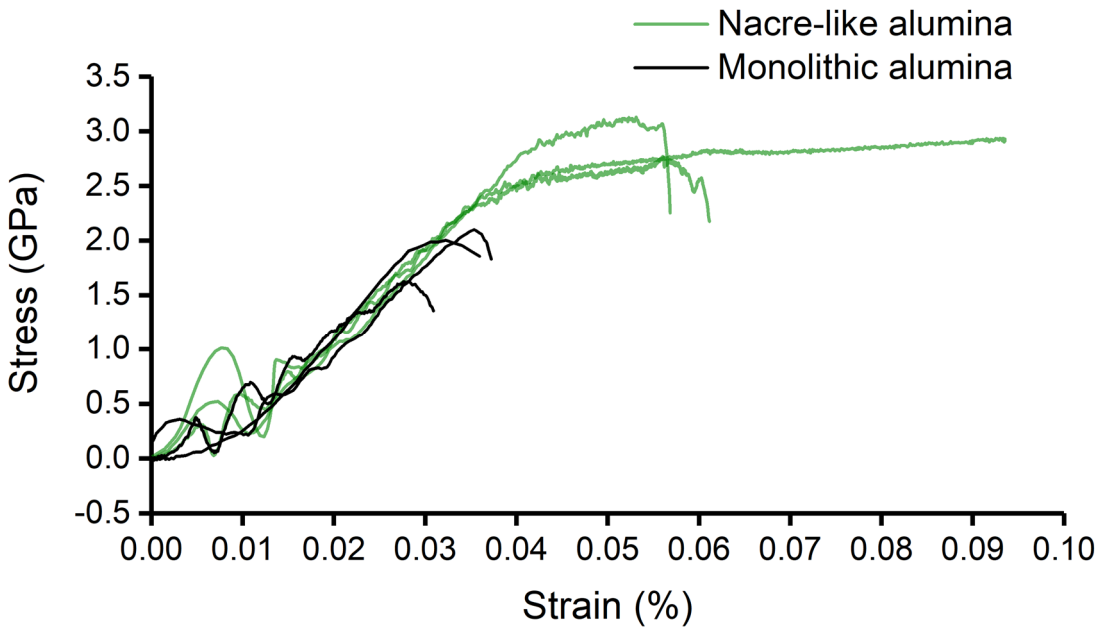


Figure 4.17 – Comparison of the mechanical behaviour of monolithic and nacre-like alumina under dynamic compression.

The stress-strain curves of the nacre-like alumina instead show a noticeably higher strength. Additionally, the final part of the stress-strain curves shows the ability of the nacre-type alumina to continue to carry load following the onset of damage before the complete failure of the material. In this test one of the specimens, despite developing internal cracks, survived the compression test without failing. This specimen is represented by the longest curve in Figure 4.17.

From these tests, it is evident that the presence of platelet-like grains increases the high-rate compressive strength with respect to the monolithic material significantly as well as providing an inelastic deformation plateau in lieu of the usual sudden brittle failure of monolithic alumina. This behaviour can be explained by the presence of the crack deflection and crack branching mechanisms seen in these materials.

Visual evidence of the behaviour described can be obtained from the high-speed camera recording presented in Figure 4.18, showing the different failure mechanisms. Whilst the monolithic alumina (top row) exhibits a uniform and brittle failure (sudden and complete failure of the specimens at the onset of damage), the nacre-like specimen (bottom row) shows

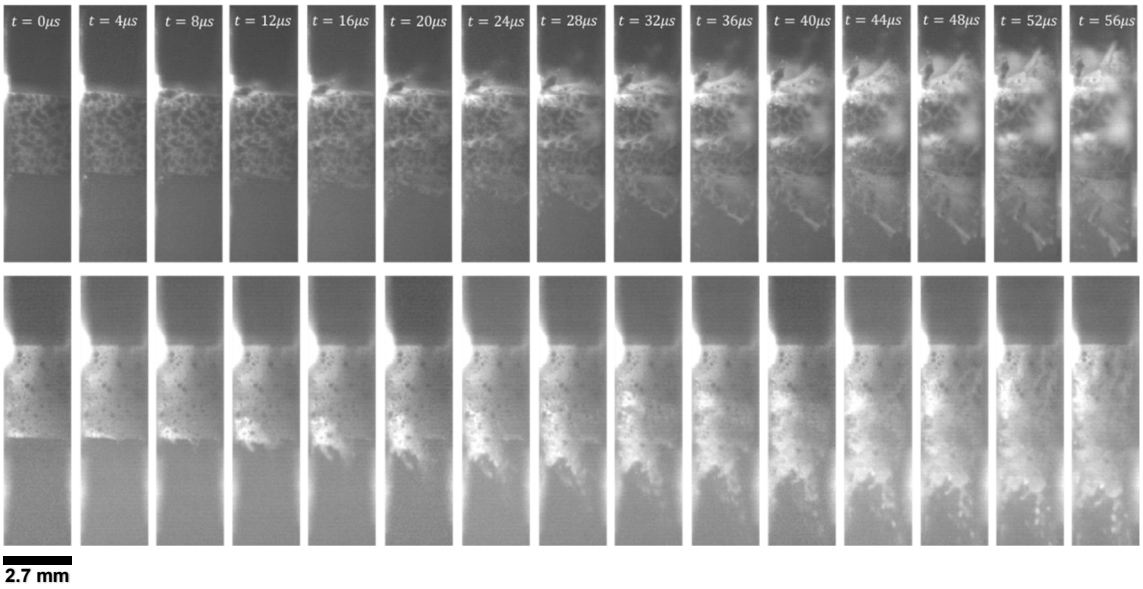


Figure 4.18 – Failure mechanisms of monolithic (top) and nacre-like (bottom) alumina under high strain rate compression.

a much more gradual failure, with the cracks initiating at the bottom of the specimen and spreading throughout the domain, thus delaying the occurrence of the final failure.

The measured stress-strain curves and the direct observation of the failure of the specimens, provide evidence of the occurrence of the crack deflection mechanism in the nacre-like alumina also during split-Hopkinson bar compression tests. The results of these tests show that nacre-like alumina has improved performance over monolithic alumina at high strain rates.

4.3.5 Mechanical response upon impact

To verify the effect of the crack-deflection mechanism observed for high-rate compression, the nacre-like alumina was also tested upon impact at different velocities. The results of the tests carried out on both monolithic and nacre-like alumina are reported in Table 4.1, showing a clear improvement in performance provided by the crack-deflection mechanism observed in the other tests presented. The presence of platelet-like grains makes the material capable of withstanding impact velocities substantially higher than monolithic alumina by absorbing the energy via the propagation of diffuse cracks within the domain. In contrast with monolithic or even armour-grade alumina materials where specimens have to be laterally constrained to prevent alumina from falling apart after impact[265], the nacre-like alumina

presented in this work is able to sustain extensive cracking without compromising the overall structural integrity of the specimen.

Figure 4.19 reports the visual comparison of the impact of a steel spherical projectile on the monolithic (top row) and nacre-like (bottom row) alumina, with impact velocities equal to 207 m/s and 204 m/s, respectively. The different energy absorption mechanisms leading to the contrasting performances of the materials can be clearly observed.

	Impact velocity [m/s]	Kinetic energy [J]	Post-mortem status
Monolithic alumina	136	1.05	Intact
	150	1.28	Broken
	179	1.82	Broken
	207	2.44	Broken
Nacre-like alumina	204	2.37	Diffuse cracks
	215	2.63	Diffuse cracks
	253	3.64	Diffuse cracks
	272	4.21	Diffuse cracks

Table 4.1 – An overview of the impact velocities, calculated kinetic energy of the projectile and resulting post-mortem visual analysis of specimens after impact-testing, showing a clear improvement in performance provided by the nacre-like alumina.

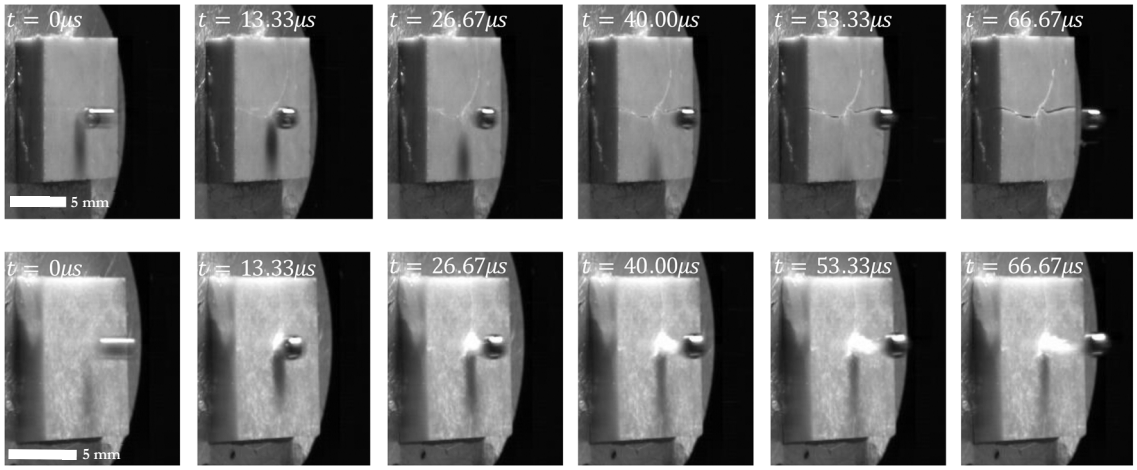


Figure 4.19 – Impact of a steel sphere against monolithic (top) and nacre-like (bottom) alumina targets measuring 12x12x2.7 mm.

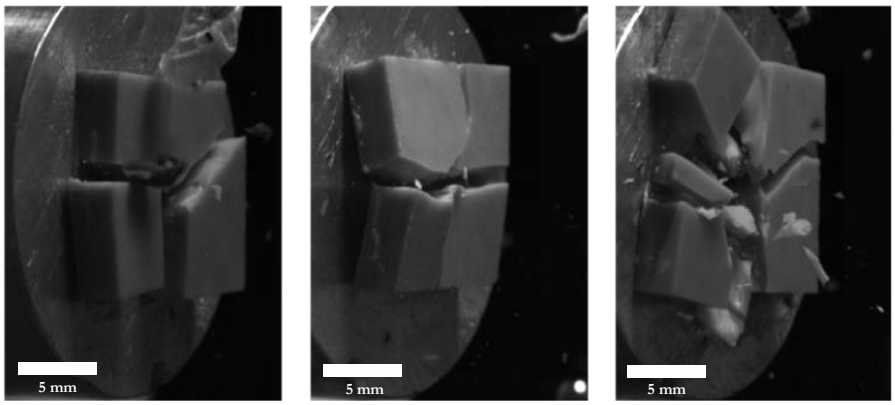


Figure 4.20 – Post-impact fragmentation of different monolithic alumina targets measuring 12x12x2.7 mm. (Compare the intact platelet-like alumina in Figure 4.21)

In the monolithic alumina four radial cracks propagate from the impact area, leading to the rapid and complete failure of the specimen. An example of the extent of the failure of the monolithic alumina specimens is given by the high-speed camera frames in Figure 4.20. The post-impact images show the extreme fragmentation of the target tiles.

The nacre-like alumina, on the contrary, remained intact with diffuse cracks visible in the structure after an impact of similar and higher kinetic energy (Table 4.1). The growth of a higher number of diffuse cracks radiating and branching from the impact area indicates a more uniform spread of the damage within the whole volume. Additionally, the projectile causes pulverisation of the target at the contact point (clearly visible in Figure 4.19) leading to the formation of an impact crater.

The profilometry and the 3D reconstruction of the impact zone, for the test on nacre-like alumina impacted at a velocity of 253 m/s, is reported in Figure 4.21. Analysis of the 3D reconstruction of the impact area shows the formation of a crater, measuring almost 0.15 mm in depth and 1.5 mm in diameter. The extension of the cracks propagating from the impact crater can be observed in the SEM images shown in Figure 4.22. The missing chip of material along the bottom of the crater (still visible in Figure 4.21) was lost during the preparation of the specimen (i.e. blowing off contaminants from the impact test using compressed air) prior to SEM. Additionally, the back face of the target also shows an extensive net of cracks propagating from the impact point. Despite the wide extent of the propagation of cracks, the specimen maintains its structural integrity. Maintaining structural

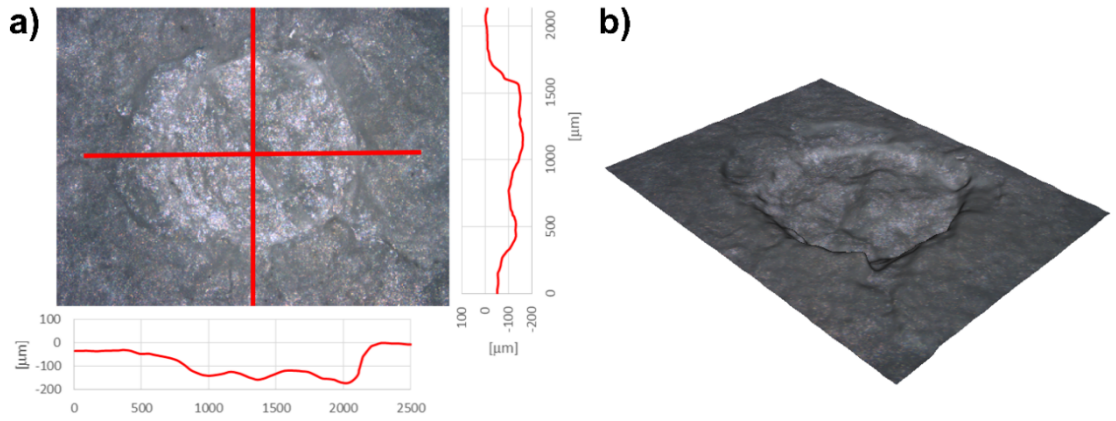


Figure 4.21 – a) Profilometry after impact on nacre-like alumina and b) 3D reconstruction of the impact crater (right).

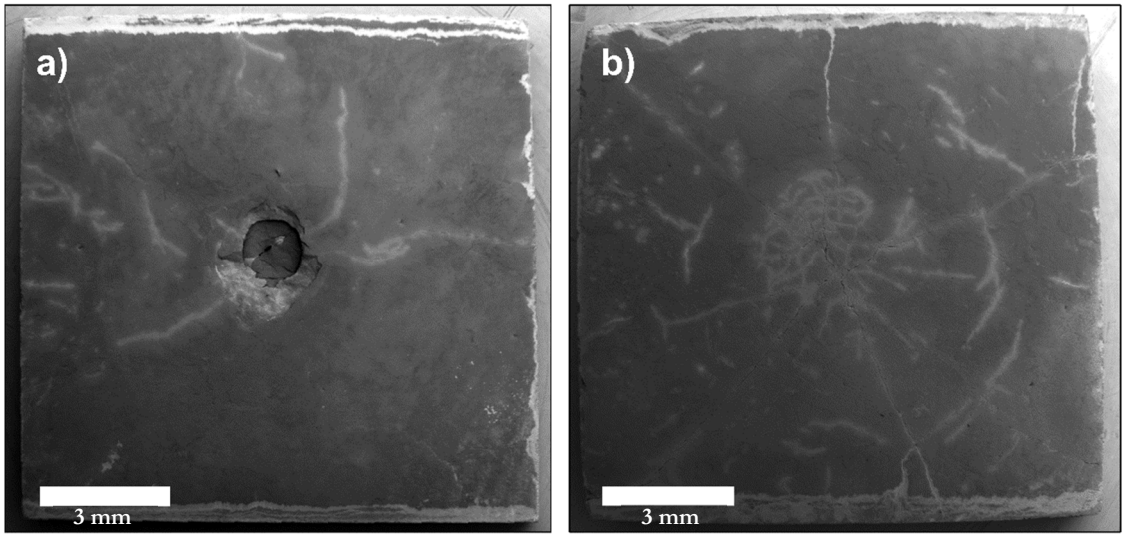


Figure 4.22 – SEM micrographs of a) the front and b) the back of the nacre-like alumina target, showing the net of radial cracks propagating from the impact point throughout the whole domain.

integrity after impact is an important feature for the multi-hit capability of the material; it has been shown that cracks in alumina ballistic armour have a negligible effect on performance as long as structural integrity is maintained[266].

A detail of the cracks developing along the back surface is presented in Figure 4.23, showing the presence of the deflection mechanism more clearly. The dispersion of kinetic energy through the deflection of cracks leads to the improvement in performance of nacre-like alumina over the monolithic material. It is also worth noticing that these materials are tested without confining them as is commonly done for ballistic tests, where confinement has been shown to dramatically increase compressive strength[267].

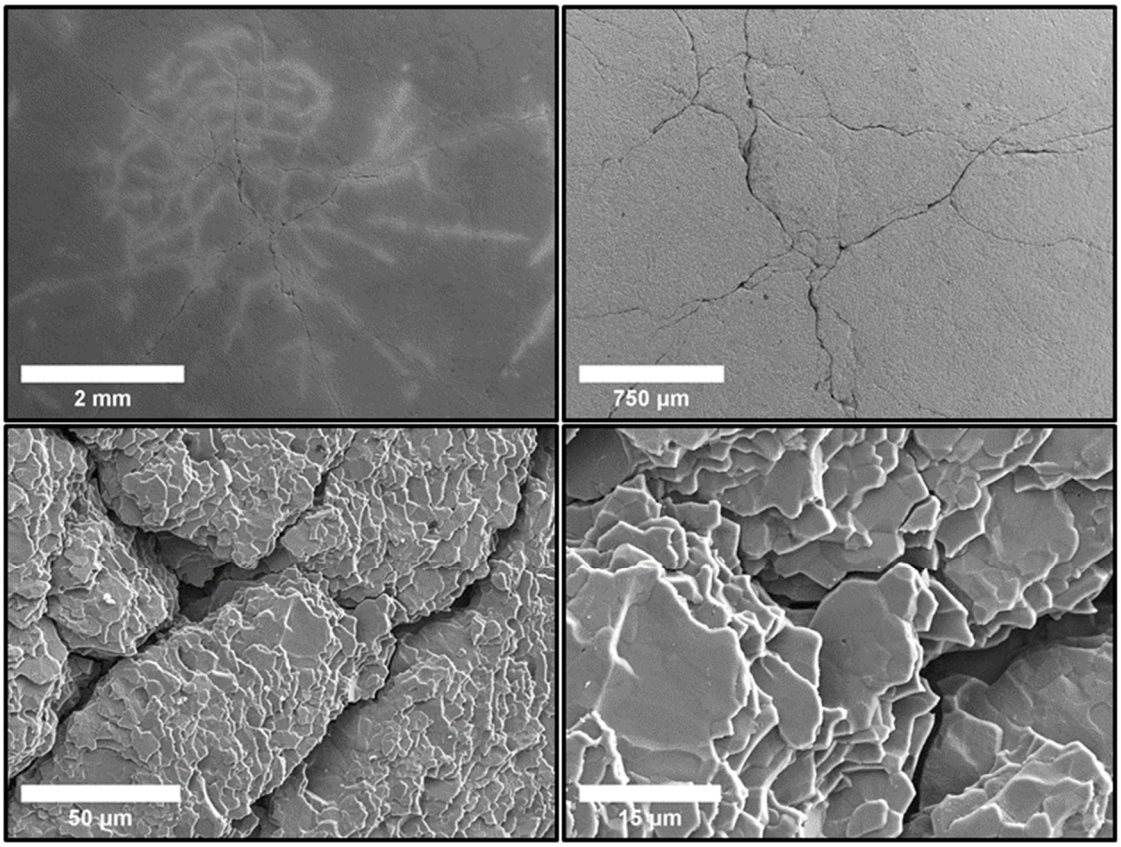


Figure 4.23 – SEM micrographs showing a zoom-in of the back-face cracks at the impact point.

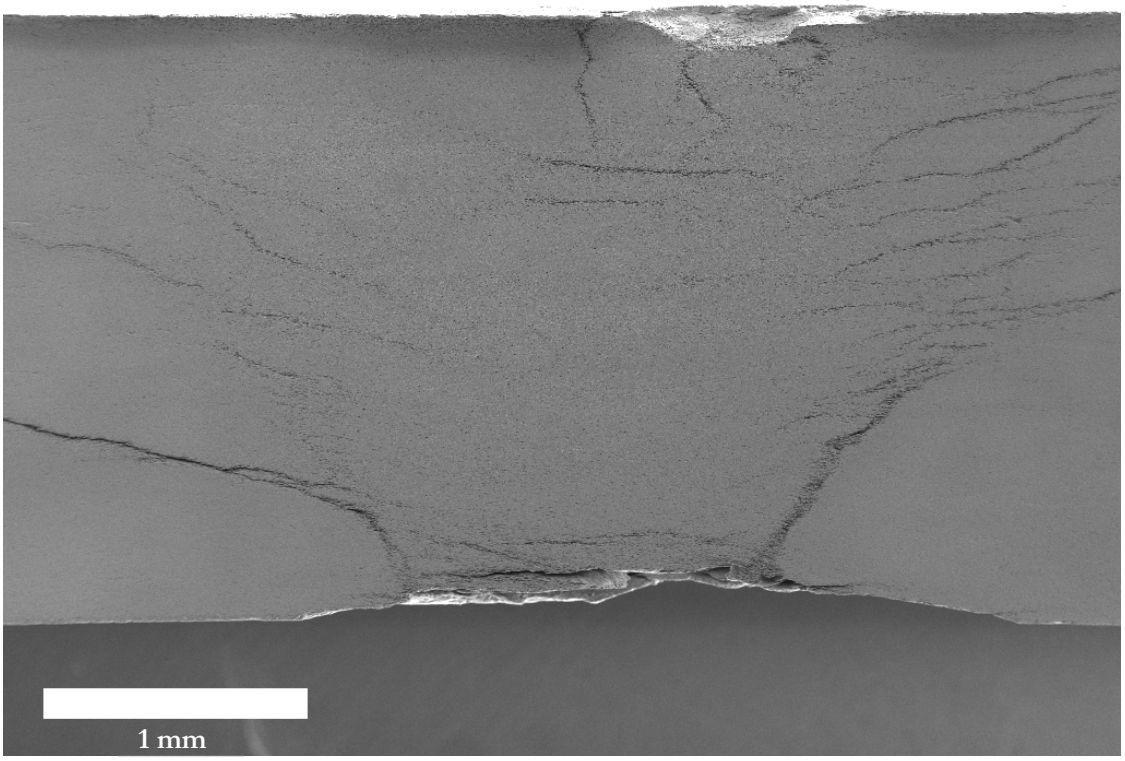


Figure 4.24 – SEM micrograph showing a cross-section of the impact crater (bottom of the image), revealing large outward crack deflection.

To visualize the deflection mechanism throughout the thickness of the impact specimen, a cross section at the impact crater is presented in Figure 4.24. Cracking is deflected and dispersed outward into the alumina. This is especially clear when considering the Hertzian cone-crack which is deflected into multiple lateral cracks which propagate along the platelet-like grains.

4.4 Conclusions

Micron-sized alumina platelet powders have been used to generate nacre-like alumina with different grain sizes. For microstructures in which grain growth has taken place, the grains still have anisotropic (platelet-like) shapes due to the templating effect of the starting platelet powder. The mechanical behaviour of nacre-like alumina manufactured at different temperatures and pressures has been correlated to their microstructures. Regardless of sintering temperature and resulting grain growth, these materials show crack deflection mechanisms and residual strength after failure independent of sintering temperature. It is shown that nacre-like aligned platelet-grains can be maintained while achieving a dense ceramic by using SPS and that this results in specimens with radically different fracture behaviour. The main feature of these materials is that due to interlocking platelets and crack deflection, the material stays intact with internal cracking instead of breaking destructively as monolithic alumina does. This is especially evident in impact testing of these materials, where even after a four times kinetic energy-increase of the projectile, the specimen did not fail, and only diffuse cracks were observed. This reflects a tendency for cracks to deflect along a direction parallel to the platelets. When these materials were tested in dynamic loading conditions, they show significant improvement over monolithic alumina both in terms of strength and accommodated strain.

Chapter 5 – Nacreous MWCNT/alumina composites

5.1 Introduction

This chapter describes the mechanical properties of composites that combine a nacreous bioinspired ceramic microstructure with CNT reinforcement using different manufacturing and dispersion methods.

5.1.1 MWCNT/alumina composite materials

Several researchers have combined MWCNTs with alumina to create a reinforced ceramic; Sarkar *et al.*[268] fabricated MWCNT/Al_2O_3 composites by wet-mixing and pressure-less sintering (PLS) in argon at 1700 °C. Sikder *et al.*[269] use spark plasma sintering (SPS) for the same powders and find that dense composites can be fabricated at a much lower temperature of 1300 °C. For PLS studies, composites containing up to 0.6 vol.% MWCNTs were 97-99% dense but beyond that concentration, sintered samples were more porous (<92%) while for SPS studies, composites showed high densities (>97.5%) even at 2.4 vol% MWCNTs[268,269]. However, Ghobadi et al.[270] create composites with similar density using PLS at 1600 °C (98.8% for a 2vol% MWCNT loading) indicating that both methods are feasible to create dense MWCNT/alumina composite materials, with SPS being more time and energy efficient.

In SPS, SWCNTs have been shown to be prone to breakdown when used to create SWCNT/alumina composites[100,271]. As a result, SWCNTs are not very effective to reinforce alumina in SPS[272]. The more easily and cheaply produced MWCNTs are therefore the preferred type of CNT to reinforce alumina. In a large number of studies[121,273,274] a superior

fracture toughness compared to pure alumina is reported when MWCNTs are incorporated. However, in most studies, fracture toughness (K_{Ic}) values are recorded through indentation which has been regarded to be an inadequate method to record fracture toughness in ceramics as mentioned in Section 1.3.1[44,45]. The work by Xia *et al.*[274] is however worth noting as they provide convincing evidence for the toughening effect of CNTs in a ceramic matrix. Their SEM data clearly shows crack deflection, crack bridging and nanotube pull-out toughening mechanisms in CNT/alumina composites.

As discussed in 1.5.4., dispersion of MWCNTs remains one of the main challenges. For example, when using ultrasonication to disperse MWCNTs in alumina, concentrations <0.6 vol% showed MWCNTs that successfully bridge alumina grains in the microstructure but at higher concentrations, agglomeration of MWCNTs and entrapment of MWCNT clusters are observed[268,269].

5.1.2 Acid treated MWCNTs in alumina matrices

Acid treatment of MWCNTs is a popular method to improve dispersion in the alumina matrix. Acid treated MWCNTs are of particular interest in composite manufacturing as acid treatments can modify the MWCNT surface to be more hydrophilic by introducing carboxylic acid groups on the surface[275]. This significantly improves dispersibility of MWCNTs.

Yamamoto *et al.*[119] show that compared to the same amount of ultrasonicated MWCNTs, acid treated MWCNTs result in much higher bending strength and toughness values in MWCNT-alumina composites. In their work they hypothesise that while acid treatments introduce defects in the MWCNTs, as is observed in TEM[119], this increases frictional resistance through the mechanical interlocks induced by the chemically modified MWCNTs, which can be responsible for the increased strength and toughness. This is however unlikely as data on individual MWCNTs indicate that defects weaken the structure of the MWCNT[111–113]. The observed increase in strength is likely because acid treated CNTs are better dispersed:

from their data it can be observed that the final density is less (by a few %) for all composites with pristine MWCNT's compared to the acid-treated ones with the same CNT loading. it is therefore likely that the dispersion of pristine MWCNTs was much poorer. A homogeneous dispersion of MWCNTs suppresses the degradation of the density of the composite, increases the amount of crack-bridging effects and therefore leads to an improvement in the observed mechanical properties[276,277].

Application of well-dispersed, acid treated MWCNTs in composites has been demonstrated by several researchers using glass matrices at the University of Oxford[278] and Tohoku university[279]. The latter group also made MWCNT-composites using other ceramic matrices[280] like ZrB_2[281] and alumina[119,282]. A very good dispersion of MWCNTs is achieved in the liquid phase through coagulation of MWCNTs with ceramic nanoparticles. In the MWCNT/alumina composites made from these coagulated powders using SPS, several known fracture toughening mechanisms have been demonstrated[282]. Yamamoto *et al.*[119,277,283] find that low amounts of acid-treated MWCNTs (<1 vol%) benefit the mechanical properties[119] for which they report very high bending strengths of 689.6 ± 29.1 MPa (Note that they measure the bending strength of pure alumina to be ~500 MPa). Greater amounts (>1 vol%) were seen to decrease strength[119] as well as density[277].

SENB fracture toughness measurements have been done by Estili *et al.*[284] on alumina composites with acid treated MWCNTs decorated with alumina nanoparticles[282] , densified in SPS at 1300 °C[285]. They show that for these materials, toughness increases up to a MWCNT loading of 10 vol%, as does flexural strength (6.71 MPa$\sqrt{m^2}$ and 483 MPa respectively). They show that further increases in MWCNT loading decreased both strength and toughness. Kasperski *et al.*[286] also use acid treated MWCNTs to reinforce alumina in SPS (between 3-4 vol%) and conclude the opposite: fracture toughness decreases with only a marginal strength increase for certain MWCNT-types. It is notable that the latter study gives error values of 20-30% while Estili *et al.*[284] do not, but a large spread in strength and toughness

values of 20-30% can be noticed in their data as well. The difference in perspective of Kasperski *et al.*[271] is likely due to the fairly high strength and toughness values measured for pure alumina; 413 ± 84 MPa and 5.4 ± 1.4 MPa$\sqrt{m^2}$ respectively. The differences between studies may lie in the quality of the MWCNT dispersion, which is dependent on the acid treatment procedure. Wang *et al.*[287] show that for 2 hours of acid treatment at different temperatures, strength and toughness in the final composite can differ by more than 100%. In their extensive study, they find that while most MWCNT reinforcements decrease strength and toughness, some composites with 5vol% MWCNT show improvements over monolithic alumina.

Generally, In studies of MWCNT/alumina composites, bending strength is reported to improve by 6-40% compared to monolithic alumina[121]. This was primarily achieved by matrix grain refinement by MWCNTs and proper interface formation that ensured effective load sharing between matrix and filler. The work of Zhu et al.[288] stands out from other studies as they measure a 67% increase in bending strength (The final composite had a bending strength above 500MPa compared to 300MPa for pure alumina) by supporting zirconia nanoparticles on the carbon nanotubes, which improve the interaction between CNTs and alumina matrix and show to enhance dispersion of CNTs by separating CNT bundles[288].

While all these studies use non-bioinspired alumina, they underline the potential of MWCNT reinforcement in alumina matrices and the importance of a homogeneous MWCNT dispersion.

5.2 Materials and methods

Freeze cast alumina scaffolds and alumina platelet powders, combined with a MWCNT phase, were densified into MWCNT/alumina composites that mimic the microstructure of nacre. Freeze cast scaffolds were infiltrated, and alumina platelets were coated with a MWCNT phase using CVD as described in Chapter 3. The alumina platelets were

investigated further and combined with a MWCNT phase using a range of various other MWCNT coating techniques. The combined material was then densified using FAST/SPS at different temperatures. The resulting alumina/MWCNT composites were polished and cut into three-point bend test beams to test their mechanical properties. These mechanical tests are supported by SEM observations and sintering data to both optimize and understand these novel bioinspired composite materials.

5.2.1 MWCNT dispersion method

For pure ceramic samples, 15g (±1%) of monocrystalline[261] α-alumina platelets in powder form (RonaFlair® White Sapphire, MERCK, median diameter 8.4 μm, thickness 0.2-0.5 μm) was used. For alumina platelet/MWCNT composites, 4-15g of alumina platelets were used per sample. The MWCNT dispersion methods used are detailed below;

Dispersion through Sonication

Nanocyl7000 MWCNTs were suspended in either acetone, chloroform or N,N-Dimethylformamide (DMF) and sonicated in a sonic bath for 60 minutes. After sonication the platelets were added, and the mixture was sonicated for an additional 15 minutes. The platelet/MWCNT mixture was then left to dry in a fume hood. (the mixture with DMF took more than a week before a dry powder was obtained). The dry powders where then manually stirred with a thin spatula until a soft homogeneous powder was obtained.

Dispersion through acid treatment

Nanocyl7000 MWCNTS are dispersed in water by chemical oxidation, following an acid treatment procedure described by Xiao *et al.*[289]. 3g of MWCNTs was placed in a 3-neck round bottom flask fitted with a water-cooled refluxing condenser, a teflon coated thermocouple, and a magnetic stir bar. 200ml of 70% nitric acid (HNO_3) was added and the mixture was stirred and heated to 80°C using a PID controlled heating mantle. The acid reflux reaction was maintained for 18h; The reaction was then stopped as Xiao *et al.*[289] found that MWCNTs

are significantly shortened and the yield is significantly reduced at longer refluxing times. Immediately after cooling, the reaction mixture was washed using the following steps:

1) 7x 5 minutes of centrifugation at 4000 RPM, re-dispersing in H_2O
2) A further 2x 5 minutes of centrifugation at 4600 RPM, re-dispersing in H_2O/Ethanol (1:1 ratio)
3) A further 2x 5 minutes of centrifugation at 4600 RPM, re-dispersing in Ethanol.
4) A further 2x 5 minutes of centrifugation at 4000 RPM, re-dispersing in H_2O

After the washing procedure a small sample vial was taken out of the batch and weighed before and after drying, after which a MWCNT concentration could be determined to accurately calculate the MWCNT content in the final composite.

Alumina platelets were dispersed in water using BASF *Dispex*® A40 (25 mg). the mixture was gently shaken and placed in a sonic bath for 5 minutes, after which the acid treated MWCNTs and dispersed alumina platelets were combined in a plastic container. This mixture was then shaken and sonicated for another 5 minutes after which it was dropped in liquid nitrogen to yield a light powder after freeze drying.

Dispersion through powder mixing

Nanocyl7000 MWCNTs were crushed with a mortar and pestle to get rid of large chunks, after which the MWCNTs were mixed in their dry form with alumina platelets and shaken vigorously by hand and a vortex mixer to disperse the powders.

Dispersion through chemical vapour deposition

An optimized chemical vapour deposition (CVD) procedure as detailed in Chapter 3 was used to coat the alumina with MWCNTs in-situ. For freeze-cast alumina scaffolds, a modified RCA treatment as outlined in section 3.2.1 was done before infiltration, after which the scaffold was infiltrated with FSP iron oxide nanoparticles. The sample was then annealed in a 21mm quartz tube in argon for 10 minutes, after which a precursor gas mixture was led through the quartz tube for 30 minutes at 0.625 slm

(0.6 slm Ar and 0.025 slm C_2H_2). When using alumina platelets, the FSP iron oxide nanoparticle-coated powder (Method B in Section 3.2.2) of alumina platelets was annealed in a 28mm quartz tube in argon for 60 minutes, after which a precursor gas mixture was led through the quartz tube for 10 minutes at 1.04 slm (0.7 slm Ar, 0.3 slm H_2, and 0.04 slm C_2H_2). To generate larger samples, this procedure was repeated multiple times until enough material was obtained.

Dispersion through high shear mixing

A GM laboratory high shear mixer model 'A' by Joshua Greaves & Sons was used to disperse Nanocyl7000 MWCNTs. The shear mixer was first cleaned with ethanol and run at 6000 rpm for 15 minutes the clean the stator and left to dry. Then, 600 ml of type II H_2O (<50 ppb organic carbon) was mixed with 6.775 g Nanocyl7000 MWCNTs. Due to the hydrophobic nature of The MWCNTs, they float on the surface, so the solution was gently stirred with a spatula until a suspension was formed. The solution was then mixed for 7 hours. During this time, the MWCNTs are forced through small holes of the shear stator and subjected to an intense shearing action, dispersing them. The dispersed MWCNTs were then added to a suspension of 9.0 g alumina platelets which were dispersed in 20 ml water using BASF *Dispex*® A40 (25 mg). The mixture was then shaken by hand and placed in a sonic bath for 6 minutes to ensure dispersion without affecting the platelets or MWCNTs significantly. The pH of this solution was 8.2. In one case, the pH of the dispersion was modified to 0.94 with 600mg HCL (32%). The mixture was then frozen to prevent phase segregation and freeze dried to yield the MWCNT coated alumina power.

Dispersion through dry mixing a freeze dried MWCNT aerogel.

A centrifuge tube with 0.25M NaOH aqueous suspension was prepared, to help remove the catalytic support, amorphous carbon, and the catalyst metal particles during sonication without damaging the sidewalls[290]. Then 2.3 wt% (of the total liquid) MWCNTs (Nanocyl7000) was added to this solution. The suspension was then exposed to an ultrasonic

horn for 15 seconds, after which the suspension was shaken to account for any inhomogeneities in the ultrasonic field. This was repeated 10 more times until the suspension was extremely viscous. Immediately afterwards, the centrifuge tube was deposited into liquid nitrogen until the volume was completely frozen. The ice was then sublimed over a course of 48 hours, leaving a very lightweight freestanding MWCNT aerogel. The aerogel was easily broken up and mixed with alumina platelets in dry form to generate a 3.8wt% MWCNT powder. The powder was vigorously shaken by hand and a vortex mixer until homogeneity was achieved.

For samples sintered at 1300°C, 300 mesh crystalline graphite powder from Alfa Aesar (99% pure) was used to promote crack branching which was mixed with alumina platelets in dry for using a vortex mixer for 30 minutes. For samples sintered at 1500°C, 600g TypeII water was shear mixed at 6000 RPM for 3 minutes with 0.6g sodium dodecyl benzyl sulphonate (SDBS, a common anionic surfactant) to aid exfoliation. Then 30g of graphite powder with >85% of graphite flakes having a 44 μm diameter (Easy Composites Ltd.) was hand mixed into the solution until all graphite was in suspension. The suspension was then shear mixed for 3 hours using an emulsifying stator. To have a good comparison with the MWCNT aerogel, the sediment was freeze-casted into a powder which was mixed with alumina platelets in dry form to generate a 5.3wt% graphite powder, representing an equivalent loading in volume% to the 3.8wt% MWCNT composite.

5.2.2 Glass phase coating method

To create borosilicate glass, a sol-gel method adapted from the doctoral thesis of Bryan Tsu-Te-Chu[291] was used. Tetraethyl orthosilicate (TEOS, Sigma Aldrich) and Trimethyl borate (TMB, Sigma Aldrich) were used as precursors. The precursors were dissolved in steps; 38 ml TEOS was mixed with 38 ml ethanol and 3.8 ml distilled water and 0.5ml hydrochloric acid (37%). The resulting mixture was sonicated for 5 minutes, until the solution was a clear colourless liquid. Then 5.4 ml TMB (to have ~12.5% B_2O_2 in the final product) was added

after which another 5 minute sonication step followed. This solution was stored and separately, 15 g of alumina platelets were dispersed in TypeII water using Dispex (38 mg in 40 ml) and the pH was adjusted to better disperse the platelets using ammonium hydroxide. The amount of sol needed to create a 1-6 wt% coating was then calculated using the percentage of TEOS/TMB in the sol mixture and the densities of TEOS (0.933 g/ml) and TMB (0.932 g/ml). The TEOS/TMB mixture was then added to the alumina platelet suspension and the solution was sonicated for 15 minutes in a sonic bath and freeze dried.

To create a glass phase in between the platelets, LUDOX HS-40 colloidal silica was used, which has 40 wt% 12 nm silica particles in water with 0.4 wt% sodium to stabilize the suspension (which translates to 1wt% of the solid silica content after freeze drying). 2.9 alumina wt% silica nanoparticles and 3.0 alumina wt% TMDAR 200 nm alumina nanoparticles were mixed with dispex A40 as a dispersant and 0.66 alumina wt% Carbopol 2691 as a rheology modifier. The resulting mixture was sonicated for 10 minutes in a sonic bath after which the alumina platelets were added, and the mixture was shaken and sonicated for another 5 minutes. This solution was then mixed in a vortex mixer and immediately afterwards dropped in liquid nitrogen (in a plastic centrifuge tube). The resulting powder (after freeze drying) was directly used in SPS at 1600°C which according to the eutectic phase diagram should yield liquid phase sintering, delaying the sintering of alumina as described in Bouville *et al.*[35]

5.2.3 Sintering method

FAST/SPS has been done at both Queen Mary University of London in collaboration with Dr. Harshit Porwal and at the University of Oxford. Freeze-cast MWCNT-infiltrated composites (pre-pressed at 0.2 ton on a 30 mm die), CVD-MWCNT-coated alumina platelets, dry mixed alumina platelets with Nanocyl 7000 MWCNTs and one sample of freeze-dried MWCNTs dry mixed with alumina platelets sintered at 1800 °C (all pre-pressed at 1 ton on a 30 mm die) were sintered at Queen Mary using a HPD25/1 sintering press

(FCT, Germany) at 1500, 1600 and 1800 °C. The samples were loaded in a graphite die measuring 30 mm in diameter. The freeze casted scaffolds were packed with 400 nm alumina particles (AES 11c, Sumitomo, Japan). After calibrating the voltage and current values for each sample type to ensure stable temperature control, the following procedure was started:

1. 450-1200 °C, 7 MPa (SPS minimum Pressure), heating rate: 200 °C/min
2. 1200-[Sintering temperature], 7-45 MPa, heating rate: 100 °C/min
3. [Sintering temperature], 45 MPa, dwell time: 5 min
4. [Sintering temperature]-1200 °C, 45-7 MPa, cooling rate: 100 °C/min
5. 1200-[Room temperature], 7 MPa, cooling rate 100 °C/min

The exact same parameters were used to sinter a control sample consisting of only pure alumina platelets. When a sintering temperature of 1800 °C was used, a slower heating rate was used from 1200 °C onwards of 20 °C/min.

For all other composites, FAST/SPS was done in Oxford using a FSP507 Fast Sintering Press manufactured by Dr Fritsch, Germany. For these samples the graphite die size was slightly larger, with an inner diameter of 40 mm and outer diameter of 80 mm. To protect the die and punches, the inside of the die and punches were lined with graphite paper (GEEGRAF flexible graphite foil, Gee Graphite, later SIGRAFLEX Z grade flexible graphite foil, SGL carbon). The sample was first pre-pressed using a hydraulic press to 15.5 MPa and then densified using the field assisted sintering technique at temperatures at 1300°C and 1500°C in vacuum (0.3 mbar) with a carbon felt insulation around the die. The temperature was measured at the wall of the die using a pyrometer. The dwell time was 5-15 min, with a heating rate of 100 °C/min. The pressure was increased linearly to 70 MPa (maximum pressure for an intact graphite die) during heating and maintained at those levels during the entire dwell time. After the sintering process, the sample was cooled naturally without applied pressure to the die. The surface of the disks was then ground to smooth the edges and remove residual graphite paper, and one surface of each disk was polished using

diamond impregnated lapping pads and grinding wheels going down to a particle size of 1 μm.

5.2.4 Density measurements

To determine the density and porosity of a sample, Archimedes' principle was applied following the ISO2738 standard method. The ISO2738 standard is originally meant for porous metals and proposes oil as the impregnation fluid. This is adapted for use in ceramics by using deionised water, which is more easily removed after measurement[292]. The specimen is boiled in water, which decreases the surface tension by 20%[293]. During boiling, the air in the pores and channels expands and is partially replaced by water. While cooling the sample submerged in water, the remaining air in the pores contracts, creating negative pressure ('vacuum') that effectively aids impregnation of the specimen[294].

According to Archimedes[295], an object immersed in a fluid (a liquid or a gas), will have an apparent weight less than its real weight equal to the weight of the fluid it displaces. This is also known as the principle of buoyancy. Since the balances used respond to weight but are calibrated in mass units, the principle applies to mass through the linear relation $\boldsymbol{w = m * g}$ and Archimedes' principle may be rewritten as: $\boldsymbol{m_a = m_r - m_f}$ where $\boldsymbol{m_a}$ is the apparent mass while the specimen is immersed in the fluid, $\boldsymbol{m_r}$ is the 'real' mass in air and $\boldsymbol{m_f}$ is the mass of the displaced fluid. Putting this principle into practice, the specimen is weighed:

$\boldsymbol{M_1}$ = Dry mass of a porous specimen

$\boldsymbol{M_2}$ = Apparent mass of the specimen while fully impregnated and immersed in the impregnation fluid.

The total (apparent solid) volume $\boldsymbol{V_t}$ and bulk density $\boldsymbol{\rho_b}$ (including pores) are determined with[296]:

(19) $$V_t = \frac{M_1 - M_2}{\rho_f} \qquad \rho_b = \frac{M_1}{M_1 - M_2} * \rho_f = \frac{M_1}{V_t}$$

With $\boldsymbol{\rho_f}$ the fluid density. The total porosity is then calculated by dividing the bulk density $\boldsymbol{\rho_b}$ by the theoretical density.

5.2.5 Characterisation

Sintered and polished disks were cut into rectangular beams using a diamond saw following the 'Standard Test Method for Flexural Strength of Advanced Ceramics at Ambient Temperature' (ASTM C1161-13). The width of the beams was adjusted depending on the height of the ceramic disk. A Shimadzu loading frame with a 5 kN load cell was set-up with a three-point bend jig with a 20 mm span between bottom rollers, and the beams were loaded in the direction perpendicular to the platelets with a stroke speed of 0.5 mm/min. The resulting force-deflection curves were then converted to stress-strain curves using standard formulae outlined in ASTM C1161-13. For work of fracture (WoF) calculations, the area under curves showing graceful failure (i.e. unnotched beams showing no fast fracture, as well as notched beams) was divided by two times the cross-sectional area of the fracture beam. Single edge V-notched beam (SEVNB) tests were done with normalized crack lengths a/W between 0.35-0.6 with 'a' the crack length and 'W' the width of the beam. A razorblade cutter was used with 6 μm diamond paste until a sufficiently deep notch was cut. Then 1 μm paste was used to sharpen the notch. K_{Ic} values were calculated using ASTM E1820-11. After failure, the tested beams were coated with 3-15 nm platinum and carefully transferred to a Merlin (Zeiss) SEM with Energy dispersive X-ray (EDX) analysis capability to image the fractured region. Imaging was done with an acceleration voltage of 5.0 kV and beam current of 500 pA using both a conventional secondary electron detector and a (more surface-sensitive) Inlens detector. TEM images are taken by Dr Dominique D. Piche using a JEOL 3000F microscope (300 kV acceleration voltage). Optical images are taken using a Canon PowerShot G9 X Mark II.

5.3 Results and discussion

Bioinspired freeze-cast alumina scaffolds and nacre-like alumina platelets are here for the first time used to generate bioinspired alumina/MWCNT composites. An array of different techniques was used to disperse MWCNTs through the alumina. In many of these procedures, there is a trade-off between MWCNT purity, dispersion, length, defectiveness and scalability. The aim of this chapter is to identify the best processing route and resulting microstructural features to optimally incorporate MWCNTs in a nacre-like alumina microstructure and ultimately mimic the mechanical response of nacre to generate a strong, non-brittle and multifunctional composite.

PART A – Bioinspired alumina scaffolds

In this section, bioinspired freeze cast scaffolds, infiltrated *in-situ* with MWCNTs using the CVD procedure optimized in Chapter 3, were densified using SPS and their mechanical properties examined.

5.3.1 Freeze-cast MWCNT-infiltrated composites

MWCNT-infiltrated freeze-cast specimens with aligned lamellae were packed in a graphite die with alumina powder with the orientation of the lamellae perpendicular to the pressing direction. The amount of packing powder must be carefully calculated to not cause an uneven force distribution over the material inside the die. If the amount of packing powder is too high, due the porous nature and thus lower density of the specimen compared to the packing powder, the final sintering pressure may be mostly applied to the packing powder. At the same time, not enough packing powder means that the force will only be applied to the specimen, exceeding the intended applied force by a large amount as this is calculated over the complete die area. To properly pack the sample in the die, the MWCNT-infiltrated

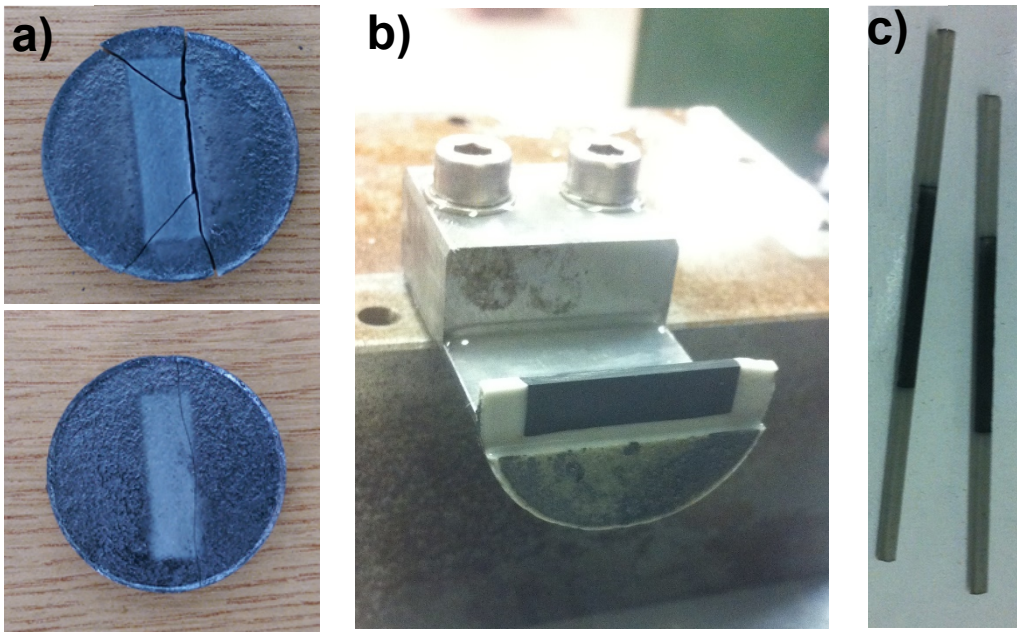


Figure 5.1 – Optical images of composites made by densifying a MWCNT-infiltrated freeze-cast alumina scaffold. a) Disks right after sintering showing thermal stress has resulted in cracking of the specimen, b) A disk mounted on a surface grinder to expose the MWCNT infiltrated phase embedded in packing powder and c) the matchstick sized specimens as prepared for bend testing.

scaffold together with pure alumina packing powder was pre-pressed using a hydraulic press. A series of pressures was investigated, and initial tests showed that a low pre-pressing pressure of around 5-8 MPa was sufficient to pack the scaffold in the die.

After sintering, the boundary between the packing powder and the MWCNT composite was observed to be prone to crack formation (Figure 5.1a), which is likely due to thermal stresses. While these thermal stresses can be minimized by adjusting the sintering procedure in terms of heating and cooling rates, dwell time, sintering pressure and the time that the pressure is applied, most samples gotten from these experiments are largely intact and provide enough material for mechanical characterisation.

After the disk was sintered, the packing powder was ground away on both sides, leaving the bare composite material (Figure 5.1b) which could then be polished and cut into matchstick-sized bend specimens. Figure 5.1c shows that in case of smaller scaffolds, the packing powder effectively aided the testing procedure by increasing the length of the cut bend specimens, thus enabling the testing of smaller samples in three-point bend tests.

The side and fracture surface of the bend specimens was imaged in SEM (Figure 5.2). Through a combination of freeze casting, CVD and SPS, the alignment of the MWCNT-coated lamellae was retained in the sintered composite. The relatively thin layer of MWCNTs (compared to the lamellae thickness) together with the fast sintering time inherent to the SPS

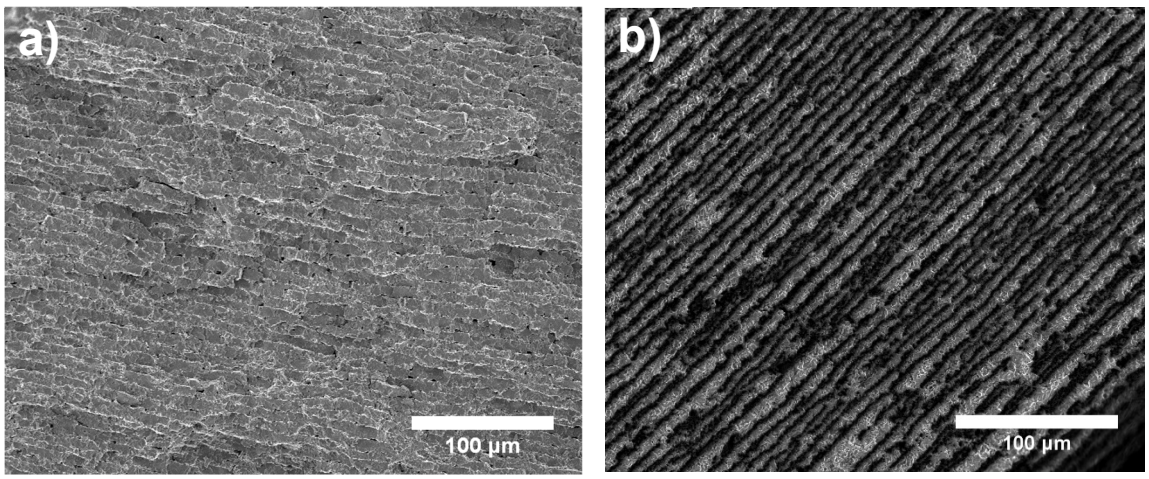


Figure 5.2 – SEM images of a composite beam made by densifying a MWCNT-infiltrated freeze-cast alumina scaffold, showing that lamellae and their alignment were retained during the SPS procedure. a) the fracture surface after a 3pt bend test and b) the side of the beam.

procedure prevented grain growth and loss of the layered structure during sintering. However, the bend test data in Figure 5.3 indicate that the lamellar structure does not translate to nacre-like mechanical behaviour. The bend specimens break destructively and have a response that is very much like monolithic alumina – brittle failure.

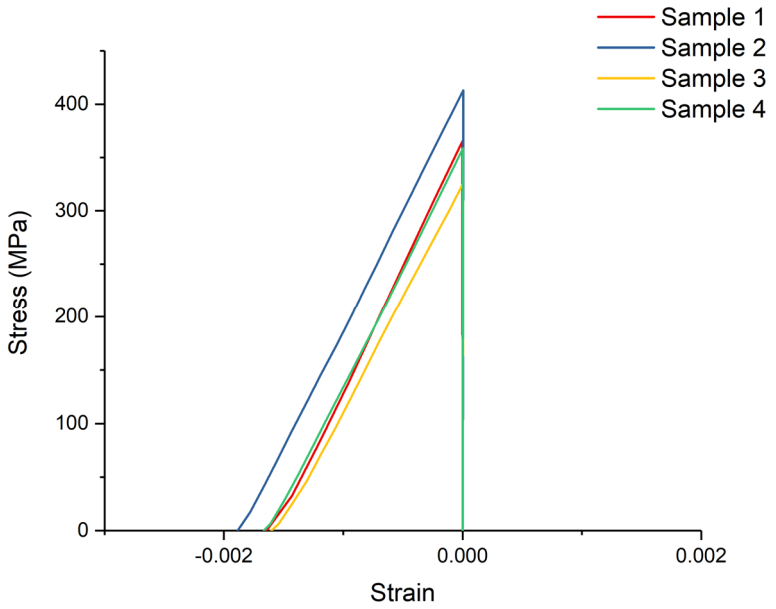


Figure 5.3 – Three-point bend test stress-strain curves (unnotched) of composites made by densifying a MWCNT-infiltrated freeze-cast alumina scaffolds, sintered for 5 minutes at 45 MPa and 1600 °C. The graph shows the completely brittle failure of these composites.

PART B – MWCNT-coated alumina platelets – Low temperature sintering

In this section, alumina platelets are coated with MWCNTs using two different dispersion methods. Mechanical dispersion by ultrasonication is compared to chemical dispersion through acid treatment. The optimal sintering parameters developed for pure alumina platelet materials in Chapter 4, which yielded a nacre like microstructure with minimal grain growth, are used to sinter the coated powders into composites. The influence of the MWCNT phase and the dispersion method on the final composite is investigated.

5.3.2 Nacre-like composites using sonicated MWCNTs

Sonication is a well-established method of dispersing MWCNTs. During sonication, sound waves in the liquid media generate alternating high-pressure and low-pressure cycles. During the low-pressure cycle, small vacuum bubbles are generated. These bubbles grow until they collapse violently during a high-pressure cycle which generates a strong shear force which can exfoliate MWCNT bundles[122]. Although it has been shown that sonication can introduce defects and reduce the length of CNTs by scission[297], the benefit that dispersion in a ceramic matrix offers is likely to outweigh the individual damage of MWCNTs. In aqueous solutions, the MWCNTs need either metal decoration or surfactants to maintain a stable suspension[298].

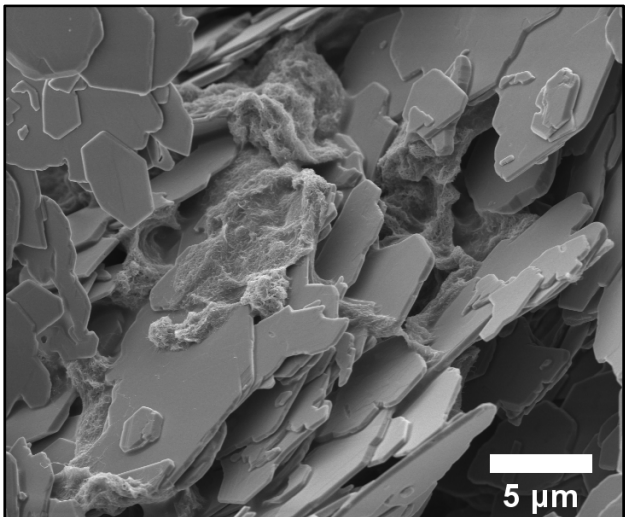


Figure 5.4 – SEM image of alumina platelets mixed with MWCNTs using sonication (4 wt% in Chloroform).

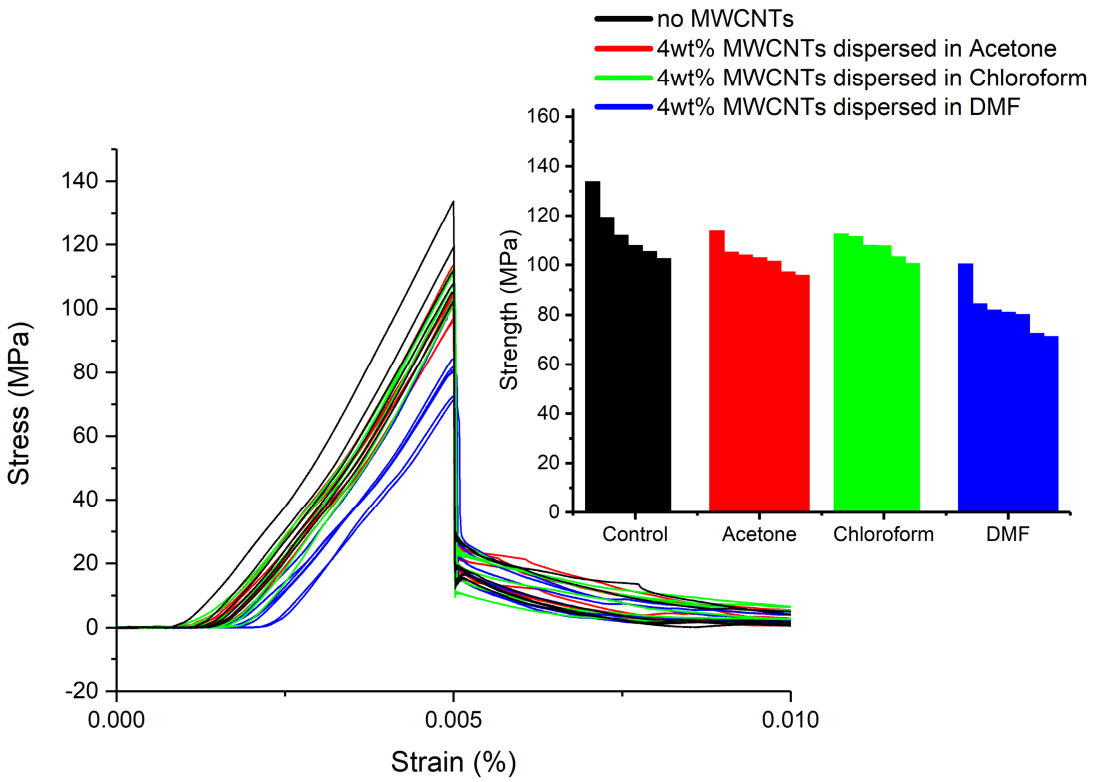


Figure 5.5 – Three-point bend test stress-strain curves and strengths of nacre-like alumina composites made with 4 wt% sonicated MWCNTs dispersed in different solvents. The composites were sintered for 15 minutes at 70 MPa and 1300 °C.

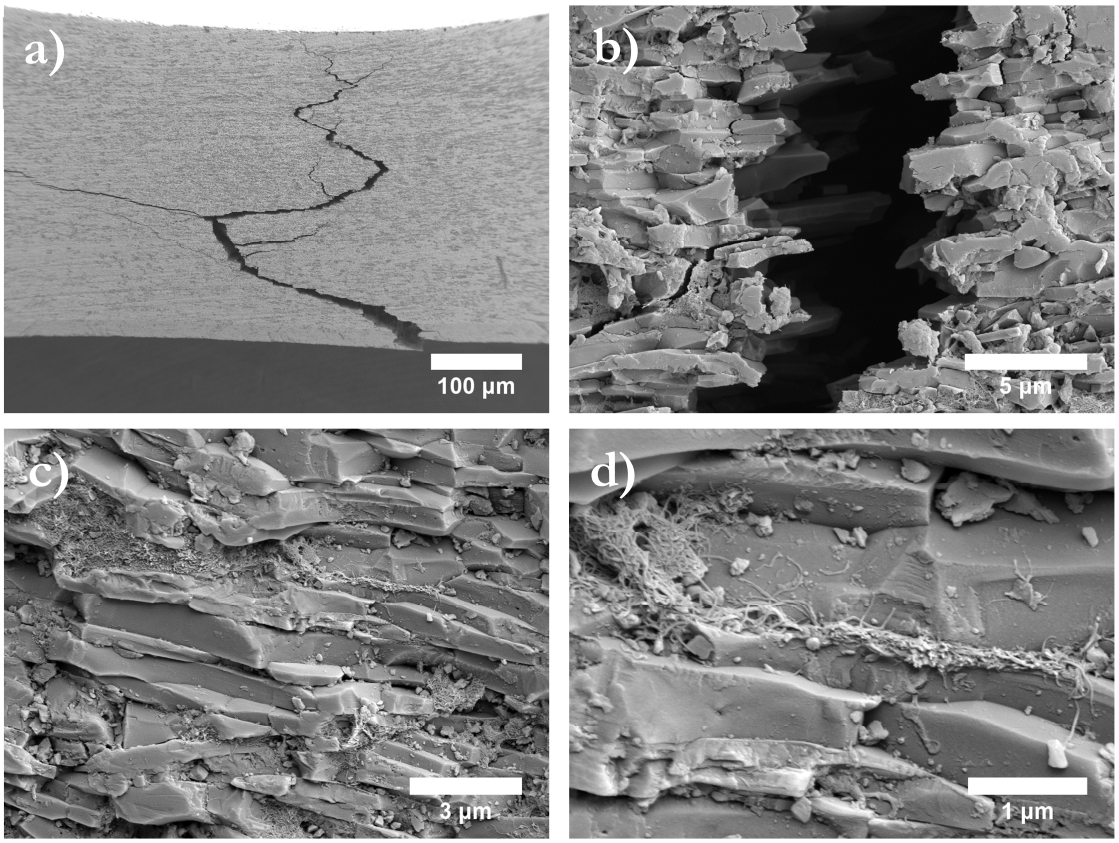


Figure 5.6 – SEM images of nacre-like alumina composites made with MWCNTs, incorporated using sonication in acetone. The images are of the side of a specimen tested in three-point bend and show a) crack propagation through the beam, b) a close up of the crack through the sample, c+d) a close-up of the microstructure showing the MWCNT distribution.

Other solvents such as dimethylformamide (DMF)[299], chloroform[300] and acetone[301] have proven to yield stable suspensions without any surfactant. These three solvents are used here in conjunction with a sonication procedure to create pure suspensions of MWCNTs, which are mixed with alumina platelets in solution. Figure 5.4 shows that the initial dispersion of MWCNTs on the platelets through sonication is not entirely successful, as not all platelet surfaces are covered by MWCNTs, which is the case for all three solvents compared here. The final composite (Figure 5.6c-d) however shows that a large amount of MWCNTs was incorporated between the platelets after sintering (although a majority were still clumped together in small 'yarns'). Figure 5.5 shows that the composites made with MWCNTs dispersed in chloroform and acetone show similar mechanical behaviour, while MWCNT dispersion in DMF decreased the strength of the composite. Although DMF is known to disperse MWCNTs very well[299], the composites with DMF-dispersed MWCNTs have a lower strength than any of the other dispersants used. The reduced strength in these experiments could indicate that the MWCNTs were less dispersed in DMF than in the other solvents (forming agglomerates which can act as crack initiators). Alternatively, the fact that DMF is a much larger and heavier molecule with a much higher boiling point, means that it is more likely to stay as a contamination on the alumina platelets. Figure 5.6a-b shows that there is a large amount of crack deflection but that the MWCNTs do not tend to bridge the cracks. Incorporation of MWCNTs through the sonication methods used here does not seem to improve the mechanical properties of a structure of purely aligned platelets – In fact, the mechanical response is surprisingly similar to that of the samples where no MWCNTs were incorporated, with only a minimal decrease in strength.

5.3.3 Nacre-like composites using acid treated MWCNTs.

While acid treatments inherently introduce defects, which are detrimental to the mechanical properties of the MWCNTs, the SPS process likely helps to anneal the MWCNT phase while the composite is densified, resulting in much more crystalline MWCNTs in the final

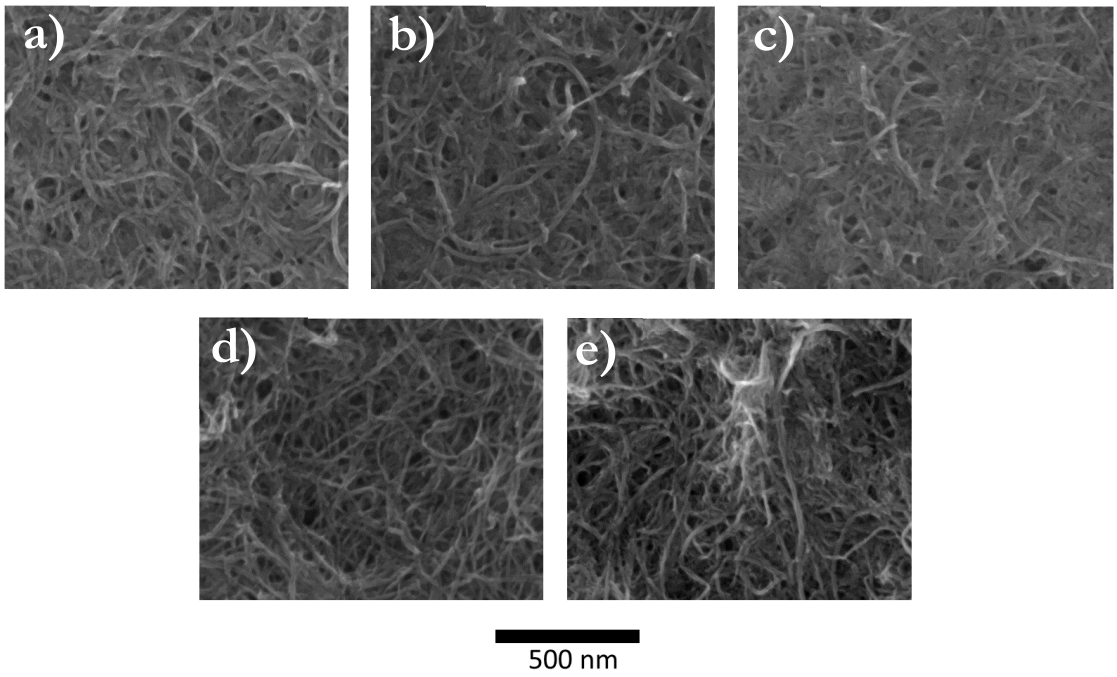


Figure 5.7 – SEM micrographs showing acid treated MWCNTs after each washing/purification step to monitor that they are pure, well dispersed and maintain their length and structural integrity. The images are taken after a) 7x 5 minutes of centrifugation at 4000 RPM, re-dispersing in H_2O b) a further 2x 5 minutes of centrifugation at 4600 rpm, re-dispersing in H_2O/Ethanol. c) a further 2x 5 minutes of centrifugation at 4600 rpm, re-dispersing in Ethanol. d) a further 2x 5 minutes of centrifugation at 4000 RPM, re-dispersing in H_2O and e) the final re-dispersion in H_2O.

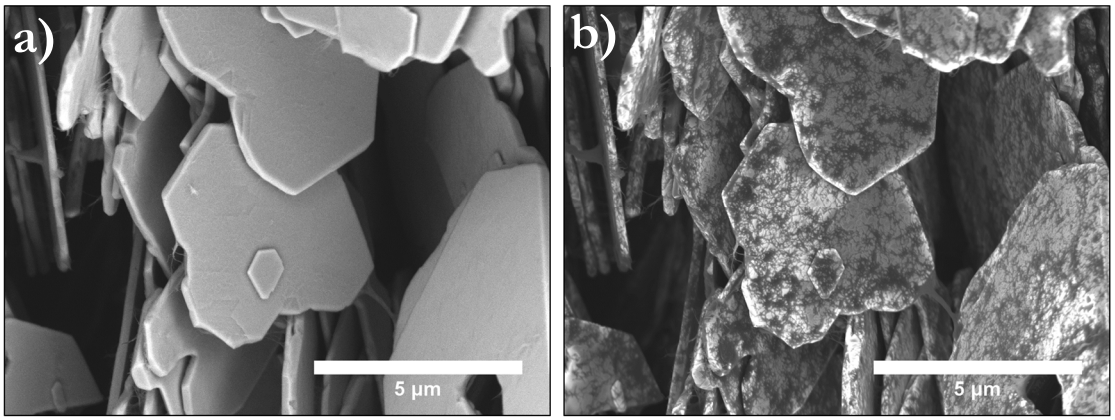


Figure 5.8 – SEM images of a homogeneous acid treated MWCNT coating on nacre-like alumina platelets in a 2:98 weight ratio, using a) a secondary electron detector and b) an In-lens detector, both at an acceleration voltage of 5kV. The images show that a regular SEM SE detector does not have enough surface sensitivity to detect the coating.

composite. In addition, the benefits of an extremely well-dispersed MWCNT phase may counteract the effect of the increased defectiveness of the MWCNTs.

Although the acid treated MWCNTs are not bonded through a catalyst particle and their orientation is parallel to the platelets, the attachment of these MWCNTs can be established through the reaction of the outer layers of the MWCNTs with alumina or by embedding them into the platelets through indentation (an SEM image of this can be found in Section 5.3.7, Figure 5.33b). The grain growth inhibition provided by the acid treated MWCNT-

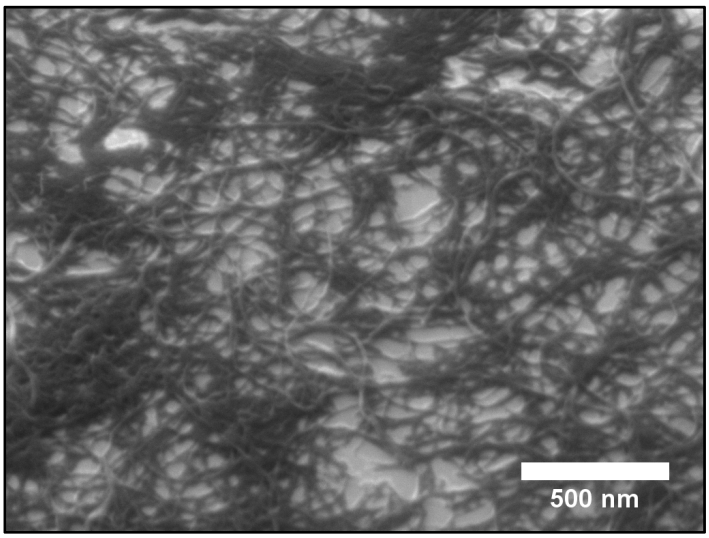


Figure 5.9 – SEM image of a homogeneous acid treated MWCNT coating on a nacre-like alumina platelet, showing that the majority of MWCNTs are free-standing.

phase maintains the dimensions of the platelets to be nacre-like, enabling them to slide while at the same time restraining the sliding movement by bridging between adjacent platelets.

To make sure the nitric acid and any salts and amorphous carbon generated during the acid treatment is washed away, an extensive washing procedure is used which is monitored by drop casting MWCNTs after each treatment step. Figure 5.7 shows that while after initial washing in water some film-like material is present between the MWCNTs, this is reduced significantly through the washing procedure.

MWCNT coating of alumina platelets is done by freezing a solution of dispersed acid treated MWCNTs and alumina platelets, after which the solution is freeze-dried. This procedure maintains the homogeneous distribution of both alumina particles and MWCNTs and yields a 'fluffy' powder which can then be easily pressed and aligned in SPS.

Figure 5.8 displays the result of this coating procedure for 2wt% MWCNT content in the composite, showing that a homogeneous coating can only be observed using an In-Lens secondary electron detector, which mainly collects electrons originating from the upper region of the interaction volume and is therefore very surface-sensitive. A zoom in of such a coated platelet is found in Figure 5.9, on a comparable magnification as the drop casts in Figure 5.7. Figure 5.9 shows that the acid treated MWCNTs are well-separated and

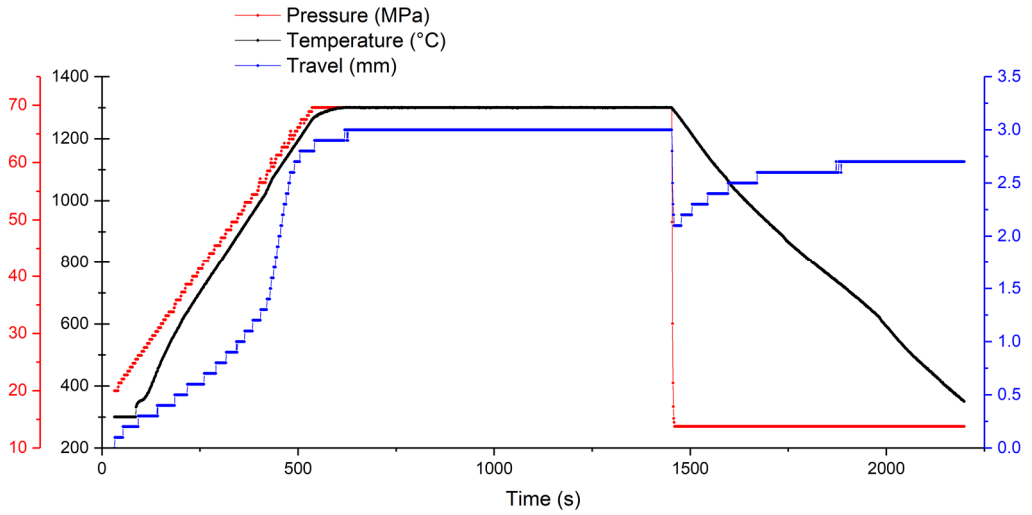


Figure 5.10 – Sintering curve showing the temperature and pressure in SPS and the resulting piston movement for platelets coated with 2 wt% Nitric acid treated MWCNTs. The absence of piston movement during sintering indicates that maximum density is achieved quickly.

homogeneously coated on the platelet surface. Some darker areas can still be observed, which are most likely remaining carbonaceous deposits. These could potentially be reduced by optimizing the acid treatment procedure; shorter treatment times at different temperatures can be applied or longer washing procedures can be used which will yield higher purity MWCNTs at the cost of the loss of a lot more material during such a procedure.

The acid treated MWCNT coating can act as a barrier for grain growth, and therefore longer sintering times are feasible. The alumina platelets were coated with 0.3 wt%, 1 wt% and 2 wt% respectively and densified using SPS for 15 minutes. Figure 5.10 shows the sintering curves for an acid treated MWCNT coating of 2wt%, showing that even for this amount of coating the sintering curve plateaus within one minute of reaching the sintering temperature. No more piston movement indicates maximum shrinkage under these conditions is achieved. The densities of the composites coated with coated with 0.3wt%, 1wt% and 2wt% acid treated MWCNTs were 3.958±0.025 g/cm^3, 3.907±0.025 g/cm^3 and 3.834±0.025 g/cm^3 respectively. Assuming a MWCNT density[302] of 1.75 g/cm^3 and alumina density[254] of 3.98 g/cm^3, their relative densities are therefore 99.9 %, 99.4 % and 98.8 % respectively, decreasing with MWCNT loading. Figure 5.11 shows that the resulting strengths also decrease significantly with MWCNT loading. The composites, while showing tortuous crack paths as can be observed in Figure 5.12, do not exhibit a high residual strength and fail mostly

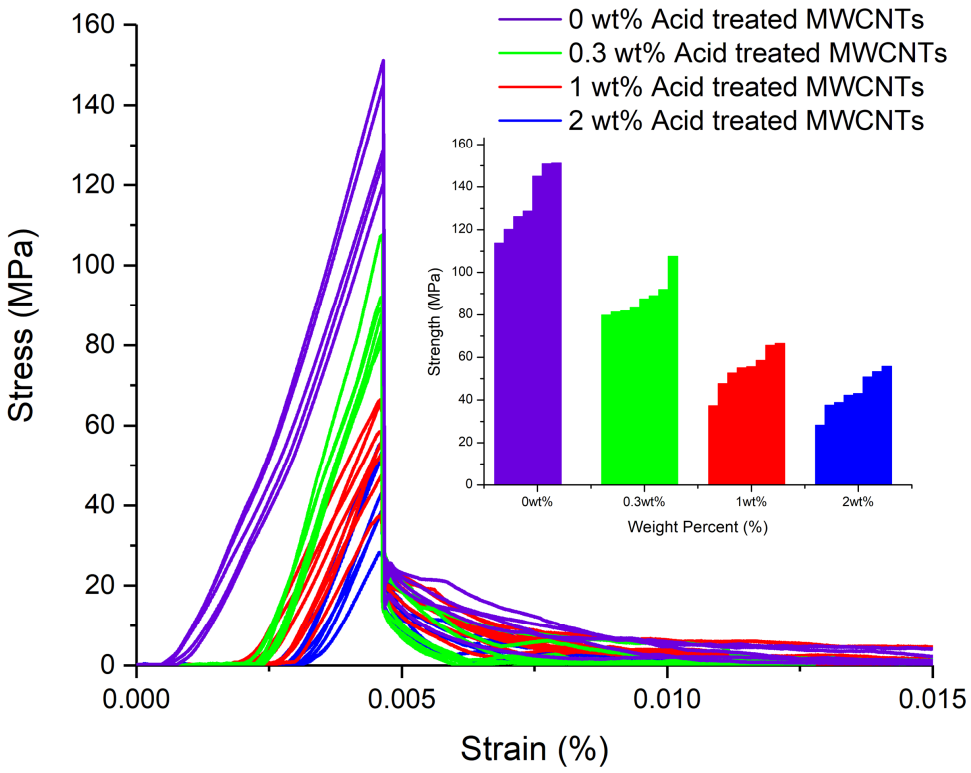


Figure 5.11 – Three-point bend test stress-strain curves of composites made with platelets coated with nitric acid treated MWCNTs, showing that by increasing the amount of MWCNTs, the composite strength was significantly decreased.

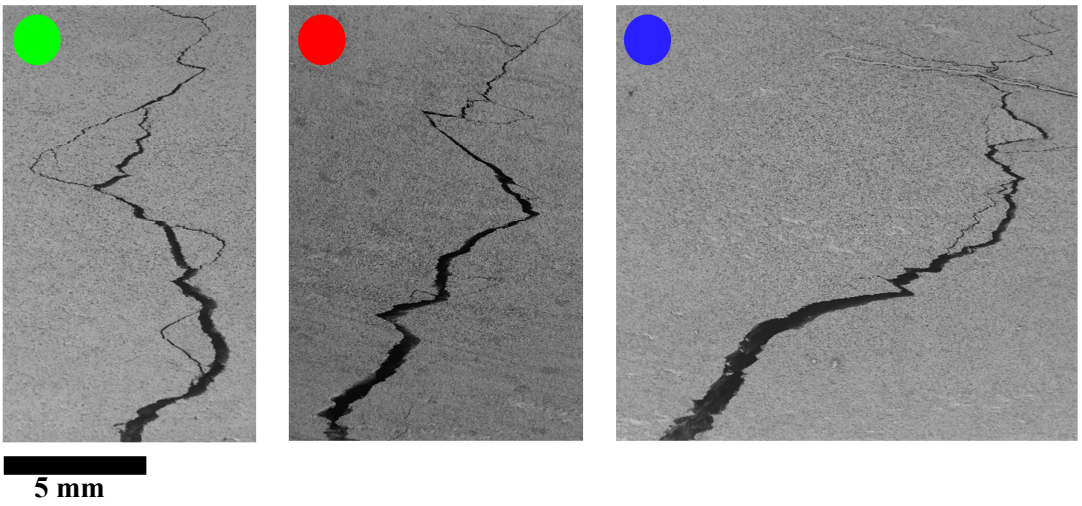


Figure 5.12 – SEM images of crack propagation of acid treated MWCNT/alumina platelet composites tested in three-point bend, showing similar crack propagation for composites with different MWCNT loading.

in a brittle fashion. Shirasu *et al.*[276] see the same reduction in strength with increasing MWCNT content when testing acid treated CNTs in an alumina nanoparticle matrix. A close-up of the crack in a 2wt% acid treated MWCNT composite is displayed in Figure 5.13, showing crack propagation is deflected around alumina platelets. Figure 5.14 shows that the MWCNT phase is compressed into a thin film that is present in between the platelet structure closely mimicking nacre which has a similar soft phase to hard phase distribution. Apart from the mostly maintained platelet thickness, the MWCNT phase does not show much crack

bridging in the composite. Figure 5.15 shows the acid treated MWCNT phase before and after sintering. Where before sintering a large amount of connections could be observed between the platelets in the form of MWCNT bundles, after sintering the amount of platelet-platelet connections has drastically reduced. In addition, where the bundles before sintering look stretched and 'sticky', with many tubes connecting to the base of the alumina platelets, the few connections left after sintering that these stretched, and 'sticky' connections are lost entirely.

The change in the MWCNT phase can be monitored using Raman spectroscopy to see if any change in the MWCNT structure has occurred during sintering. Figure 5.16 shows that while the characteristic D' peak associated with double resonance Raman scattering processes in defective graphitic materials[197] gets more pronounced after acid treatment, after sintering the shape of the peak closely resembles the pure untreated material again. This indicates that the

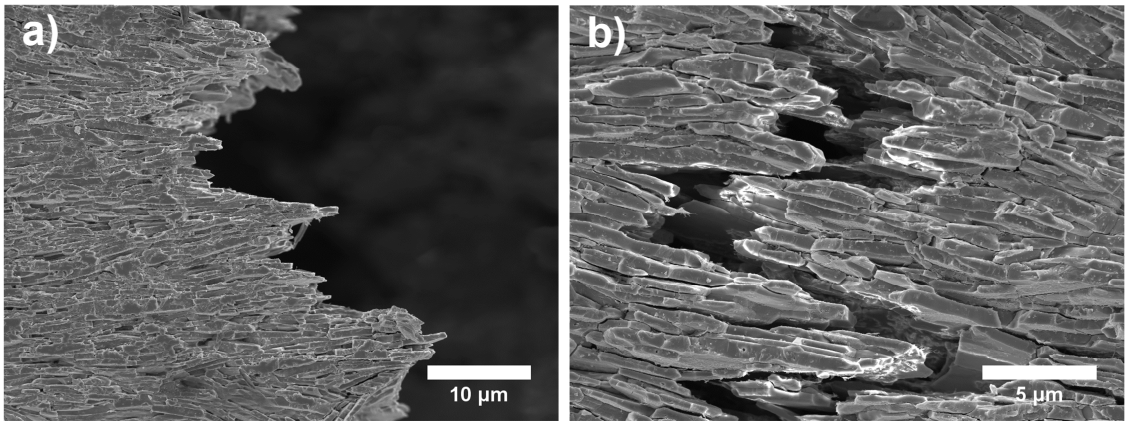


Figure 5.13 – SEM image of a 2wt% acid treated MWCNT/alumina composite after three-point bend testing showing a) the bottom of the beam where crack faces are far apart and b) the top of the beam with crack faces interlocked.

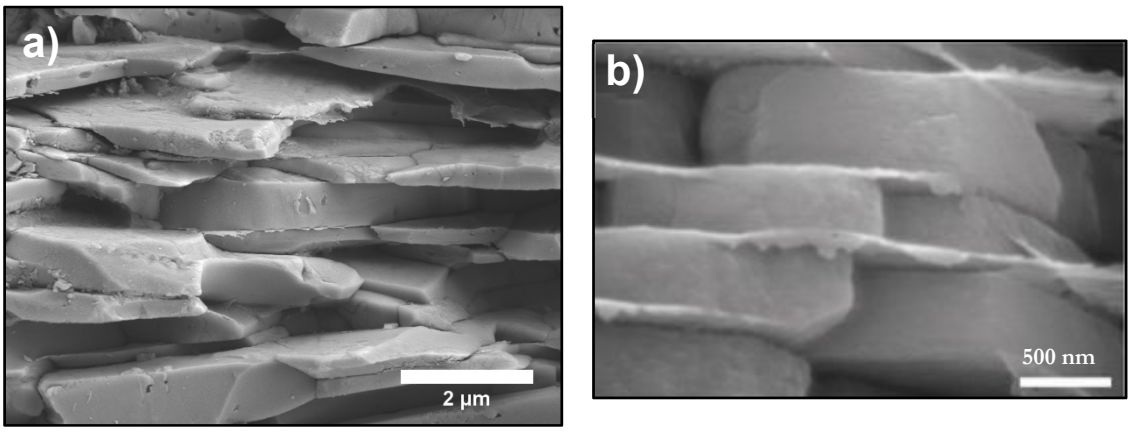


Figure 5.14 – SEM image of a) a 2wt% acid treated MWCNT/alumina composite showing thin layers of compressed MWCNTs between the platelets and b) Nacre, showing a thin protein layer between platelets (Adapted from Bouville *et al.*[35]).

MWCNTs are annealed within the composite structure during the sintering procedure. Annealing of MWCNTs is regarded as effective above temperatures of 1800 °C[303], and for annealed MWCNTs at these temperatures a similar decrease of the characteristic D' peak has been shown[304]. The annealing of MWCNTs during the SPS procedure at 1300°C can be attributed to the electric current through the sample, as current-induced annealing has been seen before in graphene[305]. While the composite structure very closely resembles that of nacre (Figure 5.15), the relatively brittle nature can be explained by state of the MWCNT phase in between the platelets – the MWCNTs have formed a thin layer of poorly bonded compressed tubes, showing an absence of fibre reinforcement effects. The decreasing strength with MWCNT content can be explained by the effect the MWCNTs have on the modification of the platelet surface; MWCNTs can roll in between two separated rubbing surfaces and act as ball bearings[306]. In essence, the MWCNT coating has formed a very thin and weak interface. While this leads to crack deflection, the propagating crack can easily propagate through the MWCNT layer. It is also known that pristine MWCNTs slide easily relative to each other to

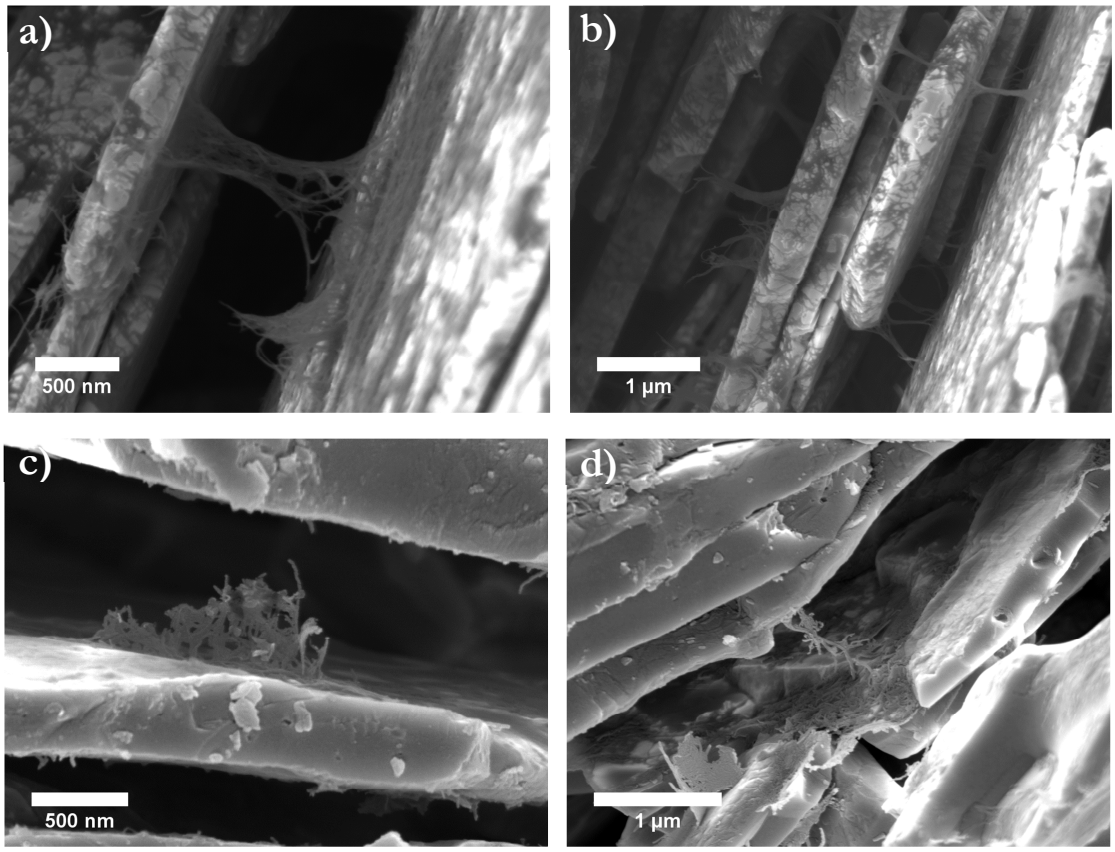


Figure 5.15 – SEM images of alumina platelets coated with acid treated MWCNT, showing bridging of platelets by (bundles of) MWCNTs a-b) before sintering and c-d) after sintering.

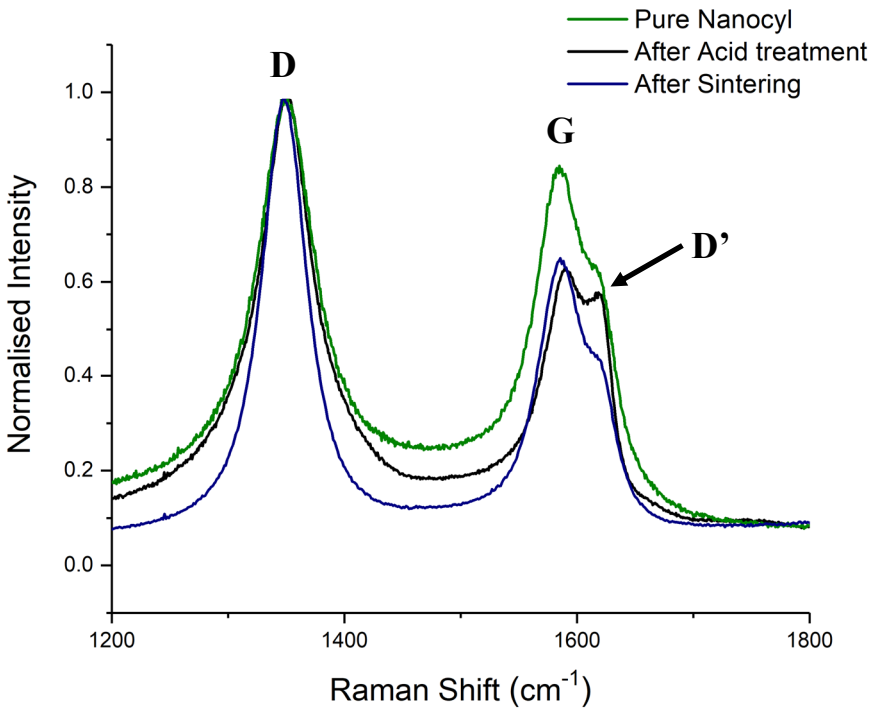


Figure 5.16 – Raman spectra of pure Nanocyl and acid treated MWCNTs before and after sintering, showing that the D' peak gets more pronounced after acid treatment, and reduces in intensity again after sintering. The decrease in the I_D/I_G ratio is likely due to the removal of amorphous carbon during the acid treatment.

create any useful resistance to sliding[99], with any resistance being due to defects or functional groups, which according to the Raman data is severely reduced after the sintering procedure. Thus, when platelets slide there is not much friction to resist separation of platelets. Another factor to consider is that the inhibition of grain growth through a MWCNT coating, also inhibits the formation of wavy platelets which seem to have such a large effect on the strength of nacre[19,56].

5.3.4 Nacre-like composites using graphite reinforcement.

Graphite flakes are another attractive carbon material for reinforcement of ceramic composites due to their high strength layered structure that allows for self-lubrication, with excellent high temperature and thermal shock resistance, and high fracture toughness[307]. They have been previously successfully used in epoxy[308], glass[309] and ceramic[307] matrices, including zirconia densified in SPS[310]. In the alumina platelet microstructure, large-sized flakes may be used as a source of extrinsic toughening though crack bridging and pull-out behind the crack tip.

One sample was made with large (~50 μm) graphite flakes incorporated in the microstructure. The strength of these composites was very similar to the strength of alumina made with pure platelets only with an arguably more brittle character as the residual strength after fracture is reduced (Figure 5.17a). This is unexpected as from the micrograph the predicted crack bridging and pull-out is observed (Figure 5.17b-c).

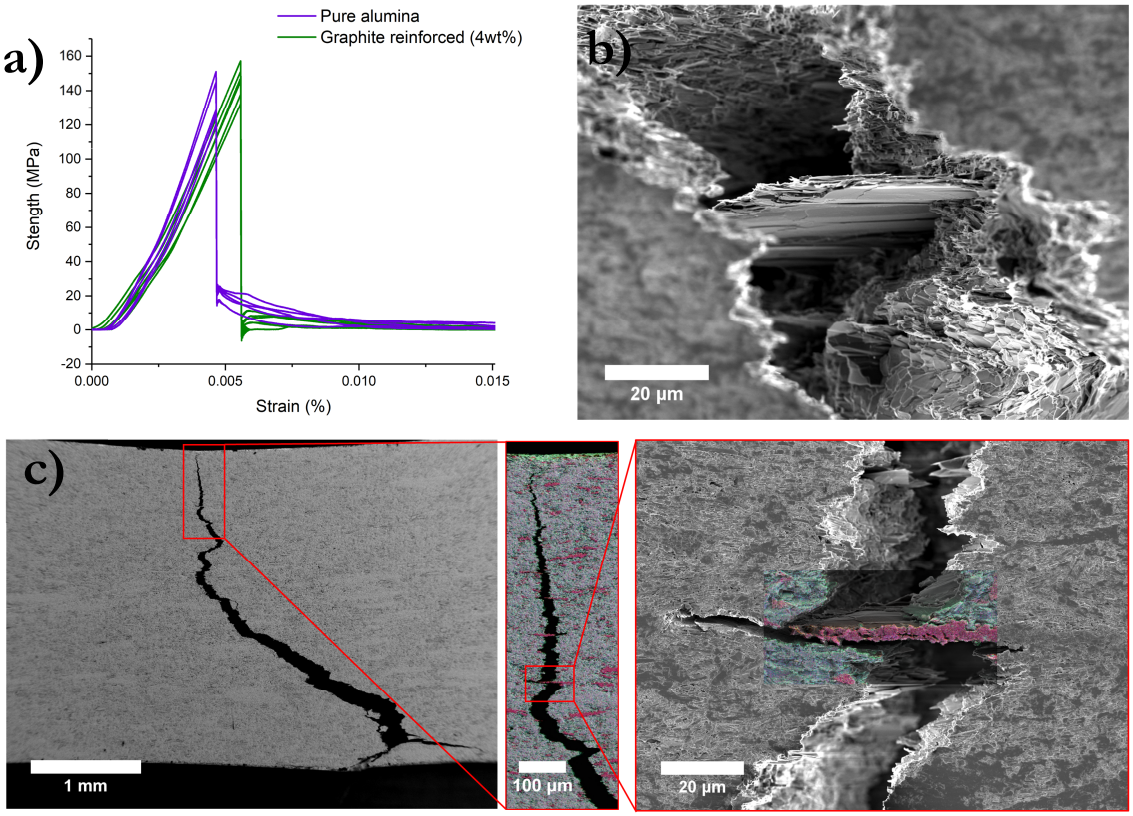


Figure 5.17 – a) three-point bend test data for pure platelet-alumina and graphite reinforced (4wt%) platelet-alumina sintered for 15 minutes at 70 MPa and 1300 °C. b) a close-up in SEM of the crack showing a graphite flake embedded in the structure, bridging the crack. c) A zoom-in of the macroscopic crack in SEM to an area where graphite is seen to have pulled out of its socket. A coloured EDX map is overlaid on the image; blue shows the alumina signal and pink the carbon signal.

PART C – MWCNT-coated alumina platelets – High temperature sintering.

The sintering parameters used for composite formation in Part B are based on the best performing sintering parameters of ceramics made of pure alumina platelets from experiments outlined in Chapter 4. However, the MWCNT phase arguably inhibits the grain growth of alumina. Therefore, higher temperatures can be used to sinter MWCNT/alumina composites without compromising the nacre-like dimensions of the alumina platelets and consequently the nacre-like microstructure of the composite, while at the same time improving density and resulting strength. To further accentuate that for these composites a higher sintering temperature may be beneficial in spite of the possibility of grain growth occurring (and thus a less nacre-like final product), it should be noted that previous research on composites using alumina platelets together with a glass phase at 1500 °C[35] yielded impressive results in terms of failure strength and residual strength. Especially considering that sintering of composites at 1300°C using both mechanical and chemical MWCNT dispersion methods yielded weaker materials (part B), here, nacre-like composites made with alumina platelets and MWCNTs are examined, sintered at temperatures of 1500 °C and higher. In addition, other sintering parameters for these materials are further improved upon.

5.3.5 Alumina platelets with powder mixed MWCNTs

The simplest way to disperse MWCNTs in an alumina-platelet matrix, is by introducing the MWCNTs in their pure as-synthesized form, dispersed in dry powder mixing procedure. The result is a powder in which clumps of MWCNTs exist, often hundreds of micrometres in diameter (Figure 5.18). Although this procedure minimizes damage to the MWCNTs themselves, these clumps are both poorly dispersed and poorly attached to the platelets. However, it is important to note that composites made from these powders provide a

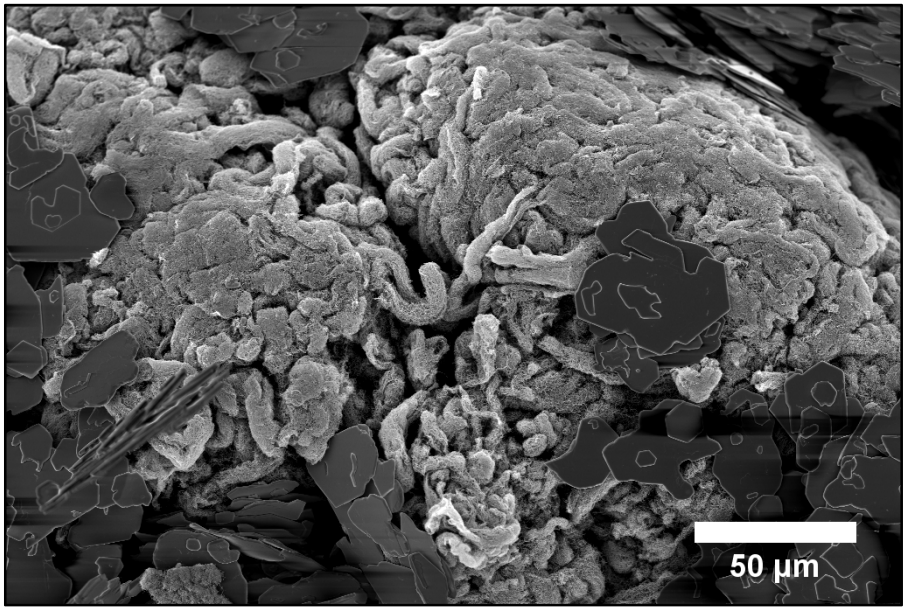


Figure 5.18 – SEM image of a dry mixed power of commercial MWCNTs with alumina platelets, showing a poor dispersion with clusters of MWCNT 'yarns'.

valuable benchmark when comparing other methods of dispersion, providing a reliable baseline on the improvement that dispersion of MWCNTs has on the resulting composite. In addition, these composites give insight in the crack propagation as a function of MWCNT loading and the effect of defects in the form of MWCNT yarns in the nacre like structure.

Powders of platelet-alumina with 3.7 wt%, 7.2 wt%, 12.5 wt%, and 18.3 wt% MWCNTs were sintered for ~15 minutes at 1500 °C and 45 MPa. The sintering curves in Figure 5.19 show that there is still piston movement after 15 minutes, as the sintering curve is diverging

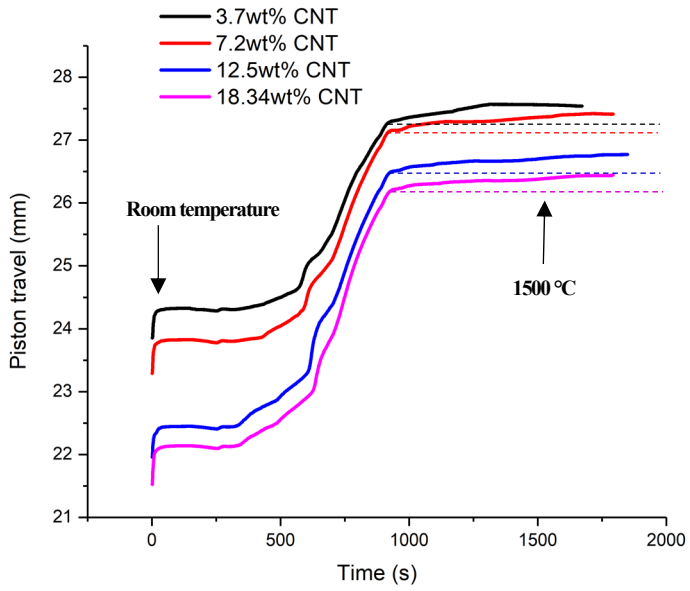


Figure 5.19 – SPS Sintering curves for different weight percentages of nacre-like alumina composites made with MWCNTs, incorporated using a dry powder mixing procedure, showing piston movement throughout the sintering procedure. The composites were sintered for ~15 minutes at 42 MPa and 1500 °C

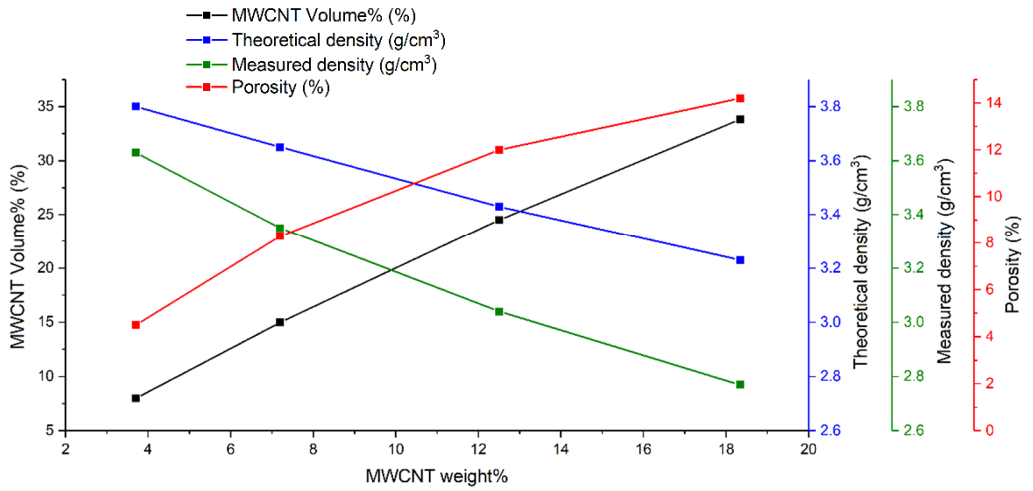


Figure 5.20 – Graph showing the composite density and porosity and the volume percentage of MWCNTs as a function of the weight percentage of MWCNTs of nacre-like alumina composites made with MWCNTs, incorporated using a dry powder mixing procedure, The data show that increasing MWCNT content lowers the density of nacre-like composites. In this Figure a MWCNT density[302] of 1.75 g/cm^3 and alumina density[254] of 3.98 g/cm^3 are used.

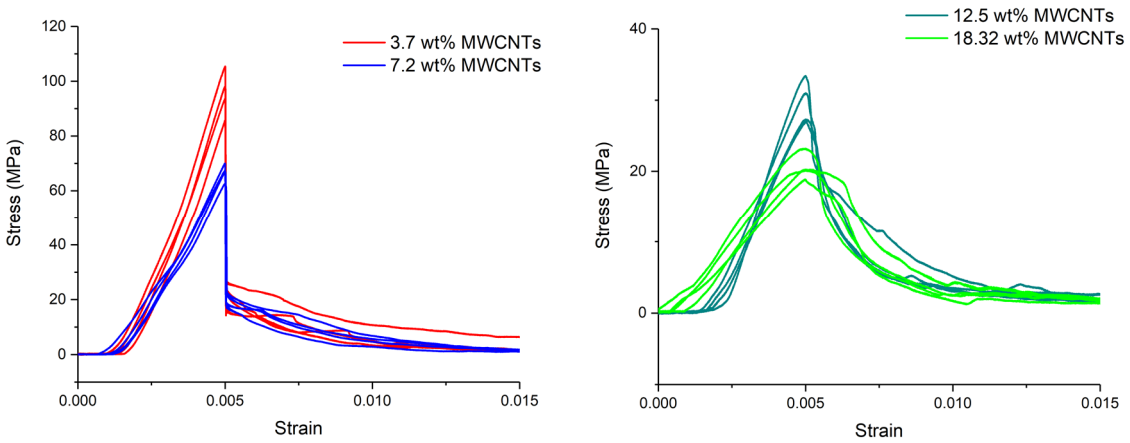


Figure 5.21 – Three-point bend test stress-strain curves of nacre-like alumina composites made with MWCNTs, incorporated using a powder mixing procedure. The graphs show that by increasing the amount of MWCNTs, the composite strength was significantly decreased.

from the horizontal dashed line which represents no piston movement. This indicates that the MWCNT phase is inhibiting densification, resulting in composites that are not fully densified. Note that while the MWCNT percentages are precisely measured, there are volume differences between the powders due to the different MWCNT loading, and some material may be lost during loading the final loading of the die. Therefore, while the shape of the curve can give meaningful sintering information, it is less meaningful to compare the exact height of the curves.

While Figure 5.19 gives us qualitative information on the densification during SPS, this is quantified in Figure 5.20, which shows that densification is increasingly inhibited with

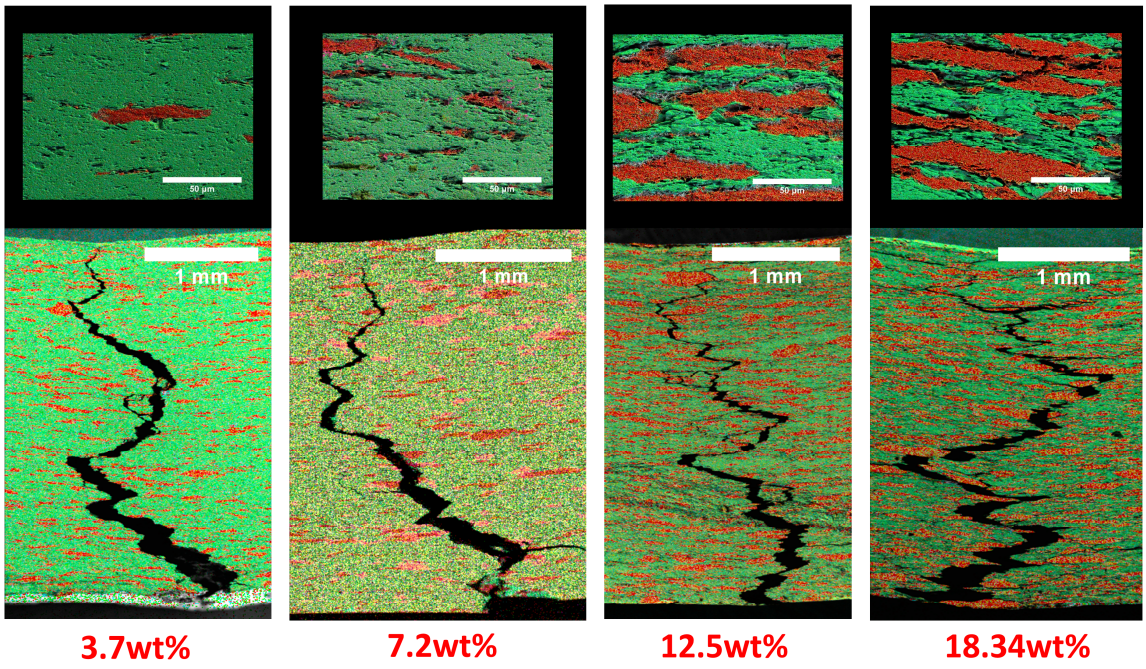
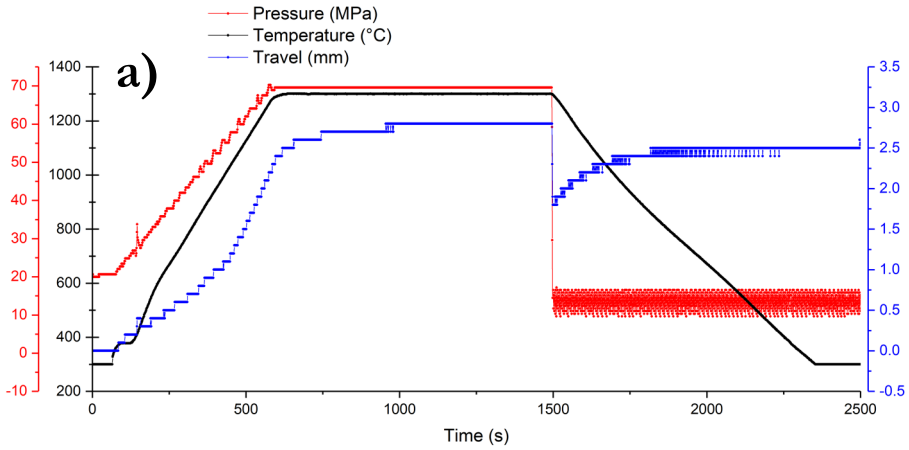


Figure 5.22 – SEM images of nacre-like alumina composites made with MWCNTs, incorporated using a dry powder mixing procedure. An EDX colour map is overlaid on the images, showing the Carbon (MWCNT) phase in red, and Alumina in green.



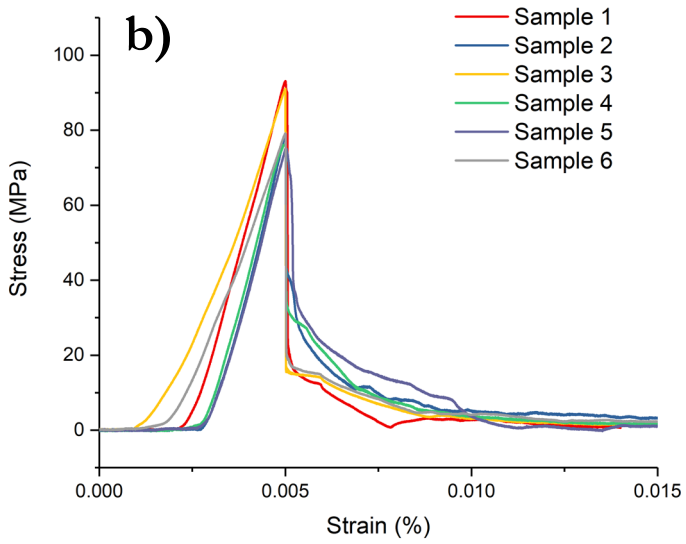


Figure 5.23 – a) Sintering curves and b) three-point bend test stress-strain curves of a nacre-like alumina composite made with 3.7 wt% MWCNTs, incorporated using a dry powder mixing procedure. The composite was sintered at for 15 minutes at 1500 °C and 70 MPa.

increasing MWCNT content; the measured density diverges significantly from the theoretical density. Therefore, the resulting porosity increases with MWCNT content. Three-point bend test data in Figure 5.21 show that the increasing MWCNT content and resulting porosity results in decreasing strengths. Figure 5.21 also shows that between a MWCNT loading of 7.2wt% and 12.5wt%, a transition from brittle fracture to non-brittle fracture is observed. From a weight percentage 12.5wt% onwards, a large percentage of the crack front propagates through the MWCNT 'yarns' and the interface of the yarns and the platelets. The crack path in these high-MWCNT content composites is visibly less straight (Figure 5.22). The crack is deflected more as it propagates through the composite's poorly bonded regions more easily, resulting in a more tortuous and longer crack path. Because they are relatively large, the MWCNT clusters are clearly visible with EDX, which enables a good visualisation of the distribution of MWCNT clusters in the structure.

To exclude that these effects are due to a poor sintering procedure, a sample with 3.7wt% dry mixed MWCNT content (a MWCNT volume% of 7.81%) was sintered for 15 minutes at 70 MPa, which is the maximum pressure that the graphite die can sustain without breaking. The resulting sintering curve in Figure 5.23a flattens around the 6.5-minute mark and yields a porosity of 5.4%, which is similar to the porosity obtained when sintering at 45MPa (4.5%). The three-point bend graphs in Figure 5.23b and strength values are also minimally affected by the significant increase in sintering pressure, from which it can be concluded that the poor MWCNT dispersion and not sintering pressure is the main contributor to the poor mechanical behaviour of these composites.

5.3.6 Nacre-like composites using CVD-grown MWCNTs – Densification.

Here, alumina platelets which were coated *in-situ* with MWCNTs using the CVD procedure optimized in Chapter 3 were used to create MWCNT/alumina composites. Because of the physical restraint to grain growth that the coating provides, sintering was done at 1600 ^{o}C

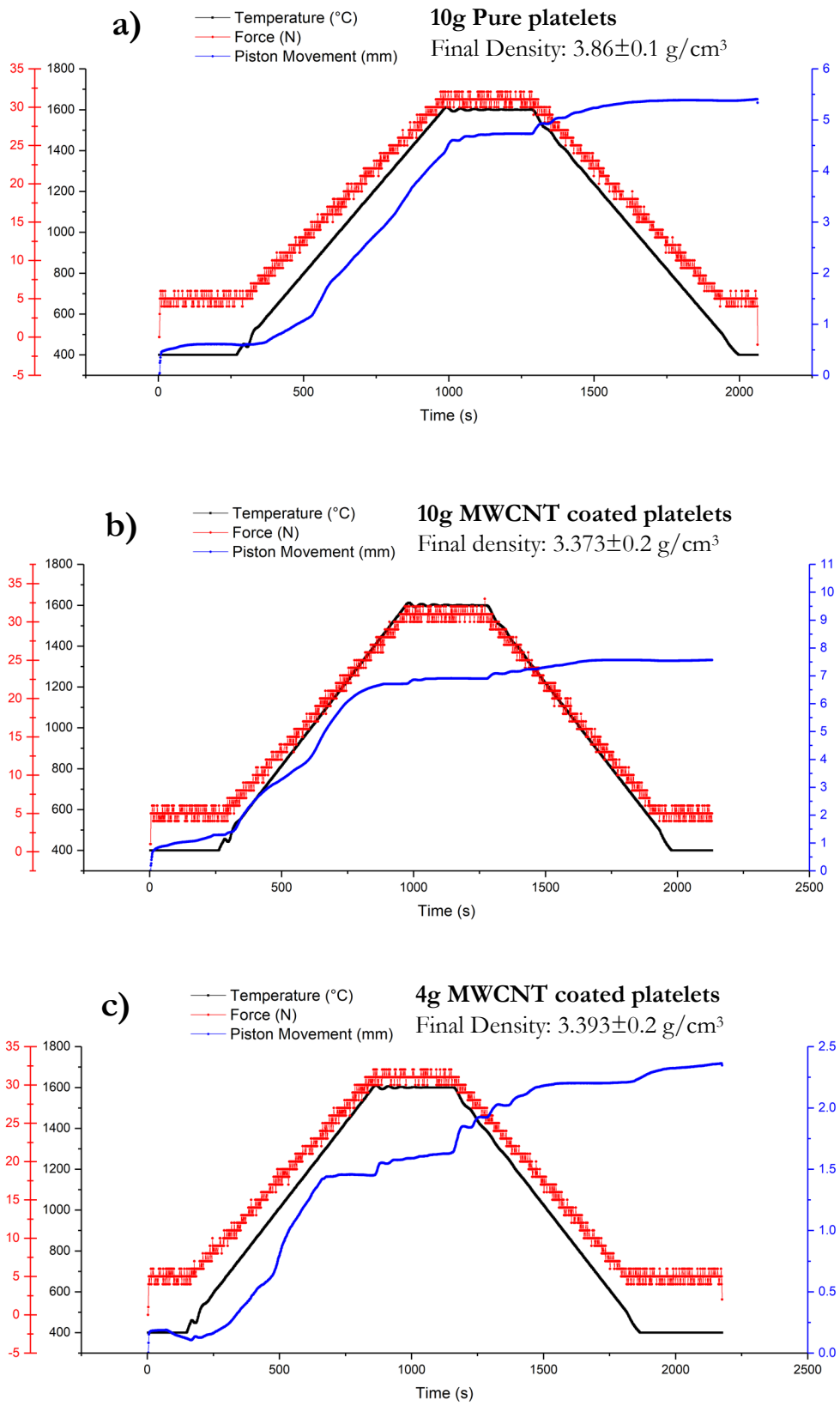


Figure 5.24 – Sintering curves showing the temperature and force ramp (on a 30 mm cylindrical punch) in SPS and the resulting piston movement of a) Pure platelets and b-c) MWCNT coated platelets. The graph shows that the piston movement plateaus before reaching the final pressure and temperature in the case of MWCNT-coated platelets.

and 45MPa. For fair comparison, the same sintering conditions were used for both alumina platelets and MWCNT-coated alumina platelets. There is a clear difference in sintering behaviour in SPS, however. The sintering curves in Figure 5.24 show that for pure alumina platelets, the piston movement plateaus when the temperature and pressure ramp is completed. The pure alumina-platelet sample (10g) had a density of 3.86±0.1 g/cm^3. Calculating the total porosity as the difference between theoretical full density of alumina (3.98 g/cm^3)[254] and measured density, this results in a porosity between 1-5%. For the MWCNT coated platelets the piston movement graph plateaus during the temperature and pressure ramp, around 1200 °C and 20 MPa. This plateau indicates that the MWCNT phase is resisting further densification. As expected from this plateau formation, sintering conditions used for pure alumina platelets did not yield a fully densified composite when those same condition were used to sinter MWCNT-coated platelets. The sample of

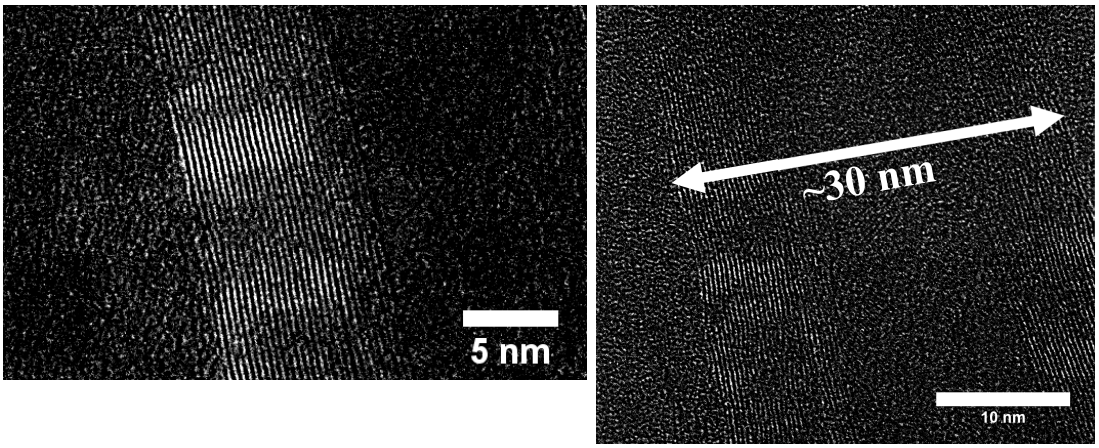


Figure 5.25 – TEM images showing 28 graphitic walls and a diameter of ~30 nm of the produced MWCNTs, from which the theoretical density of the MWCNT phase in the composite can be determined.

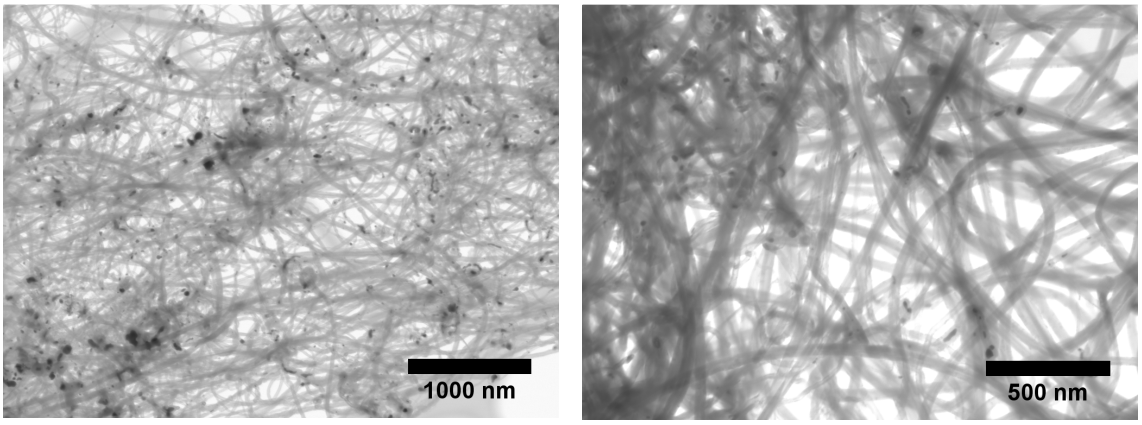


Figure 5.26 – STEM images of MWCNTs grown on alumina platelets, showing catalyst-particles inside the MWCNT structure.

MWCNT-coated platelets (10g) had a density of 3.37±0.20 g/cm^3. Sintering less material (4g) did not significantly affect the sintering behaviour and resulted in a similar density of 3.393±0.2 g/cm^3. Calculating the porosity of these composites is not trivial as their theoretical density is unknown, and determining the porosity through water impregnation methods is unreliable as carbon nanotubes are highly hydrophobic[311]. To calculate the theoretical density, Thermo-Gravimetric Analysis (TGA) analysis of the MWCNT-coated alumina platelet powder (performed in Section 3.3.8) can be used, which indicated that the MWCNT loading on the coated powder is 21 wt%. It is reasonable to assume that the MWCNT to alumina ratio is very similar in the sintered disks. The theoretical density of the MWCNTs therefore needs to be obtained which can vary from below 0.5 g/cm^3 to above 3 g/cm^3, depending on the diameter and number of walls of the produced MWCNTs[312]. Figure 5.25 shows TEM images of the grown MWCNTs, from which the diameter and number of walls of the MWCNTs can be obtained, which are around 30 nm with 28 walls respectively. According to Laurent *et al.*[312] the theoretical density of the produced MWCNTs is therefore around 2 g/cm^3. However, this is not taking into account residual iron catalyst particles that fill the MWCNTs; Scanning Transmission Electron Microscopy (STEM) data taken of the grown MWCNTs in Figure 5.26 show evidence of residual catalyst particles present within the MWCNT structure. The presence of iron oxide catalyst particles can significantly alter the theoretical density of the MWCNT phase, and it is hard to properly quantify from STEM. In addition, not all iron oxide is situated within the MWCNTs and iron nanoparticles that are situated on the surface of the alumina have to be taken into account, which will also contribute to the theoretical density of the total composite and for which only an upper limit in the form of the catalyst particle loading is known (2 wt%). Concluding, it is very hard to define the theoretical density precisely, and thus also the total porosity of the MWCNT composites. Nevertheless, using the weight fraction of the MWCNTs and iron oxide together with their theoretical densities the relative density of the composite is estimated to be 80-95%. Another way to determine how many pores are left in the structure after sintering, is

to visually inspect the material in SEM, although there is the possibility that grinding and cutting procedures may dislodge material and give a false sense of porosity in the structure.

5.3.7 Nacre-like composites using CVD-grown MWCNTs – Mechanical properties.

Three-point bend tests of the MWCNT/alumina composites show that by incorporating MWCNTs in the ceramic structure, the brittle behaviour usually observed in ceramics has been replaced by the more gradual failure as observed in nacre. Figure 5.27 shows that the strength of the MWCNT/alumina composite is between 30-70MPa, showing a bimodal distribution of strength values. The lower strength values can be due to the difficulties in polishing such relatively porous structures – a perfectly polished surface was not obtained and thus imperfections at the surface may lead to crack initiation below the ideal strength of the composite. The relatively porous structure did provide other challenges in the manufacturing of matchstick sized specimens as well; not applying a perfect homogeneous pressure in grinding can quickly cause a height variation within the sample and in addition, grinding with very rough sandpaper may pull out bigger chunks of material. Furthermore, manual cutting using a clamp and diamond saw that is moved through mechanical knobs contributed to a width variation in the above specimen. Both height and width variation within the sample tested in Figure 5.27 was around 10%.

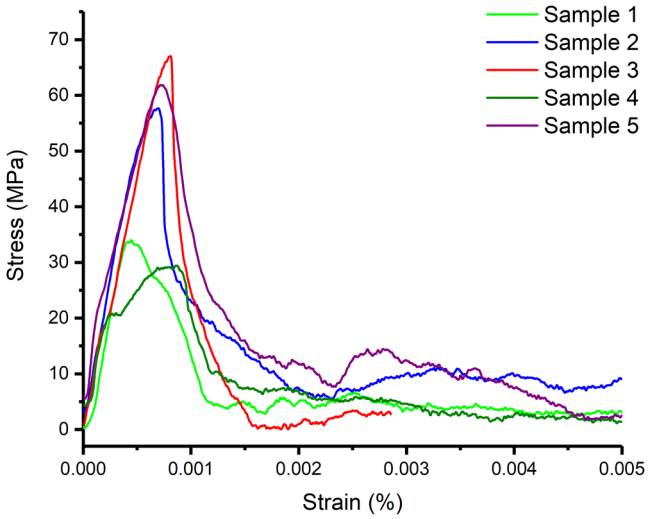


Figure 5.27 – Three-point bend test stress-strain curves of MWCNT-coated alumina platelet composites.

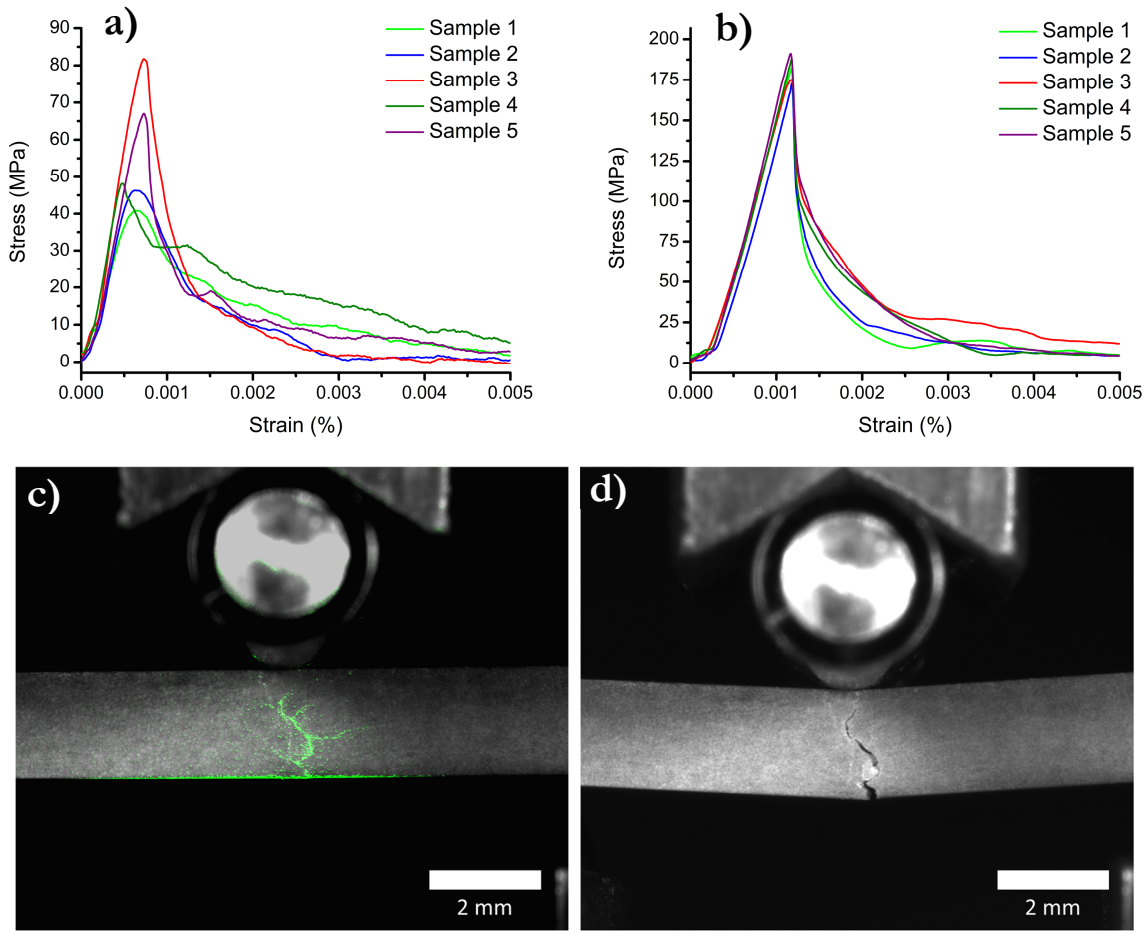


Figure 5.28 – Three-point bend test stress-strain curves of a) Alumina in a brick-and-mortar structure of aligned platelets and b) MWCNT-coated alumina platelet composites, showing that the MWCNT incorporation results in graceful failure. d) The pure alumina beam with a frame just after crack initiation coloured green overlaid on a frame without any cracks, showing the internal damage and d) the beam showing the fracture path and macroscopic interlocking well after the fracture event in the three-point bend test.

To improve the reliability of the measurements, the experiment was repeated using a custom diamond blade mounted on a microscope-guided dicer, commonly used to cut silicon wafers. In addition, milder polishing methods with diamond impregnated polymer sheets were used and common silicon carbide sandpaper was avoided altogether. The width and height variation were reduced to around 1% using these methods.

The resulting MWCNT/alumina composites show slightly higher strengths of 40-80MPa after the modification of the sample preparation method, and reproducibly exhibit the highly nacre-like non-brittle behaviour observed before (Figure 5.28a). However, the large variation in strength between samples seems inherent to the material and they have relatively low strength values compared to pure alumina platelet materials; ceramics made of pure alumina platelet powder, sintered using the same sintering procedure, exhibit strengths between 175-195 MPa (Figure 5.28b). Their failure mechanism is slightly different though; when these

pure alumina platelet ceramics (without the MWCNT-coating) were tested in three-point bend tests, the load-displacement curve shows that instead of a pure 'nacre-like' gradual failure as observed in the MWCNT/alumina composite, the pure alumina platelet ceramic initially fails in a brittle fashion as evidenced by the vertical line in the load displacement curve. After this initial brittle zone, further crack growth is resisted. SEM revealed thickened platelet-like structures with a thickness around 5-10 times that of the platelets pre-sintering (Figure 5.30b). The thickened platelets were aligned in a nacre-like brick-and-mortar structure. These structures dissipate fracture energy through a very tortuous crack path (Figure 5.31) and show crack branching and crack deflection (Figure 5.31a-b), platelet-interlocking (Figure 5.31c), as well as crack deflection around platelets and crack bridging (Figure 5.31d).

In contrast with non-bioinspired/conventional alumina and the MWCNT-coated freeze-cast composites which break violently in a brittle fashion and show a straight crack with both pieces being catapulted from the bending rig, both the pure alumina platelet and MWCNT-coated platelet composites have wavy fracture surfaces (Figure 5.30a,c), show tortuous crack paths and hold together on the bending rig after failure (Figure 5.28d-e), accentuating their non-brittle nature. While having a lower strength, there were several notable improvements that the MWCNT-coated alumina platelet composites had over the alumina platelet-only ceramics. Most importantly, load-displacement data (Figure 5.28a) revealed that composites made with MWCNT-coated alumina building blocks do not have an initial brittle zone but fail in a completely non-brittle fashion, showing a stable graceful failure from the onset of fracture which mimics the mechanical response of nacre in three-point bend tests completely. Figure 5.29 and 5.30d show that the CVD-grown MWCNTs act as a spacer and prevent the platelets from sintering into thicker platelet structures. From this observation it is likely that the catalyst particles located at the origin of the MWCNTs play a minimal role in the mechanical response of the composite other than the attachment of the MWCNTs. A maintained small platelet-size allows for platelet-platelet interactions such as interlocking and

sliding to occur on a 5-10x smaller scale than when grain growth occurs. In addition, the MWCNTs grown from the catalyst particles are well attached to the platelets as evidenced by crack-bridging mechanisms where MWCNTs are stretched in between two crack surfaces both when the crack runs parallel to the platelets (Figure 5.32a-b and orthogonal to the platelets (Figure5.32c). Evidence of this extrinsic toughening was observed up to large crack surface separations of tens of microns where longer tubes are still bridging the crack (Figure 5.32b). MWCNTs were observed to have indented the alumina platelets, and as a result were embedded in the alumina surface (Figure 5.33b). This can improve the toughening resulting from fibre bridging by generating a stronger attachment of the MWCNTs to the alumina surface. In other studies, wetting of the carbon nanotubes by alumina has been observed[313], this could potentially further increase the MWCNT attachment to the platelets, assisting toughening mechanisms. During crack growth, the attachment of MWCNTs can result in cascading MWCNT pull-outs as evidenced by large clusters of MWCNT-coated platelets that bridge the crack (Figure 5.32a-b, 5.33a). Since the MWCNT-coated alumina platelet composites fracture in a stable manner, a quantitative measure of this toughening by determining the work of fracture γ_f can be obtained. The work of fracture is defined as the area under the load-displacement curve of a specimen in stable fracture, divided by twice the cross-sectional area of that specimen and is between 67-106 J/m^2 (An average of 80 J/m^2 over 5 measurements) for the composites in Figure 5.28a. Monolithic alumina has a fracture toughness K_c between 3.0-6.0 MPa$\sqrt{}$m and a Young's modulus E between 410-380 GPa[80]. Using the Griffith energy criterion for crack growth, the critical mechanical-energy release rate is $G_c = 2\gamma_f = K_{Ic}^2/E$ [73]. Monolithic alumina therefore has a work of fracture between 11-47 J/m^2. The MWCNT-coated alumina platelet composites show a significantly higher work of fracture which is in agreement with the observed toughening mechanisms.

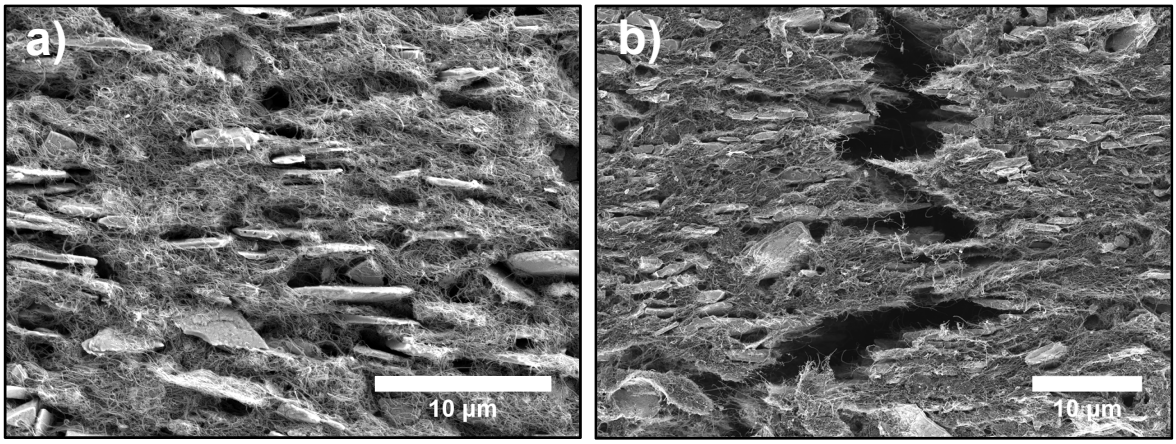


Figure 5.29 – SEM micrographs of the side view of a sintered MWCNT/alumina composite, showing a) a large amount of porosity within the structure and b) a crack propagating through the composite.

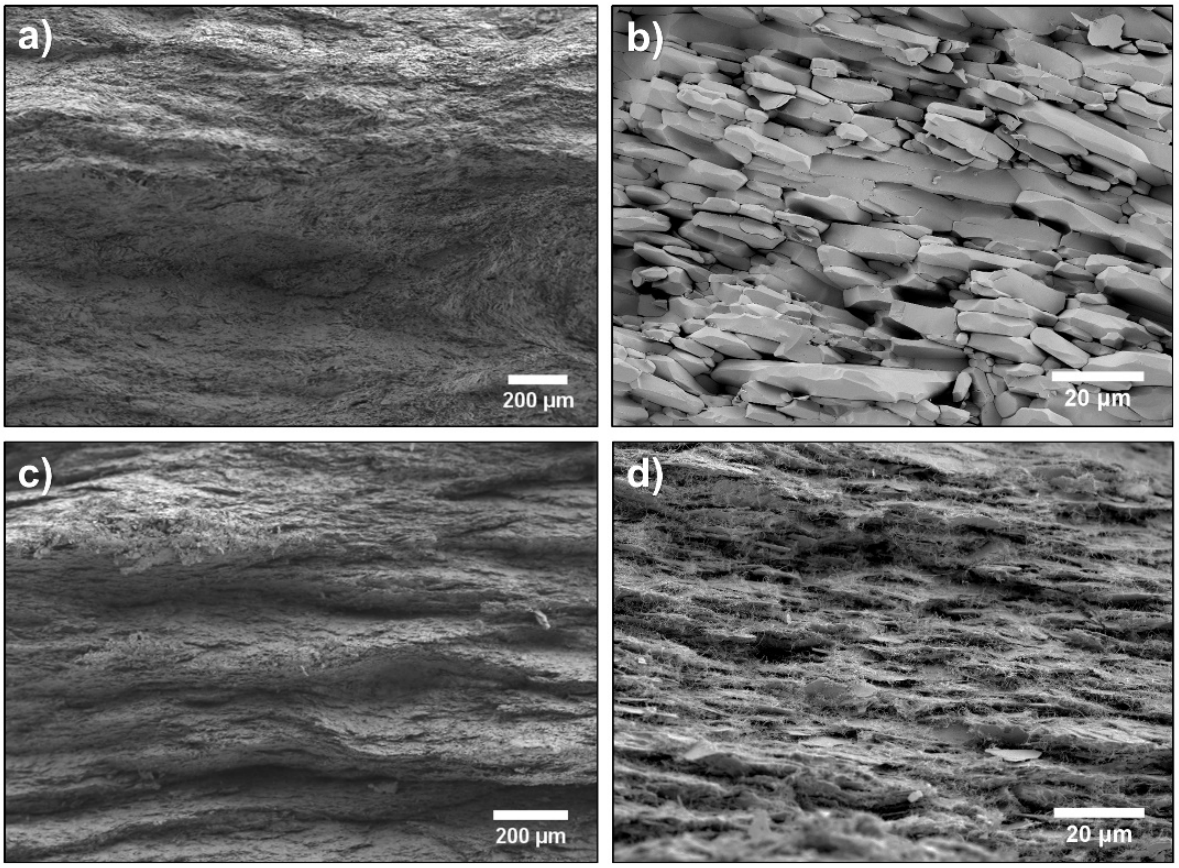


Figure 5.30 – SEM micrographs of a fracture surface of a broken beam of a-b) densified alumina platelets and c-d) densified MWCNT-coated alumina platelets.

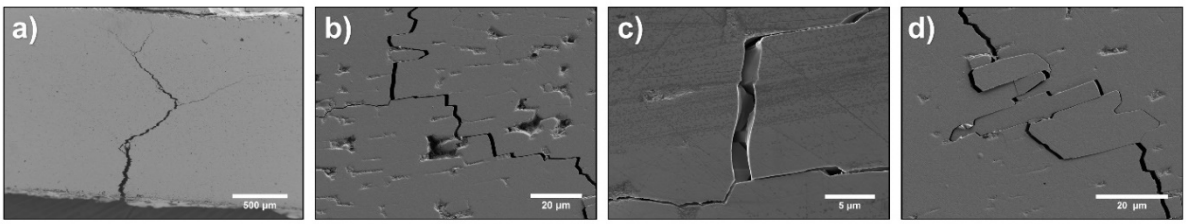


Figure 5.31 – SEM micrographs of a polished beam of sintered alumina platelets after three-point bend testing, taken from the side of the beam, showing a) macroscopic crack branching and deflection b) microscopic crack branching and deflection c) platelet-interlocking and d) crack bridging.

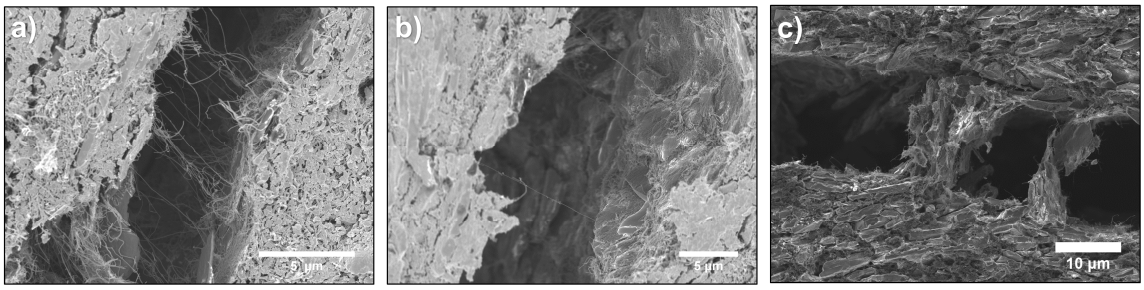


Figure 5.32 – SEM micrographs of a sintered and polished beam of MWCNT-coated platelets after a three-point bend test showing a crack propagating parallel to the platelets, showing a) crack-bridging of stretched MWCNTs over distances of around a) 5 µm and b) 20 µm. c) crack bridging of chunks of platelets attached with clusters of MWCNTs.

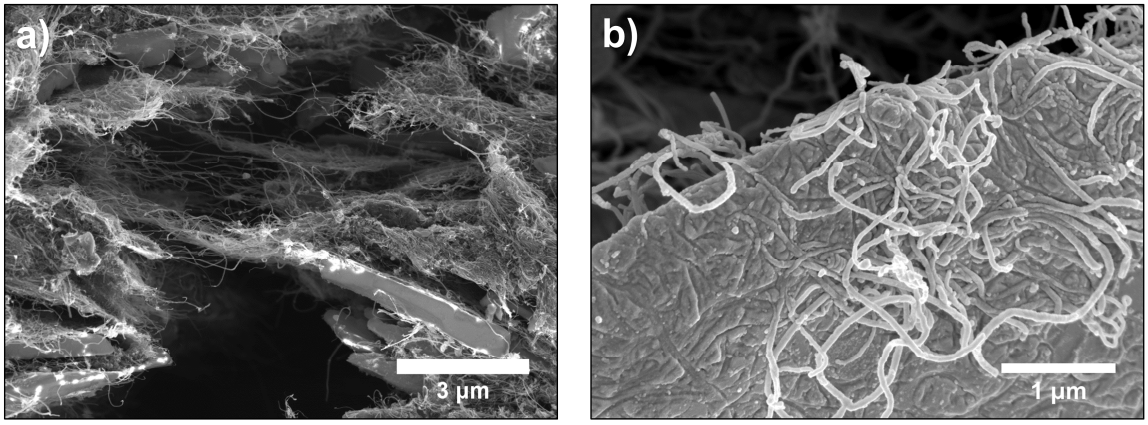


Figure 5.33 – SEM micrographs of a sintered and polished beam of MWCNT-coated platelets after a three-point bend test showing a crack propagating orthogonal to the platelets showing a) Crack bridging of MWCNTs and b) a MWCNT-coated alumina platelet after sintering, showing a modified surface as a result from the SPS procedure.

The MWCNT-coated platelets have also great potential as fillers in epoxy and polymer matrix composites[37,76,77]. In addition, these intercalated MWCNT networks can potentially be used to monitor the formation of defects and cracks, or as a Joule heater[78]. As MWCNT's have been shown to increase electrical conductivity in non-bioinspired composites before[26–28,79], resistivity measurements of the MWCNT-reinforced composites were done, which yielded values between 0.16 Ωcm (high current) and 1.03 Ωcm (low current). These values accentuate the potential for application in a multifunctional composite.

5.3.8 Viability of the CVD approach in lab-scale composite manufacturing

To further improve the composites described in 5.3.6, optimising the sintering procedure, using shorter MWCNTs or introducing a third phase are all promising manufacturing routes toward a fully dense nacre-like MWCNT-reinforced ceramic that is toughened and non-brittle while maintaining a high strength.

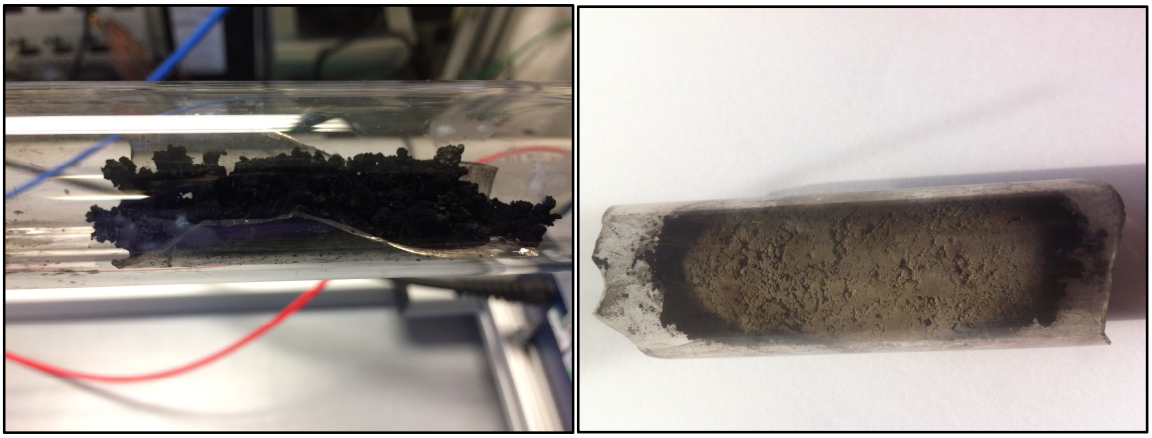


Figure 5.34 – Optical image of MWCNT coated alumina platelets showing a) a dark black material resulting from the deposited MWCNTs and b) a grey material on the bottom of the powder, indicating the carbon precursor did not reach this part of the powder.

However, scientifically rigorous research towards optimizing these composites is held back by the small quantities in which the powders are produced. Quantities per CVD run are in the 1-gram range per CVD procedure. Larger quantities often have the problem of large volumes of powder with inhibited MWCNT growth, due to the carbon precursor gases not being able to reach inside the powder (Figure 5.34). To generate composite disks with sufficient diameter and thickness, 8-9g of material is needed per sample, which translates to around 12 hours for just the MWCNT coating procedure. In addition, when the composite changes significantly in terms of MWCNT loading or when other materials are added, the conductivity can be greatly affected. As the sintering method uses electrical current to densify the sample, this means that the SPS/FAST sintering press has to be recalibrated to make sure intact disks are generated that are exposed to a controlled amount of current and heat, which doubles the amount of material needed per condition. Even when correctly calibrated,

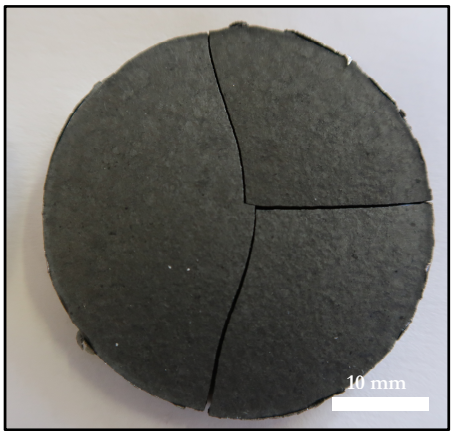


Figure 5.35 – Optical image of a MWCNT/alumina composite disk that has cracked during the SPS procedure.

in some cases fracture the composite disk during SPS was observed (Figure 5.35). In these cases an insufficient amount of testable composite beams (or none at all in the case of both a vertical and horizontal fracture) was obtained, further increasing the time cost to research these composites.

To be able to have sufficient material to explore a meaningful parameter space, it is therefore vital to upscale the CVD procedure. To do this, a thin layer of alumina platelets coated with catalyst particles was placed in a custom quartz tube with sufficient length to be able to move over different sections while gases are running. This procedure can significantly reduce the time taken to coat the alumina platelets with MWCNTs. However, a drawback of this method is that platelets are exposed to the carbon precursor not only in the designated zone where the temperature profile is 800C, but also to lower temperatures. The different temperatures

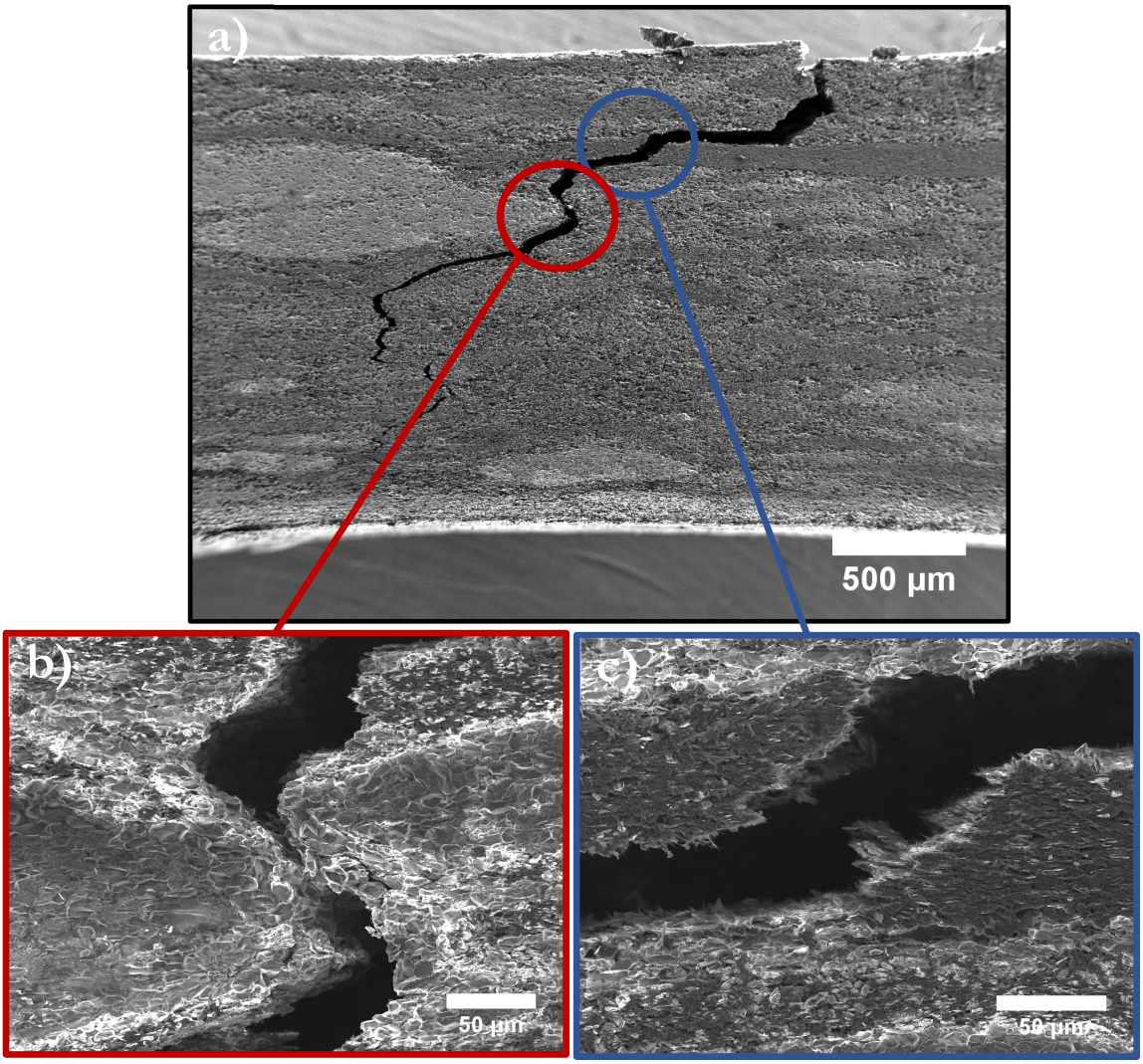


Figure 5.36 – SEM micrographs of the side of a beam of sintered, inhomogeneously coated platelets after a three-point bend test showing a) crack propagation through both b) MWCNT-deprived and c) fully coated regions.

affect the catalyst activity and precursor decomposition, and as a result amorphous carbons deposit on the platelets. Schu *et al.*[227] found that in the presence of an amorphous carbon coating, only graphitic encapsulation of the particles is obtained, without MWCNT growth. The process therefore inherently will yield an inhomogeneous powder, resulting in an inhomogeneous composite (Figure 5.36).

To ensure that the exposure of the platelets to the carbon precursor and temperature is well controlled while still allowing gaseous carbon species to reach all platelets, freeze casting presents a solution. By freeze-casting alumina platelets, a very porous green body of alumina platelets can be generated. This makes it possible to massively increase the reactive surface area by flowing the gases through this porous scaffold, instead of over a more compacted powder. In this way the full volume of the quartz tube inside the 800 °C zone of the tube furnace can be utilised and homogeneous exposure to the CVD gases of a large amount of alumina platelets at once is ensured.

One of the challenges here is the chemistry that is involved to disperse alumina platelets for freeze casting. The volume of the platelets is 10^5-10^6 times bigger compared to alumina nanoparticles, which increases the sedimentation behaviour significantly. To generate a scaffold of alumina platelets, a well dispersed suspension is needed which is only obtained with significantly increased quantities of chemicals such as polymer binder. The large amount of polymer binder in the scaffold is not suitable for CVD – the polymer stay in the structure and interferes chemically with the catalyst and substrate in the CVD procedure as well as the sintering procedure, is not stable at high temperatures and collapses the scaffold when heated during CVD. A solution to create a purely alumina/MWCNT composite and maintain a rigid scaffold structure during CVD, is presented by including alumina nanoparticles. Alumina nanoparticles can bind the alumina platelets in a sintering step before CVD, so that a rigid porous structure is maintained to facilitate gas flow through the sample without the drawbacks of a polymeric binder. In this separate sintering step, any leftover polymer binder

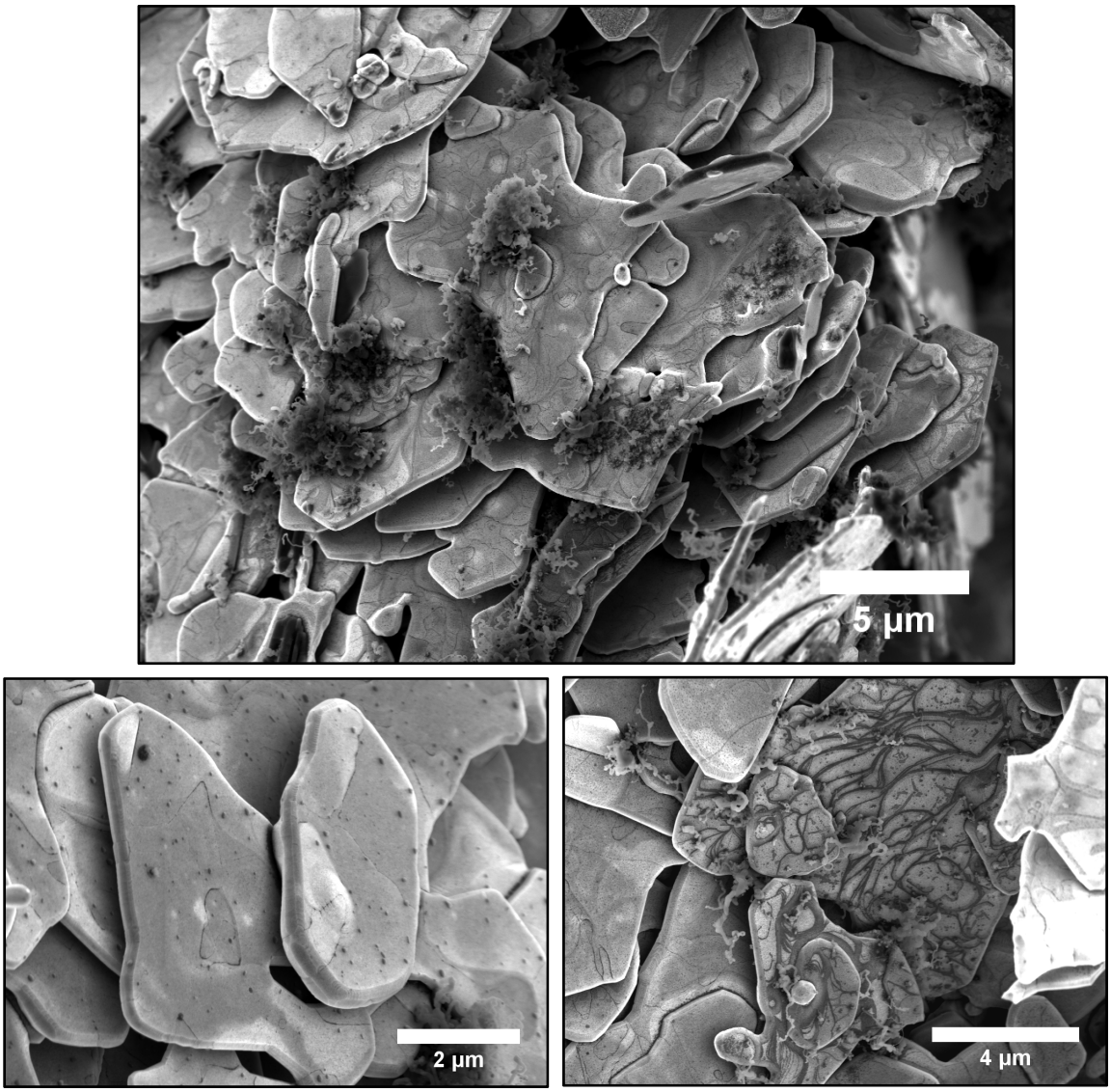


Figure 5.37 – SEM micrographs of a platelets with 3wt% 400nm alumina nanoparticles in a freeze cast scaffold (freeze cast using a 10° copper surface, with a 1 °C/min cooling rate and a 2hour pressure-less sintering step) Showing that after CVDP[14] no MWCNT coverage is obtained.

is burned away while at the same time the alumina platelets are sintered together through micron-sized mineral bridges, initiated by the alumina nanoparticles.

While this procedure produces a rigid green body of alumina platelets, the introduced alumina nanoparticles/bridges in the structure can diminish strength as shown in Section 4.3.2. Irrespective of the loss of strength, the scaffolds did not yield MWCNT growth in CVD when subjected to the pre-sintering procedure (Figure 5.37). This may be due to the basic conditions used to generate a good suspension. The freeze casting slurry left large amounts of NaCl on the surface which has long been known to be able to react with alumina to create sodium aluminate[314]. Even if these issues are solved by tailoring the sintering and

dispersion method, and using cleaning procedures after sintering, alumina platelets connected by mineral bridges in a pre-sintering scaffold are less mobile due to the alumina nanoparticle bonds/mineral bridges that were generated. This may depreciate the movement of the platelets when pressed in SPS and therefore interfere with the self-alignment in SPS that platelets exhibit[259], and therefore result in a much less nacre-like microstructure. In addition to unaligned platelets in the structure, inconsistent large-scale alignment may also result in large sections of platelets being crushed during SPS.

In summary, the fabrication and optimisation of composites made of coated MWCNT-alumina platelet building blocks is held back by the small quantities that can be produced in reliable quality using lab-scale equipment. Upscaling of the shown method has been attempted using a moving furnace and freeze-cast porous structures, but both have drawbacks resulting in inhomogeneous composites. Successful upscaling of the shown method would require an industrial scale setup where the 800 °C zone of the furnace is significantly enlarged so more powder can be coated at the same time.

5.3.9 Nacre-like composites using shear mixed MWCNTs

Although sonication is a very popular technique to disperse CNTs, Huang *et al.*[315] show that the stress input level delivered by sonication is much higher than the fracture resistance of MWNTs. It makes sense therefore, to look for an alternative method that delivers a milder energy density to promote the breaking up of MWCNT aggregates without breaking them. High shear mixing, a technique already used to exfoliate graphite[316] as well as 2D nanomaterials[317], is in this regard of great interest; the energy level generated in high shear mixing is orders of magnitude lower than an ultrasonic cavitation event and therefore promises to be a better dispersion method for MWCNTs if it is able to provide enough energy to de-agglomerate MWCNT powders. Indeed, high shear mixing has recently been found to be both highly efficient, up scalable and much less damaging than sonication for

the dispersion of CNTs[318,319]. Therefore, high shear mixing is used here to separate the MWNT-aggregates without causing much damage to MWCNTs.

After removal of the shear stress the MWCNTs will likely re-agglomerate over time, and sediment as a result. Therefore, the alumina platelets/MWCNT were mixed right after the shear mixing procedure. The final mixture of MWCNTs and platelets were not shear mixed together but subjected for a short time to a sonic bath, after which the mixture was freeze dried to yield a homogeneous powder.

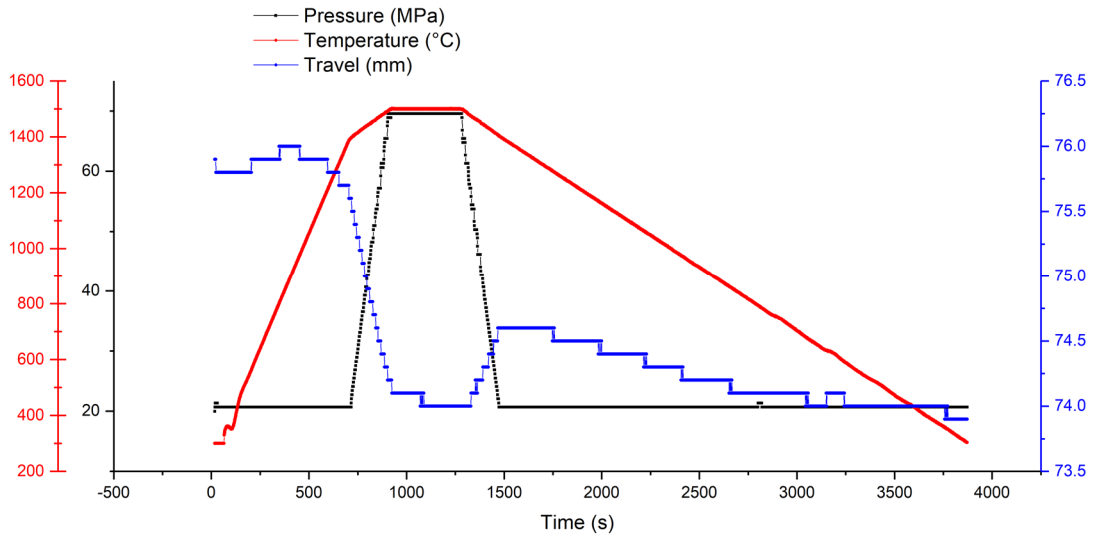


Figure 5.38 –Sintering curves of a nacre-like alumina composite made with 2.5 wt% shear mixed MWCNTs. The composites were sintered at for 5 minutes at 70 MPa and 1500 °C.

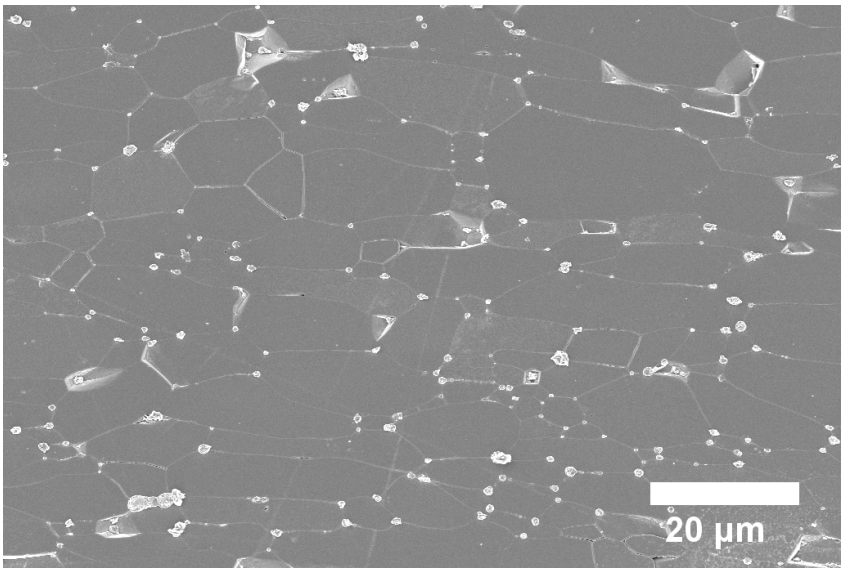


Figure 5.39 – SEM image of the side of a polished beam of sintered pure alumina platelets without MWCNT addition, showing the grain structure. The material near the grain boundaries is considered a non-native contamination, likely deposited during the removal of the epoxy which was used to embed the sample for polishing.

The sintering procedure used for these samples was re-evaluated; the dwell time was reduced from 15 minutes to 5 minutes as sintering curves of previous composites show a flat sintering curve much earlier than 15 minutes, and a reduced dwell time is known to reduce the amount of grain growth[253]. The heating rate in SPS has been found not to influence the final microstructure of alumina[320] under normal conditions and only affects the density when extremely high (>300 °C/min)[252] (although extremely high heating rates in SPS may cause large thermal gradients in the sample). A fast cooling rate however can introduce thermal residual stresses in the material, which can cause cracks and microcracks to appear in the microstructure. Natural cooling used before in the system is about 125 °C/min which is here drastically reduced to 30 °C/min to reduce any thermal stresses during cooling. A third parameter that was re-evaluated was the time and temperature at which the pressure was applied. It has been shown in both SPS of aluminium alloys[321] and silicon carbide ceramics[322] that later application of pressure can aid in reducing trapped air in the structure. The pressure was therefore ramped up only between 1400°C-1500°C where the heating rate was changed from 100 °C/min to 30 °C/min. All these parameters together with the sintering curve can

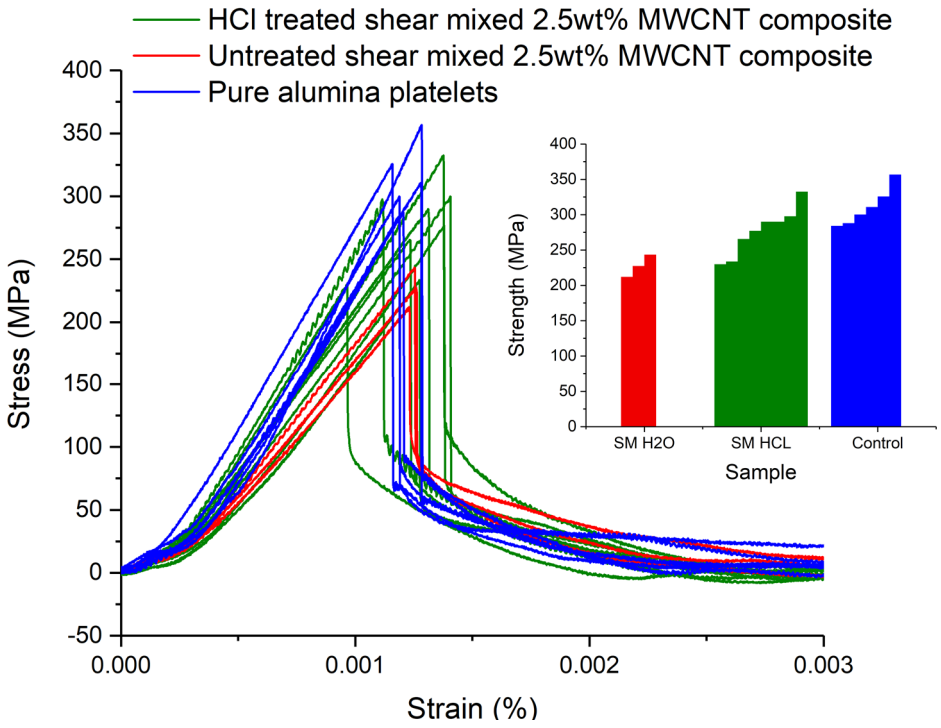


Figure 5.40 – Three-point bend test stress-strain curves of a nacre-like alumina composite made with 2.5 wt% shear mixed MWCNTs.

be observed in Figure 5.38. The resulting microstructure can still be considered mostly platelet-like, but it is evident from the size increase of the platelet-like grains that a lot of grain growth has taken place (Figure 5.39). Figure 5.40 shows that this sintering procedure yields alumina with residual strength and ultimate tensile strengths that are more than twice those seen in previous experiments.

Two dispersions of shear mixed MWCNT and alumina platelets were compared, one in water (Ph=8.2) and one where the pH was modified with HCl (Ph=0.94). From the stress strain curves of the composites in Figure 5.40, it is clear that the strength of the composites is not improved over a pure alumina platelet sample. Modifying the pH during dispersion does affect the final strength of the composite, indicating that the dispersion of MWCNTs is i

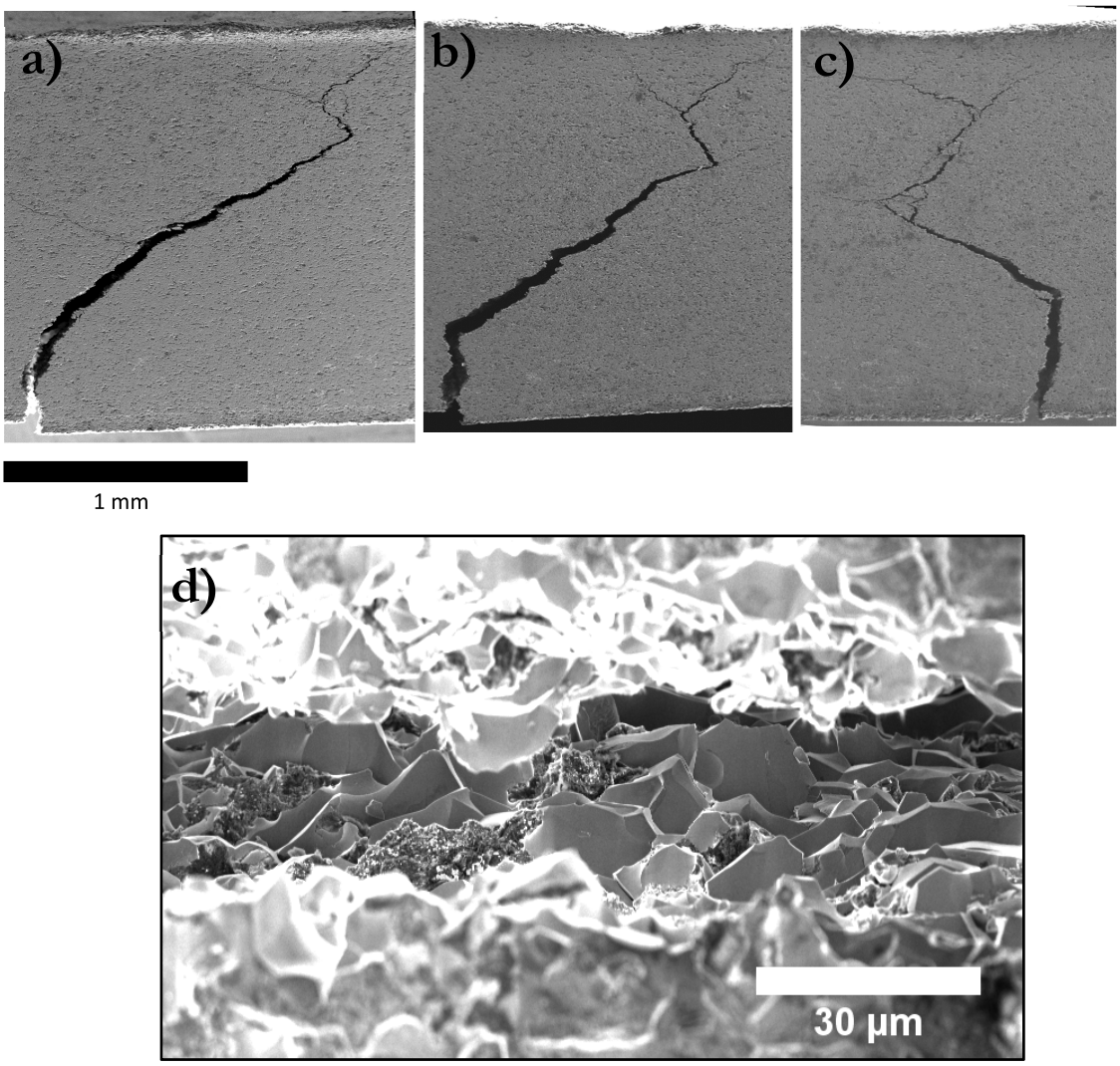


Figure 5.41 – a-c) SEM images of fracture paths of three composite beams made with 2.5wt% shear-mixed MWCNTs, showing large crack deflection and branching, and d) a SEM image taken from the crack initiation point showing the fracture surface under a 90° angle and MWCNT distribution.

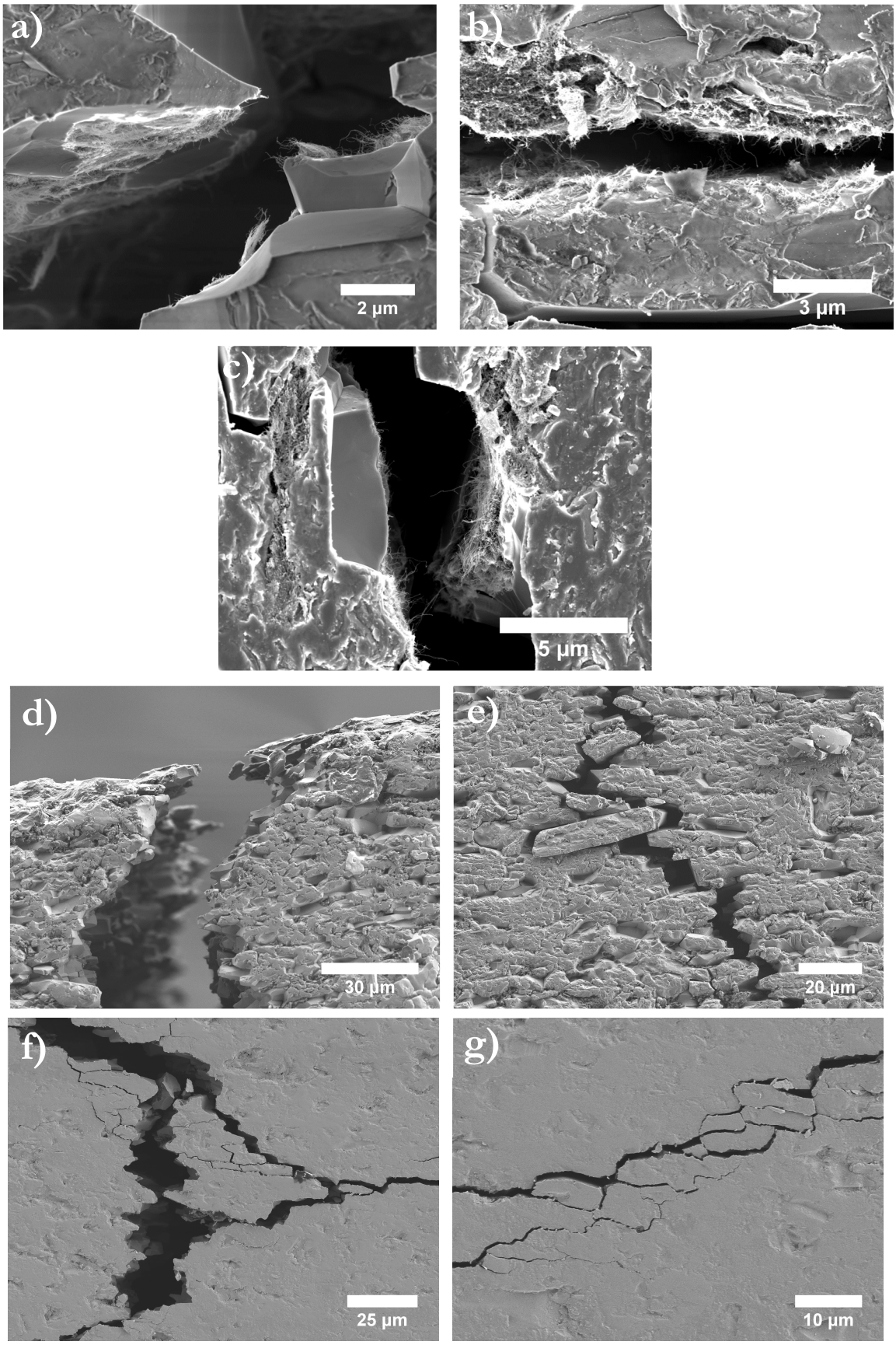


Figure 5.42 – SEM images of fracture paths of a composite beams made with 2.5wt% shear-mixed MWCNTs, showing a-c) MWCNTs coating both fracture surfaces, stretching across the crack and d-e) the crack path and deflection around the grains both at the crack initiation point as well as on the opposite side of the beam. f-g) the crack path in a polished beam showing crack deflection and interlocking mechanisms.

ndeed a major factor in composite performance. The strength of the untreated MWCNT composite and pure alumina ceramic is much like that of monolithic alumina, while at the same time the composites have a residual strength of over 50MPa after failure. These materials therefore are very promising to replace current monolithic alumina in applications where such a different fracture mechanism and residual strength is beneficial.

Figure 5.41a-c depicts the macroscopically deflected fracture paths, where it is noticeable that the crack has a large sideways component, often propagating diagonally through the material. Branching of the crack is also evident in the structure. Figure 5.41d views the crack from the perspective of the surface where the crack initiated, where the rough fracture surface is visible from a 90° angle with platelet-like grains sticking out. It is clear from this image that the MWCNTs are not homogeneously coating the platelets but have instead formed aggregates which intercalate the platelet-like grains (this is the case independent of the pH of the dispersion). Although there is evidence of fibres on both crack faces in Figure 5.42a-c, in this case the attained dispersion was confined to dispersion of small MWCNT 'yarns' which do not seem to have a large influence on the mechanical behaviour of the composite compared to the pure platelet-like alumina ceramic. Figure 5.42d-g) shows that sintering at 1500°C has resulted in large platelet-like grains which exhibit crack deflection, branching and interlocking similarly as platelet-like alumina sintered at lower temperatures.

5.3.10 Nacre-like composites using MWCNT aerogels

Complete graceful failure of bioinspired MWCNT/alumina has been observed in two instances; when a high concentration of MWCNTs are mixed with alumina platelets in powder form (Figure 5.21) and when MWCNTs are grown in situ on the platelets (Figure 5.28a). Both composites are characterized by a large 'chunks' of intertwined MWCNT 'yarns' in the composite structure. Here, a dense and highly connected MWCNT phase is generated by manufacturing a MWCNT aerogel using freeze casting, depicted in Figure 5.43. This aerogel is then mixed with alumina platelets using a vortex mixer and subjected to the

improved sintering procedure developed in section 5.3.8. (sintering temperature of 1500 °C for 5 minutes). Figure 5.44a shows that the resulting composite displays residual strength from the onset of failure. These composites replicate the 'graceful' failure shown in composites in sections 5.3.4 and 5.3.6, while having a significantly higher work of fracture between 130-184 Jm^{-2} and strengths between 120-160 MPa. Figure 5.44c shows that the graceful failure is replicated irrespective of grain growth, as specimens sintered under more extreme sintering conditions (1800 °C for 15 minutes), do similarly fail in a non-brittle manner. Figure 5.45 shows the non-brittle failure is also found irrespective of testing method; when the sample is tested in four-point bending the curve after crack initiation depends on where the crack has initiated, as a crack close to one of the rollers causes an uneven force distribution. Nevertheless, the sample fails gracefully and the increasing strength after initial fracture in four-point bending is a testament to the macroscopic interlocking mechanism.

his is significant as it shows that the platelet-like character of the grains is maintained even when a lot of grain growth has taken place due to high temperatures and dwell time. The strength and work of fracture of the composites sintered at 1800 °C however is much lower than those sintered at 1500 °C, which is likely due to the increased grain size of these composites (Figure 5.46), allowing for larger defects to exist in the structure. The composite beams sintered at 1500 °C were polished and acid treated with a piranha solution to remove the carbon content, and then thermally etched at 1200 °C to reveal the grain structure. The result is depicted in Figure 5.47. The aspect ratio of the platelet-like grains observed in Figure 5.47 is between 4.5-10, indicating that a very platelet-like character is maintained for these composites sintered at 1500 °C. Large voids of up to 100 μm are present within the microstructure where the MWCNT reinforcement used to be situated, and there is irregular grain growth at the intersection of the alumina and MWCNT phase leading to extremely 'wavy' platelet-like grains.

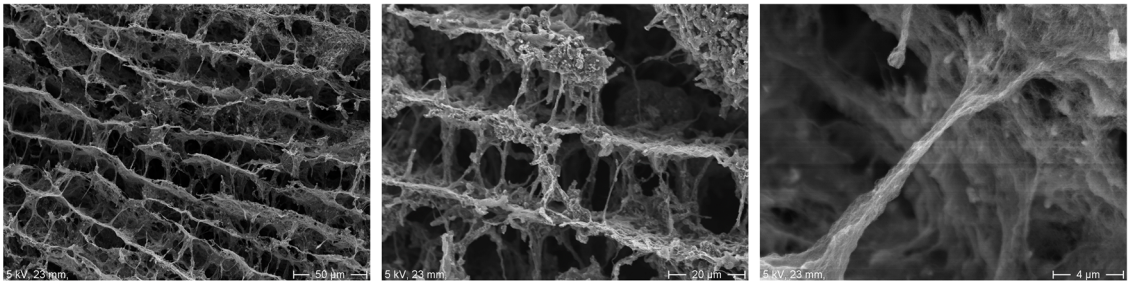


Figure 5.43 – SEM images showing a free-standing MWCNT aerogel created by freezing a viscous suspension of MWCNTs at different magnifications.

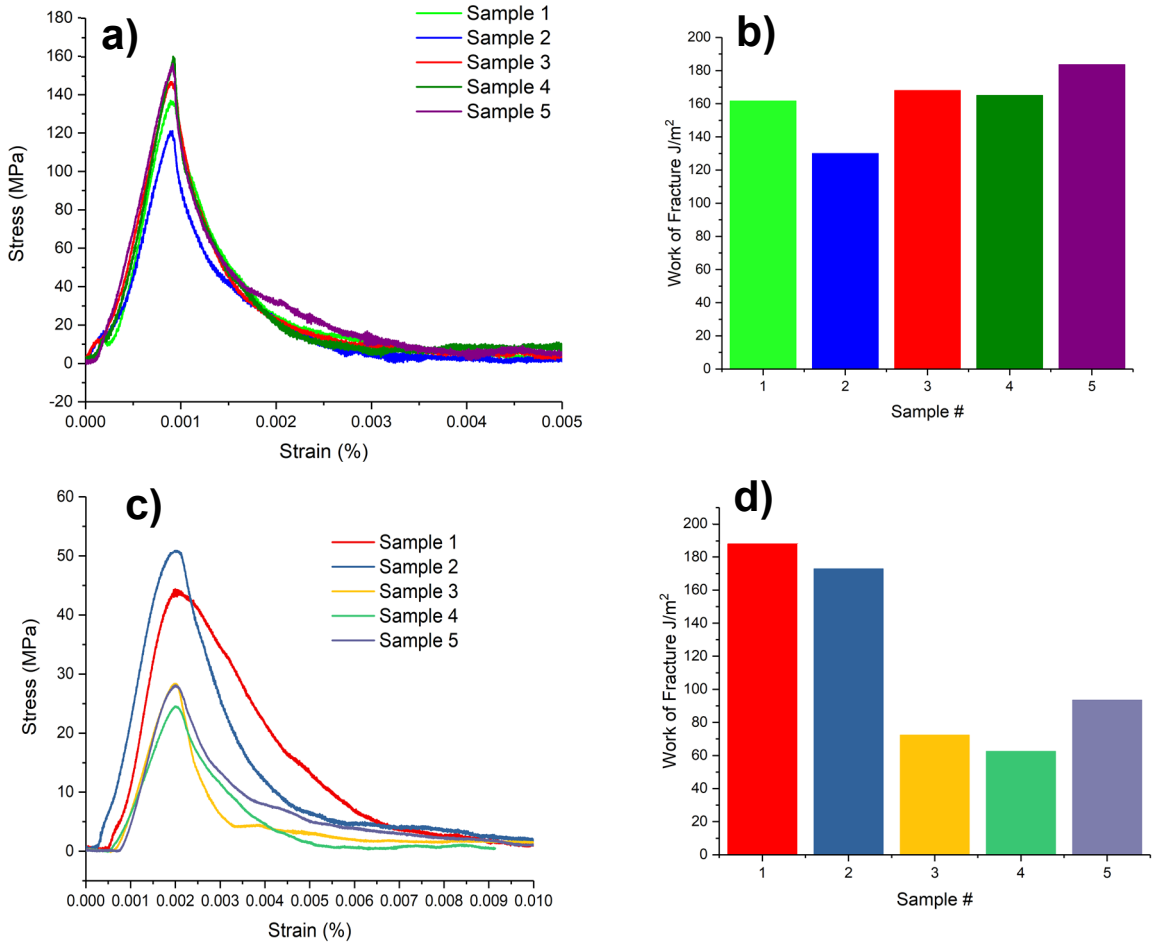


Figure 5.44 – Three-point bend test stress-strain curves and calculated work of fracture of MWCNT/alumina composites with 3.8wt% MWCNT aerogel content. a-b) sintered at 70 MPa and 1500 °C for 5 minutes and c-d) sintered at 42 MPa and 1800 °C for 15 minutes.

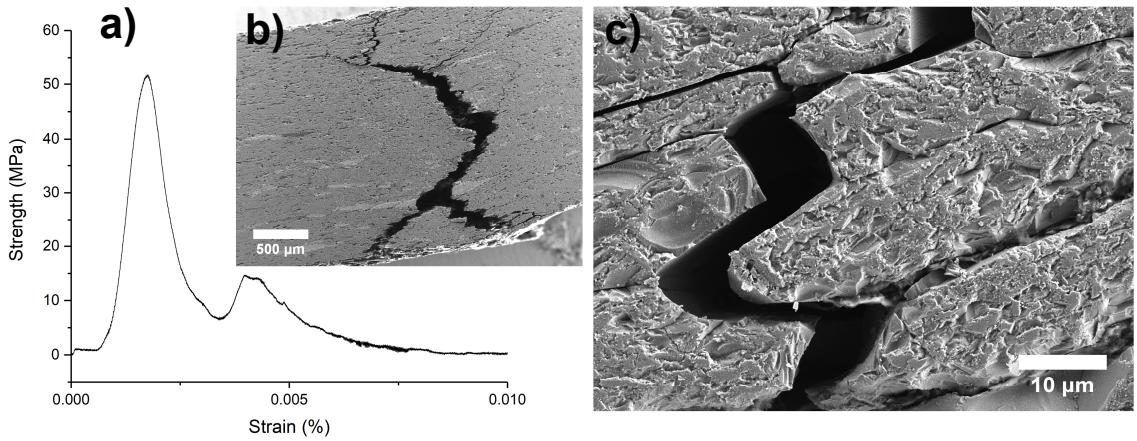


Figure 5.45 – a) Four-point bend test stress-strain curve for a MWCNT/alumina composite with 3.8wt% MWCNT aerogel content, sintered at 42 MPa and 1800 °C for 15 minutes b) Its corresponding fracture path and c) a close-up of the fracture path showing that the platelet-like morphology and 'waviness' are maintained.

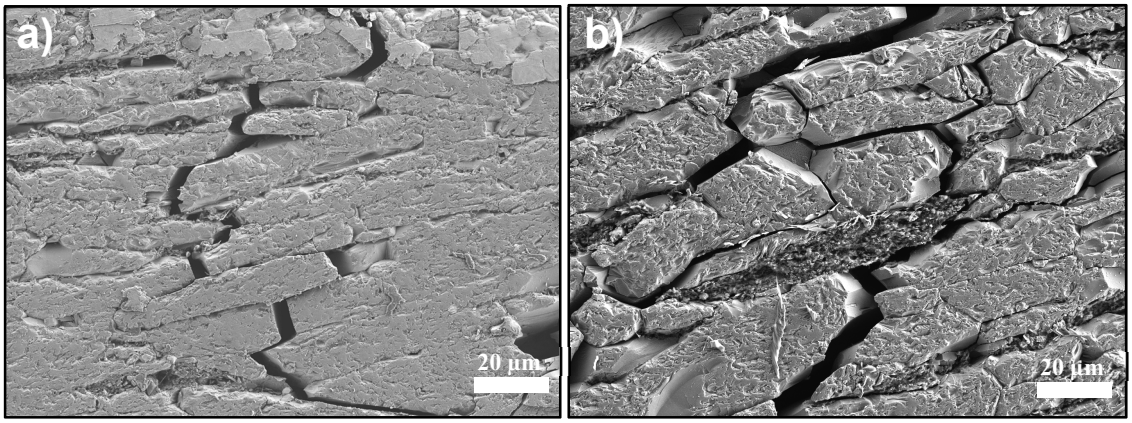


Figure 5.46 – SEM images of the crack paths in MWCNT/alumina platelet nacre-like composites showing a) a composite densified at 1500 °C for 5 minutes at 70 MPa and b) at 1800 °C for 15 minutes at 42 MPa.

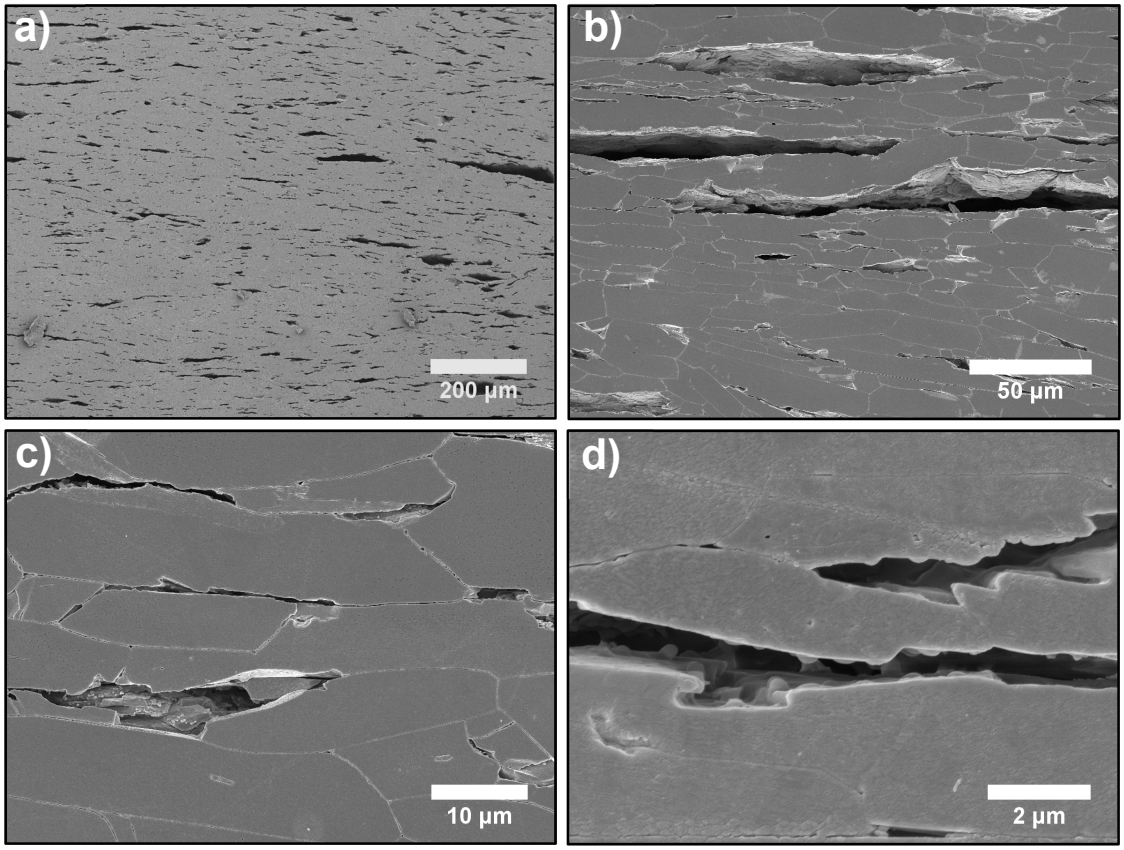


Figure 5.47 – SEM images of a polished, acid treated, and thermally etched beam of a MWCNT/alumina platelet composite beam sintered at 1300 °C for 5 minutes. a) SEM Image showing the holes in the structure, left after removal of the MWCNTs. b-c) higher magnification SEM images of the microstructure, showing the effect of MWCNT inclusions on grain shape, grain waviness and grain size distribution in the material.

5.3.11 Nacre-like composites using graphite inclusions

To fully investigate the role of the MWCNT phase, a comparison was made with composites manufactured using 5.3 wt% freeze dried graphite, which was shear mixed to de-agglomerate and reduce the size of the powder to µm-sized flakes.

The resulting composite does not show a similar graceful failure as when the MWCNT aerogel was incorporated (Figure 5.48a). Instead, after an initial brittle zone, the composite displays a residual strength around 50 MPa, much like the composites made with shear mixed

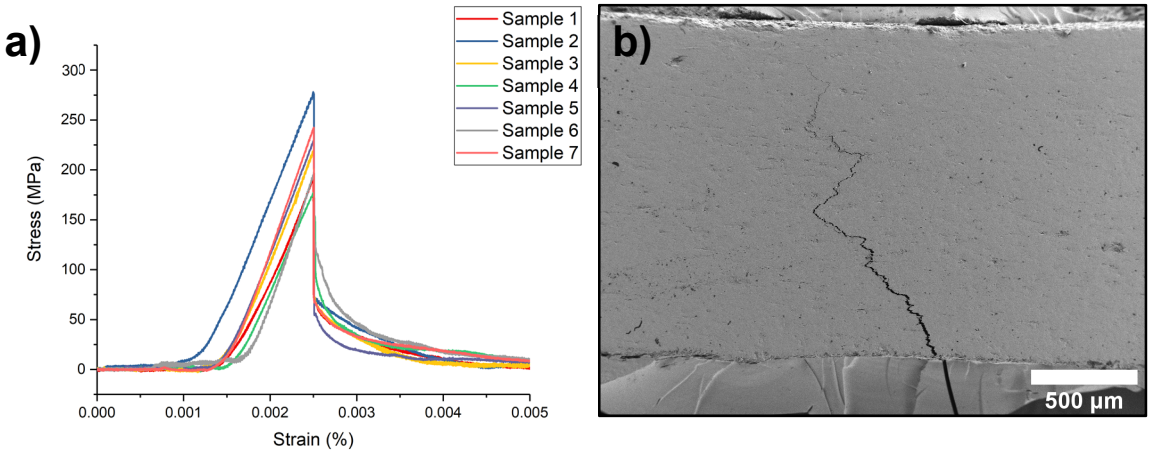


Figure 5.48 – a) Three-point bend test stress-strain curves of graphite/alumina platelet composites with 5.3wt% graphite content b) SEM image of the crack path in such a composite, where the bending test was stopped just after the fracture initiation.

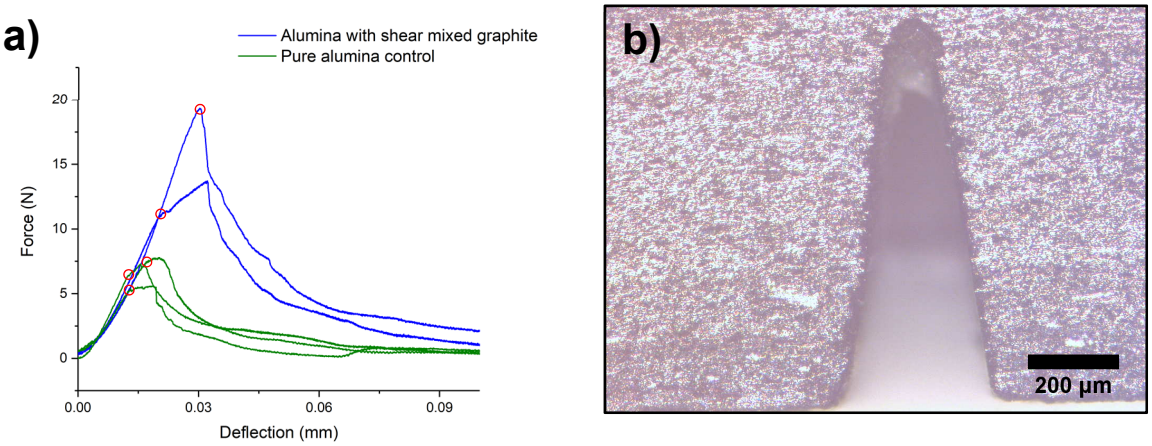


Figure 5.49 – a) SEVNB three-point bend tests curves for pure alumina and alumina containing shear mixed graphite, the end of the linear-elastic zone is marked in red. b) Optical image of a typical notch.

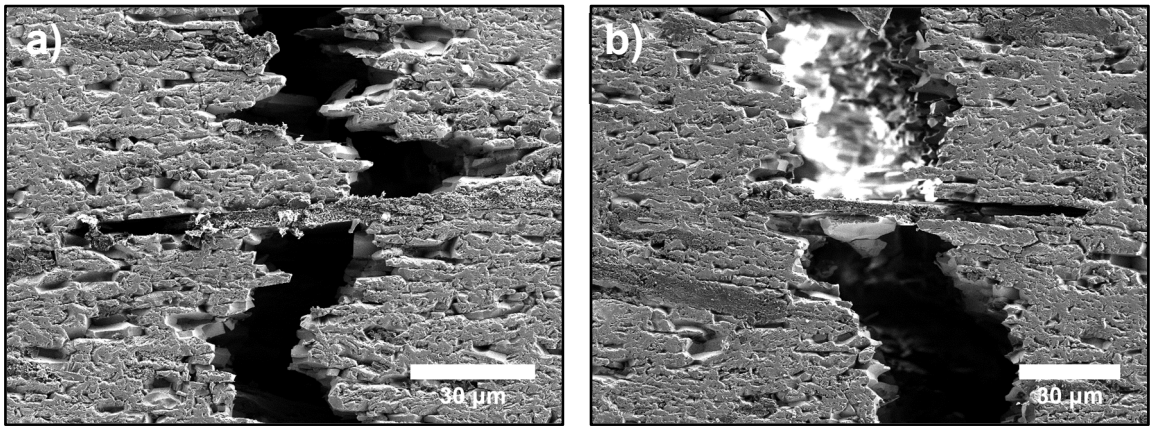


Figure 5.50 – SEM images of the crack path in a graphite/alumina platelet nacre-like composite showing large crack branching of graphite flakes in the structure, as a result from pulling out during fracture.

MWCNTs. The crack initiation toughness K_{Ic} is measured using the single-edge V-notched beam (SEVNB) method. Figure 5.49 the resulting SEVNB tests, where the specimen fail gracefully, with specimens showing stable crack propagation after the linear elastic zone as seen in similar composites tested by Bouville *et al.*[35]. The fracture toughness (K_{Ic}) of the pure alumina specimens measured in Figure 5.49a) are 2.26, 2.39 and 2.59 MPa$\sqrt{m^2}$ while the

fracture toughness of the nacre-like alumina specimens with graphite inclusions have an K_{Ic} of 1.96 and 2.43 MPa$\sqrt{m^2}$. (note that the pure alumina samples break at lower forces due to a smaller beam size). While ideally a larger number of tests should be done to determine the toughness values more precisely, it is clear from these measurements that the initial K_{Ic} values are comparable to those of monolithic alumina. It is worth noting that the K_{Ic} is here calculated using the force at the end of the linear elastic zone, at the beginning of stable crack propagation (marked in red in Figure 5.49a). It cannot be ruled out that instead of stable crack propagation, plastic deformation takes place ahead of the crack tip as is the case in nacre[2]. However, it is clear from Figure 5.49a that toughening is developed during crack growth.

A defining microstructural feature of the composites where graphite is incorporated is the crack bridging and pull-out of graphite flakes, visible in Figure 5.50. From the graceful failure observed in SEVNB tests, work of fracture values of ~140 Jm^{-2} were calculated (much larger the 11-47 J/m^2 of alumina calculated in section 5.3.7).

5.3.12 Glass phase coating of nacre-like alumina platelets

In this section, the use of a glass phase surrounding the MWCNTs between the platelets is explored. The glass phase addition aims to enhance the toughening effect of the MWCNTs between platelets by anchoring the MWCNTs to the platelets, thus increasing the sliding resistance and the amount of MWCNTs that are bound to more than one platelet. In addition, the glass phase will severely decrease the porosity of the composites as it is expected to fill any gaps left between platelets during sintering, shown previously by Deville *et al.*[35].

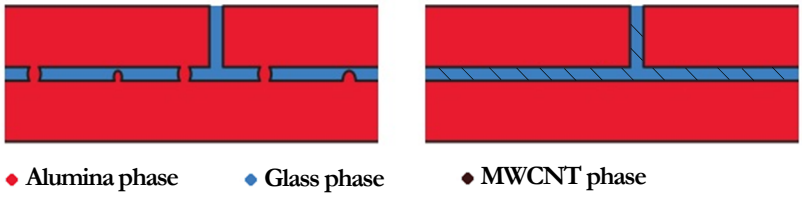


Figure 5.51 – Schematic representation of a) the nacre-like structure manufactured by Deville *et al.* and b) the proposed nacre like structure with MWCNTs manufactured here (Adapted from Deville *et al.*[35]).

A schematic overview of the model structure compared to a nacre-like structure without MWCNTs is given in Figure 5.51.

Alumina platelets have previously been used to reinforce borosilicate glass to increase toughness[91]. Mukhopadhyay *et al.*[323], who create a borosilicate glass by using a modified recipe published earlier[324] show that MWCNTs bind very well to this glass as the MWCNTs themselves are observed to break instead of pulling out. Borosilicate glasses are known for their very low thermal expansion coefficient, making them resistant to thermal shock. This makes this type of glass especially useful to use in SPS to embed MWCNTs. Monteiro *et al.*[325] show that when sintering alumina borosilicate composites at 1100 °C and 74 MPa there is negligible open porosity and high relative density. These two parameters are therefore followed here to create reinforced MWCNT-alumina bioinspired composites. Using a sintering temperature of 1100 °C also ensures the alumina platelets do not experience much grain growth as Santanach *et al.*[253] show that in 5-minute SPS procedures of pure alumina, grain growth was only observed at a sintering temperature of 1200 °C and higher. Using a sintering temperature of 1100 °C thus maximizes the number of platelet-platelet interfaces while at the same time enabling the glass phase to spread under pressure (The softening point of borosilicate glass is 820 °C).

Three samples with 1 wt% borosilicate glass were manufactured at 1100 °C, sintered for 900s. A sample containing pure alumina platelets, platelets that were coated with acid treated MWCNTs, and platelets that had MWCNTs dispersed through a shear mixing procedure were compared. The latter was also manufactured with 6wt% borosilicate glass to see the effect of glass concentration on the mechanical response in three-point bend tests. While for the 6 wt% borosilicate samples the glass phase was very clear from SEM observations (Figure 5.52 a-b), for the 1wt% samples (Figure 5.52c-d and Figure 5.53, acid treated) (Figure 5.52e-f, shear mixed) it was difficult to locate the glass particles on the platelets before sintering.

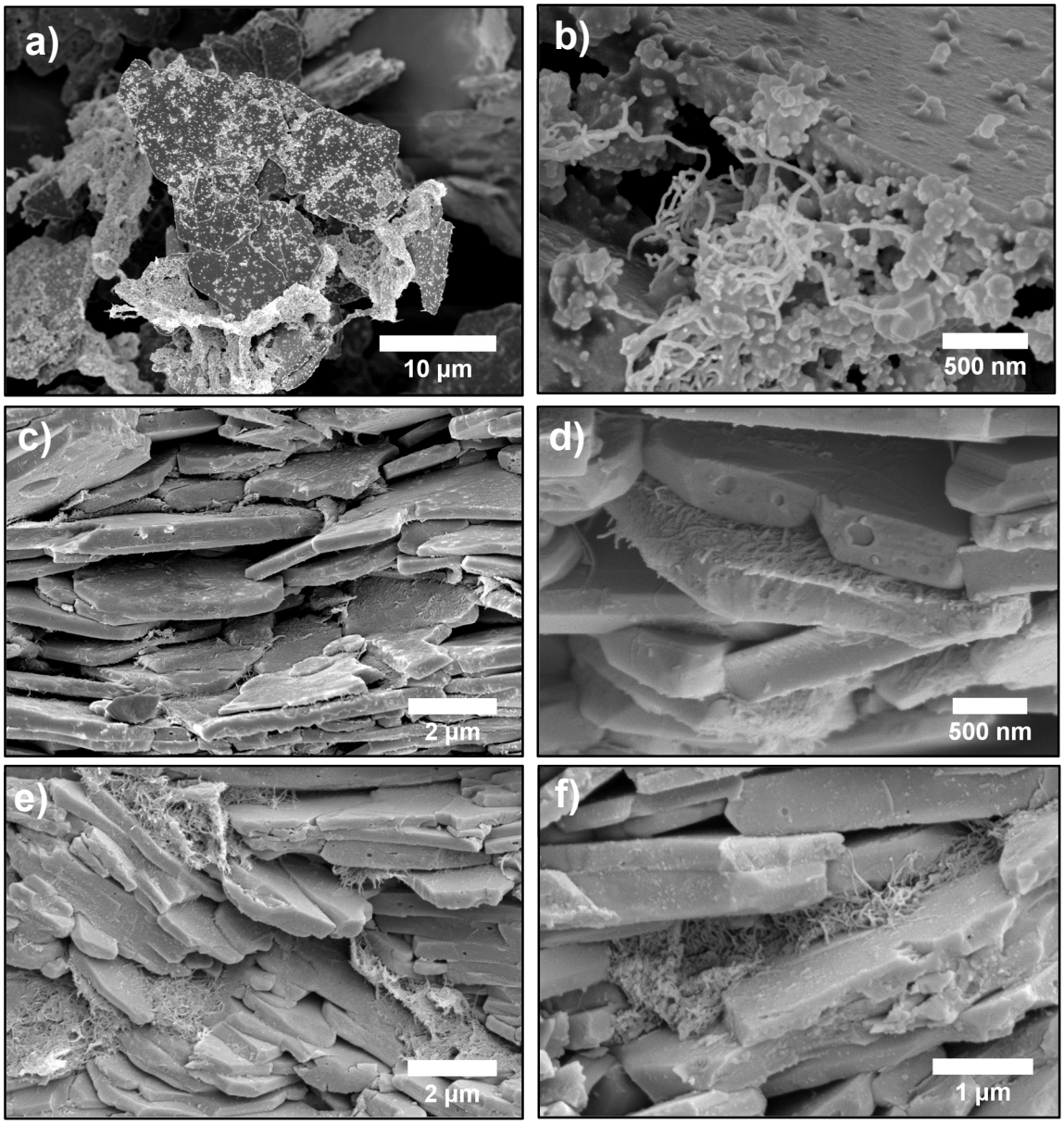


Figure 5.52 – SEM images of a-b) a 6 wt% borosilicate-coated alumina platelet powder mixed with shear mixed MWCNTs before sintering, showing MWCNTs embedded inside the glass phase. c-d) a sintered composite made with 1wt% borosilicate-coated alumina platelets mixed with acid treated MWCNTs e-f) a sintered composite made with 1 wt% borosilicate-coated alumina platelets mixed with shear-mixed MWCNTs.

Nevertheless, borosilicate glass inclusion, independent of MWCNT coating or amount of glass inside the microstructure, transformed the mechanical behaviour of the composites. Almost no macroscopic crack deflection was observed for all borosilicate glass-coated composites; cracks propagated straight through the beams as shown in Figure 5.53b. On a microscopic level it was more difficult to ascertain how the crack propagated, as due to the brittle fracture the two halves of the beam catapulted from the bending rig. However, close to the fracture surface a broken platelet was found, showing minimal crack deflection, after which the crack is stopped at the glass phase and failure of the platelet occurs (Figure 5.54). Figure 5.55 shows that regardless of loading or MWCNT dispersion, all glass-coated

composites have a typical brittle behaviour. In addition, all samples tested cracked after the SPS procedure, resulting in some cases in only one beam being able to be cut with reliable length for bend testing. Due to their brittle fracture and low strengths, these samples were not reproduced to expand the dataset.

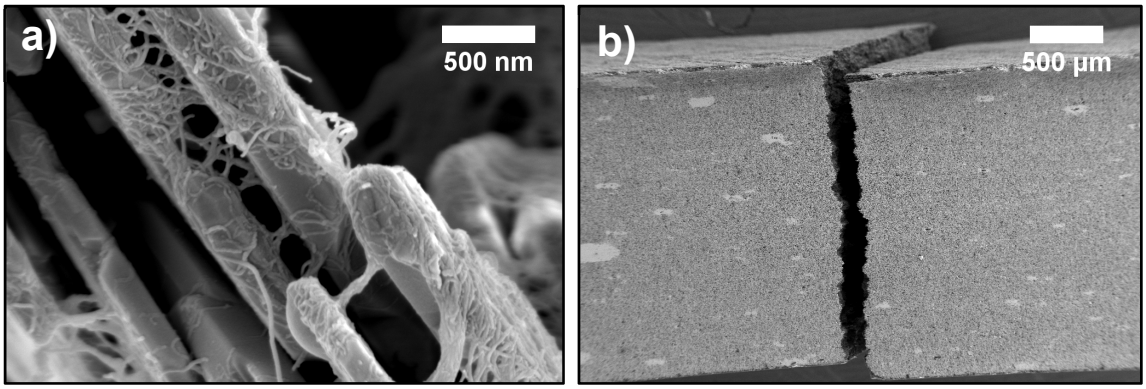


Figure 5.53 – SEM images of a) 1 wt% borosilicate-coated platelets before sintering with MWCNTs dispersed through with acid-treatment and b) the fracture through a composite beam made from these platelets, showing brittle fracture and minimal crack deflection.

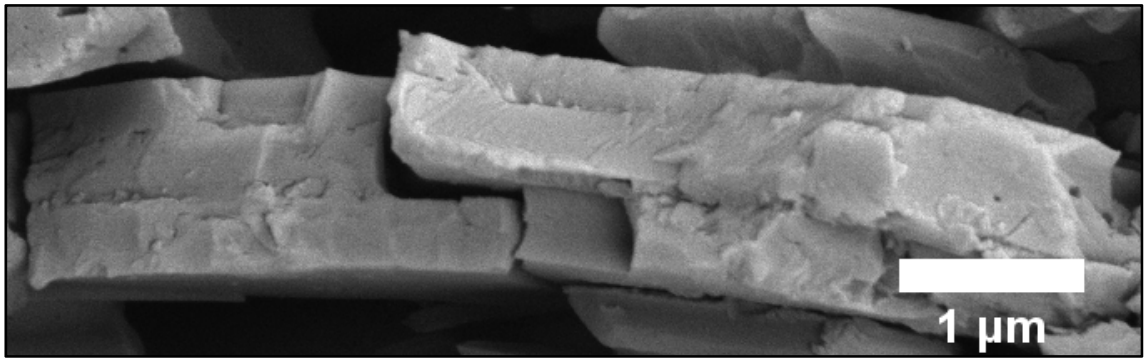


Figure 5.54 – SEM image of the side of a fractured borosilicate/alumina platelet composite, showing a close-up of a stack of platelets. The image shows that only minimal crack deflection takes place, after which the crack propagates through the platelet.

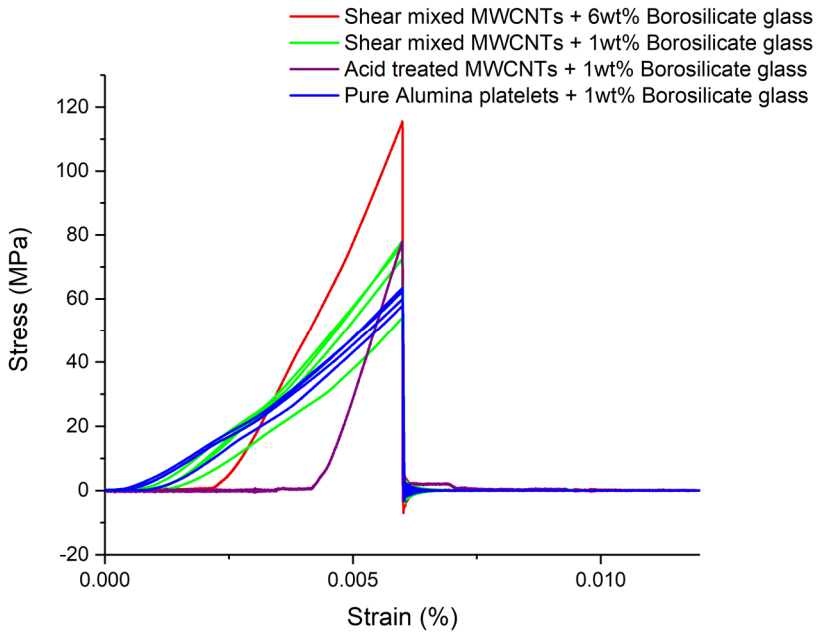


Figure 5.55 – Three-point bend test stress-strain curves of several samples of nacre-like alumina with MWCNTs and borosilicate glass incorporated in the structure, showing a brittle mechanical behaviour and poor strength values for all tested samples. All samples were sintered at 1100 and 70MPa.

The brittle failure of composites made from alumina and glass has been observed before by Bouville *et al.*[35] although they use a silica glass instead of borosilicate. Interestingly, they report that while inserting glass makes the structure brittle, the combination of the glass phase with alumina nanoparticles leads to significant toughening and non-brittle behaviour. Therefore, a composite made here with alumina and sodium silicate glass was made and sintered at 1600 °C for 5 minutes at 42MPa to make sure the glass phase melts while the rapid processing ensures that the alumina does not dissolve in the glass phase and limits grain growth.

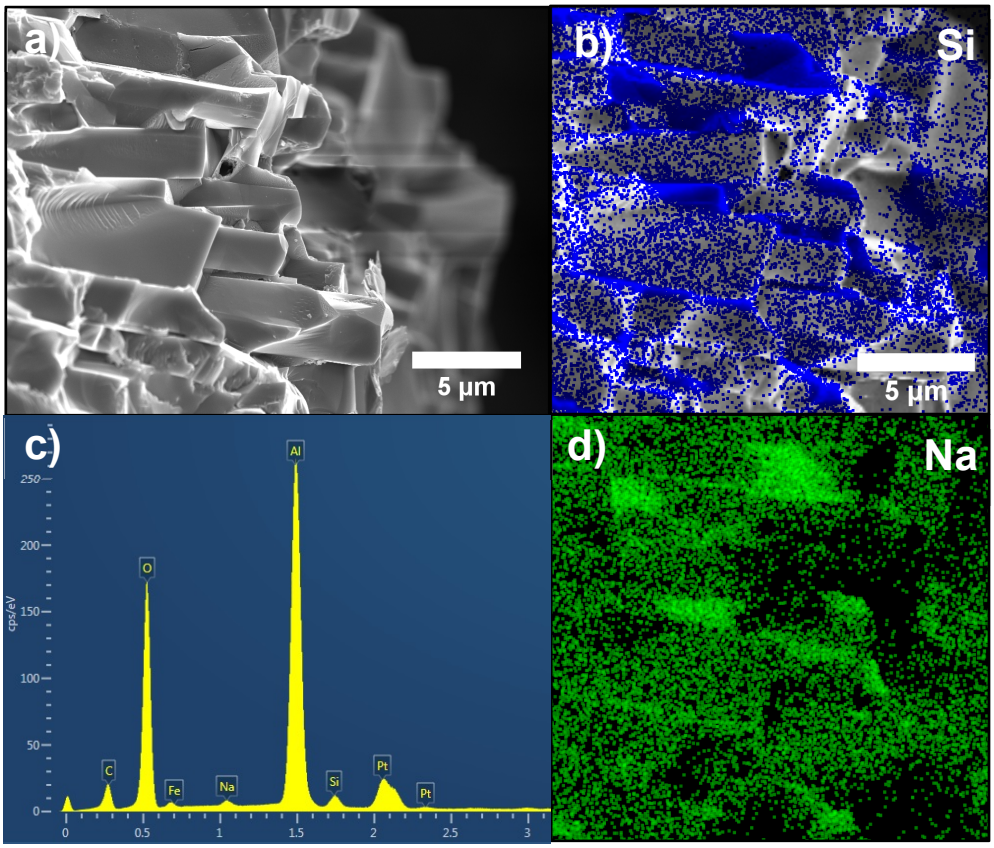


Figure 5.56 – Elemental analysis on the side of a fracture beam with 2.88wt% silica. a) High resolution SEM image of the analysed spot b) EDX map of the silicon signal overlaid onto the SEM image c) EDX spectrum d) EDX map of the sodium signal.

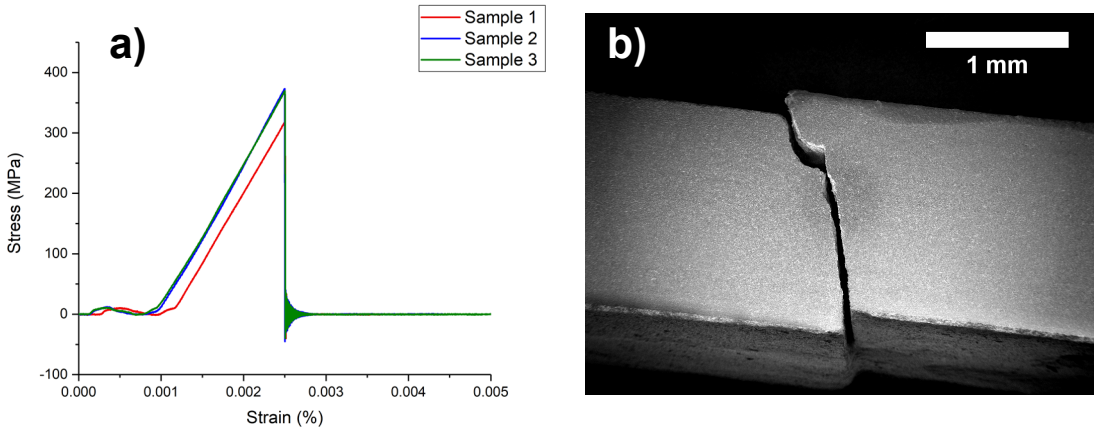


Figure 5.57 – SEM images of a) 1 wt% borosilicate-coated platelets before sintering with MWCNTs dispersed through with acid-treatment and b) the fracture through a composite beam made from these platelets, showing brittle fracture and minimal crack deflection.

Figure 5.56 depicts a close-up of the microstructure, which has 2.88 wt% silica incorporated, clearly showing the silica glass phase distributed in between platelets. In addition, a sodium signal is observed in the glass phase which can be due to the silica nanoparticle stock, as the nanoparticles are sodium-stabilized dispersions translating to about 1wt% of the glass phase being sodium. The amount of sodium signal however indicates that perhaps the de-ionized water used was of a poor grade and still contained sodium salts. The glass phase in these composites therefore is likely sodium silicate.

Figure 5.57 shows that just like the borosilicate glass, the sodium silicate glass inclusion results in a brittle composite. The greatly increased strengths of the sodium silicate glass composites are likely due to the higher sintering temperatures, fusing the glass to the alumina platelets and ensuring high enough density; Density measurements revealed borosilicate glass composites to have a very poor density with porosities between 15.4-19.3%, while sodium silicate glass composites had porosities between 3.1-4.3% (using a theoretical density of 2.23 g/cm^3 and 2.4 g/cm^3 for borosilicate and sodium silicate glass respectively).

5.4 Conclusion

In this chapter a variety of methods were used to generate bioinspired MWCNT/alumina composites. When freeze cast aligned lamellar scaffolds infiltrated with MWCNTs are sintered, the resulting composite shows completely brittle failure. The layered MWCNT/alumina structure does not provide any benefit over pure alumina.

When using alumina platelets to generate nacre-like MWCNT composites, mechanically dispersing MWCNTs through sonication did not yield a homogeneous coating of MWCNTs on the platelets irrespective of solvent used. Acid treatments were key to creating a dispersion of MWCNTs that homogeneously coated the platelets, resulting in a perfectly nacre-like structure with not only a maintained platelet size, but also with a thin layer of fibrous carbon between the platelets (not unlike the biological fibres seen in nacre). For both dispersion methods however, the MWCNT inclusion degraded the material strength when sintered using the best sintering conditions for platelet-like alumina (determined in Chapter 4).

By sintering at higher temperatures and using the CVD MWCNT coating technique optimised in Chapter 3, complete transition from brittle failure to graceful failure was shown. Although the strength of the MWCNT/platelet composite was only about half of that of the platelet-only ceramic, the composites were much tougher and lighter, and their strength was already at a usable level. Various toughening mechanisms were active due to the combination of platelets and MWCNTs, which are seen to be stretched across the crack face. The non-catastrophic failure as well as the increased electrical conductivity and reduced weight are advantageous properties. There was a relatively large volume fraction of CNTs in these composites compared to nacre, which has an organic phase content of not more than 5wt%[36,326]. It is very likely that the strength of these composites can be improved by tailoring the MWCNT length and coverage in CVD; the CNTs can be shortened by reducing the carbon precursor exposure in CVD and the amount of CNTs grown can be reduced by coating the platelets with a smaller amount of catalyst particles. This will not only improve

the density of the final composite but will yield a microstructure that more closely resembles nacre. The produced MWCNT-coated alumina platelet composites in this work show the feasibility and advantages of combining alumina platelets with MWCNTs *in-situ,* used as MWCNT-coated platelet building blocks for ceramic composites. Reducing the sintering dwell time, heating and cooling rates, and delaying the pressure application yielded alumina with platelet-like grains and significantly higher strength of over 300MPa. In addition, the material maintains a residual strength of over 50 MPa after failure. While MWCNTs dispersion through shear mixing did not improve the mechanical properties of composites with shear mixed MWCNTs, composites exhibiting graceful failure and a strength of 120-160 MPa were successfully produced by using freeze dried MWCNT aerogels. The MWCNT inhibits grain growth locally, yielding very 'wavy' platelets that plastically deform during sintering and easily interlock. It is likely that the strength of these composites can be further improved by having a more homogeneous distribution of the MWCNT aerogel throughout the material as specimens which had the MWCNT phase removed showed a wide distribution of aerogel sizes in the microstructure.Increasing the density of the composite and increasing the bonding of MWCNTs to the alumina platelets through glass coating methods was not successful, as for both borosilicate and sodium silicate glasses, even at low concentrations of 1wt%, the composites showed a transition to complete brittle fracture due to the strong interface that the glasses create. From the glass-coated composites tested in this chapter, it can be concluded that a weak interface is needed to unlock the toughening mechanisms seen in nacre. Weak interfaces alone however are not enough, as was observed when an acid treated MWCNT coating was applied to the platelets, resulting in poor strength in the final composite. The 'wavy' character of grains observed at higher temperatures are likely key for increased strength and residual strength in biomimetic composites. Such 'wavy' grains promote crack deflection, interlocking and platelet pull-out effects which play a significant role in the strengthening and toughening of nacre[7,64].

Summary and Outlook

In this work, different methodologies were applied to replicate the nacre microstructure using alumina and carbon nanotubes. In this context, the first objective was to generate a large-scale aligned lamellar microstructure. To do this, the freeze casting of alumina foams was explored. It is shown that the density, lamellar thickness and surface roughness of these foams can be modified by changing the freeze casting conditions. The challenge in this technique is not to achieve local alignment, but to achieve large-scale alignment in a consistent and reproducible manner. It was found that using recently reported alignment methods such as 1D ice initiation[140] and patterning[138] did not yield (large scale) alignment. However, by using a polished copper slope, the scaffolds were consistently comprised of single aligned domains. Although these domains often branch out, leading to misaligned lamellae over larger length scales, some large-scale aligned alumina foams could be obtained.

These porous scaffolds were infiltrated *in situ* with MWCNTs, and complete coverage of the internal surfaces was achieved using CVD. Even when considering scaffolds which consist of misaligned single domains, the achievement of cm-scale MWCNT-functionalised microstructures with continuous and separated pores is interesting for a range of applications such as gas flow cells, filtration and fluid cell setups. Considering the high amount of control over both the alumina and MWCNT morphology, further research could likely optimise the pore-sizes and further increase the MWCNT surface area for such applications.

For the manufacturing of biomimetic composites however, only completely aligned samples were taken for densification in SPS, which were pressed parallel to the alignment of the lamellae. The resulting composites show that the lamellar alignment is maintained after densification. However, the mechanical response is unlike nacre and the composites fail in a brittle fashion. To come closer to the nacre microstructure, alumina platelets with the exact dimensions of nacre's calcium carbonate platelets were investigated. Translating the freeze-casting technique to these platelets was challenging; the increased particulate size means that

the platelets sediment in suspension, and the slurry had to be modified with several additives to obtain a consistent lamellar arrangement of platelets in a porous foam. This also changed ice growth dynamics and resulted in loss of the large-scale alignment. In addition, residual chemicals were seen to inhibit MWCNT growth in the platelet-alumina foams.

The natural tendency of platelets to align under pressure proved to be sufficient to align the platelets over large length scales and thus create nacre-like ceramics. Various sintering temperature and pressure combinations were explored to create nacre-like alumina using these platelets, and the resulting textured alumina was seen to be able to show significant improvement over monolithic alumina when tested at high strain rate. In impact tests, the textured alumina remains intact with a diffuse crack pattern. This is in stark contrast to monolithic alumina, which is completely fragmented after impact. These materials therefore hold great promise in applications where such damage diffusion mechanisms are desirable, such as in armour and construction solutions.

To reinforce the ceramic with MWCNTs, a recipe was developed for a highly crystalline and homogeneous coating on the pure platelet-powder, yielding a combined building block. Identifying the catalysis and growth mechanism was useful to better understand the resulting MWCNT coating and its potential for reinforcement. It is shown that iron oxide catalyst particles are immobilized by reacting with the alumina surface, converting to a hercynite spinel at 800 °C in argon atmosphere. The strong attachment of the MWCNTs to the alumina platelet surface is demonstrated by MWCNTs that stretch across the crack face. The resulting composites show a nacre-like fracture behaviour, where after the initial fracture event the material fails gracefully. In addition, the MWCNT phase increases the electrical conductivity of the material. The strength of these composites however is relatively low, as long MWCNTs are observed to inhibit densification. To improve the strength of these composites, the amount of MWCNTs in the composite can be reduced by reducing the CVD dwell time and/or catalyst density. Future work could entail creating a setup for up-scaled production that allows the generation of large quantities of the shown combined alumina

platelet-MWCNT building blocks with a homogeneous coating. The MWCNT phase as well as the sintering procedure can then be varied in a systematic study to optimize these composites.

In addition to coating the alumina platelet *in-situ*, other methods to incorporate MWCNTs in a biomimetic alumina matrix have been compared. Especially interesting was the successful coating of acid treated MWCNTs on the platelets, which resulted in a very homogeneous thin layer of MWCNTs on the platelets, which is often entangled between platelets as well. The resulting microstructure mimics nacre very closely, maintaining the nacre-like platelet size due to grain growth inhibition of the thin layer of MWCNTs material between the platelets. However, these composites did not exhibit graceful failure and had poor strength. This result indicates that a maintained aligned platelet structure with a weak interface is not sufficient to mimic nacre's mechanical response. In these composites, mineral connections and waviness through grain growth that promote interlocking mechanisms, are not present, and thus not much resistance to crack propagation is provided. In addition, due to the defective nature of acid treated MWCNTs, they break easily, and these composites are not toughened by MWCNTs that bridge cracks or restrain platelet movement.

The sintering procedure was examined and improved upon, resulting in nacre-like alumina that displayed both high strength of over 300MPa and maintains an impressive residual strength of over 50 MPa after failure. These new sintering parameters were used on composites made with MWCNT aerogels, which resulted in graceful failure in (unnotched) three-point bend testing with strengths between 120-160MPa, while a same amount of graphite inclusion showed a brittle behaviour. The MWCNT phase in this case is seen to inhibit and modify grain growth leading to 'wavier' platelet-like grains with high aspect ratio, which are likely restraining the movement of platelets through interlocking and provide frictional resistance during platelet-platelet sliding. The presented work shows that to achieve a composite with both high strength and toughness such as nacre, it is important to optimize the sintering conditions for high density while maintaining platelets with high aspect ratio. It

was shown that the strength of the interface must be relatively weak compared to the alumina to induce crack branching and deflection, and that irregularly shaped platelet-like grains and mineral connections improve the strength and toughness of such composites. It is seen that MWCNTs can effectively mimic the protein fibres of nacre as complete nacre-like graceful failure is observed when these are included through either *in-situ* growth from bound catalyst particles or highly interconnected MWCNT aerogels.

Precise determination of the J_c toughness and R-curve plotting for each specimen has not been attempted in this dissertation as other characterisation techniques gave a sufficient amount of information to understand and improve the created composites and this allowed for a wider range of materials to be investigated. However, future study of the fracture toughness properties of materials that show complete nacre-like behaviour and residual strength may be beneficial to quantify the toughening that such microstructures provide.

In addition, suggested future experiments entail a better understanding of the temperature gradients in SPS of large ceramic composite discs as created in this study. Often, manufactured discs suffered from breakage after SPS, which reduced the number of useable samples or in some cases destroyed the ceramic disc. For example, although insulation material around the graphite die is usually recommended to reduce the temperature gradient, too much insulation has been shown to increase the temperature gradient in the case of alumina[327] which may cause the recurring problem of fracture in manufactured composite discs. A good understanding of these dynamics is also useful when upscaling/increasing disc sizes where this temperature gradient is likely even more severe.

In closing, this dissertation has detailed the synthesis of MWCNTs in and on biomimetic scaffolds, the creation of composites made of nacre-like alumina and MWCNTs and the characterisation of the mechanical response of such composites. Thus, the work presented in this thesis contributes towards a deeper understanding of biomimetic composite material design to replace current brittle ceramic material solutions.

Bibliography

1. Ritchie, R. O. The conflicts between strength and toughness. *Nat. Mater.* **10**, 817–822 (2011).

2. Launey, M. E. & Ritchie, R. O. On the fracture toughness of advanced materials. *Adv. Mater.* **21**, 2103–2110 (2009).

3. Demetriou, M. D. *et al.* A damage-tolerant glass. *Nat. Mater.* **10**, 123–128 (2011).

4. Meyers, M. A., Chen, P. Y., Lin, A. Y. M. & Seki, Y. Biological materials: Structure and mechanical properties. *Prog. Mater. Sci.* **53**, 1–206 (2008).

5. Jeronimidis, G. & Atkins, A. G. Mechanics of biological materials and structures: Nature's lessons for the engineer. *Proc. Inst. Mech. Eng. Part C J. Mech. Eng. Sci.* **209**, 221–235 (1995).

6. Fratzl, P. Biomimetic materials research: what can we really learn from nature's structural materials? *J. R. Soc. Interface* **4**, 637–642 (2007).

7. Meyers, M. A., Lin, A. Y. M., Chen, P. Y. & Muyco, J. Mechanical strength of abalone nacre: Role of the soft organic layer. *J. Mech. Behav. Biomed. Mater.* **1**, 76–85 (2008).

8. Currey, J. D. D. Mechanical properties of mother of pearl in Tension. *Proc. R. Soc. B Biol. Sci.* **196**, 443–463 (1977).

9. Menig, R., Meyers, M. H., Meyers, M. A. & Vecchio, K. S. Quasi-static and dynamic mechanical response of Haliotis rufescens (abalone) shells. *Acta Mater.* **48**, 2383–2398 (2000).

10. Fleischli, F. D., Dietiker, M., Borgia, C. & Spolenak, R. The influence of internal length scales on mechanical properties in natural nanocomposites□: A comparative study on inner layers of seashells. **4**, 1694–1706 (2008).

11. Gosline, J. M., Vincent, J. F. V & Currey, J. D. *The Mechanical Properties of Biological*

Materials. Symp. Soc. Exp. Biol. Cambridge University Press vol. 34 (Cambridge : Cambridge University Press for the Society for Experimental Biology, 1980).

12. Levy, M., Bass, H. E., Stern, R. R. & Keppens, V. *Handbook of elastic properties of solids, liquids, and gases*. (2001).

13. Atkins, A. . & Mai, Y.-W. *Elastic and plastic fracture: metals, polymers, ceramics, composites, biological materials*. (Chichester: Ellis-Horwood, 1985).

14. Currey, J. D. Mechanical properties of mollusc shell. *Symp. Soc. Exp. Biol.* **34**, 75–97 (1980).

15. The mechanical design of nacre. *Proceedings of the Royal Society of London. Series B. Biological Sciences* vol. 234 415–440 (1988).

16. Menig, R., Meyers, M. H., Meyers, M. A. & Vecchio, K. S. Quasi-static and dynamic mechanical response of Strombus gigas (conch) shells. *Mater. Sci. Eng. A* **297**, 203–211 (2001).

17. Wang, R. Z., Suo, Z., Evans, A. G., Yao, N. & Aksay, I. A. Deformation mechanisms in nacre. *J. Mater. Res.* **16**, 2485–2493 (2001).

18. Davidson, M. S. Towards an Understanding of the Role of Aragonite in the Mechanical Properties of Nacre. *Energy* (Stanford Linear Accelerator Center, 2009).

19. Katti, K. S. & Katti, D. R. Why is nacre so tough and strong ? **26**, 1317–1324 (2006).

20. André Meyers, M. & Chen, P.-Y. *Biological Materials Science: Biological Materials, Bioinspired Materials, and Biomaterials*. (Cambridge University Press, 2014).

21. Wegst, U. G. K. & Ashby, M. F. The mechanical efficiency of natural materials. *Philos. Mag.* **84**, 2167–2181 (2004).

22. Bhushan, B. & Fuchs, H. *Applied Scanning Probe Methods XIII: Biomimetics and Industrial Applications*. (Springer Science & Business Media, 2008).

23. Ritchie, R. O. *et al.* Measurement of the toughness of bone: A tutorial with special reference to small animal studies. *Bone* **43**, 798–812 (2008).

24. Lin, A. & Meyers, M. A. Growth and structure in abalone shell. *Mater. Sci. Eng. A* **390**, 27–41 (2005).

25. Gao, H., Ji, B., Jager, I. L., Arzt, E. & Fratzl, P. Materials become insensitive to flaws at nanoscale: lessons from nature. *Proc. Natl. Acad. Sci.* **100**, 5597–5600 (2003).

26. Currey, J. D. & Taylor, J. D. The mechanical behaviour of some molluscan hard tissues. *J. Zool.* **173**, 395–406 (1974).

27. Currey, J. D., Zioupos, P., Peter, D. & Casinos, A. Mechanical properties of nacre and highly mineralized bone. *Proc. R. Soc. B Biol. Sci.* **268**, 107–111 (2001).

28. Katti, K. S., Katti, D. R., Pradhan, S. M. & Bhosle, A. Platelet interlocks are the key to toughness and strength in nacre. *J. Mater. Res.* **20**, 1097–1100 (2005).

29. Neves, N. M. & Mano, J. F. Structure/mechanical behavior relationships in crossed-lamellar sea shells. *Mater. Sci. Eng. C* **25**, 113–118 (2005).

30. Chen, Q. & Pugno, N. M. Bio-mimetic mechanisms of natural hierarchical materials: A review. *J. Mech. Behav. Biomed. Mater.* **19**, 3–33 (2013).

31. Song, F., Zhang, X. H. & Bai, Y. L. Microstructure in a biointerface. 639–641 (2002).

32. Wang, J., Cheng, Q. & Tang, Z. Layered nanocomposites inspired by the structure and mechanical properties of nacre. *Chem. Soc. Rev.* **41**, 1111–1129 (2012).

33. Lackner, J. M., Waldhauser, W., Major, B., Major, L. & Kot, M. Plastic deformation in nano-scale multilayer materials - A biomimetic approach based on nacre. *Thin Solid Films* **534**, 417–425 (2013).

34. Sun, J. Y. & Tong, J. Fracture Toughness Properties of Three Different Biomaterials Measured by Nanoindentation. *J. Bionic Eng.* **4**, 11–17 (2007).

35. Bouville, F. *et al.* Strong, tough and stiff bioinspired ceramics from brittle constituents. *Nat. Mater.* **13**, 508–514 (2014).

36. Sun, J. & Bhushan, B. Hierarchical structure and mechanical properties of nacre: a review. *RSC Adv.* **2**, 7617–7632 (2012).

37. Hernandez, S. & Brebbia, C. A. *Design and nature VI : comparing design in nature with science and engineering.* (Southampton : WIT, 2012).

38. Medeiros, S. K., Albuquerque, E. L., Maia, F. F., Caetano, E. W. S. & Freire, V. N. Structural, electronic, and optical properties of CaCO3 aragonite. *Chem. Phys. Lett.* **430**, 293–296 (2006).

39. Barthelat, F., Rim, J. E. & Espinosa, H. D. A Review on the Structure and Mechanical Properties of Mollusk Shells – Perspectives on Synthetic Biomimetic Materials.

40. Tattersall, H. . & Tappin, G. The Work of Fracture and its Measurement in Metals , Ceramics and other Materials. *J. Mater. Sci.* **1**, 296–301 (1966).

41. Davidge, R. . *Mechanical Behaviour of Ceramics.* (Cambridge solid state science series, 1979).

42. Sarikaya, M., Gunnison, K. E., Yasrebi, M. & Aksay, I. A. Mechanical property-microstructural relationships in abalone shell. *J. Mater. res.* **174**, 109–116 (1990).

43. Olusunle, S. O. O., Siyanbola, W. O., Adetunji, A. R., Adeoye, M. O. & Adewoye, O. O. Effect of Buffer Solutions on the Flow and Fracture in Calcite. *J. Miner. Mater. Charact. Eng.* **8**, 189–201 (2009).

44. Quinn, G. D. & Bradt, R. C. On the Vickers Indentation Fracture Toughness Test. *J. Am. ceram. Soc.* **90**, 673–680 (2007).

45. Quinn, G. D. Fracture Toughness of Ceramics by the Vickers Indentation Crack Length Method: A Critical Review. 45–62 (2008) doi:10.1002/9780470291313.ch5.

46. Kruzic, J. J., Kim, D. K., Koester, K. J. & Ritchie, R. O. Indentation techniques for evaluating the fracture toughness of biomaterials and hard tissues. *J. Mech. Behav. Biomed. Mater.* **2**, 384–395 (2009).

47. Kamat, S., Su, X., Ballarini, R. & Heuer, A. . Structural basis for the fracture toughness of the shell of the conch Strombus gigas. *Nature* **405**, (2000).

48. Lv, J., Jiang, Y. & Zhang, D. Structural and Mechanical Characterization of Atrina Pectinata and Freshwater Mussel Shells. *J. Bionic Eng.* **12**, 276–284 (2015).

49. Barhli, S. M., Mostafavi, M., Cinar, A. F., Hollis, D. & Marrow, T. J. J-Integral Calculation by Finite Element Processing of Measured Full-Field Surface Displacements. *Exp. Mech.* **57**, 997–1009 (2017).

50. Becker, T. H., Mostafavi, M., Tait, R. B. & Marrow, T. J. An approach to calculate the J-integral by digital image correlation displacement field measurement. *Fatigue Fract. Eng. Mater. Struct.* **35**, 971–984 (2012).

51. Barthelat, F. & Espinosa, H. D. An experimental investigation of deformation and fracture of nacre-mother of pearl. *Exp. Mech.* **47**, 311–324 (2007).

52. Rabiei, R., Bekah, S. & Barthelat, F. Failure mode transition in nacre and bone-like materials. *Acta Biomater.* **6**, 4081–4089 (2010).

53. Kakisawa, H. & Sumitomo, T. The toughening mechanism of nacre and structural materials inspired by nacre. *Sci. Technol. Adv. Mater.* **12**, 064710 (2011).

54. Barthelat, F. & Espinosa, H. D. An experimental investigation of deformation and fracture of nacre-mother of pearl. *Exp. Mech.* **47**, 311–324 (2007).

55. Wang, J., Cheng, Q. & Tang, Z. Layered nanocomposites inspired by the structure and mechanical properties of nacre. *Chem. Soc. Rev.* **41**, 1111–1129 (2012).

56. Barthelat, F., Tang, H., Zavattieri, P. D., Li, C. M. & Espinosa, H. D. On the

mechanics of mother-of-pearl: A key feature in the material hierarchical structure. *J. Mech. Phys. Solids* **55**, 306–337 (2007).

57. Askarinejad, S., Choshali, H. A., Flavin, C. & Rahbar, N. Effects of tablet waviness on the mechanical response of architected multilayered materials: Modeling and experiment. *Compos. Struct.* **195**, 118–125 (2018).

58. Wei, X., Naraghi, M. & Espinosa, H. D. Optimal length scales emerging from shear load transfer in natural materials: Application to carbon-based nanocomposite design. *ACS Nano* **6**, 2333–2344 (2012).

59. Okumura, K. & Gennes, P.-G. Why is nacre strong? Elastic theory and fracture mechanics for biocomposites with stratified structures. *Eur. Phys. J. E* **4**, 121–127 (2001).

60. Yao, H., Song, Z., Xu, Z. & Gao, H. Cracks fail to intensify stress in nacreous composites. *Compos. Sci. Technol.* **81**, 24–29 (2013).

61. Smith, B. L. *et al.* Molecular mechanistic origin of the toughness of natural adhesives, fibres and composites. *Nature* **399**, 761–763 (1999).

62. Rief, M., Gautel, M., Schemmel, A. & Gaub, H. E. The mechanical stability of immunoglobulin and fibronectin III domains in the muscle protein titin measured by atomic force microscopy. *Biophys. J.* **75**, 3008–3014 (1998).

63. Evans, a. G. *et al.* Model for the robust mechanical behavior of nacre. *J. Mater. Res.* **16**, 2475–2484 (2001).

64. Song, F., Soh, A. K. & Bai, Y. L. Structural and mechanical properties of the organic matrix layers of nacre. *Biomaterials* **24**, 3623–3631 (2003).

65. Schäffer, T. E. *et al.* Does Abalone Nacre Form by Heteroepitaxial Nucleation or by Growth through Mineral Bridges? *Chem. Mater.* **9**, 1731–1740 (1997).

66. Barthelat, F., Li, C.-M., Comi, C. & Espinosa, H. D. Mechanical properties of nacre constituents and their impact on mechanical performance. *J. Mater. Res.* **21**, 1977–1986 (2006).

67. Askarinejad, S. & Rahbar, N. Toughening mechanisms in bioinspired multilayered materials. *J. R. Soc. Interface* **12**, (2015).

68. Zhang, Y., Yao, H., Ortiz, C., Xu, J. & Dao, M. Bio-inspired interfacial strengthening strategy through geometrically interlocking designs. *J. Mech. Behav. Biomed. Mater.* **15**, 70–77 (2012).

69. Katti, D. R., Pradhan, S. M. & Katti, K. S. Modeling the organic-inorganic interfacial nanoasperities in a model bio-nanocomposite, nacre. *Rev. Adv. Mater. Sci.* **6**, 162–168 (2004).

70. Niebel, T. P., Carnelli, D., Binelli, M. R., Libanori, R. & Studart, A. R. Hierarchically roughened microplatelets enhance the strength and ductility of nacre-inspired composites. *J. Mech. Behav. Biomed. Mater.* **60**, 367–377 (2016).

71. Fan, S. & Yilong, B. Mineral bridges of nacre and its effects. *Acta Mech. Sin.* **17**, (2001).

72. Shao, Y., Zhao, H. P. & Feng, X. Q. Optimal characteristic nanosizes of mineral bridges in mollusk nacre. *RSC Adv.* **4**, 32451–32456 (2014).

73. Gu, G. X., Libonati, F., Wettermark, S. D. & Buehler, M. J. Printing nature: Unraveling the role of nacre's mineral bridges. *J. Mech. Behav. Biomed. Mater.* **76**, 135–144 (2017).

74. Begley, M. R. *et al.* Micromechanical models to guide the development of synthetic 'brick and mortar' composites. *J. Mech. Phys. Solids* **60**, 1545–1560 (2012).

75. Podsiadlo, P. *et al.* Layer-by-layer assembly of nacre-like nanostructured composites with antimicrobial properties. *Langmuir* **21**, 11915–11921 (2005).

76. Das, P. *et al.* Nacre-mimetics with synthetic nanoclays up to ultrahigh aspect ratios. *Nat. Commun.* **6**, 5967 (2015).

77. Yao, H.-B., Ge, J., Mao, L.-B., Yan, Y.-X. & Yu, S.-H. 25th Anniversary Article: Artificial Carbonate Nanocrystals and Layered Structural Nanocomposites Inspired by Nacre: Synthesis, Fabrication and Applications. *Adv. Mater.* **26**, 163–188 (2014).

78. Bonderer, L. J., Studart, A. R. & Gauckler, ludwig J. Bioinspired design and assembly of Platelet Reinforced Polymer Films. *Science (80-.).* **319**, 1069–1073 (2008).

79. Yao, H. Bin, Tan, Z. H., Fang, H. Y. & Yu, S. H. Artificial nacre-like bionanocomposite films from the self-assembly of chitosan-montmorillonite hybrid building blocks. *Angew. Chemie - Int. Ed.* **49**, 10127–10131 (2010).

80. Munch, E. *et al.* Tough, bio-inspired hybrid materials. *Science (80-.).* **322**, 1516–1520 (2008).

81. Launey, M. E., Munch, E., Alsem, D. H., Barth, H. B. & Saiz, E. Designing highly toughened hybrid composites through nature-inspired hierarchical complexity. *Acta Mater.* **57**, 2919–2932 (2009).

82. Bai, H. *et al.* Bioinspired Hydroxyapatite/Poly(methyl methacrylate) Composite with a Nacre-Mimetic Architecture by a Bidirectional Freezing Method. *Adv. Mater.* **28**, 50–56 (2016).

83. Launey, M. E. *et al.* A novel biomimetic approach to the design of high-performance ceramic – metal composites. 741–753 (2010).

84. Wat, A. *et al.* Bioinspired nacre-like alumina with a bulk-metallic glass-forming alloy as a compliant phase. *Nat. Commun.* **10**, 1–12 (2019).

85. Gao, H. L. *et al.* Mass production of bulk artificial nacre with excellent mechanical properties. *Nat. Commun.* **8**, (2017).

86. Shukla, D. K. & Parameswaran, V. Epoxy composites with 200 nm thick alumina platelets as reinforcements. *J. Mater. Sci.* **42**, 5964–5972 (2007).

87. Shukla, D. K., Kasisomayajula, S. V. & Parameswaran, V. Epoxy composites using functionalized alumina platelets as reinforcements. *Compos. Sci. Technol.* **68**, 3055–3063 (2008).

88. Erb, R. M., Libanori, R., Rothfuchs, N. & Studart, A. R. Composites reinforced in three dimensions by using low magnetic fields. **202508**, 199–204 (2012).

89. Petrini, M., Ferrante, M. & Su, B. Fabrication and characterization of biomimetic ceramic/polymer composite materials for dental restoration. *Dent. Mater.* **29**, 375–381 (2013).

90. Song, P. *et al.* Thermally stable, conductive and flame-retardant nylon 612 composites created by adding two-dimensional alumina platelets. *Compos. Part A Appl. Sci. Manuf.* **97**, 100–110 (2017).

91. Šandera, P. *et al.* Toughening effects quantification in glass matrix composite reinforced by alumina platelets. *Acta Mater.* **56**, 2908–2918 (2008).

92. Grossman, M. *et al.* Mineral Nano-Interconnectivity Stiffens and Toughens Nacre-like Composite Materials. *Adv. Mater.* **29**, (2017).

93. Munch, E. *et al.* Tough, Bio-Inspired Hybrid Materials. *Am. Assoc. Adv. Sci.* **322**, 1516–1520 (2008).

94. Clegg, W. J., Kendall, K., Alford, N. M. N., Button, T. W. & Birchall, J. D. A simple way to make tough ceramics. *Nature* **347**, 455–457 (1990).

95. Dimas, L. S. & Buehler, M. J. Tough and stiff composites with simple building blocks. *J. Mater. Res.* **28**, 1295–1303 (2013).

96. Yu, M. Strength and Breaking Mechanism of Multiwalled Carbon Nanotubes Under

Tensile Load. *Science (80-.).* **287**, 637–640 (2000).

97. Chang, C., Hsu, I., Aykol, M., Hung, W. & Chen, C. A New Lower Limit for the Ultimate Breaking Strain of Carbon Nanotubes. **4**, 5095–5100 (2010).

98. Downes, R., Wang, S., Haldane, D. & Liang, Z. Mechanisms of strain induced alignment of carbon nanotubes (CNT): Process scale-up and quasi-continuous highly aligned cnt material. *ICCM Int. Conf. Compos. Mater.* **2013-July**, 1529–1536 (2013).

99. Paci, J. T., Furmanchuk, A., Espinosa, H. D. & Schatz, G. C. Shear and friction between carbon nanotubes in bundles and yarns. *Nano Lett.* **14**, 6138–6147 (2014).

100. Thomson, K. E., Jiang, D., Ritchie, R. O. & Mukherjee, A. K. A preservation study of carbon nanotubes in alumina-based nanocomposites via Raman spectroscopy and nuclear magnetic resonance. *Appl. Phys. A Mater. Sci. Process.* **89**, 651–654 (2007).

101. Ahmad, I., Yazdani, B. & Zhu, Y. Recent Advances on Carbon Nanotubes and Graphene Reinforced Ceramics Nanocomposites. *Nanomaterials* **5**, 90–114 (2015).

102. Kim, P., Shi, L., Majumdar, A. & McEuen, P. L. Thermal Transport Measurements of Individual Multiwalled Nanotubes. *Phys. Rev. Lett.* **87**, 215502 (2001).

103. Yu, C., Shi, L., Yao, Z., Li, D. & Majumdar, A. Thermal conductance of an individual single-wall carbon nanotube above room temperature. *Nano Lett* **5**, 1842–1846 (2005).

104. Pop, E., Mann, D., Wang, Q., Goodson, K. & Dai, H. J. Thermal conductance of an individual single-wall carbon nanotube above room temperature. *Nano Lett.* **6**, 96–100 (2006).

105. Hone, J., Whitney, M., Piskoti, C. & Zettl, A. Thermal conductivity of single-walled carbon nanotubes. *Phys. Rev. B* **59**, R2514–R2516 (1999).

106. Vargas-Bernal, R. & Herrera-Prez, G. Carbon Nanotube- and Graphene Based Devices, Circuits and Sensors for VLSI Design. *VLSI Des.* (2012) doi:10.5772/38743.

107. Meo, M. & Rossi, M. Tensile failure prediction of single wall carbon nanotube. *Eng. Fract. Mech.* **73**, 2589–2599 (2006).

108. Xiao, J. R., Gama, B. A. & Gillespie, J. W. An analytical molecular structural mechanics model for the mechanical properties of carbon nanotubes. *Int. J. Solids Struct.* **42**, 3075–3092 (2005).

109. Ogata, S. & Shibutani, Y. Ideal tensile strength and band gap of single-walled carbon nanotubes. 1–4 (2003) doi:10.1103/PhysRevB.68.165409.

110. Lee, C., Wei, X., Kysar, J. W. & Hone, J. Measurement of the Elastic Properties and Intrinsic Strength of Monolayer Graphene. **321**, 385–388 (2008).

111. Mielke, S. L. *et al.* The role of vacancy defects and holes in the fracture of carbon nanotubes. **390**, 413–420 (2004).

112. Khare, R. *et al.* Coupled quantum mechanical / molecular mechanical modeling of the fracture of defective carbon nanotubes and graphene sheets. 1–12 (2007) doi:10.1103/PhysRevB.75.075412.

113. Lei, Z. X. & Liew, K. M. Multiscale MDFEM for modeling mechanical behavior of carbon nanotubes. *Appl. Math. Model.* **69**, 466–492 (2019).

114. Yu, M. F., Files, B. S., Arepalli, S. & Ruoff, R. S. Tensile loading of ropes of single wall carbon nanotubes and their mechanical properties. *Phys. Rev. Lett.* **84**, 5552–5555 (2000).

115. Son, H. *et al.* Strain and friction induced by van der Waals interaction in individual single walled carbon nanotubes. *Appl. Phys. Lett.* **90**, 253113 (2007).

116. Peng, B. E. I. *et al.* Measurements of near-ultimate strength for multiwalled carbon nanotubes and irradiation-induced crosslinking improvements. **3**, (2008).

117. Demczyk, B. G. *et al.* Direct mechanical measurement of the tensile strength and

elastic modulus of multiwalled carbon nanotubes. **334**, 173–178 (2002).

118. Falvo, M. R., Clary, G. J., Ii, R. M. T. & Chi, V. Bending and buckling of carbon nanotubes under large strain. *Lett. to Nat.* **389**, 582–584 (1997).

119. Yamamoto, G., Omori, M., Hashida, T. & Kimura, H. A novel structure for carbon nanotube reinforced alumina composites with improved mechanical properties. *Nanotechnology* **19**, (2008).

120. Gu, Z. *et al.* Aligned carbon nanotube-reinforced silicon carbide composites produced by chemical vapor infiltration. *Carbon N. Y.* **49**, 2475–2482 (2011).

121. Sarkar, S. & Das, P. K. PROCESSING AND PROPERTIES OF CARBON NANOTUBE / ALUMINA NANOCOMPOSITES : A REVIEW. **37**, (2014).

122. Cheng, Q., Debnath, S., Gregan, E. & Byrne, H. J. Ultrasound-Assisted swnts dispersion: Effects of sonication parameters and solvent properties. *J. Phys. Chem. C* **114**, 8821–8827 (2010).

123. Thakur, V. K. & Thakur, M. K. *Chemical Functionalization of Carbon Nanomaterials: Chemistry and Applications*. (CRC press, 2015).

124. Deville, S., Saiz, E. & Tomsia, A. P. Ice-templated porous alumina structures. *Acta Mater.* **55**, 1965–1974 (2007).

125. Naglieri, V., Bale, H. A., Gludovatz, B., Tomsia, A. P. & Ritchie, R. O. On the development of ice-templated silicon carbide scaffolds for nature-inspired structural materials. *Acta Mater.* **61**, 6948–6957 (2013).

126. Bai, H. *et al.* Biomimetic gradient scaffold from ice-templating for self-seeding of cells with capillary effect. *Acta Biomater.* **20**, 113–119 (2015).

127. Fukushima, M., Yoshizawa, Y. & Ohji, T. Macroporous Ceramics by Gelation-Freezing Route Using Gelatin. *Adv. Eng. Mater.* **16**, 607–620 (2014).

128. Zhang, Y., Zuo, K. & Zeng, Y. P. Effects of gelatin addition on the microstructure of freeze-cast porous hydroxyapatite ceramics. *Ceram. Int.* **35**, 2151–2154 (2009).

129. Soltmann, U., Bo, H., Koch, D. & Grathwohl, G. Freeze gelation: a new option for the production of biological ceramic composites (biocers). *Mater. Lett.* **57**, 2861–2865 (2003).

130. Deville, S. Freeze-casting of porous ceramics: A review of current achievements and issues. *Adv. Eng. Mater.* **10**, 155–169 (2008).

131. Miller, S. M., Xiao, X. & Faber, K. T. Freeze-cast alumina pore networks: Effects of freezing conditions and dispersion medium. *J. Eur. Ceram. Soc.* **35**, 3595–3605 (2015).

132. Deville, S., Tomsia, A. P. & Saiz, E. The Materials that Came in from the Cold: Nacre-like Bioceramics through Freezing. *Proc. 10th Conf. Eur. Ceram. Soc.* (2007).

133. Deville, S., Saiz, E., Nalla, R. K. & Tomsia, A. P. Freezing as a Path to Build Complex Composites. **311**, (2006).

134. Deville, S., Maire, E., Lasalle, A. & Bogner, A. In Situ X-Ray Radiography and Tomography Observations of the Solidification of Aqueous Alumina Particle Suspensions—Part I: Initial Instants. *J.Am. Ceram. Soc.* **92**, 2489–2496 (2009).

135. Porter, M. M. *et al.* Magnetic freeze casting inspired by nature. *Mater. Sci. Eng. A* **556**, 741–750 (2012).

136. Toledo, E. J. L., Ramalho, T. C. & Magriotis, Z. M. Influence of magnetic field on physical – chemical properties of the liquid water : Insights from experimental and theoretical models. *J. Mol. Struct.* **888**, 409–415 (2008).

137. Chang, K. & Weng, C.-I. The effect of an external magnetic field on the structure of liquid water using molecular dynamics simulation. *J. Appl. Phys.* **100**, 1–6 (2006).

138. Munch, E., Saiz, E., Tomsia, A. P. & Deville, S. Architectural control of freeze-cast

ceramics through additives and templating. *J. Am. Ceram. Soc.* **92**, 1534–1539 (2009).

139. Bouville, F. *et al.* Templated Grain Growth in Macroporous Materials. *J. Am. Ceram. Soc.* **97**, 1736–1742 (2014).

140. Bai, H., Chen, Y., Delattre, B., Tomsia, A. P. & Ritchie, R. O. Bioinspired large-scale aligned porous materials assembled with dual temperature gradients. *Sci. Adv.* **1**, 1–8 (2015).

141. Zeng, J., Zhang, Y., Zhou, K. C. & Zhang, D. Effects of alcohol additives on pore structure and morphology of freeze-cast ceramics. *Trans. Nonferrous Met. Soc. China (English Ed.* **24**, 718–722 (2014).

142. Mizuno, K., Miyashita, Y., Shindo, Y. & Ogawa, H. NMR and FT-IR Studies of Hydrogen Bonds in Ethanol-Water Mixtures. *J. Phys. Chem.* **99**, 3225–3228 (1995).

143. Wegst, U. G. K., Bai, H., Saiz, E., Tomsia, A. P. & Ritchie, R. O. Bioinspired structural materials. **14**, 23–36 (2015).

144. Hunger, P. M., Donius, A. E. & Wegst, U. G. K. Platelets self-assemble into porous nacre during freeze casting. *J. Mech. Behav. Biomed. Mater.* **19**, 87–93 (2013).

145. Singh, B. P., Menchavez, R., Takai, C., Fuji, M. & Takahashi, M. Stability of dispersions of colloidal alumina particles in aqueous suspensions. *J. Colloid Interface Sci.* **291**, 181–186 (2005).

146. Iijima, S. Helical microtubules of graphitic carbon. *Nature* **354**, 56–58 (1991).

147. Cao, L. *et al.* The growth of carbon nanotubes in aluminum powders by the catalytic pyrolysis of polyethylene glycol. *Carbon N. Y.* **50**, 1057–1062 (2012).

148. Güler, Ö. & Evin, E. Carbon nanotubes formation by short-time ball milling and annealing of graphite. *Optoelectron. Adv. Mater. Rapid Commun.* **6**, 183–187 (2012).

149. Vander Wal, R. L., Ticich, T. M. & Curtis, V. E. Diffusion flame synthesis of single-

walled carbon nanotubes. *Chem. Phys. Lett.* **323**, 217–223 (2000).

150. Scott, C. D., Arepalli, S., Nikolaev, P. & Smalley, R. E. Growth mechanisms for single-wall carbon nanotubes in a laser-ablation process. **580**, 573–580 (2001).

151. Arora, N. & Sharma, N. N. Arc discharge synthesis of carbon nanotubes: Comprehensive review. *Diam. Relat. Mater.* **50**, 135–150 (2014).

152. Shah, K. A. & Tali, B. A. Synthesis of carbon nanotubes by catalytic chemical vapour deposition : A review on carbon sources , catalysts and substrates. *Mater. Sci. Semicond. Process.* **41**, 67–82 (2016).

153. Mubarak, N. M., Abdullah, E. C., Jayakumar, N. S. & Sahu, J. N. An overview on methods for the production of carbon nanotubes. *J. Ind. Eng. Chem.* **20**, 1186–1197 (2014).

154. Guo, T., Nikolaev, P., Thess, A., Colbert, D. T. & Smalley, R. E. Catalytic growth of single-walled manotubes by laser vaporization. *Chem. Phys. Lett.* **243**, 49–54 (1995).

155. Jiang, W., Molian, P. & Ferkel, H. Rapid Production of Carbon Nanotubes by High-Power Laser Ablation. *J. Manuf. Sci. Eng.* **127**, 703 (2005).

156. Eklund, P. C. *et al.* Large-Scale Production of Single-Walled Carbon Nanotubes Using Ultrafast Pulses from a Free Electron Laser. *Nano Lett.* **2**, 561–566 (2002).

157. Rafique, M. M. A. & Iqbal, J. Production of Carbon Nanotubes by Different Routes — A Review. *J. Encapsulation Adsorpt. Sci.* **1**, 29–34 (2011).

158. Kumar, M. & Ando, Y. Chemical Vapor Deposition of Carbon Nanotubes : A Review on Growth Mechanism and Mass Production. **10**, 3739–3758 (2010).

159. Radushkevich, L. . & Lukyanovich, V. . O strukture ugleroda, obrazujucegosja pri termiceskom razlozenii okisi ugleroda na zeleznom kontakte. *Zurn Fis. Chim* **26**, 88–95 (1952).

160. Monthioux, M. & Kuznetsov, V. L. Guest Editorial Who should be given the credit for the discovery of carbon nanotubes ? *Carbon N. Y.* **44**, 3–6 (2006).

161. Jourdain, V. & Bichara, C. Current understanding of the growth of carbon nanotubes in catalytic chemical vapour deposition. *Carbon N. Y.* **58**, 2–39 (2013).

162. Shukrullah, S., Mohamed, N. M., Shaharun, M. S. & Naz, M. Y. Parametric study on vapor-solid-solid growth mechanism of multiwalled carbon nanotubes. *Mater. Chem. Phys.* **176**, 32–43 (2016).

163. Tripathi, G. *et al.* A comparative study of arc discharge and chemical vapor deposition synthesized carbon nanotubes. *Int. J. Hydrogen Energy* **37**, 3833–3838 (2012).

164. Rul, S., Lefèvre-Schlick, F., Capria, E., Laurent, C. & Peigney, A. Percolation of single-walled carbon nanotubes in ceramic matrix nanocomposites. *Acta Mater.* **52**, 1061–1067 (2004).

165. Takagi, D., Homma, Y., Hibino, H. & Suzuki, S. Single-Walled Carbon Nanotube Growth from Highly Activated Metal Nanoparticles. (2006).

166. Arcos, T. D. L. *et al.* The Influence of Catalyst Chemical State and Morphology on Carbon Nanotube Growth. 7728–7734 (2004).

167. Rümmeli, M. H. *et al.* Catalyst size dependencies for carbon nanotube synthesis. *Phys. Status Solidi Basic Res.* **244**, 3911–3915 (2007).

168. Gohier, A., Ewels, C. P., Minea, T. M. & Djouadi, M. A. Carbon nanotube growth mechanism switches from tip- to base-growth with decreasing catalyst particle size. **6**, 2–9 (2008).

169. José-Yacamán, M. *et al.* Surface diffusion and coalescence of mobile metal nanoparticles. *J. Phys. Chem. B* **109**, 9703–9711 (2005).

170. Song, I. K., Yu, W. J., Cho, Y. S., Choi, G. S. & Kim, D. The determining factors for

the growth mode of carbon nanotubes in the chemical vapour deposition process. *Nanotechnology* **15**, S590–S595 (2004).

171. Hasegawa, K. *et al.* Growth window and possible mechanism of millimeter-thick single-walled carbon nanotube forests. *J. Nanosci. Nanotechnol.* **8**, 6123–6128 (2008).

172. Quinton, B. T. *et al.* Influence of oxide buffer layers on the growth of carbon nanotube arrays on carbon substrates. *Carbon N. Y.* **87**, 175–185 (2015).

173. Youn, S. K. *et al.* Temperature gradient chemical vapor deposition of vertically aligned carbon nanotubes. *Carbon N. Y.* **54**, 343–352 (2013).

174. Dichiara, A. & Bai, J. The growth of carbon nanotube multilayers on ceramic μ-particles by catalytic chemical vapour deposition. *Diam. Relat. Mater.* **29**, 52–58 (2012).

175. Jones, A. C. & Hitchman, M. L. Overview of Chemical Vapour Deposition. (2009).

176. Dupuis, A. C. The catalyst in the CCVD of carbon nanotubes-a review. *Prog. Mater. Sci.* **50**, 929–961 (2005).

177. Vm, S., Mohamed, A. R., Abdullah, A. Z. & Chai, S. Role of Reaction and Factors of Carbon Nanotubes Growth in Chemical Vapour Decomposition Process Using Methane — A Highlight. **2010**, (2010).

178. Sinnott, S. B. *et al.* Model of carbon nanotube growth through chemical vapor deposition. *Chem. Phys. Lett.* **315**, 25–30 (1999).

179. Baker, R. T. K., Harris, P. S., Thomas, R. B. & Waite, R. J. Formation of filamentous carbon from iron, cobalt and chromium catalyzed decomposition of acetylene. *J. Catal.* **30**, 86–95 (1973).

180. Noda, S., Tsuji, Y., Murakami, Y. & Maruyama, S. Combinatorial method to prepare metal nanoparticles that catalyze the growth of single-walled carbon nanotubes. *Appl. Phys. Lett.* **86**, 1–3 (2005).

181. Jung, D. W. *et al.* Optimizing Control of Fe Catalysts for Carbon Nanotube Growth. *J. Nanosci. Nanotechnol.* **12**, 5663–5668 (2012).

182. Suriani, A. B., Azira, A. A., Nik, S. F., Md Nor, R. & Rusop, M. Synthesis of vertically aligned carbon nanotubes using natural palm oil as carbon precursor. *Mater. Lett.* **63**, 2704–2706 (2009).

183. Li, Q., Yan, H., Zhang, J. & Liu, Z. Effect of hydrocarbons precursors on the formation of carbon nanotubes in chemical vapor deposition. *Carbon N. Y.* **42**, 829–835 (2004).

184. Zhong, G. *et al.* Acetylene: A key growth precursor for single-walled carbon nanotube forests. *J. Phys. Chem. C* **113**, 17321–17325 (2009).

185. Chen, C. S. & Hsieh, C. K. Effects of acetylene flow rate and processing temperature on graphene films grown by thermal chemical vapor deposition. *Thin Solid Films* **584**, 265–269 (2015).

186. He, D. & Bai, J. Acetylene-Enhanced Growth of Carbon Nanotubes on Ceramic Microparticles for Multi-Scale Hybrid Structures **. *chem. Vap Depos.* **17**, 98–106 (2011).

187. Khedr, M. H., Halim, K. S. A. & Soliman, N. K. Effect of temperature on the kinetics of acetylene decomposition over reduced iron oxide catalyst for the production of carbon nanotubes. *Appl. Surf. Sci.* **255**, 2375–2381 (2008).

188. Soltani, R., Ali, M., Sani, F. & Mohaghegh, F. The Effect of Temperature and N 2 : C 2 H 2 Flow Rate on the Growth of Carbon Nanotubes Synthesized by CCVD of Acetylene on Alumina – Zirconia Matrix The Effect of Temperature and N 2 : C 2 H 2 Flow Rate on the Growth of Carbon Nanotubes Synthesized by CC. **4046**, (2015).

189. Ghemes, C. Synthesis of Long and Spinnable Multi-Walled Carbon Nanotubes. *J. Adv. Res. Phys.* **3**, 2011–2013 (2012).

190. Kong, J. & Cassell, A. M. Chemical vapor deposition of methane for single-walled carbon nanotubes. 567–574 (1998).

191. Kern, W. The Evolution of Silicon Wafer Cleaning Technology. *J. Electrochem. Soc.* **137**, 1887 (1990).

192. Zhang, D., Wang, Y. & Gan, Y. Characterization of critically cleaned sapphire single-crystal substrates by atomic force microscopy, XPS and contact angle measurements. *Appl. Surf. Sci.* **274**, 405–417 (2013).

193. Piche, D. *et al.* Targeted T 1 Magnetic Resonance Imaging Contrast Enhancement with Extraordinarily Small CoFe 2 O 4 Nanoparticles. *ACS Appl. Mater. Interfaces* (2019) doi:10.1021/acsami.8b17162.

194. Dillon, F. *et al.* Flame spray pyrolysis generated transition metal oxide nanoparticles as catalysts for the growth of carbon nanotubes. *RSC Adv.* **3**, 20040–20045 (2013).

195. Pimenta, M. A. *et al.* Studying disorder in graphite-based systems by Raman spectroscopy. *Phys. Chem. Chem. Phys.* **9**, 1276–1291 (2007).

196. Antunes, E. F. *et al.* Comparative study of first- and second-order Raman spectra of MWCNT at visible and infrared laser excitation. *Carbon N. Y.* **44**, 2202–2211 (2006).

197. Bokobza, L., Bruneel, J.-L. & Couzi, M. Raman Spectra of Carbon-Based Materials (from Graphite to Carbon Black) and of Some Silicone Composites. *C—Journal Carbon Res.* **1**, 77–94 (2015).

198. Lee, C. J., Park, J. & Yu, J. A. Catalyst effect on carbon nanotubes synthesized by thermal chemical vapor deposition. *Chem. Phys. Lett.* **360**, 250–255 (2002).

199. Hoecker, C., Smail, F., Bajada, M., Pick, M. & Boies, A. Catalyst nanoparticle growth dynamics and their influence on product morphology in a CVD process for continuous carbon nanotube synthesis. *Carbon N. Y.* **96**, 116–124 (2016).

200. Hofmann, S. *et al.* In situ observations of catalyst dynamics during surface-bound carbon nanotube nucleation. *Nano Lett.* **7**, 602–608 (2007).

201. Liu, H. *et al.* Growth of Single-Walled Carbon Nanotubes from Ceramic Particles by Alcohol Chemical Vapor Deposition. *Appl. Phys. Express* **014001**, 1–4 (2008).

202. Huang, S., Cai, Q., Chen, J., Qian, Y. & Zhang, L. Metal-catalyst-free growth of single-walled carbon nanotubes on substrates. *J. Am. Chem. Soc.* **131**, 2094–2095 (2009).

203. Liu, B. *et al.* Metal-catalyst-free growth of single-walled carbon nanotubes. *J. Am. Chem. Soc.* **131**, 2082–2083 (2009).

204. Schneider, J. J. *et al.* Catalyst free growth of a carbon nanotube-alumina composite structure. *Inorganica Chim. Acta* **361**, 1770–1778 (2008).

205. Sui, Y. C. *et al.* Growth of carbon nanotubes and nanofibres in porous anodic alumina film. *Carbon N. Y.* **40**, 1011–1016 (2002).

206. Tripathi, N., Mishra, P., Joshi, B. & Islam, S. S. Catalyst free , excellent quality and narrow diameter of CNT growth on Al 2 O 3 by a thermal CVD technique. *Phys. E Low-dimensional Syst. Nanostructures* **62**, 43–47 (2014).

207. Huber, T. A., Kopac, M. C. & Chow, C. The quantitative removal of metal catalyst from multi-walled carbon nanotubes with minimal tube damage . *Can. J. Chem.* **86**, 1138 (1146).

208. Pumera, M. Carbon nanotubes contain residual metal catalyst nanoparticles even after washing with nitric acid at elevated temperature because these metal nanoparticles are sheathed by several graphene sheets. *Langmuir* **23**, 6453–6458 (2007).

209. Joshi, R. Patterned growth of ultra long carbon nanotubes . Properties and systematic investigation into their growth process †. (2010) doi:10.1039/b919579c.

210. Ivanov, V. *et al.* The study of carbon nanotubules produced by catalytic method. *Chem.*

Phys. Lett. **223**, 329–335 (1994).

211. Deng, W. Q., Xu, X. & Goddard, W. A. A two-stage mechanism of bimetallic catalyzed growth of single-walled carbon nanotubes. *Nano Lett.* **4**, 2331–2335 (2004).

212. Deck, C. P. & Vecchio, K. Prediction of carbon nanotube growth success by the analysis of carbon-catalyst binary phase diagrams. *Carbon N. Y.* **44**, 267–275 (2006).

213. Gan, B. *et al.* Y-junction carbon nanotubes grown by in situ evaporated copper catalyst. *Chem. Phys. Lett.* **333**, 23–28 (2001).

214. Qin, Y., Zhang, Q. & Cui, Z. Effect of synthesis method of nanocopper catalysts on the morphologies of carbon nanofibers prepared by catalytic decomposition of acetylene. *J. Catal.* **223**, 389–394 (2004).

215. Zhang, Z. *et al.* Growth and field emission property of coiled carbon nanostructure using copper as catalyst. *Appl. Surf. Sci.* **256**, 4417–4422 (2010).

216. Zhou, W. *et al.* Copper catalyzing growth of single-walled carbon nanotubes on substrates. *Nano Lett.* **6**, 2987–2990 (2006).

217. Dileobrian, R. A., Raffaelle, J. L. P., Dileo, R. A. & Landi, B. J. Purity assessment of multiwalled carbon nanotubes by Raman spectroscopy Purity assessment of multiwalled carbon nanotubes by Raman spectroscopy. **064307**, (2016).

218. Nikolaev, P. *et al.* Gas-phase catalytic growth of single-walled carbon nanotubes from carbon monoxide. 91–97 (1999).

219. Lee, H., Yamaoka, S., Murayama, N. & Shibata, J. Dispersion of Fe3O4 suspensions using sodium dodecylbenzene sulphonate as dispersant. **61**, 3974–3977 (2007).

220. Ward, J. W., Wei, B. Q. & Ajayan, P. M. Substrate effects on the growth of carbon nanotubes by thermal decomposition of methane. *Chem. Phys. Lett.* **376**, 717–725 (2003).

221. Fuge, R. *et al.* Influence of different hydrocarbons on the height of MWCNT carpets: Role of catalyst and hybridization state of the carbon precursor. *Diam. Relat. Mater.* **90**, 18–25 (2018).

222. Meysami, S. S., Koós, A. A., Dillon, F., Grobert, N. & Koo, A. A. Aerosol-assisted chemical vapour deposition synthesis of multi-wall carbon nanotubes: I. Mapping the reactor. *Carbon N. Y.* **58**, 151–158 (2013).

223. Meysami, S. S., Dillon, F., Dutta, M., Grobert, N. & Koo, A. A. Aerosol-assisted chemical vapour deposition synthesis of multi-wall carbon nanotubes : III. Towards upscaling. **8**, 0–8 (2015).

224. Han, S., Liu, X. & Zhou, C. Template-free directional growth of single-walled carbon nanotubes on a- and r-plane sapphire. *J. Am. Chem. Soc.* **127**, 5294–5295 (2005).

225. Baker, R. T. K. & Waite, R. J. Formation of carbonaceous deposits from the platinum-iron catalyzed decomposition of acetylene. *J. Catal.* **37**, 101–105 (1975).

226. Endo, M. *et al.* Formation of vapor-grown carbon fibers in Co-Co2-H2 mixtures, I. Influence of carrier gas composition. *Carbon N. Y.* **30**, 859–863 (1992).

227. Schu, C., Rellinghaus, B., Lafdi, K., Schultz, L. & Bu, B. Catalyst Poisoning by Amorphous Carbon during Carbon Nanotube Growth : Fact or Fiction ? 8928–8934 (2011) doi:10.1021/nn2031066.

228. Behr, M. J., Gaulding, E. A., Mkhoyan, K. A. & Aydil, E. S. Effect of hydrogen on catalyst nanoparticles in carbon nanotube growth. *J. Appl. Phys.* **108**, (2010).

229. Ago, H. *et al.* Gas analysis of the CVD process for high yield growth of carbon nanotubes over metal-supported catalysts. *Carbon N. Y.* **44**, 2912–2918 (2006).

230. Baker, R. T. K., Yates, D. J. C. & Dumesic, J. A. Filamentous Carbon Formation over Iron Surfaces. *Coke Form. Met. Surfaces* **202**, 1–21 (1982).

231. Bertoni, G. *et al.* Growth of multi-wall and single-wall carbon nanotubes with in situ high vacuum catalyst deposition. *Carbon N. Y.* **42**, 423–460 (2004).

232. Wirth, C. T. *et al.* The Phase of Iron Catalyst Nanoparticles during Carbon Nanotube Growth. (2012).

233. Homma, Y. *et al.* Role of Transition Metal Catalysts in Single-Walled Carbon Nanotube Growth in Chemical Vapor Deposition. *J. Phys. Chem. B* **107**, 12161–12164 (2003).

234. Robertson, J. *et al.* Controlling the Catalyst During Carbon Nanotube Growth. **8**, (2008).

235. Amama, P. B. *et al.* Role of water in super growth of single-walled carbon nanotube carpets. *Nano Lett.* **9**, 44–49 (2009).

236. Meshot, E. R. Dynamics and Limiting Mechanisms of Self-Aligned Carbon Nanotube Growth by. (2012).

237. Homma, Y., Yamashita, T., Finnie, P., Tomita, M. & Ogino, T. Single-Walled Carbon Nanotube Growth on Silicon Substrates Using Nanoparticle Catalysts. *Jpn. J. Appl. Phys.* **41**, L89–L91 (2002).

238. Kaneko, A., Yamada, K., Kumahara, R., Kato, H. & Homma, Y. Comparative Study of Catalytic Activity of Iron and Cobalt for Growing Carbon Nanotubes on Alumina and Silicon Oxide. *J. Phys. Chem. C* **116**, 26060–26065 (2012).

239. Achtergracht, N. Temperature-Programmed Reduction of Co0 / Ai203 Catalysts. **54**, 38–54 (1985).

240. Moulijn, J. A., Van Diepen, A. E. & Kapteijn, F. Catalyst deactivation: Is it predictable? What to do? *Appl. Catal. A Gen.* **212**, 3–16 (2001).

241. Bom, D. *et al.* Thermogravimetric Analysis of the Oxidation of Multiwalled Carbon

Nanotubes: Evidence for the Role of Defect Sites in Carbon Nanotube Chemistry. *Nano Lett.* **2**, 615–619 (2002).

242. MEYERS, C. E., MASON, T. O., PETUSKEY, W. T., HALLORAN, J. W. & BOWEN, H. K. Phase Equilibria in the System Fe-Al-O. *J. Am. Ceram. Soc.* **63**, 659–663 (1980).

243. Shishin, D., Prostakova, V., Jak, E. & Decterov, S. A. Critical Assessment and Thermodynamic Modeling of the Al-Fe-O System. *Metall. Mater. Trans. B Process Metall. Mater. Process. Sci.* **47**, 397–424 (2016).

244. Reynolds, W. C. & Perkins, H. C. *Engineering Thermodynamics, second ed. McGraw-Hill, New York* (1977).

245. Tripathi, N., Mishra, P., Joshi, B. & Islam, S. S. Precise control over physical characteristics of carbon nanotubes by differential variation of Argon flow rate during chemical vapor deposition processing: A systematic study on growth kinetics. *Mater. Sci. Semicond. Process.* **35**, 207–215 (2015).

246. Kauffman, S. . & Leidner, J. The Preparation and Classification of High Aspect Ratio Mica Flakes for Use in Polymer Reinforcement. *Powder Technol.* **9**, 125–133 (1988).

247. Feilden, E. *et al.* Micromechanical strength of individual Al2O3platelets. *Scr. Mater.* **131**, 55–58 (2017).

248. Le Ferrand, H., Bouville, F., Niebel, T. P. & Studart, A. R. Magnetically assisted slip casting of bioinspired heterogeneous composites. *Nat. Mater.* 1–17 (2015) doi:10.1038/nmat4419.

249. Pelissari, P. I. B. G. B. *et al.* Nacre-like ceramic refractories for high temperature applications. *J. Eur. Ceram. Soc.* **38**, 2186–2193 (2018).

250. Guillon, O. *et al.* Field-assisted sintering technology/spark plasma sintering: Mechanisms, materials, and technology developments. *Adv. Eng. Mater.* **16**, 830–849

(2014).

251. Wang, S. W., Chen, L. D. & Hirai, T. Densification of Al2O3 powder using spark plasma sintering. *J. Mater. Res.* **15**, 982–987 (2000).

252. Shen, Z., Johnsson, M., Zhao, Z. & Nygren, M. Spark Plasma Sintering of Alumina. **27**, 1921–1927 (2002).

253. Santanach, J. G. *et al.* Spark plasma sintering of alumina: Study of parameters, formal sintering analysis and hypotheses on the mechanism(s) involved in densification and grain growth. *Acta Mater.* **59**, 1400–1408 (2011).

254. Dale L. Perry. *Handbook of Inorganic Compounds*. (CRC press, 2011).

255. De Cola, F., Pellegrino, A., Barbieri, E. & Penumadu, D. Void ratio based representative volume element for modelling the high strain rate behaviour of granular materials. *Int. J. Impact Eng.* **91**, 46–55 (2016).

256. Pellegrino, A. & Wear, Á. A. Á. The Dynamic Response of Etnean Sand and the Effect of Its Impingement on Ti-6Al-4 V Alloy. *J. Dyn. Behav. Mater.* **2**, 438–451 (2016).

257. Falco, S. Numerical modelling and experimental characterisation of mechanical performance of ceramic materials at multiple scales. (University of Oxford, 2015).

258. Ratzker, B., Wagner, A., Sokol, M., Kalabukhov, S. & Frage, N. Stress-enhanced dynamic grain growth during high-pressure spark plasma sintering of alumina. *Acta Mater.* **164**, 390–399 (2019).

259. Behr, S., Vainio, U., Müller, M., Schreyer, A. & Schneider, G. a. Large-scale parallel alignment of platelet-shaped particles through gravitational sedimentation. *Sci. Rep.* **5**, 9984 (2015).

260. Chaim, R. Grain growth during spark plasma and flash sintering of ceramic

nanoparticles : a review. 3087–3105 (2018) doi:10.1007/s10853-017-1761-7.

261. Sokolov, A. S. & Harris, V. G. 3D crystallographic alignment of alumina ceramics by application of low magnetic fields. *J. Eur. Ceram. Soc.* **38**, 5257–5263 (2018).

262. Song, F. & Bai, Y. L. Effects of nanostructures on the fracture strength of the. *J. Mater. Res.* **18**, 1741–1744 (2003).

263. Evers, K., Porwal, H., Todd, R. I. & Grobert, N. MWCNT-coated alumina micro-platelets for nacre-like biomimetic composites. *Carbon N. Y.* **145**, 586–595 (2019).

264. Kaczmarek, W. A., Calka, A. & Ninham, B. W. Evaluation of Fe contamination in ball milling of nonmagnetic materials by VSM. *Phys. Status Solidi* **141**, K123–K126 (1994).

265. Compton, B. G., Gamble, E. A. & Zok, F. W. Failure initiation during impact of metal spheres onto ceramic targets. *Int. J. Impact Eng.* **55**, 11–23 (2013).

266. Horsfall, I. & Buckley, D. The effect of through-thickness cracks on the ballistic performance of ceramic armour systems. *Int. J. Impact Engng* **18**, 309–318 (1996).

267. Lankford Jr., J. The Role of Dynamic Material Properties in the Performance of Ceramic Armor. *Int. J. Appl/ Ceram. Technol* **10**, 205–210 (2004).

268. Sarkar, S. & Das, P. K. Temperature and load dependent mechanical properties of pressureless sintered carbon nanotube / alumina nanocomposites. *Mater. Sci. Eng. A* **531**, 61–69 (2012).

269. Sikder, P. *et al.* Improved densification and mechanical properties of spark plasma sintered carbon nanotube reinforced alumina ceramics. *Mater. Chem. Phys.* **170**, 99–107 (2016).

270. Ghobadi, H., Nemati, A., Ebadzadeh, T., Sadeghian, Z. & Barzegar-Bafrooei, H. Improving CNT distribution and mechanical properties of MWCNT reinforced

alumina matrix. *Mater. Sci. Eng. A* **617**, 110–114 (2014).

271. Thomson, K. E., Jiang, D., Yao, W., Ritchie, R. O. & Mukherjee, A. K. Characterization and mechanical testing of alumina-based nanocomposites reinforced with niobium and/or carbon nanotubes fabricated by spark plasma sintering. *Acta Mater.* **60**, 622–632 (2012).

272. Wang, X., Padture, N. P. & Tanaka, H. Contact-damage-resistant ceramic/ single-wall carbon nanotubes and ceramic/graphite composites. **3**, 539–544 (2004).

273. Lee, K., Mo, C. Bin, Park, S. Bin & Hong, S. H. Mechanical and electrical properties of multiwalled CNT-alumina nanocomposites prepared by a sequential two-step processing of ultrasonic spray pyrolysis and spark plasma sintering. *J. Am. Ceram. Soc.* **94**, 3774–3779 (2011).

274. Xia, Z., Riester, L., Curtin, W. A., Li, H. & Sheldon, B. W. Direct observation of toughening mechanisms in carbon nanotube ceramic matrix composites. **52**, 931–944 (2004).

275. Le, V. T. *et al.* Surface modification and functionalization of carbon nanotube with some organic compounds. *Adv. Nat. Sci. Nanosci. Nanotechnol.* **4**, (2013).

276. Shirasu, K., Yamamoto, G., Nozaka, Y., Wang, W. & Hashida, T. Relationship between microstructure and mechanical properties in acid-treated carbon nanotube-reinforced alumina composites. *J. Mater. Sci.* **50**, 6688–6699 (2015).

277. Yamamoto, G., Omori, M., Yokomizo, K. & Hashida, T. Mechanical properties and structural characterization of carbon nanotube/alumina composites prepared by precursor method. *Diam. Relat. Mater.* **17**, 1554–1557 (2008).

278. A. Mukhopadhyay *et al.* Thermal and electrical properties of aluminoborosilicate glass – ceramics containing multiwalled carbon nanotubes. *Scr. Mater.* **65**, 408–411 (2011).

279. Mukhopadhyay, A. *et al.* Thermal and electrical properties of aluminoborosilicate

glass-ceramics containing multiwalled carbon nanotubes. *Scr. Mater.* **65**, 408–411 (2011).

280. Estili, M. *et al.* Multiwalled carbon nanotube-reinforced ceramic matrix composites as a promising structural material. *J. Nucl. Mater.* **398**, 244–245 (2010).

281. Wu, W. W., Estili, M., Zhang, G. J. & Sakka, Y. Dispersion and structural evolution of multi-walled carbon nanotubes in ZrB2 matrix. *Ceram. Int.* **43**, 10533–10539 (2017).

282. Estili, M. *et al.* The homogeneous dispersion of surfactantless, slightly disordered, crystalline, multiwalled carbon nanotubes in α-alumina ceramics for structural reinforcement. *Acta Mater.* **56**, 4070–4079 (2008).

283. Yamamoto, G., Omori, M., Yokomizo, K., Hashida, T. & Adachi, K. Structural characterization and frictional properties of carbon nanotube/alumina composites prepared by precursor method. *Mater. Sci. Eng. B Solid-State Mater. Adv. Technol.* **148**, 265–269 (2008).

284. Estili, M., Sakka, Y. & Kawasaki, A. Unprecedented simultaneous enhancement in strain tolerance, toughness and strength of Al2O3 ceramic by multiwall-type failure of a high loading of carbon nanotubes. *Nanotechnology* **24**, (2013).

285. Estili, M., Kawasaki, A. & Sakka, Y. Highly Concentrated 3D Macrostructure of Individual Carbon Nanotubes in a Ceramic Environment. 4322–4326 (2012) doi:10.1002/adma.201201134.

286. Kasperski, A., Weibel, A., Estournès, C., Laurent, C. & Peigney, A. Multi-walled carbon nanotube-Al2O3 composites: Covalent or non-covalent functionalization for mechanical reinforcement. *Scr. Mater.* **75**, 46–49 (2014).

287. Wang, W. L., Yamamoto, G., Shirasu, K., Nozaka, Y. & Hashida, T. Microstructure and mechanical properties of multi-walled carbon nanotube/alumina composites prepared by a novel flocculation method. *16th Eur. Conf. Compos. Mater. ECCM 2014*

22–26 (2014).

288. Zhu, Y. F., Shi, L., Liang, J., Hui, D. & Lau, K. tak. Synthesis of zirconia nanoparticles on carbon nanotubes and their potential for enhancing the fracture toughness of alumina ceramics. *Compos. Part B Eng.* **39**, 1136–1141 (2008).

289. Xiao, A. W., Tkaczyk, M. & Jones, R. S. "Buckyfilms" – Electrophoretic and Electrochemical Methods for Robust Carbon Nanotube Films.

290. Mahalingam, P., Parasuram, B., Maiyalagan, T. & Sundaram, S. Chemical Methods For Purification Of Carbon Nanotubes-A Review. *J. Environ. Nanotechnol* **1**, 53–61 (2012).

291. Chu, B. T.-T. Carbon nanotube reinforced inorganic matrix. (University of Oxford, 2008).

292. Kwan, Y. B. P. & Alcock, J. R. The impact of water impregnation method on the accuracy of open porosity measurements. *J. Mater. Sci.* **37**, 2557–2561 (2002).

293. Goldberg, I. S., Garcia, M., Maswadi, S., Thomas, R. J. & Clark III, C. D. Conduction and Convection of Heat Produced by the Attenuation of Laser Beams in Liquids. (2007).

294. Vieira, A. W. *et al.* Comparison of methods for determining the water absorption of glazed porcelain stoneware ceramic tiles. *Mater. Res.* **20**, 644–650 (2017).

295. Heath, T. L. The Works of Archimedes. *Www-Tc.Pbs.Org* 326 (1897) doi:10.1038/057409a0.

296. BSI. Advanced technical ceramics — Monolithic ceramics — General and textural properties. in *Part 2: Determination of density and porosity* vol. BS EN 623- (1993).

297. Hennrich, F. *et al.* The mechanism of cavitation-induced scission of single-walled carbon nanotubes. *J. Phys. Chem. B* **111**, 1932–1937 (2007).

298. Sezer, N. & Koç, M. Stabilization of the aqueous dispersion of carbon nanotubes using different approaches. *Therm. Sci. Eng. Prog.* **8**, 411–417 (2018).

299. Inam, F., Yan, H., Reece, M. J. & Peijs, T. Dimethylformamide: An effective dispersant for making ceramic-carbon nanotube composites. *Nanotechnology* **19**, (2008).

300. Ba, M., Novak, M., Kokanovi, I. & Babi, D. Composites of multiwall carbon nanotubes and conducting polyaniline : Bulk samples and fi lms produced from a solution in chloroform. **19**, 775–779 (2019).

301. Sun, G., Liu, Z. & Chen, G. Dispersion of pristine multi-walled carbon nanotubes in common organic solvents. *Nano* **5**, 103–109 (2010).

302. Shaffer, B. M. S. P. & Windle, A. H. Fabrication and Characterization of Carbon Nanotube / Poly (vinyl alcohol) Composites. 937–941 (1999).

303. Andrews, R., Jacques, D., Qian, D. & Dickey, E. C. Purification and structural annealing of multiwalled carbon nanotubes at graphitization temperatures. *Carbon N. Y.* **39**, 1681–1687 (2001).

304. Behler, K., Osswald, S., Ye, H., Dimovski, S. & Gogotsi, Y. Effect of thermal treatment on the structure of multi-walled carbon nanotubes. *J. Nanoparticle Res.* **8**, 615–625 (2006).

305. Prasad, N., Kumari, A., Bhatnagar, P. K., Mathur, P. C. & Bhatia, C. S. Current induced annealing and electrical characterization of single layer graphene grown by chemical vapor deposition for future interconnects in VLSI circuits. *Appl. Phys. Lett.* **105**, (2014).

306. Reinert, L., Suárez, S. & Rosenkranz, A. Tribo-mechanisms of carbon nanotubes: Friction and wear behavior of CNT-reinforced nickel matrix composites and CNT-coated bulk nickel. *Lubricants* **4**, (2016).

307. Zhang, X., Wang, Z., Sun, X., Han, W. & Hong, C. Effect of graphite flake on the

mechanical properties of hot pressed ZrB2-SiC ceramics. *Mater. Lett.* **62**, 4360–4362 (2008).

308. Su, Z. *et al.* Multifunctional anisotropic flexible cycloaliphatic epoxy resin nanocomposites reinforced by aligned graphite flake with non-covalent biomimetic functionalization. *Compos. Part A Appl. Sci. Manuf.* **109**, 472–480 (2018).

309. Sun, Y. F., Shek, C. H., Guan, S. K., Wei, B. C. & Geng, J. Y. Formation, thermal stability and deformation behavior of graphite-flakes reinforced Cu-based bulk metallic glass matrix composites. *Mater. Sci. Eng. A* **435–436**, 132–138 (2006).

310. Liu, J. *et al.* Spark plasma sintering of graphene platelet reinforced zirconia composites with improved mechanical performance. *Mater. Sci. Eng. A* **688**, 70–75 (2017).

311. Walther, J. H., Jaffe, R., Halicioglu, T. & Koumoutsakos, P. Carbon nanotubes in water: Structural characteristics and energetics. *J. Phys. Chem. B* **105**, 9980–9987 (2001).

312. Laurent, C., Flahaut, E. & Peigney, A. The weight and density of carbon nanotubes versus the number of walls and diameter. *Carbon N. Y.* **48**, 2994–2996 (2010).

313. Balani, K. & Agarwal, A. Wetting of carbon nanotubes by aluminum oxide. *Nanotechnology* **19**, (2008).

314. Clews, F. H. The Interaction of Sodium Chloride and Alumina. *About J. Chem. Soc. Trans.* **735**, (1925).

315. Huang, Y. Y. & Terentjev, E. M. Dispersion of carbon nanotubes: Mixing, sonication, stabilization, and composite properties. *Polymers (Basel).* **4**, 275–295 (2012).

316. Yi, M. & Shen, Z. A review on mechanical exfoliation for the scalable production of graphene. *J. Mater. Chem. A* **3**, 11700–11715 (2015).

317. Biccai, S. *et al.* Exfoliation of 2D materials by high shear mixing. *2D Mater.* **6**, (2019).

318. Graf, A. *et al.* Large scale, selective dispersion of long single-walled carbon nanotubes

with high photoluminescence quantum yield by shear force mixing. *Carbon N. Y.* **105**, 593–599 (2016).

319. Park, Y. M., Lee, D. H., Hwang, W. R., Lee, S. B. & Jung, S. Il. Hydrodynamics of CNT dispersion in high shear dispersion mixers. *Korea Aust. Rheol. J.* **26**, 347–353 (2014).

320. Demuynck, M., Erauw, J. P., Van der Biest, O., Delannay, F. & Cambier, F. Densification of alumina by SPS and HP: A comparative study. *J. Eur. Ceram. Soc.* **32**, 1957–1964 (2012).

321. Liu, D. *et al.* Spark plasma sintering of cryomilled nanocrystalline Al alloy - Part II: Influence of processing conditions on densification and properties. *Metall. Mater. Trans. A Phys. Metall. Mater. Sci.* **43**, 340–350 (2012).

322. Guillard, F., Allemand, A., Lulewicz, J. D. & Galy, J. Densification of SiC by SPS-effects of time, temperature and pressure. *J. Eur. Ceram. Soc.* **27**, 2725–2728 (2007).

323. Mukhopadhyay, A., Chu, B. T. T., Green, M. L. H. & Todd, R. I. Understanding the mechanical reinforcement of uniformly dispersed multiwalled carbon nanotubes in alumino-borosilicate glass ceramic. **58**, 2685–2697 (2010).

324. Chiou, S. & Hahn, H. T. Ultrasonic Sol/Gel Processing of Aluminoborosilicate Glass and Its Composite with Carbon Fiber Reinforcement. *J. Am. Ceram. Soc.* **77**, 155–160 (1994).

325. Monteiro, R. C. C. & Lima, M. M. R. A. Effect of compaction on the sintering of borosilicate glass/alumina composites. *J. Eur. Ceram. Soc.* **23**, 1813–1818 (2003).

326. López, M. I. & Meyers, M. A. The organic interlamellar layer in abalone nacre: Formation and mechanical response. *Mater. Sci. Eng. C* **58**, 7–13 (2016).

327. Achenani, Y., Saâdaoui, M., Cheddadi, A., Bonnefont, G. & Fantozzi, G. Finite element modeling of spark plasma sintering: Application to the reduction of

temperature inhomogeneities, case of alumina. *Mater. Des.* **116**, 504–514 (2017).

328. Lin, A. Y., Chen, P. & Andre, M. The growth of nacre in the abalone shell. **4**, 131–138 (2008).

329. Deville, S. Ice-templating, freeze casting: Beyond materials processing. *J. Mater. Res.* **28**, 2202–2219 (2013).

330. Deville, S. Freeze-Casting of Porous Biomaterials: Structure, Properties and Opportunities. 1913–1927 (2010) doi:10.3390/ma3031913.